Microfluidics for assessing the behaviour of deformable biological objects

PhD Thesis

Joana Fidalgo

James Weir Fluids Laboratory

Mechanical and Aerospace Engineering

University of Strathclyde

Glasgow 2019

This thesis is the result of the author's original research. It has been composed by the author and has not been previously submitted for examination, which has led to the award of a degree.

The copyright of this thesis belongs to the author under the terms of the United Kingdom Copyright Acts as qualified by University of Strathclyde Regulation 3.50. Due acknowledgement must always be made of the use of any material contained in, or derived from, this thesis.

<div align="right">

Joana Fidalgo

February 2019

</div>

Abstract

Biological fluids, composed of polymeric solutions or suspensions of deformable particles, commonly present complex rheological behaviour. It is well known that particle-fluid interactions at the microscale dictate the macroscopic flow behaviour of these fluids, however the exact link in numerous situations is still missing. Recently, microfluidic techniques have been widely employed to study the dynamics of microscopic particles under flow. Even though such techniques present a range of advantages, including the precise control of the flow conditions, as well as the consumption of a small amount of sample, the design of the microfluidic geometries still mostly relies on a trial-and-error approach. In this thesis, we experimentally test a set of microfluidic geometries, the design of which was previously optimised based on theoretical considerations or by means of numerical simulations in order to achieve specific flow conditions. In addition, we have used complex observation techniques to study the dynamics of solutions and suspensions under flow, identifying microscopic dynamics as well as the major limitations of the microfluidic devices. Biological fluids such as solutions of DNA molecules and red blood cells suspensions were investigated in shear-dominated and extension-dominated flows and the performance of the optimised flow geometries for the study of such biological fluids was demonstrated.

Keywords: experimental microfluidics; optimised geometries; biological fluids; DNA solution; Red Blood Cell suspension; fluid-structure interaction; low Reynolds number

Résumé

Les fluides biologiques, qui sont composés de solutions de polymères ou de suspensions de particules déformables, présentent généralement un comportement rhéologique complexe. Il est bien connu que les interactions particules-fluide à l'échelle microscopique dictent le comportement macroscopique de ces fluides en écoulement, mais le lien exact dans de nombreuses situations est toujours méconnu. Récemment, l'utilisation de techniques microfluidiques a été largement développée pour étudier la dynamique de particules microscopiques sous écoulement. Même si ces techniques présentent de nombreux avantages, notamment le contrôle précis des conditions d'écoulement, et la consommation de faibles quantités d'échantillon, les géométries microfluidiques sont encore essentiellement conçues par une approche essai/erreur. Dans cette thèse, nous testons expérimentalement un ensemble de géométries microfluidiques, dont la conception a été auparavant optimisée pour des conditions d'écoulement spécifiques, à partir de considérations théoriques ou au moyen de simulations numériques. Pour étudier la dynamique des solutions et des suspensions sous écoulement, des techniques d'observation complexes ont été développées et ont permis de d'identifier la dynamique microscopique ainsi que les principales limitations des dispositifs microfluidiques existants. Dans cette thèse, des solutions de molécules d'ADN et des suspensions de globules rouges ont été étudiées dans des écoulements dominés par le cisaillement et par l'extension et la performance des géométries optimisées pour l'étude de ces fluides biologiques a été démontrée.

Mots-clé: microfluidique expérimentale; géométries optimisées; fluides biologiques; Solution d'ADN; Suspension de globules rouges; interaction fluide-structure; faible nombre de Reynolds

To my dear parents…

Aknowledgements

I would like to express my gratitude to those who were involved in this PhD, making it an incredible journey.

First of all, I would like to thank my supervisor Mónica Oliveira for giving me the oportunity to do a PhD in this topic, which I was really interested about for a long time. I was very happy to find her guidance and encouragement along the way, as well as her patience to deal with my anxious moments. I am very thankful for her kindness and true example of endurence. Also, for giving me the freedom I needed to manage this PhD.

Secondly, I would like to thank Anke Lindner. I am really grateful that she accepted to co-supervise this PhD, allowing me to make part of her research group where I always felt welcome and where I could easily discuss my work and grow up as a researcher. I believe this was a great advantage for my PhD and I am truly thankful for having her constant guidance with a great amount of optimism. That was precious in many times along the project.

I would also like to thank Prof. Fernão de Magalhães for his previous mentoring at FEUP. I truly enjoyed the years spent in this institution, before starting the PhD. I grew up a lot under his supervision and I also understand now that I would not have the required skills to embrace this PhD without this previous training. I am thankful for his mentorship, for his constant encouragement, his calm and patience along the years. In the same way, I would like to thank Ângela Dias for teaching me about the persistance and resilience necessary to pursue a PhD, always doing it with a smile. I would also like to thank Nuno Azevedo who made me aware of this PhD grant and for his trust in me to do the job.

I would like to aknowledge Rui Lima for his constant availability throughout the project, providing me the access to his laboratory so I could learn the techniques necessary to perform blood experiments, as well as interesting discussions. Thank you also to his students for receiving me so well, in particular to Diana Pinho.

I would like to thank my coworkers Yanan Liu, Charles Zhou and Konstantinos Zografos as well as Olivia du Roure, Thierry Darnige, Timm Krüger, Miguel O.Bernabeu and Manuel Alves for very useful discussions, allowing me to widen my knowledge on the field. This also allowed me to better plan my experiments, interpretate the results and understand them from another point of view. Thank you also to Laura Casanellas and Charles Dûchene for presenting me the microfabrication techniques and to the students whom I had the oportunity to teach in the laboratory, Thomas Lund and Sérgio Costa, whose questions always made me research a bit more.

Contents

List of Figures

Chapter 4

Chapter 7

Appendix A

Appendix C

Appendix D

Appendix E

List of Tables

Glossary

Δt	time-step
Δx	displacement step
Δp	pressure drop
Λ	viscosity ratio
Ω	angular velocity
α	inflow contraction
β	geometrical confinement
$\dot{\gamma}$	shear rate
$\dot{\varepsilon}$	strain rate
η	viscosity as a function of shear rate
θ	angle
λ	relaxation time
λ_{EX}	excitation wavelength
λ_{EM}	emission wavelength
μ	constant viscosity
ρ	density
τ	shear stress
p	pressure
Ca	Capillary number
c*	overlap concentration
d	diameter
D	diffusion coefficient
De	Deborah number
D_h	hydraulic diameter
D_{hole}	flow extension diameter
f_{camera}	camera frequency
f_{stage}	stage frequency
F	force
h	channel depth
i	network generation
L	length
L_c	contour length
L_p	persistence length

k	consistency index
k_B	Boltzmann constant
K_s	membrane shear elasticity
m	body mass
M	torque
M_w	molecular weigth
n	power-law index
N_A	Avogadro constant
Pe	Peclet number
Re	Reynolds number
r	radius
R_g	radius of gyration
T	temperature
t_R	residence time
t_{obs}	time of observation
Q	flow rate
V	volume
u	velocity
w	channel width
Wi	Weissenberg number
X	branching parameter
x,y,z	Cartesian coordinates

Acronyms

2D	Two dimensional
3D	Three dimensional
AFM	Atomic force microscopy
AR	Aspect ratio
bp	base pair
CAD	Computer aided design
CCD	Charged coupled device
CFL	Cell-free layer
CP	Cone-plate
CR	Contraction ratio
DOF	Depth of Field
DNA	Deoxyribonucleic acid
λ-DNA	Lambda-phage DNA
Dx40	Dextran 40
DMSO	Dimethyl sulfoxide
EDTA	Ethylenediamine tetraacetic acid
Hct	Hematocrit
NA	numerical aperture
PAA	Polyacrylic Acid
PDMS	Polydimethylsiloxane
PMMA	Poly(methyl methacrylate)
PP	Plate-plate
PS	Physiologic saline
PTV	Particle tracking velocimetry
RBC	Red blood cell
ROI	Region of interest
TB	Tumbling
TT	Tank treading
WB	Whole blood

CHAPTER 1

General Introduction

1.1 Characterisation of biological fluids

Biological fluids are typically complex fluids formed by particle suspensions or polymeric solutions. Common examples include: cells (a suspension of organelles), blood (a suspension of cells, platelets and proteins among other compounds), respiratory mucus, synovial fluid or vitreous humor (solutions of specific polymers).

It is well known that the overall rheological properties of these fluids are determined by events occurring at the microscopic level, this is, the interaction of the suspended particles or polymers with the suspending fluid. In the case of suspensions, the particle properties such as shape, size or deformability, as well as the nature of the suspending fluid (being Newtonian or non-Newtonian), will determine the flow properties when a certain stress is applied. The study of the microscopic dynamics is thus of extreme importance to understand processes occurring at the macroscale, but also for designing applications at the microscale, such as the microscopic separation of individual components from a biological sample for subsequent lab-on-a-chip diagnosis.

Microfluidics is an interesting technique for such studies since it allows the precise control of the flow variables, either by imposing a flow rate or pressure difference in the microfluidic channel of different geometries, according to the study in mind. There have been several studies on the use of microfluidic devices to study the behaviour of microscopic particles in flow, or the flow of polymeric solutions. These studies often lye in the biological and biomedical field, where the design of the microfluidic device plays an important role. A brief overview of this field and its use in key areas are highlighted in the following sections (sections 1.2 and 1.3).

Important progress has been made over the years, on the characterisation of microscopic particle dynamics under flow using microfluidic devices. Nonetheless, the geometries used are often relatively simple while the flow control and the observation conditions are not always optimal. In this thesis, we rely on a rational approach beyond simple trial-and-error for intelligent channel design in order to build microfluidic devices with specific flow

1

properties. Also, sophisticated observation techniques were implemented to improve the analysis of the objects transported in the flow. Biological particles, such as red blood cells, as well as polymers (DNA) were used to probe the efficiency of these devices.

In the next sections recent findings on microfluidics and its use for the investigation of biological fluids will be given and the thesis outline will be presented.

1.2 Microfluidics

Microfluidics refers to science and engineering systems used to handle and study fluids at the small length scale, in the order of tens to hundreds of micrometers.[1] Figure 1.1 presents the length scales of common biological objects, from protein molecules to complex living organisms.[2] From the broad range of scales presented, we will focus on the microscale, which is typical of biological elements such as cells or polymeric filaments.
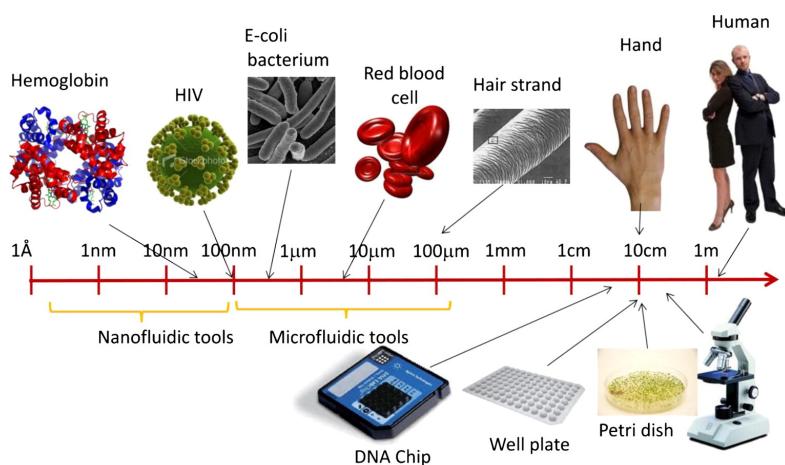
Figure 1.1: Length scales of typical biological objects ranging from proteins to complex living organisms (adapted from Nguyen *et al.*[2]).

Despite a few exceptions involving very viscous fluids (e.g. lava), the fluid flow at the macro scale is often dominated by inertia. A simple example is the mixing of milk in a cup of coffee, where the fluid will continue in motion after the spoon is removed. On the contrary, in microfluidics, inertia is small[3] or even negligible and the flow is laminar. Indeed, as consequence of the small length scale associated to microfluidic flows, the surface forces (such as those associated with viscous friction, surface tension or molecular diffusion) dominate over volume forces (such as gravity or inertia) due to the high surface-to-volume ratio.

Microfluidics presents several advantages, one of them being the low volume of sample and reagents required to perform an experiment, as well as the small amount of waste produced.[4] This consideration is particularly attractive if the amount of available sample is limited or expensive, as is typical for biological and pharmacological fluids, respectively. Another important advantage of this technology is the low-cost production of the microfluidic devices. There is an extensive list of fabrication techniques available but the most commonly used are photo-lithography and soft-lithography[5] for the production of the mould and polymeric channels, respectively. Even though the mould can be expensive, when a high resolution is required, it can also be reused to produce a large number of replica channels.

As a result, microfluidics has been applied in distinct fields of research, from chemistry to engineering, biology[6] or medicine.[7,8] Examples of common operations are enhanced oil recovery (EOR),[9] drug delivery,[2,10] bio-sensing,[11] single cell analysis,[12] synthesis,[13] separation,[14] purification[15,16] or rheology-on-a-chip (ROC).[3] The integration of microfluidic components, performing multiple operations in one single device has led to Lab-on-a-chip (LOC),[2] point-of-care (POC)[17] diagnostic devices and micro Total Analysis Systems (µTAS).[18] Some of these are commercially available,[19] mainly for medical diagnostics, and are particularly valuable in physical locations where standard laboratory facilities or financial resources are scarce.[19]

Arguably the majority of such devices are still designed empirically based on a trial and error approach and, as consequence, to obtain a microfluidic device with the desired performance often becomes a time consuming and expensive process. Thus, it becomes imperative to find accurate tools to predict the optimal geometry design for the application under consideration. For the last 50 years, computer power and numerical methods have been improved massively[20] and several algorithms have been proposed to simulate fluid flows at the microscale, depending on the fluid properties and flow conditions. In the context of device design, numerical simulations can play an important role predicting the microfluidic geometry, using an intelligent approach, to achieve a better performance. Also, numerical simulations have proved to be efficient in predicting the shape of complex biological objects under flow, such as red blood cells (RBC)[21,22] or DNA molecules,[23,24] which are the two biological elements studied in this work.

1.3 Examples of microfluidic devices for studying biological fluids

In the last years, several research studies have been presented on the use of microfluidic devices for biological applications. The careful design of the channel's dimensions and

features has been demonstrated crucial to create the most favorable hydrodynamic conditions, according to the application in mind. A few examples of studies involving complex microfluidic geometries for point-of-care diagnosis, generation of gradients, targeted drug delivery and cell/particle separation are described below:

- Point-of-care *in vitro* diagnosis

Healthy RBC are highly deformable so they can easily flow along the microvasculature, in particular passing through the capillaries, which can be as small as half their size. Some pathological conditions play an important impact on the mechanical properties of the RBC membrane, compromising its flexibility. As a consequence, the occlusion of smaller vessels might occur, followed by local inflammation and tissue necrosis. Thus, the flow of RBCs along microfluidic devices with specific designs could provide a simple test to detect unhealthy blood cells and, therefore, blood diseases. For example, Rosenbluth *et al.*[25] proposed a microfluidic device where single-cells pass through an *in vitro* capillary network. They found out that infected erythrocytes, provided by patients with sepsis and leukostasis, presented longer residence time in the capillaries when compared to the control healthy cells, mainly due to the increased mechanical resistance to deformation. Also, Yaginuma *et al.*,[26] presented a study on RBC deformation in a homogeneous extensional flow field generated by a hyperbolic-shaped microchannel. They suggest that due to the strong extensional flow, the healthy cells are highly deformed close to the channel contraction, in contrast to the rigid cells that maintain their initial shape, and therefore, this geometry could be used as a point-of-care diagnostics for blood diseases associated with cell rigidity.

- Generation of chemical gradients using microfluidic networks

A particular attention has been devoted to microfluidic geometries for the generation of gradients (for example chemical or oxygen gradients) in biological activities, since these gradients exist *in vivo* and play an important role in the regulation of cell function. For instance, chemotaxis refers to the migration of organisms towards environmental conditions they find attractive, or away from surroundings they find repellent, according to a chemical gradient.[27] This biased movement explains the migration of neutrophils into regions of infection, after local release of chemoattractants by the host cell or microorganism.[28] Dertinger *et al.*[29] demonstrated how a complex geometry design, constituted by consecutive branching points, could be used to generate stable gradients for both biological and non-biological research. This microfluidic network allowed a controlled mixing by diffusion, due to the laminar and side-by-side movement of the fluid along the channels.

Also Chang *et al.*[30] demonstrated with success how to subject a cell culture to a chemical and oxygen gradient, using a sandwich device combining PDMS and PC (polycarbonate). In this study, a network of channels feeds a chamber, on the lower PDMS plate, where the cells were cultured. This means the amount of nutrients and chemicals varies across the chamber width and perpendicularly to the flow direction. A thin and permeable PDMS layer divides the PDMS bottom and PC upper layer of the device, where a serpentine channel provides the oxygen flow for cell maintenance. With a simple apparatus the authors managed to simultaneously test the effects of chemical and oxygen concentrations, on the cell growth.

- Generation of shear gradients using microfluidic networks

Besides the examples previously described on the generation of chemical gradients, other microfluidic geometries were designed with the purpose of generating a shear gradient to either solutions or suspensions of objects under flow. For example, Kou *et al.* [31] used a microfluidic system to test the dynamics of cytosolic calcium concentration $[Ca^{2+}]$ in osteoblasts. For this, the authors built four chambers of different widths connected to the same fluid inlet. The flow rate provided to each chamber was the same but the shear stress imposed to the cells cultured inside them was distinct, generating a diverse cell response. They found out that the cytosolic calcium concentration increased proportionally to the shear stress applied to the cells.

- Targeted drug delivery using local shear variations

Other studies focused on the use of microfluidic channels to investigate the regression of atherosclerosis, thrombosis or embolism with targeted drug release. These pathologies are associated to a high mortality rate and are mainly characterised by the narrowing of the blood vessels. The peak in shear stress caused by the channel constriction, when compared to a constant shear stress in a healthy and non-deformed blood vessel, corresponds to the trigger for the mechanism of local drug release. Korin *et al.* [32] presented an encouraging study using contraction-expansion geometry to mimic a narrowed blood vessel. They used aggregates of shear activated nano-therapeutics (SA-NT), with sizes close to human platelets (1-5 μm), and proved that the local release of these aggregates in the channel constriction was, at least, 10 times larger than the amount released in a non-constricted channel. These results were confirmed by a parallel *in vivo* study, where the same drug was administrated intravenously to a mouse with a thrombus. The SA-NT aggregates were efficiently released in the constricted area, allowing the successful dissolution of the blood clot in less than five minutes. Another study, by Holme *et al.*,[33] used a microfluidic system with a constricted channel to study the effect of the liposome shape on the drug release. In this case, the

nanotherapeutic particles were encapsulated in liposomal vesicles of lenticular shape. These are stable at steady shear stress conditions but particularly sensitive to the peak of shear stress, in the constriction of the channel, optimising the release of the encapsulated drug.

- Cell/particle separation

Several methods have been proposed to separate, concentrate or analyse particles in microfluidic devices,[34] since these operations are commonly required for clinical analysis. The complexity of biological samples, as whole blood or saliva, as well as the small concentration of the analyte for detection, requires successful separation and purification processes to achieve accurate and reliable results. The separation might be accomplished either by active or passive techniques, where the former relies on an external field in order to cause a preferential movement of the particles, such as electric field or acoustophoresis, and the latter relies on processes like sedimentation, filtration, lateral displacement or hydrodynamic effects.[35] In general, separation using passive methods is preferred since it requires a simpler device, at a lower cost, and with easier possibility to integrate with biosensors. Yamada et al. [36] presented a study where a mixture of rat liver cells was successfully separated, by hydrodynamic filtration, according to their size. The cell suspension was infused in a microchannel with lateral branches and, while the smaller cells were removed through the side branches, the larger ones travelled along the main channel for posterior separation into distinct groups. This method allowed a good efficiency of separation without compromising the cell viability.

An important separation process, which is still receiving great attention at the moment, is the extraction of plasma from the whole blood, based on hydrodynamic effects. In this case, the separation is a contribution of the biophysical properties of the sample, as the size, shape and deformability of the blood cells; the geometrical effects, namely the channel's dimensions and features; and inertial effects. Tripathi et al. [35] presented an interesting review on the plasma separation from blood using passive techniques, namely on the influence of the channel's design. Also, Di Carlo[37] and Amini et al. [38] presented important reviews on the use of inertial focusing to achieve separation in microfluidic devices. They provided not only examples of experimental studies but also the background theory supporting their main results. Even though efficient blood/plasma separation can be achieved by inertial focusing, it typically requires higher velocities and, thereafter, larger volumes of sample.

Therefore, microfluidic cell sorting techniques have definitely revolutionised the way to separate and analyse cells, where in some cases the performances are comparable or even

superior to the bench top tools available. Anyhow, there is still a long path for improvement in order to make these devices commercially available.[39]

1.4 Aims and outline of the thesis

The main aim of this work is to investigate (from an experimental point of view) the performance of intelligently designed microfluidic devices (based on demanding numerical computation and/or theoretical analysis) to assess the dynamics and deformation of individual biological elements under well-controlled flow conditions. In this work, we rely on biological elements such as RBC and DNA molecules in microfluidic geometries, such as straight channels, bifurcating networks and converging-diverging geometries. While the flow is shear dominated in the straight channel, the flow in the converging-diverging geometries exhibits mixed kinematics, with a strong extensional flow along the centreline.

In this thesis we discuss the experimental implementation and setup limitations associated with using such specific designs and propose possible solutions for their future use in biological and/or biomedical applications. A list of the main tasks is described below:

- Experimental implementation and testing of bifurcating networks, the design of which is inspired by Murray's law to generate well defined flow conditions in consecutive channel generations, to analyse biopolymer dynamics and the deformation of individual objects under specific shear stress conditions in shear flow;

- Experimental implementation and testing of converging-diverging channels designed to provide an extended region of homogeneous strain rate to analyse the polymer or particle dynamics in extensional flow along the channel centreline;

- Investigation of the effect of the microfluidic channel entrance on the RBC distribution in microfluidic channels, when using a low cell volume fraction (hematocrit) under low inertia conditions, typical of microfluidics flows.

- Assessing the viability of bifurcating networks and other network inspired microfluidic geometries to study RBC suspension dynamics; for some of those geometries, we evaluate their potential for the process of RBC separation from the suspending medium;

The present work has so far led to one (1) publication in an international journal (presented in Chapter 4) and one (1) publication in a conference proceeding (presented in Appendix E). Moreover, different parts of this research have been presented in different conferences, with 3 oral presentations and 8 posters, one of which was distinguished with *best poster award*.

Following this introductory chapter, Chapter 2 presents important background on biological molecules and particles in microfluidic flows, including λ-DNA molecules and RBCs, which are the two biological elements used in this work. The information provided in this chapter allows a better interpretation of the data presented in each results chapter. Since this thesis comprises data on distinct types of microfluidic geometries and biological samples, only a general overview is provided here, with specific details presented in the introduction of each results chapter.

Chapter 3 presents a detailed description of the experimental techniques and methodology employed throughout the project, from the design and fabrication of the microfluidic devices to the methods used for fluid and flow characterisation. The generic laboratory setup and equipment used are presented. Other details, such as the preparation of samples and particularities of the microscopic setup or methodology for each set of experiments, are described in the relevant results chapters.

Chapter 4 describes the flow of a λ-DNA solution in bifurcating networks. The geometries' design was inspired by Murrays' law and allows imposing a controlled shear stress distribution according to the application in mind. These geometries were first studied by Zografos *et al.*,[40] by means of numerical simulations, and are suitable for use with both Newtonian and non-Newtonian fluids. The experimental implementation and main results achieved by the experiments, as well as the experimental limitations of the devices are described in this chapter and resulted in a publication in *Biomicrofluidics* journal.

Chapter 5 describes the flow of the same λ-DNA molecules in optimised converging-diverging channels,[41] specifically designed to generate a region of constant strain rate along a significant length of the channel centreline. These geometries demonstrate potential to evaluate the dynamics of objects sensitive to the flow gradient in extensional flow. For this purpose, a LabView interface was developed to allow the controlled displacement of the microscope platform, imposing the same velocity profile as the one described by the object under flow. This new feature would ensure the tracking of individual objects transported along the converging-diverging channel centreline and subjected to specific hydrodynamic flow conditions. The experimental implementation, the main results achieved as well as the setup limitations are described in this chapter.

Chapter 6 focuses on the RBC distribution across the width of a simple straight microfluidic channel (of aspect ratio ~3) under low inertia conditions. We discuss an interesting two-peak density resembling that obtained for experiments where inertia is significant and analyse the underlying causes for such an effect. We compare our experiments with numerical

simulations (in collaboration with colleagues at the University of Edinburgh) and discuss the effect of various parameters on the RBC distribution and the development of a cell free layer next to the channel walls.

Chapter 7 describes preliminary results on the effect of the microfluidic channel geometry on the dynamics of red blood cell suspensions. Based on a preliminary study using a bifurcating network (akin to that used in Chapter 4), new microfluidic geometries were also considered to assess the influence of individual design features on the separation efficiency. The studied features were the sequential increase in channel diameter as well as the introduction of curvature in the channel, using a straight channel of constant cross-section as control.

Chapter 8 summarises the main conclusions of this thesis and provides suggestions for future work based on the main achievements.

References

1. Zhang, J. *et al.* Fundamentals and applications of inertial microfluidics: a review. *Lab Chip* **16,** 10–34 (2016).

2. Nguyen, N. T., Shaegh, S. A. M., Kashaninejad, N. & Phan, D. T. Design, fabrication and characterization of drug delivery systems based on lab-on-a-chip technology. *Adv. Drug Deliv. Rev.* **65,** 1403–1419 (2013).

3. Lindner, A. & Arratia, P. E. Preface to Special Topic: Invited Articles on Microfluidic Rheology. *Biomicrofluidics* **10,** 043301 (2016).

4. Sia, S. K. & Whitesides, G. M. Microfluidic devices fabricated in poly(dimethylsiloxane) for biological studies. *Electrophoresis* **24,** 3563–3576 (2003).

5. Xia, Y. & Whitesides, G. M. Soft lithography. *Annu. Rev. Mater. Sci.* **28,** 153–184 (1998).

6. Beebe, D. J., Mensing, G. A. & Walker, G. M. Physics and Applications of Microfluidics in Biology. *Annu. Rev. Biomed. Eng.* **4,** 261–286 (2002).

7. Sackmann, E. K., Fulton, A. L. & Beebe, D. J. The present and future role of microfluidics in biomedical research. *Nature* **507,** 181–189 (2014).

8. Novotny, J. & Foret, F. Fluid manipulation on the micro-scale: Basics of fluid behavior in microfluidics. *J. Sep. Sci.* **40,** 383–394 (2017).

9. Lifton, V. A. Microfluidics: an enabling screening technology for enhanced oil recovery (EOR). *Lab Chip* **16,** 1777–1796 (2016).

10. Damiati, S., Kompella, U. B., Damiati, S. A. & Kodzius, R. Microfluidic Devices for Drug Delivery Systems and Drug Screening. *Genes (Basel).* **9,** 1–24 (2018).

11. Luka, G. *et al.* Microfluidics integrated biosensors: A leading technology towards lab-on-a-chip and sensing applications. *Sensors (Switzerland)* **15,** 30011–30031 (2015).

12. Reece, A. *et al.* Microfluidic techniques for high throughput single cell analysis. *Curr. Opin. Biotechnol.* **40,** 90–96 (2016).

13. Yang, S. *et al.* Microfluidic synthesis of multifunctional Janus particles for biomedical applications. *Lab Chip* **12,** 2097–2102 (2012).

14. Lenshof, A. & Laurell, T. Continuous separation of cells and particles in microfluidic systems. *Chem. Soc. Rev.* **39,** 1203–1217 (2010).

15. Wen, J., Legendre, L. A., Bienvenue, J. M. & Landers, J. P. Purification of Nucleic Acids in Microfluidic Devices. 6472–6479 (2008).

16. Slapar, V. Microfluidics. 30 (2008).

17. Jung, W., Han, J., Choi, J. W. & Ahn, C. H. Point-of-care testing (POCT) diagnostic systems using microfluidic lab-on-a-chip technologies. *Microelectron. Eng.* **132,** 46–57 (2014).

18. Manz, A., Graber, N. & Widmer, H. M. Miniaturized total chemical analysis systems: A concept for chemical sensing. *Sensors Actuators, B Chem.* **1,** 244–248 (1990).

19. Sharma, S., Zapatero-Rodríguez, J., Estrela, P. & O'Kennedy, R. Point-of-Care diagnostics in low resource settings: Present status and future role of microfluidics. *Biosensors* **5,** 577–601 (2015).

20. Klinteberg, L. A. F. Computational methods for microfluidics. (KTH School of Engineering Sciences, 2013).

21. Lanotte, L. *et al.* Red cells' dynamic morphologies govern blood shear thinning under microcirculatory flow conditions. *Proc. Natl. Acad. Sci.* **113,** E8207–E8207 (2016).

22. Guckenberger, A., Kihm, A., John, T., Wagner, C. & Gekle, S. Numerical-experimental observation of shape bistability of red blood cells flowing in a microchannel. *arXiv* (2017).

23. Pimenta, F. M. P. Application of open-source software in the design of microfluidic devices for controlled deformation of biomolecules. (2014).

24. Zhang, Y. Brownian Dynamics Simulation of DNA in Complex Geometries. 1–179 (2011).

25. Rosenbluth, M. J., Lam, W. a & Fletcher, D. a. Analyzing cell mechanics in hematologic diseases with microfluidic biophysical flow cytometry. *Lab Chip* **8,** 1062–1070 (2008).

26. Yaginuma, T., Oliveira, M. S. N., Lima, R., Ishikawa, T. & Yamaguchi, T. Human Red Blood Cell Behavior under Homogeneous Extensional Flow in a Hyperbolic-Shaped Microchannel. *Biomicrofluidics* **7,** 054110 (2013).

27. Webre, D. J., Wolanin, P. M. & Stock, J. B. Bacterial chemotaxis. *Curr. Biol.* **13,** R47-49 (2003).

28. Wang, F. The signaling mechanisms underlying cell polarity and chemotaxis. *Cold Spring Harb. Perspect. Biol.* **1,** 1–16 (2009).

29. Dertinger, S. K. W., Chiu, D. T., Noo Li Jeon & Whitesides, G. M. Generation of gradients having complex shapes using microfluidic networks. *Anal. Chem.* **73,** 1240–1246 (2001).

30. Chang, C.-W. *et al.* A polydimethylsiloxane–polycarbonate hybrid microfluidic device capable of generating perpendicular chemical and oxygen gradients for cell

culture studies. *Lab Chip* **14,** 3762–3772 (2014).

31. Kou, S. *et al.* A multishear microfluidic device for quantitative analysis of calcium dynamics in osteoblasts. *Biochem. Biophys. Res. Commun.* **408,** 350–355 (2011).

32. Korin, N. *et al.* Shear-Activated Nanotherapeutics for Drug Targeting to Obstructed Blood Vessels Netanel. (2012).

33. Holme, M. N. *et al.* Shear-stress sensitive lenticular vesicles for targeted drug delivery. *Nat. Nanotechnol.* **7,** 536–543 (2012).

34. Beech, J. P. *Microfluidics Separation and Analysis of Biological Particles.* (2011).

35. Tripathi, S., Varun Kumar, Y. V. B., Prabhakar, A., Joshi, S. S. & Agrawal, A. Passive blood plasma separation at the microscale: a review of design principles and microdevices. *J. Micromechanics Microengineering* **25,** 083001 (2015).

36. Yamada, M. *et al.* Microfluidic devices for size-dependent separation of liver cells. *Biomed. Microdevices* **9,** 637–645 (2007).

37. Di Carlo, D. Inertial microfluidics. *Lab Chip* **9,** 3038 (2009).

38. Amini, H., Lee, W. & Di Carlo, D. Inertial microfluidic physics. *Lab Chip* **14,** 2739 (2014).

39. IV, C. W. S., Ohiri, K. A., Szott, L. M. & López, P. G. Translating Microfluidics: Cell Separation Technologies and their Barriers to Commercialization. *Cytom. B Clin Cytom* **92,** 115–125 (2017).

40. Zografos, K., Barber, R. W., Emerson, D. R. & Oliveira, M. S. N. A design rule for constant depth microfluidic networks for power-law fluids. *Microfluid. Nanofluidics* **19,** 737–749 (2015).

41. Zografos, K., Pimenta, F., Alves, M. A. & Oliveira, M. S. N. Microfluidic converging/diverging channels optimised for homogeneous extensional deformation. *Biomicrofluidics* **10,** 1–21 (2016).

CHAPTER 2

Background: Biological molecules and particles in microfluidic flows

In this thesis, two distinct biological fluids were used: λ-DNA solution and RBC suspensions. The former was used as a model system to test intelligent microfluidic devices, designed based on theoretical analysis and numerical algorithms, for generating specific flow dynamics (Chapters 4 and 5). The latter was used to study the suspension flow in a range of microfluidic devices. We studied novel aspects of the spatio-temporal dynamics of red blood cell suspensions with weak cell-cell interactions under low inertia conditions, typically found in microfluidic experiments (Chapter 6) as well as the flow along complex microfluidic geometries, for potentially use in blood/plasma separation (Chapter 7). In this chapter, we discuss important properties of these biological fluids and provide the relevant background to understand their dynamics at the microscale and the experimental designs used in this thesis.

In order to study suspensions of biological objects, we used microfluidic devices for the numerous reasons already presented in Chapter 1. Therefore, in the following sections we describe the general characteristics of microfluidics, in particular of the flow in channels of rectangular cross-section, which are the ones employed in the experiments. Also, we present the differences in rheological behaviour between Newtonian fluids and non-Newtonian fluids, since the presence of polymers or particles in a Newtonian suspending medium often causes a complex behaviour. Finally, we provide the background information on the transport of bioparticles in microflows, in particular on the DNA molecules and RBC suspensions, which are the two biological objects used in this thesis.

2.1 Characteristics of the flow at microscale

Microfluidic flows typically rely on devices composed of a single channel or a network of channels of different shapes and sizes, in series and/or parallel. Such channels may present distinct cross-sections according to the fabrication method employed. However, the microfabrication techniques used in this thesis (photo and soft lithography described in detail in Chapter 3), which are arguably the most common, result in channels of square or rectangular cross section. Figure 2.1 presents a scheme of a rectangular channel and relevant parameters.
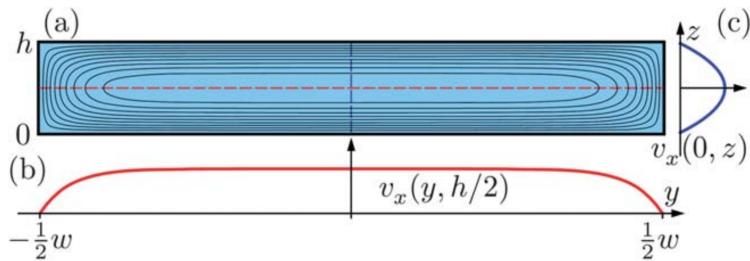
Figure 2.1: Schematic representation of a rectangular cross-section channel used in the experiments. Corresponding geometrical parameters used to calculate theoretical velocity profiles, for a perfectly developed flow of a Newtonian fluid along a rectangular channel, assuming no-slip boundary conditions at the wall (adapted from Bruus[1]).

The relevant governing equations for an isothermal incompressible flow are the conservation of mass and momentum:

$$\nabla \cdot \mathbf{u} = 0 \tag{2.1}$$

$$\rho \left(\frac{\partial \mathbf{u}}{\partial t} + \mathbf{u} \cdot \nabla \mathbf{u} \right) = -\nabla p + \nabla \cdot \boldsymbol{\tau} + \mathbf{f} \tag{2.2}$$

where $\mathbf{u}$ represents the velocity, p the pressure, ρ the density of the fluid, t is the time, ∇p is the pressure gradient, $\mathbf{f}$ is the sum of the body forces acting on the fluid, such as gravity or electrical forces, and $\boldsymbol{\tau}$ is the Cauchy stress tensor, of second order, which represents the stress state inside a body under deformation. This quantity depends on the constitutive law, and the term $\nabla \cdot \boldsymbol{\tau}$ is described by $\eta \nabla^2 \mathbf{u}$ for Newtonian fluids.

The acceleration terms are represented on the left side of the momentum conservation equation, where $\partial \mathbf{u} / \partial t$ refers to local acceleration and $\mathbf{u} \cdot \nabla \mathbf{u}$ refers to convective acceleration. The force terms are on the right side of the equation. The second term on the left side of the momentum equation refers to the inertia of the fluid and is nonlinear, making analytical solutions of the Navier-Stokes equation challenging.

2.1.1 Reynolds number and the Stokes equation

The dimensionless Reynolds number,[2] Re, quantifies the inertial to viscous forces acting in the fluid. For fluid flows in rectangular channels, typical of microfluidic devices, it can be defined as:

$$\mathrm{Re} = \frac{\text{inertial forces}}{\text{viscous forces}} = \frac{\rho \bar{u} D_h}{\mu} \tag{2.3}$$

where $\bar{u}$ corresponds to the average velocity of the fluid in the channel and D_h is the hydraulic diameter of the microfluidic channel, defined as

$$D_h = \frac{4 \cdot \text{cross sectional area}}{\text{wetted perimeter}} = \frac{2wh}{(w+h)} \tag{2.4}$$

where w and h correspond to the channel width and depth, respectively.

Microfluidic flows are typically within the laminar regime. Although moderate Reynolds numbers ($O(10^2)$) can be achieved in microfluidics, the flows at these small lengthscales very often present Reynolds number below unity (Re < 1) for which the viscous forces dominate and the inertial term in the Stokes equation can be neglected.

So, considering a Newtonian fluid in flow conditions of Re << 1, the convective term can be neglected and the Navier-Stokes equation becomes the Stokes equation, which is linear and easier to solve, using the appropriate boundary conditions:

$$0 = -\nabla p + \eta \nabla^2 \mathbf{u} \tag{2.5}$$

One particularity of the Stokes equation is that the solution can be reversed if the forces applied to the flow are also reversed, assuming that the flow is isothermal and the fluid is incompressible.

For example, one can think about a fluid (containing tracer particles for the purpose of flow visualisation), flowing along a symmetric contraction-expansion microfluidic geometry (see Figure 2.2). Assuming that the particles are small enough not to disturb the natural fluid flow and present a similar density to that of the fluid, the pathlines observed by streak imaging are symmetric and it is not possible to distinguish the direction of the flow, when Re ~0 (Figure 2.2b). However, if the flow velocity is increased, vortices form downstream the contraction for Re>>1 due to inertia (Figure 2.2c). Further in this chapter we will describe how the presence of particles in the fluid might compromise the reversibility of the flow.
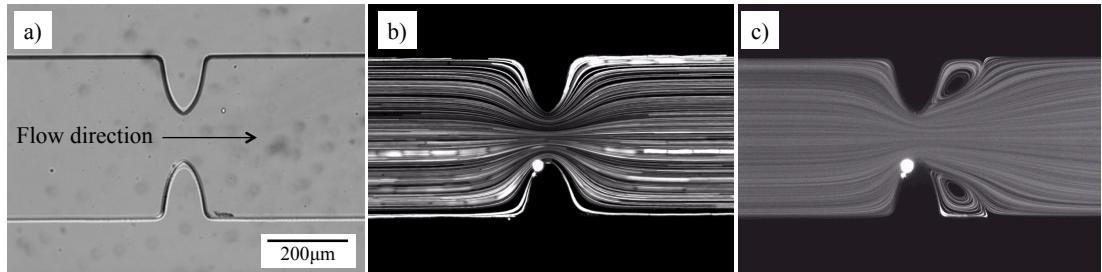
Figure 2.2: Example of reversibility for microfluidic flows at small Reynolds number using water with tracer particles of 1μm diameter. (a) Micrograph of a planar contraction expansion geometry indicating the flow direction from the left to right; (b) Symmetric pathlines observed for Re ≈ 0.1; (c) Asymmetric pathlines, with vortex formation downstream the contraction, due to inertial effects for Re ≈ 22.

2.1.2 Channel Flows

The fully-developed velocity profile for Newtonian fluid flow in rectangular channels, typical of microfluidics, can be derived from the conservation laws assuming no-slip boundary condition at the channel walls and a constant pressure gradient along the channel:[3]

$$u_x(y,z) = \frac{48Q}{\pi^3 hw} \frac{\sum_{j,odd}^{\infty} \frac{1}{j^3}\left[1 - \frac{\cosh(j\pi\frac{y}{h})}{\cosh(j\pi\frac{w}{2h})}\right]\sin(j\pi\frac{z}{h})}{\left[1 - \sum_{j,odd}^{\infty}\frac{192h}{j^5\pi^5 w}\tanh(j\pi\frac{w}{2h})\right]} \tag{2.6}$$

where Q is the flow rate, w is the channel width, h is the channel depth and - $w/2 \leq y \leq w/2$ and $0 \leq z \leq h$. Figure 2.1 also highlights the differences in the velocity profiles along the two centrelines $z = h/2$ and $y = 0$ for the case when the channel aspect ratio is different from 1 (with AR = 1 corresponding to a square cross-section). The derivation of equation 2.6 is provided in detail in reference Bruus.[3]

The magnitude of the shear rate inside a rectangular channel may thus be calculated as:

$$\dot{\gamma}(y,z) = \sqrt{\left[\frac{-\Delta P}{2\mu L}\sum_{j=0}^{\infty} a_j \cos\left(\frac{2\lambda_j z}{h}\right)\frac{2\lambda_j}{h}\sinh\left(\frac{2\lambda_j y}{h}\right)\right]^2 + \left[\frac{\Delta P}{2\mu L}\left(-2z\right) + \sum_{j=0}^{\infty} a_j \sin\left(\frac{2\lambda_j z}{h}\right)\frac{2\lambda_j}{h}\cosh\left(\frac{2\lambda_j y}{h}\right)\right]^2}$$

$$(2.7)$$

where $\lambda_j = \frac{(2j+1)\pi}{2}$ and $a_j = \frac{h^2(-1)^j}{\lambda_j^3 \cosh\left(\lambda_j \frac{w}{h}\right)}$.

The kinematic profiles corresponding to the different microfluidic geometries used in this thesis are presented in each results chapter.

2.1.3 Shear flow versus extensional flow

In this thesis, we aim at studying biological objects under both shear and extensional flow conditions, for which different types of microfluidic geometries were employed. We used straight channels, in which the flow is shear dominated and contraction-expansion channels, which exhibit mixed kinematics with shear in the region close to the channel walls and extensional flow along the channel centreline.

Figure 2.3 presents a schematic representation of the mentioned channels, highlighting the relevant gradient of the streamwise velocity, u_x. For shear-dominated flows, simple straight channels of rectangular cross-section were used. The shape of the contraction channels used in this thesis has been numerically optimised to provide a wide region of homogeneous extension rate along the centreline.[4] The rationale behind the use of such geometries and their specificities is discussed in detail in Chapter 5.

Shear Flow   **Extensional Flow**

u_x varies in the y direction u_x varies along x direction
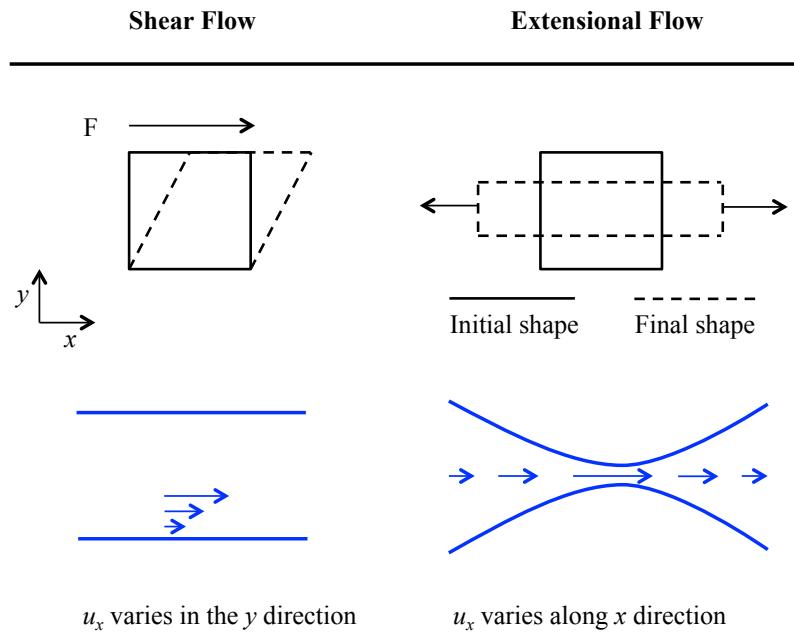
Figure 2.3: Shear flow versus extensional flow. Example of how velocity varies in shear flow, represented by the fluid transport along a simple straight microfluidic channel, and under extensional flow generated along the centreline of a converging-diverging channel.

2.2 Newtonian versus non-Newtonian rheological behaviour

Biological fluids are typically complex fluids composed of polymer/protein solutions (such as synovial fluid, vitreous humour, mucus or blood plasma) or suspensions of deformable objects (e.g. whole blood). In the first case, the characteristics of the polymer chain and its concentration determine the degree of entanglement and, therefore, the final viscosity and macroscopic rheological behaviour of the solution. In the case of particle suspensions, the size, shape, concentration and deformability of the individual objects play a role on the macroscopic behaviour. Therefore, depending on the fluid characteristics, the solutions and suspensions may exhibit Newtonian or non-Newtonian properties.[5]

The relation between stress and deformation allows distinguishing between Newtonian and non-Newtonian fluids. Incompressible Newtonian fluids are purely viscous fluids, characterised by the linear dependence between shear stress τ and shear rate $\dot{\gamma}$, according to Newton's law of viscosity:

$$\tau_{xy} = \eta \ \dot{\gamma}_{xy} \tag{2.8}$$

where the constant of proportionality represents the viscosity, η. While for Newtonian fluids, the viscosity does not depend on shear-rate (η = constant), for most biological

non-Newtonian fluids the viscosity is a function of the shear rate, $\eta(\dot{\gamma})$. Non-Newtonian fluids may exhibit distinct behaviour (cf. Figure 2.4): they can be shear-thinning (or pseudoplastic) if the viscosity decreases with the shear rate, shear-thickening (or dilatant) if the viscosity increases with the shear rate and they may also present a yield stress, below which it behaves as a solid (Bingham plastic fluids, cf. Figure 2.4).
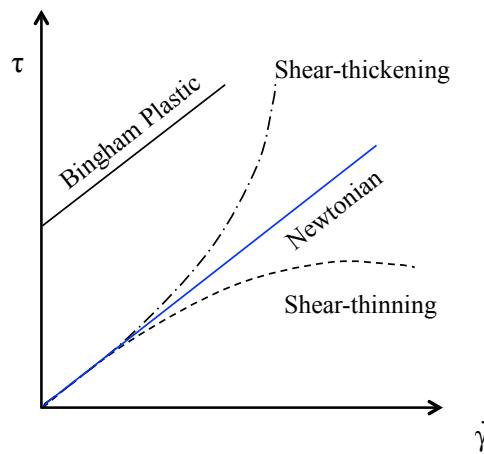
Figure 2.4: Shear stress as a function of shear rate for purely viscous fluids: Newtonian (−), Bingham plastic (−), Shear-thinning (- -) and Shear-thickening (−•−).

In addition to a shear-dependent viscosity, non-Newtonian fluids can also be time-dependent (history effect) and viscoelastic. For the former the shear stress response varies along time for a constant shear rate and temperature (e.g. thixotropic fluids) while the latter exhibits both solid-like and liquid-like behaviour and cannot be described by a simple relationship between shear stress and shear rate, as both variables are history-dependent.

Viscoelastic fluids can be characterised by the existence of an internal time scale, defined by the relaxation time λ, and the peculiar flow effects such as those presented in Figure 2.5 are only noticeable if a typical timescale of the flow, for example the shear rate is larger than the inverse of the relaxation time, this is, if the objects (example polymeric molecules) transported in the fluid are not allowed to relax during the flow. As a consequence of its non-Newtonian rheology, complex fluids may exhibit impressive flow behaviour as shown in the examples of Figure 2.5: the Weissenberg effect (a), in which a viscoelastic fluid climbs a spinning rod as consequence of normal stresses; the Barus effect (b), in which swelling of a viscoelastic jet is observed as it exits through a die; and the shear-thickening (c) of a corn starch suspension when subject to sound waves.
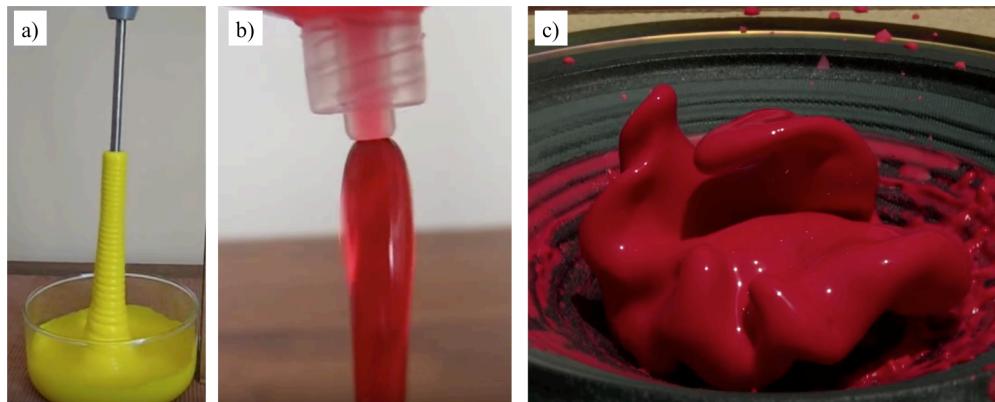
Figure 2.5: Examples of phenomena observed for non-Newtonian fluids. (a) Rod climbing (Weissenberg effect)[6], (b) die swell (Barus effect)[7] and (c) thickening effect of corn starch on a speaker[8].

When considering complex fluid flows, in addition to the Reynolds number, other important dimensionless numbers are used to quantify the relative importance of the various competing effects acting on a material (be it a fluid or a particle) and are helpful to characterise the flow. The Weissenberg number[9] Wi relates the elastic and viscous forces in a fluid and is defined as:

$$Wi = \frac{\text{elastic forces}}{\text{viscous forces}} = \lambda\,\dot{\gamma} \tag{2.9}$$

where λ is the relaxation time of the fluid and $\dot{\gamma}$ is the characteristic rate of deformation of the flow. In shear flows such rate of deformation corresponds to the shear rate $\dot{\gamma}$ while in extensional flows it corresponds to the strain rate $\dot{\varepsilon}$.

Another important parameter used to describe the flow of elastic fluids is the Deborah number, defined as the ratio of the relaxation time and the time of the observation (or the characteristic time of the experiment) t_{obs}:

$$De = \frac{\text{time of relaxation}}{\text{time of observation}} = \frac{\lambda}{t_{obs}} \tag{2.10}$$

In some cases, t_{obs} can also be defined as the residence time t_R inside the channel, therefore $t_R = L_{channel}/\overline{u}$.

2.3 Biological particles in flows

Particle suspensions in fluids are often found in engineering applications and in nature. The presence of particles suspended in the fluid may modify the fluid flow, in particular if these particles exhibit deformability. Therefore, several effects should be considered carefully as discussed next.

In the absence of other forces acting on the particle besides the drag force, the particle will move at the same velocity described by the fluid, and will also follow the fluid streamlines. However, if other forces are acting on the fluid, they may cause particle acceleration or the crossing of fluid streamlines,[10] as in the case of sedimentation. The microfluidic devices designed for particle separation make use of different forces to cause a change of particle position inside the channel and, therefore, its traveling velocity leading to a separation over time.

2.3.1 Diffusion

Since suspensions of biological particles will be used, it is important to understand if diffusion plays an important role at the time scale used here. For flows at low Reynolds numbers, mixing is only carried out by diffusion. For important mixing to occur, one would need to have residence times in the device t_R comparable to the diffusion time.

The dimensionless Peclet number Pe relates the importance of advection to diffusion events and is given by equation:

$$Pe = \bar{u} \, L/D \tag{2.11}$$

where D corresponds to the diffusion coefficient. In microfluidic experiments, typical values of Pe > 10, mean that the diffusion acts more slowly than transport by advection.[11] The diffusion coefficient D described in equation equation 2.12, is given by the Stokes-Einstein relation and represents the thermal forces and friction acting on a sphere of radius r:

$$D = \frac{k_B T}{6\pi\eta r} \tag{2.12}$$

where K_B is the Boltzmann constant ($K_B = 1.38064852\times10^{-23} \mathrm{m^2 kgs^{-2} K^{-1}}$) and T is the temperature in Kelvin. Figure 2.6 presents an example of two streams coloured with different dyes, flowing in parallel in a T-junction microfluidic device. For the typical time

scale used in microfluidic experiments, the mixing, due to diffusion at the interface, remains negligible.
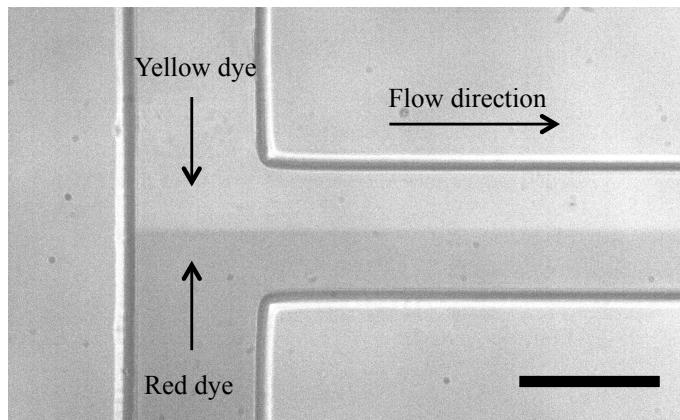
Figure 2.6: Microfluidic T-junction for mixing by molecular diffusion. The two streams correspond to Newtonian fluids coloured with different dyes, flowing at low Reynolds number. Scale bar 100μm.

In general, the smaller the particle size, the larger is the diffusion coefficient (equation 2.11) and the faster is the diffusion process[11]. For the biological particles used in this study, λ-DNA and red blood cells, the diffusion coefficients are small: Smith *et al.*[12] measured the diffusion coefficient for a λ-DNA molecule labeled with fluorescence (molecule length ~22μm) to be $D_{DNA} = 0.47 \pm 0.03 \mu m^2/s$. This means that it would take about 3.5 minutes for the molecule to effectively diffuse across a 100 μm wide microfluidic channel. Such diffusion would hardly be noticed at the experimental time scale. For a human RBC flowing in water at room temperature, assuming a flat shape with typical dimensions (radius ~4μm and thickness ~1μm), the diffusion coefficient is estimated to be $D_{RBC} = 0.1 \mu m^2/s$.[13] In comparison with DNA molecules, RBCs would take even longer time to diffuse in the same microfluidic geometry, due to their larger size. For example, the cells would take about 17 minutes to diffuse across a100 μm wide microfluidic channel. The diffusion of such elements is only significant for very long geometries and very small flow rates, as in the example presented in Figure 2.7, where a suspension of RBCs (initial cell volume fraction ~15%) is flowing in a long flat channel. At a distance of 30 mm away from the channel entrance, the effect of diffusion is already evident.[14]
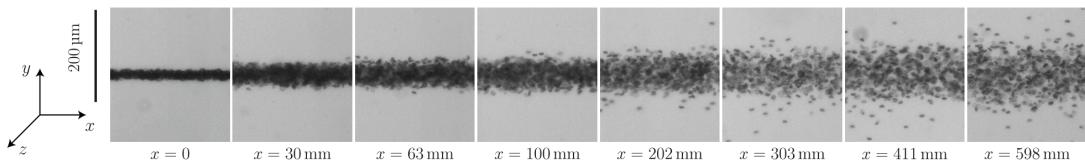
Figure 2.7: RBC diffusing along a flat channel. Initial cell volume fraction is 15% (adapted from Grandchamp et al.[14]).

In resume, for the experimental flow conditions considered in this thesis, the diffusion has a negligible contribution for the objects displacement.

2.3.2 Particle rotation/ deformation

The shape and deformability of the particles, inserted in the fluid, play an important role in microfluidic processes such as separation.[10] In particular, for the case of RBCs under shear flow, which will be considered in Chapters 6 and 7, the effects of particle deformation and rotation is of extreme importance and should be taken into account for the study. Figure 2.8 describes the scheme of a shear flow, which can be decomposed in rotational (Ω) and extensional (E) components. At low Reynolds numbers, and not considering the effect of the channel surfaces, the particle centre of mass will displace at the velocity of the streamline corresponding to its centre of mass.

In such conditions, a rigid object, such as a sphere or an elongated body, will be transported along the fluid streamlines. While a sphere would simply rotate due to the rotational component of the flow (Ω), an elongated object would tumble due to the contribution of both rotational (Ω) and elongational (E) components of the flow. However, for flexible or deformable particles, the extensional components can lead to particle deformation and will influence the transport of the object. If the latter is subjected to a shear gradient, migration across the fluid streamlines can occur. For example, flexible filaments such as DNA when subjected to both rotational and extensional components of the flow perform interesting dynamics such as extension and compression while rotating around their centre of mass. For other deformable objects, such as red blood cells or vesicles, besides rotation (tumbling), the objects may present deformable and stable configurations, forming a stable angle with the flow direction (tank treading). This behaviour will be described in more detail in section 2.5.5.

23
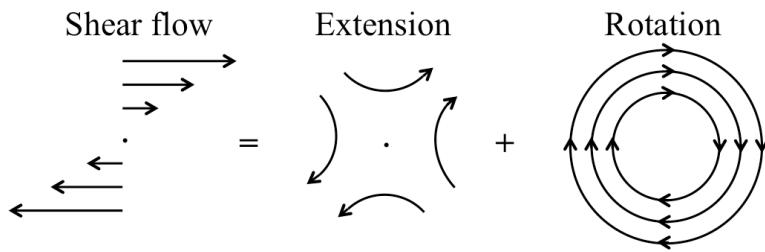
Figure 2.8: Scheme of shear flow, decomposed in rotational and extensional components.

It is important to mention that, for a deformable object, migration across streamlines can occur at low Reynolds number (Re < 1)[15] if there is a shear gradient or if the object is transported in proximity to a wall, as deformation breaks the particle symmetry and the time-reversibility of the problem.

In this thesis, two distinct biological suspensions were used: λ-DNA and RBC suspensions. The former was used as a model system to test intelligent microfluidic devices designed based on theoretical analysis and numerical algorithms for generating specific flow dynamics, while the latter was used to test microfluidic devices for blood/plasma separation and to study novel aspects of the spatio-temporal dynamics of red blood cell suspensions with weak cell-cell interaction under low inertia, typically found in microfluidic experimental conditions. In sections 2.4 and 2.5, we discuss important properties of each of these biological fluids, providing the necessary background to understand the experimental design and interpretation of results.

2.4 DNA molecules and solutions

2.4.1 Physical properties of λ-DNA molecules

Deoxyribonucleic acid (DNA) is a semi-flexible biopolymer that can be found in humans and almost all other living organisms. The λ-DNA used in this thesis work, in particular, consists of a double helix, composed by two complementary single stranded DNA, oriented in opposite directions, and connected by non-covalent hydrogen bonds (see scheme in Figure 2.9a). Each of the DNA nucleotides (repeating unit) is composed by a phosphate group, a deoxyribose (sugar) and one of the four bases (adenine A, thymine T, cytosine C and guanine G). The two DNA strands bond by forming pairs between the complementary bases A-T or C-G and λ-DNA is composed by 48502 of those basepairs (bp), with a pitch of 0.34nm.
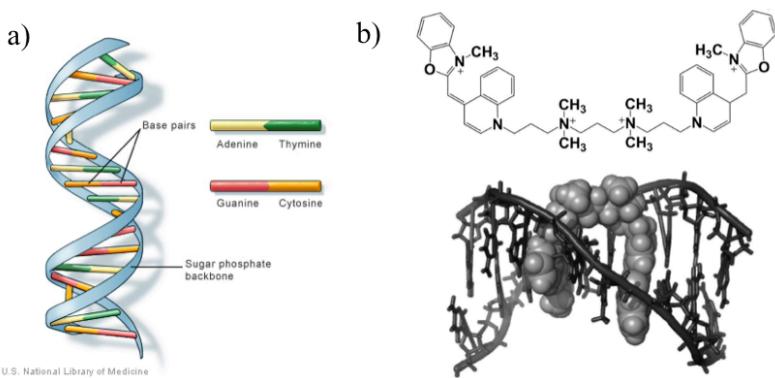
Figure 2.9: (a) Schematic representation of doubled stranded DNA, evidencing the complementary basepairs bonding the two single stranded DNA (Credit: U.S. National Library of Medicine); (b) chemical structure of YOYO-1 dye and schematic representation of the molecular complex λ-DNA-YOYO-1 for fluorescence labeling (adapted from Nyberg *et al.*[16]).

Several parameters, such as the contour length L_c, the persistence length L_p, and the ionic strength of the buffer solution are important to describe the molecule properties in suspension. The molecule contour length corresponds to the length at the maximum extension,[17] and therefore is affected when the molecule is labeled using a fluorescent dye. For example, λ-DNA molecules commonly used in microfluidic experiments, present a contour length of 16.3μm. However, when labeled with YOYO-1 fluorescent dye (see chemical structure of YOYO-1 and scheme of the DNA-YOYO-1 molecular complex in Figure 2.9b), at the ratio of 4 base pairs (bp) to 1 molecule of dye, the contour length increases about 38% and the final molecular complex presents a contour length of approximately 21-22μm). The persistence length L_p is an indication of the molecule stiffness, this is, the stiffer is the polymeric chain, the larger is the persistence length.[18] This property is directly related to the ionic strength of the buffer medium so, for large concentrations of salt (10mM), the persistence length for unlabeled λ-DNA is ~50nm[19] or 53nm[20] according to different references, while for very small salt concentrations (0.1mM), the DNA stiffens reaching persistence lengths of 350nm.[21] As a consequence, most DNA experiments reported in the literature are performed using buffers with high salt concentration to avoid molecule stiffness and to neutralise the negative charge of the DNA molecule.[16] The effect of molecule labeling on the persistence length has been subject of great discussion.[22] While some authors defend that the persistence length increases (from 50nm to 70nm for λ-DNA labeled with YOYO-1, at a ratio of 5 bp:1 molecule of dye)[23], a more recent study using atomic force microscopy (AFM) suggests that the intercalation of the molecule with YOYO-1 does not affect the persistence length of the final molecular complex.[24] Since the contour length is

much larger than the persistence length $L_c >> L_p$, and the persistence length is slightly larger than the individual DNA monomer size (0.34nm),[25] the molecule is considered to be a semi-flexible polymer. Table 2.1 summarises the properties of unlabeled λ-DNA.

Table 2.1: Resume of λ-DNA properties.

Property	Symbol	Value
Number of base pares	bp	48502
Contour length	L_c	16.3μm
Persistence length	L_p	50nm
Diffusion coefficient	D_{DNA}	0.47μm^2/s

2.4.2 DNA solutions under flow

Semi-flexible filaments, such as DNA, display a rich and complex behaviour under flow[26,27] as a result of the thermal fluctuations and viscous forces. At equilibrium, DNA exhibits a coiled shape, while under flow it can extend and/or tumble. Further information on the molecule deformation is provided in the relevant results chapters (Chapters 4 and 5). It is important to mention that, according to the properties of the suspending fluid, namely its viscosity, the molecule will present a characteristic relaxation time (λ). This parameter corresponds to the time necessary for an extended molecule, under flow, to recover into the corresponding stable coiled configuration, after the flow is interrupted.

In general, these polymeric solutions exhibit non-Newtonian rheology for high concentrations, such as viscoelasticity and shear-thinning viscosity, properties that are intimately related to the microscopic structure at molecular length scale under flow, including changes in individual molecule conformation. The ability to directly observe DNA molecules, using fluorescence labeling and advanced microscopic techniques, made it a model molecule for the study of polymeric fluids. Indeed, DNA molecules are easier to label and manipulate than synthetic polymers, such as PAA [Poly(acryl acid)] or PMMA [Poly(methyl methacrylate)], and have thus been extensively used to comprehend polymeric flow of both dilute and concentrated/entangled suspensions[28]. Typically, for the concentrated case, only a few DNA molecules are labeled so that individual molecule deformation can be studied in an entangled environment. Progress in this area allowed the design of efficient microfluidic geometries for biological applications and let to the development of new methods of analysis not available using bulk rheometry tests.[28]

The use of DNA molecules in microfluidic experiments has indeed been widespread (see reviews from Mai *et al.* [29] and Rems *et al.* [28]). λ-DNA molecules, in particular, have been frequently used as a model system since:[22]

- DNA is water-soluble, meaning it can be dispersed in the common buffer solutions used for biological experiments. Also, the typical buffers are compatible with microfluidic devices produced in PDMS, which are the most frequently used in microfluidic applications;

- DNA is a biological polymer available in monodisperse solutions, either produced by PCR or by extraction and purification of DNA from viruses and microorganisms. The monodispersion of the initial suspension is a clear advantage, simplifying the process of data analysis or interpretation of physical properties;

- DNA can present large contour lengths. The molecule may be prepared using different molecular weights, where the contour length is larger than 300nm (the threshold corresponding to the diffraction limit of the visible light). For instance, the molecule used in this study is λ-DNA, with contour length of ~21-22μm (labelled), which makes it possible to observe it directly using fluorescence illumination, and to study the molecule deformation as a function of the flow properties;

- The physical properties of the DNA were subject of numerous studies over the years, and the behaviour of DNA has been well characterised in both shear and extensional flows.[22] Figure 2.10a presents a study on the flow of a Newtonian fluid (A,B) and an entangled DNA solution (C,D) along a microfluidic gradual contraction. While for the Newtonian fluid, no flow instability is detected due to the lack of elasticity, for the DNA entangled solution, the emergence and vortex growth at the contraction is easily noticeable. Curiously, the type of geometry used in this study corresponds to a typical flow inlet used as the microfluidic device entrance and demonstrates on how the polymer concentration and flow velocity may disturb the entrance of the fluid into the microfluidic channel. Figure 2.10b presents the Wi-Re map for the flow of DNA solutions in a planar contraction geometry, adapted from Hemminger et al.[31] In this map we can determine the regions were stable flow is expected, meaning the DNA solution behaves as a Newtonian fluid or the regions characterised by vortex formation or shear banding.
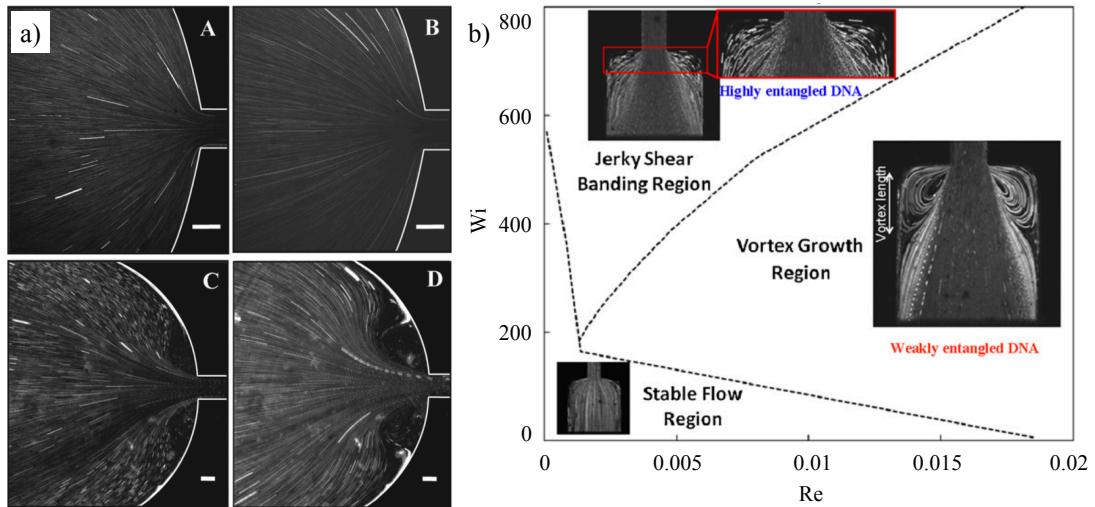
Figure 2.10: Examples of studies using DNA solutions for detection of elastic instabilities. (a) Water as a Newtonian fluid (A,B) and entangled DNA solution (C,D) flowing through a microfluidic gradual contraction, evidencing the vortices at the channel contraction due to viscoelastic effects (adapted from Gulati *et al.*[30]); (b) Wi-Re map, evidencing the regions of stable flow, vortex growth and shear banding using DNA solutions of concentration ranging from 0.1 to 1%, in a planar contraction geometry (adapted from Hemminger *et al.*[31]).

Microfluidic experiments using individual molecules (dilute regime) have highlighted the complex physics of semi-flexible molecules in both shear and extensional dominated flows.[22,32–34] Figure 2.11a and b show examples of show examples of DNA molecule deformation in shear flow and extensional flow, respectively. In both cases, the molecule was labeled using YOYO-1 dye at a ratio of 4:1 (DNA bp:dye molecule). The first study was performed by Schroeder *et al.*[35], and consists in observing individual molecular dynamics when a molecule is placed between two parallel plates displacing at the same velocity, in opposite directions. For a small shear imposed, the coiled molecule configuration starts deforming and leads to an elongated molecule aligned with the flow. The elongation is longer for larger velocities imposed to the displacing plates. The study elucidates on the possible mechanism of deformation, involving stretch and coil cycles along the flow line and/or tumbling cycles due to the inclination of the molecules and curvature of the flow (c.f. Figure 2.11a1). Figure 2.11b presents a study by Perkins *et al.*[34] using a λ-DNA molecule subjected to strong extensional flow generated by a cross-slot. The fluid streams enter the cross-slot in opposite frontal directions and exit through lateral outlets, leading to a stagnation point where the molecule presents a zero velocity but is subjected to a strong extension. In this case, instead of observing periodic cycles of extension and tumbling, as in shear flow, the molecule at the stagnation point presents continuous extension until reaching

a length close to the contour length. During this process, the molecule may present distinct configurations as the ones presented in the scheme in Figure 2.11b (left side).
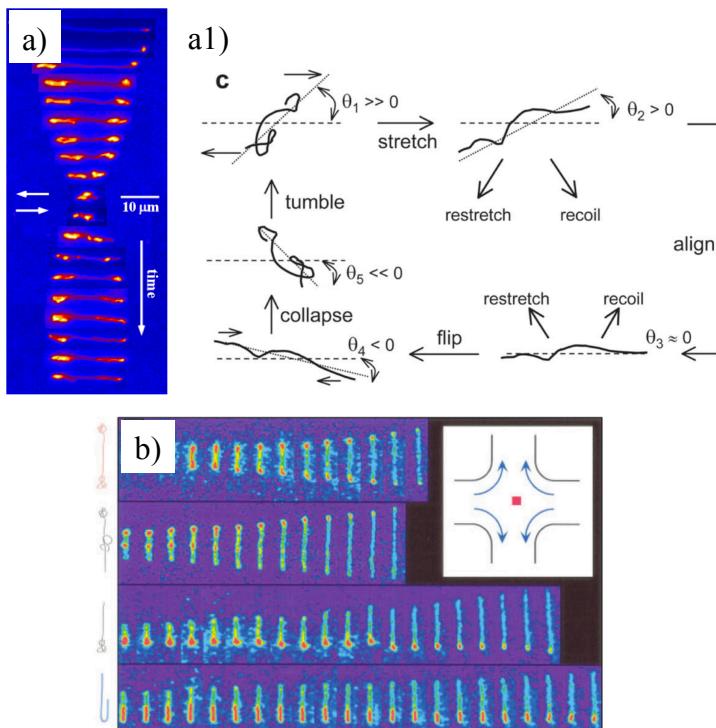
Figure 2.11: Examples of experiments using individual DNA molecules. (a) Deformation of a DNA molecule with length ≈80μm, in shear flow generated by the movement of two parallel plates,[32] and the scheme of molecule deformation leading to stretch and coil cycles or tumbling cycles (a1); (b) deformation of the λ-DNA-YOYO-1 molecular complex in extensional flow, generated by a cross-slot microfluidic device,[34] evidencing the different types of molecule conformation achieved. For both cases, DNA was labeled using YOYO-1 at the ratio 4:1 (DNA bp: molecule dye).

Figure 2.12 presents the mean fractional extension of λ-DNA molecules (given by the ratio between the average measured length of a group of molecules and the contour length) as a function of Weissenberg number, in shear flow generated by parallel plates and extensional flow generated by a cross-slot device. While for the first case, the molecule extension occurs gradually until reaching a plateau for values of 0.4 to 0.5, in extensional flow, the molecular extension is a faster phenomenon, occurring at low strain rates, and the molecule easily reaches its maximum extension that is close to the contour length.
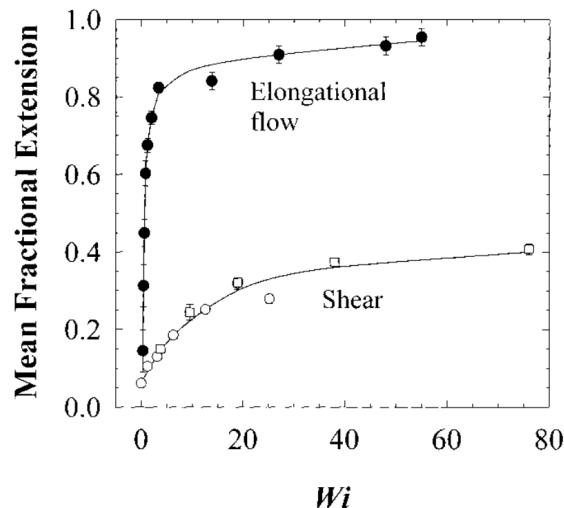
Figure 2.12: Mean fractional extension of λ-DNA molecules (determined as the average of measured length over the contour length) in shear flow generated by parallel plates (open symbols) and extensional flow generated by a cross-slot microfluidic device (filled symbols)(adapted from Smith *et al.*[36]).

Even though the majority of experiments performed using dilute molecules of DNA, consist in observing the molecule at a fixed position, for a certain period of time, only a few studies tried to observe the dynamics when the molecule is transported along the microfluidic geometry. This type of experiment is more challenging since the molecule position is constantly changing in time. Figure 2.13 presents two examples where the molecules are imaged at different positions in the channel. The first one (Figure 2.13a) uses a field of view that includes the entire region of interest, using a metal-halide lamp and a small exposure time to provide a proper molecule illumination. However, from the images obtained, using this setup the effect of blur is clearly a problem and can eventually lead to errors in data analysis. This blur results from the molecule continuous displacement during the exposure time necessary to capture the image. Another option is to use laser illumination with a smaller exposure time, trying to cover the entire region of interest. Figure 2.13b presents the resulting images, when using this setup, where the final image quality obtained is poor.

Therefore, a new methodology is necessary in which the objects are tracked during their transport along the entire ROI in the microfluidic device, ensuring an accurate image acquisition for posterior data processing. This problem was studied in this thesis and the main results are presented in Chapter 5.
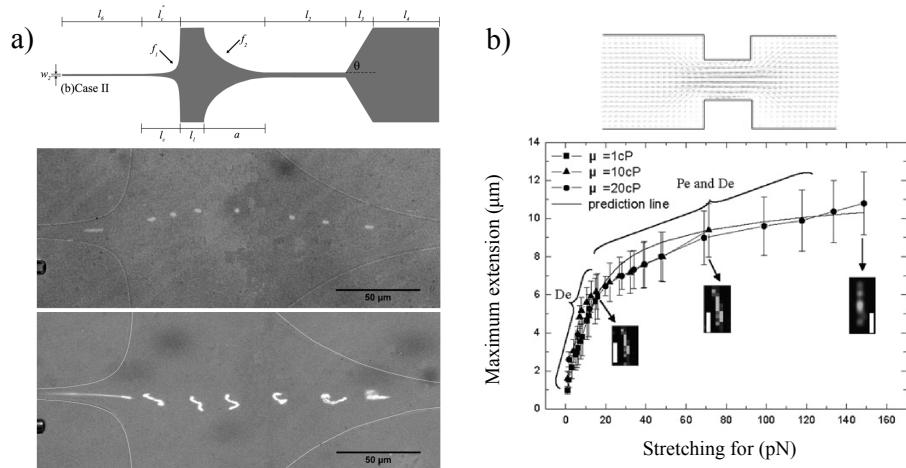
Figure 2.13: Examples of studies observing DNA molecules while transported along the microfluidic devices. (a) T4-DNA (molecule length ~70μm) flowing through an expansion followed by smooth contraction, illuminated by a metal-halide lamp (adapted from Lee and Hsieh[37]); (b) maximum extension of λ-DNA molecules as a function of the stretching force applied in a geometry of abrupt contraction-expansion. Molecule illumination using two pulsed laser (adapted from Hsieh and Liou[38]).

2.5 Blood and RBC suspensions

Whole blood (WB) or its components are frequently the object of analysis using microfluidic systems.[39–41] In this section, a brief introduction on blood composition and properties will be provided and the complex behaviour of blood flow will be highlighted.

2.5.1 Blood composition

Blood is the biofluid responsible for the oxygen delivery to cells and for the uptake of cell waste such as carbon dioxide, allowing the normal function of body tissues and organs. It is mainly composed of plasma, about 55% of its total volume, with suspended cellular elements, of which red blood cells (corresponding to a total volume of 45-50%).[42] Only about 1% of the whole blood volume corresponds to the buffy coat, composed of white blood cells and platelets.[43]

Plasma is composed by water with proteins, electrolytes, urea, glucose, cell waste or dissolved gases. Most works consider plasma to behave as a Newtonian fluid with constant shear viscosity of 1.2 mPa s, at 37°C,[44] and density of 1025 g/mL[45], which are slightly higher than the viscosity and density of water. However, recent experiments by Brust *et al.*[44] have revealed the non-Newtonian behaviour of plasma under extensional flow. Some of the plasma proteins are biomarkers allowing to identify serious pathologies, for example, pancreatic cancer[46] at an early stage. The separation of whole blood in its various components, in particular the separation of plasma from cellular elements is often required in

the context of diagnostic tests. The purity of the plasma (or serum, which corresponds to the plasma without clotting factors) is therefore often required for a correct diagnosis. Arguably the most common procedure employed for separation is centrifugation, which is laborious, time-consuming and does not allow an easy coupling with a biosensor to build a point-of-care microdevice[41]. Also, centrifugation might cause cell lysis and consequent content release into the plasma, compromising its quality and accuracy for the purpose of diagnosis. The advent of microfluidics has offered a good alternative for separating plasma from cells and detecting biomarkers using specific antibodies, in a single micro device.

Red blood cells are mainly responsible for the oxygen and carbon dioxide transport for cell maintenance. RBCs in a healthy human blood sample present a biconcave disk-like shape at rest, with diameters ranging from 7.5 to 8.7μm and thicknesses between 1.7 and 2.2μm,[47] with inner fluid consisting of a concentrated hemoglobin solution, an oxygen-binding protein[48], delimited by a flexible membrane. The surface area of a RBC is larger than that of a sphere with the same volume. This property, together with the high deformability of the membrane, is of utmost importance in blood transport in micro-circulation, since the cells are required to deform in order to pass through the capillaries, the smallest blood vessels in the microvasculature (~5 μm).[42]

Some pathologies are associated to the RBC membrane stiffness, for example diabetes mellitus or sickle cell anemia.[49] The inability of the cells to deform causes a general increase in the blood viscosity and consequent vaso-occlusion in the microcirculatory system, compromising the oxygen release to the surrounding tissues. Again, microfluidic devices represent an interesting possibility to detect pathologies associated with cell elasticity, taking advantage of the fact that healthy and non-healthy RBCs deform and migrate in distinct ways along the microfluidic device, providing different separation rates.

White blood cells and platelets are also of extreme importance. The former are associated with the immune system and trigger a cascade of signaling and chemical reactions after the invasion of a foreign body, such as a virus or bacteria. Thus, the number of white blood cells in a blood sample is a good indicator of a possible hidden infection or another medical condition, such as an autoimmune disease or a blood disorder. The analysis of the foreign nucleic acid material inside the cells allows the identification of the pathogenic parasite for appropriate treatment. Platelets are mainly responsible for the reconstruction of the endothelial surface after injury, including blood clotting after bleeding.

2.5.2 Blood rheology

Blood's non-Newtonian rheological behaviour is known to be related to the interaction and mechanical properties of the cells.[43] The high concentration of red blood cells in the whole blood and their ability to deform and aggregate are the main reason for its viscoelasticity,[43] thixotropy[50] and shear-thinning viscosity.[51]

The shear viscosity is the most well studied rheological property of blood and is an important parameter since it provides valuable information about human health. Figure 2.14a shows the dependence of the shear viscosity on the shear rate. At low values of shear rate, cells tend to aggregate forming rouleaux, mainly due to the presence of fibrinogens and other proteins in plasma.[52] In order to set the blood in motion, it is necessary to impose a minimum stress (yield stress) to the fluid. Above this critical shear rate, the larger aggregates tend to disintegrate resulting in a significant decrease in viscosity. For intermediate shear rate values, between ~10 and ~1500s^{-1}, which is a common range found in the microcirculation, the deformability and the dynamics of the cells contribute to a further viscosity drop. For larger shear rates, blood viscosity plateaus at ~4-5mPa at 37°C[41], due to the deformable cell configuration with elongated shape, aligned with the flow.
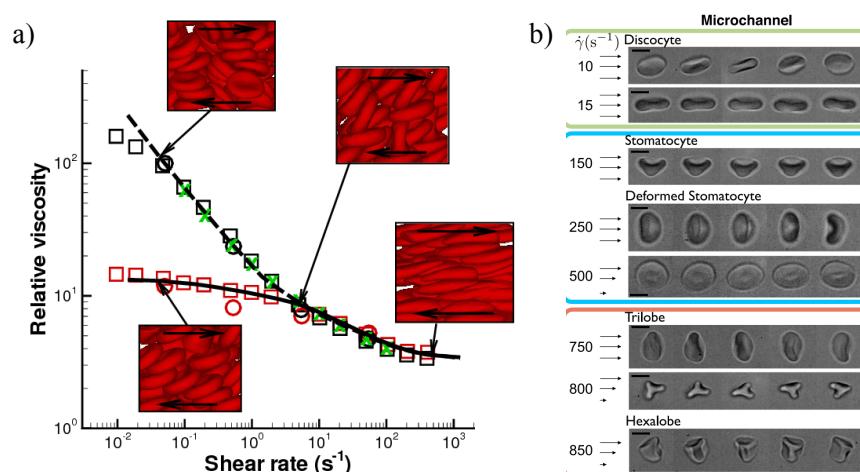
Figure 2.14: "(a) Relative whole blood viscosity as a function of the shear rate considering a sample with cell aggregation (dashed black line) and without aggregation (solid black line) (adapted from Fedosov et al.[51]); (b) Different cell shapes observed at low and intermediate shear rates (adapted from Lanotte et al.[53]).

It is commonly accepted that the deformation of red blood cells due to shear contributes to a decrease of flow resistance and consequently, the overall viscosity of the fluid. A recent study, by Lanotte et al.[53] describes a series of cell shapes found in a microfluidic device for

intermediate shear rates incluing stomatocytes, trilobes and hexalobes (Figure 2.14b). The authors suggest that such shapes may also influence the shear thinning behaviour.

In summary, the rheology of blood is strongly dependent on RBC aggregation and deformability, but also on factors such as temperature and hematocrit level, where the latter is defined by the volume fraction of red blood cells in the suspension.

2.5.3 The circulatory system

Figure 2.15a presents a scheme of the blood vessels composing the human body, where the oxygenated blood flows from the heart towards the tissues via capillaries, and the deoxygenated blood returns from the capillaries back to the heart. The structure and properties of each type of vessel are intimately related to their function. For example, the aorta and larger arteries (6-32mm) are mainly responsible for the blood distribution into the different regions in the body. In order to achieve this, the vessels divide into smaller branches, the arteries (2-6mm). Arterioles are smaller arteries (average diameter ~40µm), which are responsible for blood flow regulation according to the specific needs of the tissue or organ to be irrigated. Capillaries are the smallest vessels (with diameters ranging from 5 to 10µm), where the oxygen and cell waste uptake takes place. A unique layer of epithelial cells forms these vessels, so the exchange reaction occurs fast and efficiently. The velocity in these vessels is the smallest found in the circulatory system (~0.5-1mm/s) to allow sufficient residence time of the RBC in the vessel. After the capillaries, blood flows through venules, veins and finally through the vena cava, which drives the blood back into to the heart.

Figure 2.15b presents the pressure drop, velocity and cross-sectional area along the systemic circulation.
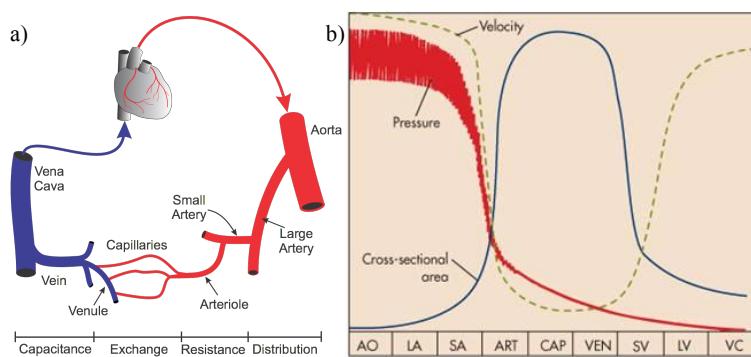
Figure 2.15: (a) Scheme of blood vessels and respective functions in systemic circulation (adapted from Klabunde[54]); (b) Pressure, velocity and cross-sectional area along blood vessels in systemic circulation (adapted from Levy *et al.*[55]).

2.5.4 Hemodynamics

Due to the complexity of the blood suspension, mainly as a result of red blood cells concentration and its mechanical properties, as previously discussed, blood flow inside vessels exhibits some remarkable effects. The understanding of the mechanisms behind such effects is important when designing microfluidic devices for blood manipulation.

Cell Free Layer and the Fåhræus effect

The first important effect to mention is the formation and development of a cell-free layer (CFL) close to the vessel walls (Figure 2.16). This is mainly a result of the cell deformability and proximity of a boundary and will be discussed in more detail in section 2.5.5. Other parameters, which might affect the thickness of the CFL, are the flow rate, hematocrit or channel dimensions.[41] As a consequence of the cell axial migration and the Poiseuille flow, the mean cell velocity is larger than the mean velocity of the surrounding fluid, causing a cell dilution along the vessel or microchannel. The Fåhræus effect refers to the reduction on the tube hematocrit (H_t) relative to the haematocrit in the original sample (H_0).[56]
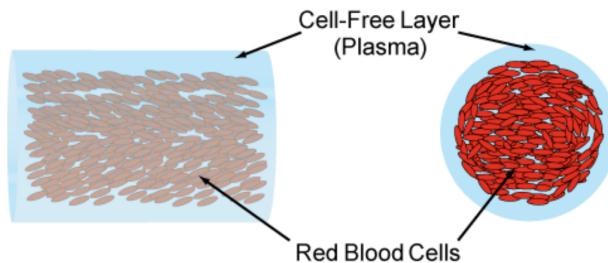
Figure 2.16: Scheme of the RBCs flowing inside a capillary. The CFL is formed close to the channel walls due to cell axial migration (adapted from Merrill[57]).

Fåhræus-Lindqvist effect

In 1931, Fåhræus and Lindqvist reported that the viscosity of human blood flowing in capillary tubes was dependent on the tube diameter.[58] The authors measured the apparent viscosity of the blood flowing in glass capillaries of different diameters, ranging from 0.040 mm to 0.505 mm, and confirmed that, for diameters of 300µm and below, the viscosity decreases for decreasing capillary diameters. For capillary tubes of larger dimensions, the fluid viscosity becomes independent of the capillary size. Further experiments were later performed on this topic, using capillaries of different sizes and Pries *et al.*[59] compiled all the data into a normalised curve of relative apparent viscosity as a function of tube diameter (Figure 2.17). This curve confirms the viscosity decrease presented

by Fåhræus and Lindqvist for capillary diameters ranging from 9μm to 300μm, but evidences an inversion of viscosity for capillaries with sizes ≤9μm, this is, sizes smaller or comparable to RBC diameter.

The information provided by such experiments is of extreme importance to understand blood flow at the microcirculation. The larger pressure drop observed for these smaller vessels, corresponding to the small arteries and arterioles (Figure 2.15b), is directly related to the blood viscosity decrease reported by Fåhræus and Lindqvist.[58] The viscosity decrease allows the heart to pump a certain amount of blood using a smaller pressure than the necessary if the blood would present a constant viscosity.
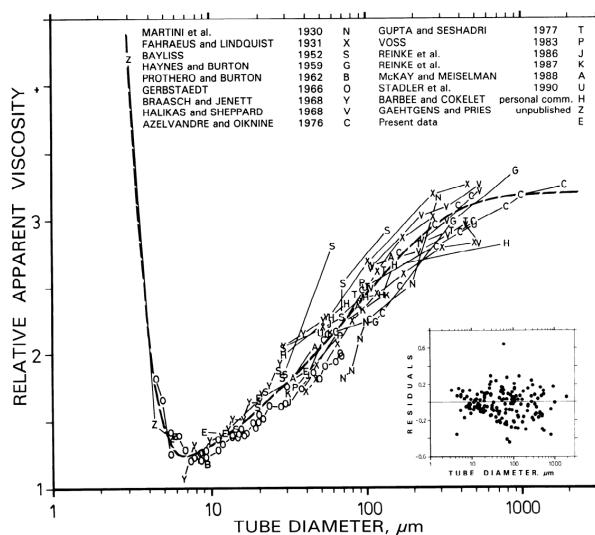
Figure 2.17: Fahraeus-Lindqvist effect, evidencing a strong dependence of relative apparent viscosity with the tube diameter (adapted from Pries *et al.* [59]).

Zweifach-Fung bifurcation effect or bifurcation law

Another interesting phenomenon, occurring in smaller vessels is the RBC partitioning at a bifurcation (Figure 2.18) and can be influenced by factors such as the sample hematocrit (Hct), the flow rate entering the main channel (Q_{total}), the flow rate ratio between the two child branches (Q_1 and Q_2), tube diameter and the cell suspending medium (plasma, physiologic solution, polymeric solutions). When a cell approaches a bifurcation, all these parameters influence the path taken by the cell including to which child branch it follows. For suspensions with larger hematocrit, the RBCs tend to occupy a larger width of the main channel due to cell-cell interactions, and the partitioning towards the child branches is more balanced, unless the flow rate ratio between the two child branches is significant.[60] For smaller hematocrits, the CFL developed along the main channel is more significant and the

cells tend to follow the larger child branch or the branch with higher flow rate. The bifurcation law states that in bifurcations at the capillary level, where the channel sizes are comparable to the RBCs diameter ($d_{channel} / d_{RBC} \approx 1$), a flow ratio of 2.5:1 is sufficient to reduce the hematocrit to zero in the child branch with lower flow rate. For larger channel dimensions, which are typically used in microfluidic devices, this relation does not verify. However, the bifurcation law[61,62] has inspired the design of microfluidic devices for the purpose of plasma separation.
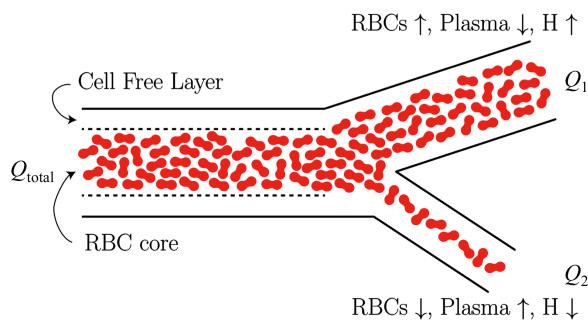
Figure 2.18: Scheme of cell suspension partitioning due to Zweifach-Fung bifurcation effect (adapted from Lee et al.[63]).

2.5.5 Cell migration and lift forces

Cell migration is a combinatorial effect of different mechanisms, acting on the cell, and is responsible for the development of a cell free layer and consequent complex blood flow observed in microvessels.[48] Figure 2.19 presents a scheme of the mechanisms involved in RBC migration.
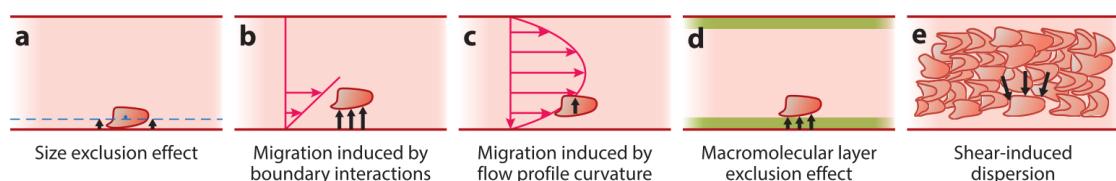
Figure 2.19: Scheme of the mechanisms responsible for cell lateral migration in microvessels. (a) Cell size exclusion, (b) cell deformability close to a boundary, (c) curvature of the velocity profile, (d) endothelial glycocalyx layer and (e) cell-cell interaction in a shear flow (adapted from Secomb[48]).

The fact that RBCs present a finite size dictates a limit for the cell radial distribution (a). This means that if a cell is travelling close to the wall, its centre of mass has a distance, at least, of half a radius away from the channel wall ($\approx 1\mu m$). Also, due to RBC deformability, the cell tends to migrate away from the wall, leaving a cell-depleted layer, as previously

discussed. The physics underlying this mechanism is not yet fully understood, but it is accepted that when fluid flow patterns deviate around the cell, there is a local increase in pressure, between the cell and the wall and, as consequence the cell is pushed towards the channel centreline (b). The curvature of the velocity profile will generate different shear rate patterns. For a Poiseuille flow, typically found in circular channels, the shear rate is always minimum at the centre of the channel and maximum at the walls, causing cell migration towards the channel centreline; however, for channels with rectangular cross-section, typical of microfluidic devices, a plug-like flow profile may be present in one direction and Poiseuille flow in the other direction. In addition, the presence of channel corners generates complex shear rate configurations on the widthwise and depthwise directions, causing a differential cell migration according to the local shear (c). Also, the presence of the glycocalyx *in vivo* (which is part of the endothelial surface layer,[64] consisting of a macromolecular layer covering the inner capillary walls) generates a layer without transported cells (d). Finally, for concentrated suspensions, the cell-cell interaction cannot be neglected, causing migration towards regions of lower hematocrit, this is, the cells move in the direction of the channel walls.

In addition to these factors causing axial migration, also the inertia of the fluid might play a role in cell migration. Making use of the channel topology, when inertia dominates over viscous forces, the cells can be directed towards specific locations inside the channel. It is commonly accepted that inertial effects are important for channel Reynolds number ≥ 1.[15] For further clarification on inertial migration, the reader is referred to references Amini and Di Carlo[65] and Di Carlo.[66]

From Tumbling to tank treading motion

In 1969, Schmid-Schönbein and Wells[67] established a relationship between the RBC shape and the shear thinning behaviour. The authors compared RBCs dispersed in a continuous medium of high viscosity, to fluid drops, which present a discoid/biconcave shape at rest and deform, according to the flow, into prolate ellipsoids oriented parallel to the flow, decreasing the overall flow resistance. In fact, several factors influence the cell shape such as the microfluidic geometry, the shear rate, the viscosity ratio (Λ) between the cell inner and outer fluids, or the membrane elasticity, determining if the isolated cells present tumbling, swinging or tank treading motion[68–71] (see scheme in Figure 2.20). Figure 2.20a presents a scheme of the particle (RBC or vesicle) shape and orientation during transport. Figure 2.20b compares the transport by tank treading (TT) and tumbling (TB) motion, where the black dot represents a fixed point in the membrane. In a TT

motion, the membrane rotates around the inner fluid at a steady state and the cell/vesicle shape oscillates at an average angle of 0-45° relative to the flow direction. In a TB motion, the cell rotates continuously around the flow axis, and the membrane follows the same movement. In this case, the point mark on the membrane will present a periodic 360° flipping motion. Between TT and TB, a swinging motion is observed. Figure 2.20c presents the microscopic images of vesicles (A,C) and RBCs (B,D) presenting both types of motion described.
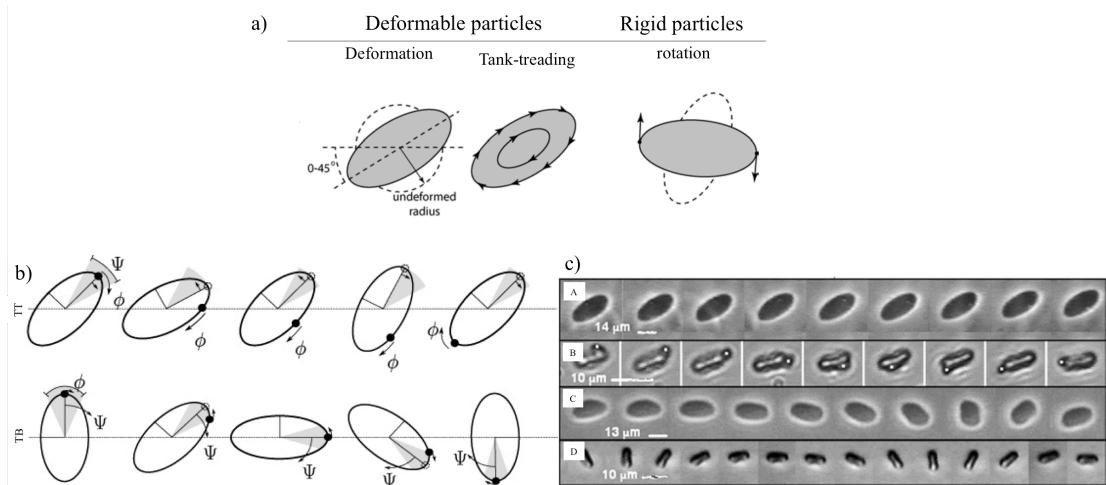
Figure 2.20: RBC/ vesicle motion under flow: a) scheme of cell motion according to their deformation (adapted from Beech[10]); (b) Scheme of TB versus TT vesicle in shear flow (adapted from Finken et al.[72]); (c) motion and deformation of vesicles and RBCs in linear shear flow. A) TT vesicle at $\Lambda = 1$ B) TT RBC with 1μm bead attached to the membrane at $\Lambda = 1/47$, $\dot{\gamma} = 6s^{-1}$ C) vesicle in unsteady TB motion $\Lambda = 8$ D) RBC in TB motion at $\Lambda = 1/47$, $\dot{\gamma} = 0.8s^{-1}$ (adapted from Abkarian et al.[73]).

The information on the cell shape and type of cell motion, including the transition from tumbling to tank treading motion, might be inferred from the Capillary number Ca. This dimensionless number is defined as the ratio of the fluid to the membrane stresses, where the latter is characterised by the cell membrane shear elasticity k_s:[74]

$$Ca = \frac{\eta \dot{\gamma} r_{RBC}}{k_s} \tag{2.13}$$

where r_{RBC} corresponds to the RBC radius, $\dot{\gamma}$ corresponds to the shear rate, and η to the outer fluid viscosity. In the limit of vanishing Ca number (Ca ≈ 0) corresponds to a rigid cell of discoid shape performing tumbling motion, while a higher Ca number (Ca ≈ 1) refers to a cell with elongated/slipper shape performing tank-treading motion. The study by Kruger et al.[71] allowed identifying a TB-TT transition region for a Ca number ranging from

0.1 to 0.3. Also, Goldsmith and Marlow[75] had previously defined a threshold of shear stress around 0.1Pa, where the RBCs would be rigid and perform tumbling motion for a $\tau \ll 0.1$Pa and RBCs would deform and perform tank treading motion for $\tau > 0.1$Pa.

2.5.6 Techniques for RBC separation and/or manipulation

The microfluidic methods used to achieve blood plasma separation can be classified in two main groups: active and passive methods. While active methods require the use of an external force field, such as acoustics, electric or magnetic field, passive methods rely on hydrodynamic effects (such as the CFL, Fåhræus effect or the bifurcation law), by controlling the design of the microfluidic device, the flow rate, the flow regime (e.g. inertia dominated) and/or cell mechanical properties.[41,76,77] The main advantage of passive systems is their simplicity, either regarding to the ease of fabrication or the ability to operate them continuously, as well as the possibility to integrate them in-line with biosensors to build point-of-care applications. Figure 2.21 presents a scheme of the passive methods commonly used for blood plasma separation where sedimentation relies on the difference between the densities of the cell and the surrounding medium and the filtration is mainly dependent on cell size. The methods using lateral displacement refer to the introduction of obstacles inside the channel, causing cell displacement. Finally, the experiments performed in this thesis concern the use of hydrodynamic effects on RBC displacement, giving emphasis to the bio-physical characteristics of the cells and the design of the microfluidic devices. The majority of experiments were performed using non-inertial lift forces.
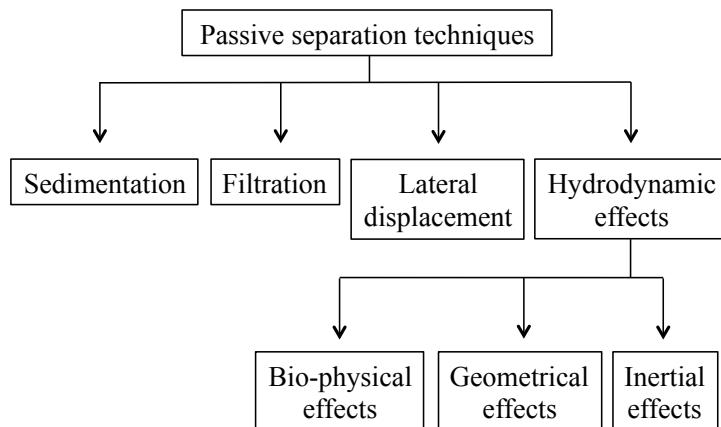
Figure 2.21: Scheme of passive separation techniques used for blood plasma separation (adapted from Tripathi et al.[41]).

2.6 Summary

In this chapter, we provided relevant background information necessary to understand the experiments performed throughout this thesis. We describe the flow at the microscale as well as the important characteristics of the different types of flow and fluids there employed.

Finally, we described the properties of the λ-DNA solutions and RBC suspensions used in this thesis, as examples of deformable biological fluids that present complex behaviour under flow. We will use such systems as models to study microfluidic geometries and experimental methodologies, as well as their limitations.

After this brief introduction, the next chapter will describe the experimental techniques used for the fabrication of the microfluidic devices, as well as the main techniques used for sample characterisation.

References

1. Bruus, H. Acoustofluidics 1: Governing equations in microfluidics. *Lab Chip* **11,** 3742–3751 (2011).

2. Reynolds, O. An Experimental Investigation of the Circumstances which determine whether the Motion of Water shall be Direct or Sinuous, and of the Law of Resistance in Parallel Channels. *R. Soc.* **174,** 935–982 (1883).

3. Bruus, H. Theoretical microfluidics. (2006).

4. Zografos, K., Pimenta, F., Alves, M. A. & Oliveira, M. S. N. Microfluidic converging/diverging channels optimised for homogeneous extensional deformation. *Biomicrofluidics* **10,** 1–21 (2016).

5. Larson, R. G. *The structure and rheology of complex fluids*. (1999).

6. Psidot. The Weissenberg Effect. Available at: https://www.youtube.com/watch?v=npZzlgKjs0I.

7. Psidot. The Barus Effect. Available at: https://www.youtube.com/watch?v=KcNWLIpv8gc.

8. Non-Newtonian Fluid in Slow Motion - The Slow Mo Guys. Available at: https://www.youtube.com/watch?v=RkLn2gR7SyE&t=44s.

9. Weissenberg, K. Proceedings of the International Congress on Rheology. *North-Holland, Amsterdam.* **1,** 29 (1949).

10. Beech, J. P. *Microfluidics Separation and Analysis of Biological Particles*. (2011).

11. Oliveira, M. S. N., Alves, M. A. & Pinho, F. T. in *Transport and Mixing in Laminar Flows: From Microfluidics to Oceanic Currents* 131–174 (2011). doi:10.1002/9783527639748.ch6

12. Smith, D. E., Perkins, T. T. & Chu, S. Dynamical Scaling of DNA Diffusion Coefficients. *Macromolecules* **29,** 1372–1373 (1996).

13. Higgins, J. M., Eddington, D. T., Bhatia, S. N. & Mahadevan, L. Statistical dynamics of flowing red blood cells by morphological image processing. *PLoS Comput. Biol.* **5,** (2009).

14. Grandchamp, X., Coupier, G., Srivastav, A., Minetti, C. & Podgorski, T. Lift and down-gradient shear-induced diffusion in red blood cell suspensions. *Phys. Rev. Lett.* **110,** (2013).

15. Geislinger, T. M. & Franke, T. Hydrodynamic lift of vesicles and red blood cells in flow — from Fåhræus & Lindqvist to microfluidic cell sorting. *Adv. Colloid*

Interface Sci. **208,** 161–176 (2014).

16. Nyberg, L., Persson, F., Åkerman, B. & Westerlund, F. Heterogeneous staining: A tool for studies of how fluorescent dyes affect the physical properties of DNA. *Nucleic Acids Res.* **41,** 1–7 (2013).

17. Ladoux, B., Quivy, J.-P., Doyle, P. S., Almouzni, G. & Viovy, J.-L. Direct imaging of single molecules: from dynamics of a single DNA chain to the study of complex DNA-protein interactions. *Sci. Prog.* **84,** 267–290 (2001).

18. Zhang, Y. Brownian Dynamics Simulation of DNA in Complex Geometries. 1–179 (2011).

19. Perkins, T. T., Quake, S. R., Smith, D. E. & Chu, S. Relaxation of a single DNA molecule observed by optical microscopy. *Science* **264,** 822–826 (1994).

20. Bustamante, C., Marko, J., Siggia, E. & Smith, S. Entropic elasticity of lambda-phage DNA. *Science (80-.).* **265,** 1600 (1994).

21. Shaqfeh, E. S. G. The dynamics of single-molecule DNA in flow. *J. Nonnewton. Fluid Mech.* **130,** 1–28 (2005).

22. Schroeder, C. M. Single Polymer Dynamics for Molecular Rheology. *J. Rheol* **62,** 371–403 (2017).

23. Teclemariam, N. P., Beck, V. A., Shaqfeh, E. S. G. & Muller, S. J. Dynamics of DNA polymers in post arrays: Comparison of single molecule experiments and simulations. *Macromolecules* **40,** 3848–3859 (2007).

24. Kundukad, B., Yan, J. & Doyle, P. S. Effect of YOYO-1 on the mechanical properties of DNA. *Soft Matter* **10,** 9721–9728 (2014).

25. Pecora, R. DNA : A Model Compound for Solution Studies of Macromolecules. *Science (80-.).* **251,** 893–898 (1991).

26. Harasim, M., Wunderlich, B., Peleg, O., Kröger, M. & Bausch, A. R. Direct observation of the dynamics of semiflexible polymers in shear flow. *Phys. Rev. Lett.* **110,** 1–5 (2013).

27. Lindner, A. & Shelley, M. in *Fluid-Structure Interactions in Low-Reynolds-Numbers Flows* 1–25 (2012).

28. Rems, L., Kawale, D., James Lee, L. & Boukany, P. E. Flow of DNA in micro/nanofluidics: From fundamentals to applications. *Biomicrofluidics* **10,** (2016).

29. Mai, D. J., Brockman, C. & Schroeder, C. M. Microfluidic systems for single DNA dynamics. *Soft Matter* **8,** 10560–10572 (2012).

30. Gulati, S., Muller, S. J. & Liepmann, D. Flow of DNA solutions in a microfluidic

gradual contraction. *Biomicrofluidics* **9,** 054102 (2015).

31.   Hemminger, O. L., Boukany, P. E., Wang, S. Q. & Lee, L. J. Flow pattern and molecular visualization of DNA solutions through a 4:1 planar micro-contraction. *J. Non Newton. Fluid Mech.* **165,** 1613–1624 (2010).

32.   Schroeder, C. M., Teixeira, R. E., Shaqfeh, E. S. G. & Chu, S. Characteristic periodic motion of polymers in shear flow. *Phys. Rev. Lett.* **95,** 1–4 (2005).

33.   Smith, D. E., Babcock, H. P. & Chu, S. Single-Polymer Dynamics in Steady Shear Flow. *Science (80-.).* **283,** 1724–1727 (1999).

34.   Perkins, T. T., Smith, D. E. & Chu, S. Single Polymer Dynamics in an Elongational Flow. *Science (80-.).* **276,** 2016–2021 (1997).

35.   Schroeder, C. M., Teixeira, R. E., Shaqfeh, E. S. G. & Chu, S. Dynamics of DNA in the flow-gradient plane of steady shear flow: Observations and simulations. *Macromolecules* **38,** 1967–1978 (2005).

36.   Smith, D. E. Single-Polymer Dynamics in Steady Shear Flow. *Science (80-.).* **283,** 1724–1727 (1999).

37.   Lee, C. H. & Hsieh, C. C. Stretching DNA by electric field and flow field in microfluidic devices: An experimental validation to the devices designed with computer simulations. *Biomicrofluidics* **7,** (2013).

38.   Hsieh, S.-S. & Liou, J.-H. DNA molecule dynamics in converging-diverging microchannels. *Biotechnol. Appl. Biochem.* **52,** 29–40 (2009).

39.   Tomaiuolo, G. Biomechanical properties of red blood cells in health and disease towards microfluidics. *Biomicrofluidics* **8,** 1–19 (2014).

40.   Sebastian, B. & Dittrich, P. S. Microfluidics to Mimic Blood Flow in Health and Disease. *Annu. Rev. Fluid Mech.* 483–504 (2018).

41.   Tripathi, S., Varun Kumar, Y. V. B., Prabhakar, A., Joshi, S. S. & Agrawal, A. Passive blood plasma separation at the microscale: A review of design principles and microdevices. *J. Micromechanics Microengineering* **25,** 83001 (2015).

42.   Brust, M. Propriétés rhéologiques des globules rouges. (2014).

43.   Sousa, P. C., Pinho, F. T., Alves, M. A. & Oliveira, M. S. N. A review of hemorheology: Measuring techniques and recent advances. *Korea Aust. Rheol. J.* **28,** 1–22 (2016).

44.   Brust, M. *et al.* Rheology of human blood plasma: Viscoelastic versus Newtonian behavior. *Phys. Rev. Lett.* **110,** 1–5 (2013).

45.   Cokelet, G. R. & Meiselman, H. J. in *Handbook of Hemorheology and*

Hemodynamics (IOS Press, 2007).

46. Honda, K. *et al.* Plasma biomarker for detection of early stage pancreatic cancer and risk factors for pancreatic malignancy using antibodies for apolipoprotein-AII isoforms. *Sci. Rep.* **5,** 1–15 (2015).

47. Diez-Silva, M., Dao, M., Han, J., Lim, C.-T. & Suresh, S. Shape and Biomechanical Characteristics of Human Red Blood Cells in Health and Disease. *MRS Bull.* **35,** 382–388 (2010).

48. Secomb, T. W. Blood Flow in the Microcirculation. *Annu. Rev. Fluid Mech.* **49,** 443–461 (2017).

49. Lanotte, L. *et al.* A new look at blood shear-thinning. *arXiv* 1–29 (2016).

50. Thurston, G. B. Rheological parameters for the viscosity viscoelasticity and thixotropy of blood. *Biorheology* **16,** 149–62 (1979).

51. Fedosov, D. A., Noguchi, H. & Gompper, G. Multiscale modeling of blood flow: from single cells to blood rheology. *Biomech. Model. Mechanobiol.* **13,** 239–258 (2014).

52. Wagner, C., Steffen, P. & Svetina, S. Aggregation of red blood cells: From rouleaux to clot formation. *Comptes Rendus Phys.* **14,** 459–469 (2013).

53. Lanotte, L. *et al.* Red cells' dynamic morphologies govern blood shear thinning under microcirculatory flow conditions. *Proc. Natl. Acad. Sci.* **113,** E8207–E8207 (2016).

54. Klabunde, R. E. *Cardiovascular Physiology Concepts*. (Lippincott Williams & Wilkins, 2012).

55. Levy, M., Koeppen, B. & Stanton, B. *Berne & Levy Principles of Physiology*. (Elsevier Mosby, 2006).

56. Fåhraeus, R. The suspension stability of the blood. *Physiol. Rev.* **9,** 241–274 (1929).

57. Merrill, E. W. Rheology of Blood. *Physiol. Rev.* **49,** (1969).

58. Fahraeus, R. & Lindqvist, T. The viscosity of the blood in narrow capillary tubes. *Am. J. Physiol.* 562–568 (1931).

59. Pries, A. R., Neuhaus, D. & Gaehtgens, P. Blood viscosity in tube flow: dependence on diameter and hematocrit. *Am. J. Physiol. Circ. Physiol.* **263,** H1770–H1778 (1992).

60. Prabhakar, A., Kumar, Y. V. B. V., Tripathi, S. & Agrawal, A. A novel, compact and efficient microchannel arrangement with multiple hydrodynamic effects for blood plasma separation. *Microfluid. Nanofluidics* **18,** 995–1006 (2015).

61. Yuan-Cheng Fung. Stochastic flow in capillary blood vessels. *Microvasc. Res.* **5,** 34–

48 (1973).

62. Yen, R. T., Fung, Y. & C. Effect of velocity distribution on red cell distribution in capillary blood vessels. *Am. Physiol. Soc.* 251–257 (1978).

63. Lee, T. R., Yoo, S. S. & Yang, J. Generalized plasma skimming model for cells and drug carriers in the microvasculature. *Biomech. Model. Mechanobiol.* **16,** 497–507 (2017).

64. Sieve, I., Münster-Kühnel, A. K. & Hilfiker-Kleiner, D. Regulation and function of endothelial glycocalyx layer in vascular diseases. *Vascul. Pharmacol.* **100,** 26–33 (2018).

65. Amini, H., Lee, W. & Di Carlo, D. Inertial microfluidic physics. *Lab Chip* **14,** 2739 (2014).

66. Di Carlo, D. Inertial microfluidics. *Lab Chip* **9,** 3038 (2009).

67. Schmid-Schönbein, H. & Wells, R. Fluid Drop-Like Transition of Erythrocytes under Shear. *Science (80-.).* **165,** 288–291 (1969).

68. Skotheim, J. M. & Secomb, T. W. Red Blood Cells and Other Nonspherical Capsules in Shear Flow: Oscillatory Dynamics and the Tank-Treading-to-Tumbling Transition. *Phys. Rev. Lett.* **98,** 078301 (2007).

69. Abkarian, M., Faivre, M. & Viallat, A. Swinging of red blood cells under shear flow. *Phys. Rev. Lett.* **98,** 2–5 (2007).

70. Sui, Y., Chew, Y. T., Roy, P., Cheng, Y. P. & Low, H. T. Dynamic motion of red blood cells in simple shear flow. *Phys. Fluids* **20,** 1–11 (2008).

71. Krüger, T., Gross, M., Raabe, D. & Varnik, F. Crossover from tumbling to tank-treading-like motion in dense simulated suspensions of red blood cells. *Soft Matter* **9,** 9008–9015 (2013).

72. Finken, R., Kessler, S. & Seifert, U. Micro-capsules in shear flow. *J. Phys. Condens. matter* **23,** (2011).

73. Abkarian, M. & Viallat, A. Vesicles and red blood cells in shear flow. *Soft Matter* 653–657 (2008).

74. Krüger, T. Effect of tube diameter and capillary number on platelet margination and near-wall dynamics. *Rheol. Acta* **55,** 511–526 (2016).

75. Goldsmith, H. L. & Marlow, J. Flow Behaviour of Erythrocytes. I. Rotation and Deformation in Dilute Suspensions. *Proc. R. Soc. B Biol. Sci.* **182,** 351–384 (1972).

76. Kersaudy-Kerhoas, M. & Sollier, E. Micro-scale blood plasma separation: From acoustophoresis to egg-beaters. *Lab a Chip - Miniaturisation Chem. Biol.* **13,** 3323–

3346 (2013).

77.   Sharma, S., Zapatero-Rodríguez, J., Estrela, P. & O'Kennedy, R. Point-of-Care diagnostics in low resource settings: Present status and future role of microfluidics. *Biosensors* **5,** 577–601 (2015).

CHAPTER 3

Experimental techniques and Methodology

The present chapter describes the general experimental procedures employed throughout the project. We describe in detail the process of microfabrication employed to produce the microfluidic platforms used in the experiments, from geometry design and mould production to the assembly of the microfluidic devices. Since different laboratory facilities were used to perform the experiments, only a generic description of the microfluidic setup is provided. Techniques used for fluid (e.g. rheology) and flow (e.g. visualisation and particle tracking velocimetry) characterisation are then introduced. Other specific information, such as details on equipment specifications and preparation protocols of the various solutions and suspensions are presented in each relevant chapter.

3.1 Fabrication of microfluidic devices

There is a broad range of techniques available for microfluidic fabrication[1] and its choice depends on the type of application, the accuracy required and the properties of the fluids to be used in the devices. In this work, photo-lithography[2,3] and soft-lithography,[3-8] techniques were used to produce the mould and polymeric channels, respectively, due to their ability to produce microfluidic geometries, with accurate definition and at a relative low cost.

The fabrication procedure involves a number of steps:

- Design of the microfluidic geometries using an appropriate CAD (computer aided design) software;

- Printing of the photo mask with the corresponding design;

- Production of the SU8 epoxy resin mould by photo-lithography;

- Fabrication of the PDMS replica by soft-lithography;

- Assembly of the PDMS-glass microdevice, using oxygen plasma.

which are described in detail in the following sub-sections.

3.1.1 Geometry design and mask production

AutoCAD® software was used to design the various masks used in this work. Each mask may contain distinct microfluidic channels (see Figure 3.1a for an example of a mask design). The masks exhibit opaque and transparent regions, which allow light to go through certain regions alone, that define the desired pattern to be transferred to the mould. Independently of the mould size, a rim of 5 to 10mm from the edge of the mask is left blank as large variations/errors in terms of channel dimensions may occur in this region. This point is further discussed in the mould manufacturing section 3.1.2.

The masks used for microfabrication purposes usually use either a film substrate or a glass/quartz substrate. The second option consists in depositing a uniform layer of chrome where the channel design is etched. Due to chrome resistance, the masks present high durability and good resolution of ±1μm.[9] However, these are more expensive than film masks and usually the investment is only worth when producing a final version of the geometry. For preliminary tests, transparent masks are typically preferred. These are less expensive and allow good performance, depending on the printer resolution. They are deformable and less stable than chrome masks and, for this reason, should be stored and used in a temperature and humidity controlled environment.

Most moulds used in this work were produced *in-house*, using transparent photomasks printed by an external company (Selba S.A., Switzerland). The photomasks are produced by

photo emulsion in acetate using a 50,800 dpi resolution (Figure 3.1b), where the areas corresponding to the channel regions are transparent and outer regions are printed in black. Figure 3.1c presents a detail of a bifurcating geometry printed in one of our film photomasks, showing the good printing quality, where only small defects are detected. For the applications in this thesis, such imperfections are not important. However, possibly due to the flexibility of the mask, together with other details on mould manufacturing, the real channel widths of PDMS devices produced using these masks deviate slightly from the theoretical ones, on the order of a few microns, affecting the accuracy of the geometry. These errors need to be quantified prior to the flow experiments and, depending on the application, can play an important role in the performance of the devices, as discussed in Chapter 4.
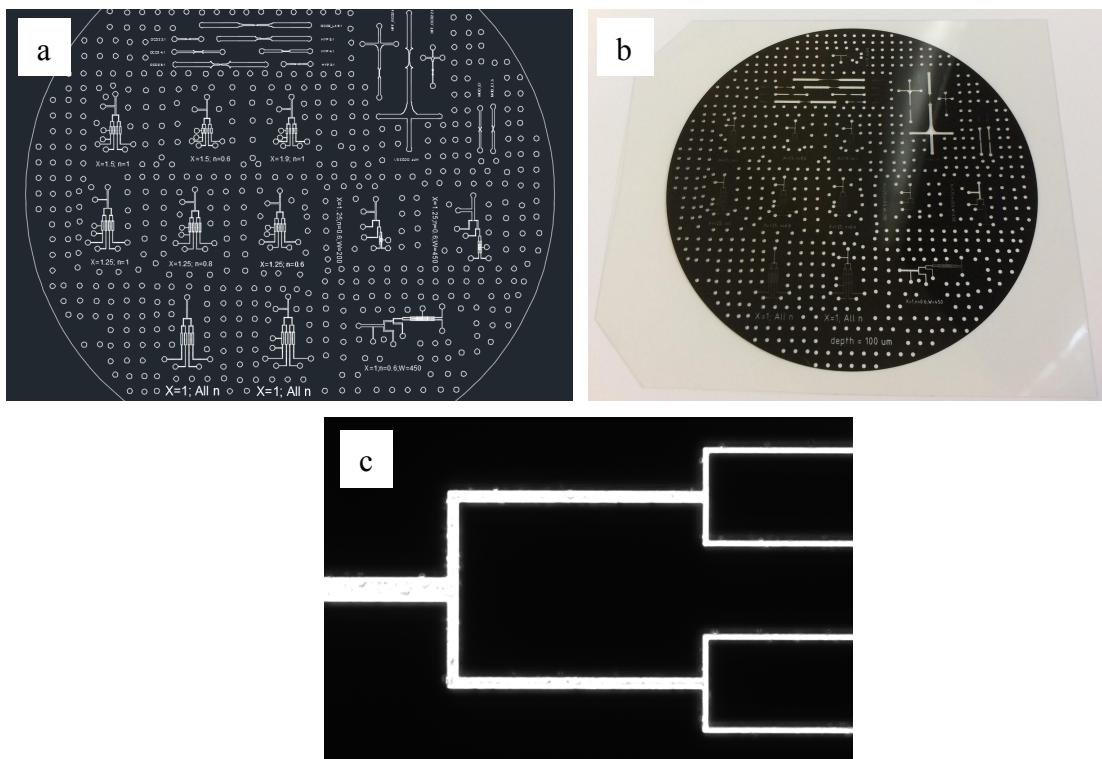
Figure 3.1: (a) CAD drawing of one of the masks, showing distinct microfluidic geometries; (b) corresponding transparent photo mask produced by Selba S.A. and (c) microscope image showing a detail of a bifurcating geometry in the same mask.

3.1.2 Production of SU8 moulds by photo-lithography

This step is one of the most critical during microfabrication, since the same mould is repeatedly used to produce polymeric channels. This means that any possible defect in the mould will be transferred to the replicas. Our moulds were produced using a

photolithography process performed in a clean room class 1000 (ISO6). Even though the epoxy-resin manufacturer[10] (MicroCHEM®) provides a standard procedure to fabricate SU8 moulds, within a channel depth error smaller than 5%, the process parameters had to be adjusted according to the equipment and conditions available in the laboratory facilities used (ESPCI and IPGG Institute, Paris).

Two different epoxy resins, SU8-2050 and SU8-2100 were used on the desired depth of the microfluidic channels. The resin EPON® SU8 is composed by a polymer with 8 epoxy groups per molecule (Figure 3.2a), an organic solvent to allow the resin handling and a photo initiator, which can be triggered by UV light or high temperature.
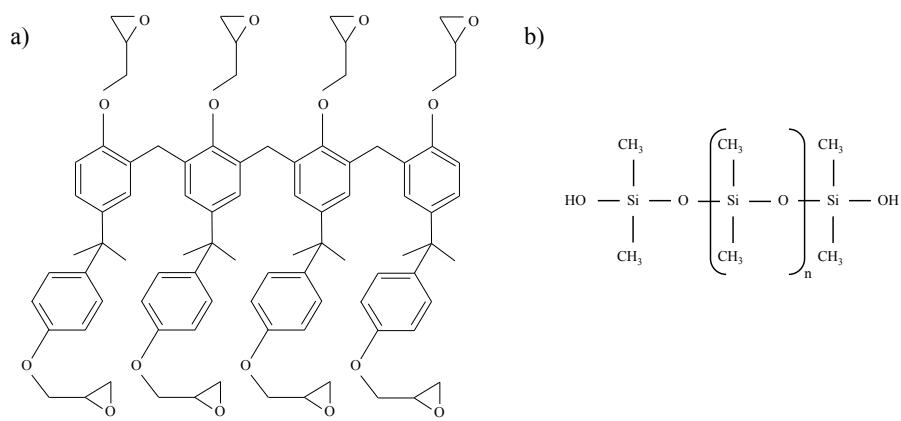
Figure 3.2: Schematic representation of SU8 molecule (a) and PDMS molecule (b).

Figure 3.3 presents a scheme of the main steps involved in SU8 mould manufacturing[11] and Table 3.1 summarises the parameters used for producing moulds of 50 and 100μm height. A more detailed description of each step is provided below.

1.   2.   3.

4.   5.   6.
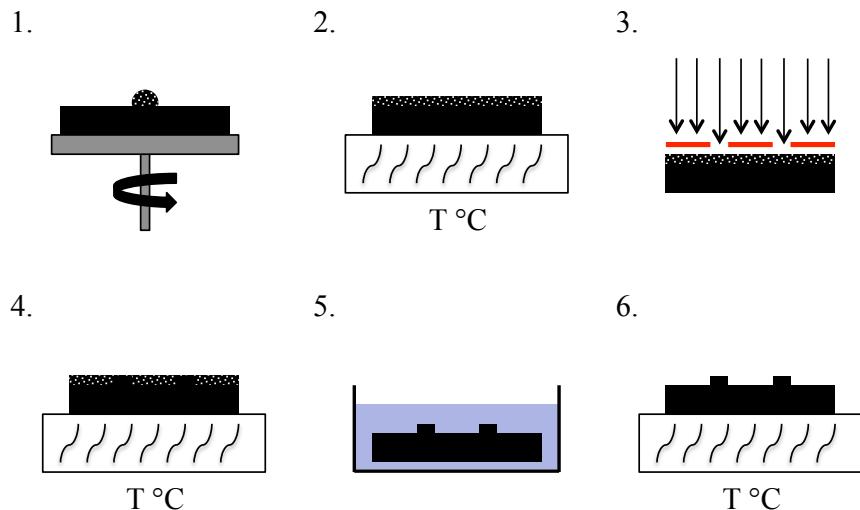
Figure 3.3: Schematic representation of the steps performed for SU8 mould fabrication by photo-lithography. (1) Deposition of the SU8 resin on the wafers surface and spin-coat, (2) soft bake, (3) UV light exposure through the mask, (4) Post exposure bake, (5) SU8 development and (6) hard bake.

Substrate cleaning

A substrate silicon (Si) wafer is cleaned using isopropanol, dried with N_2 and heated on a hot plate. This process allows removing any physical impurities as well as any moisture on the surface, promoting a good adhesion of the resin to the wafer.

1. Photoresist deposition

After cooling the substrate, a drop of resin is placed on the centre of the wafer and spin coated using a specific program so that a uniform layer of resin is achieved. First slower rotation is imposed to disperse the total resin volume across the wafer surface and a second higher speed allows tuning the desired resin height.

2. Soft bake

The wafer with the resin layer is placed on top of a hot plate for solvent evaporation. Two temperature steps are used, 65°C and 95°C, to allow a gradual evaporation of the resin solvent, and also avoid a temperature shock, which can lead to cracking. This process avoids flow of resin at room temperature, and the combination of temperature and time applied depends on the desired thickness of the resin.

After spin-coating the resin, it is common to find a resin bulge at the edge of the wafer, caused by surface tension. This effect is more pronounced in moulds of higher thickness, for which the resin used is far more viscous. Before the exposure to UV light, the outer layer of

about 5mm is removed, using a tip embedded in SU-8 developer (1-Methoxy-2-propyl acetate), so the height of the resin covering the design is uniform, and the entire surface can be brought into contact with the transparent photo mask.

3. UV light exposure

The wafer is placed in the mask aligner (MJB4 SUSS, MicroTec), making sure it is perfectly horizontal and the mask is brought into soft contact for UV exposure, to improve resolution. The UV light passing through the mask in the non-printed regions will allow the areas corresponding to the channels to crosslink. This step is extremely important and a few aspects should be checked in order to generate a good mould: the wavelength should be 365nm, as required for SU8 crosslinking, and the UV light should be collimated in order to achieve channels with vertical walls and with the desired cross-section size and shape. The exposure time to UV light is critical and depends on the SU8 thickness desired.

4. Post exposure bake (PEB)

During UV exposure, the photoactive component in the SU8 resin is activated but the full reaction is only achieved by heat. The wafer is again heated at 65°C and 95°C. As for the soft bake step, the use of temperature should be gradual to reduce the mechanical stresses inside the resin. The channel features become noticeable during this process.

5. Development

After cooling the mould, the non-cured resin is removed by placing it inside a glass recipient with SU8 developer, stirred at constant rotation for a pre-set period of time. The mould is then washed with isopropanol and dried with N_2.

6. Hard bake

At this point, the mould should be inspected using a microscope. It is common to find small cracks in the channels as result of the mechanical stresses in the resin. When this happens, the mould is heated up again for removing the cracks. With this extra heating step, the SU8 becomes harder and more resistant, which is ideal as the moulds will be used repeatedly. The glass transition temperature of the cross-linked SU8 is about 210°C.[10]

Table 3.1: Parameters used to produce the SU-8 moulds with thicknesses of ~50μm and ~100μm depth, fabricated *in-house*.

Mould depth (μm)	50	100
Resin reference	SU8-2050	SU8-2100
Substrate pre-treatment	200°C for 5min	
SU-8 coating	ramp 0 – 500rpm in 10s + 3200rpm for 30s	
Soft baking	65°C for 30s + 95°C for 6min and 30s	65°C for 5min + 95°C for 20min
UV exposure (λ = 365nm) time at 240 - 260 mJ/cm^2 exposure energy	23sec	33sec
Post exposure baking	65°C for 1min and 10s + 95°C for 6min and 10s	65°C for 5min + 95°C for 10min
SU-8 development	5min and 20s	10min
	rinse with isopropanol and dry with N_2	
Hard bake	200°C for 5-10min	

Finally, the mould is checked with a stylus profilometer (Veeco Dektak 6M) to confirm if the positive relief presents the desired height. Figure 3.4a shows an SU8 mould produced in house.
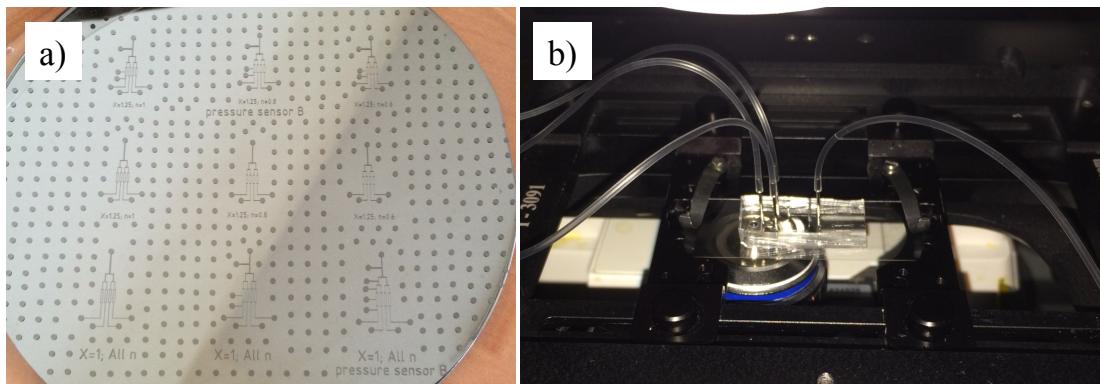
Figure 3.4: (a) Image of an SU8 mould produced by photo-lithography *in-house* and (b) example of a microfluidic device produced in PDMS by soft-lithography.

3.1.3 Production of PDMS channels by soft-lithography

The production of microfluidic devices was carried out using PDMS (Polydimethylsiloxane) elastomer (Figure 3.2b), which is arguably the most common material used for the fabrication and prototyping of such devices.[12] PDMS presents several advantages including

homogeneity and optical transparency at a large range of wavelengths (240-1100nm), allowing a clear imaging of the fluid inside the channels; its handling is straight-forward and the devices are produced at low cost; PDMS is also permeable to gases which, in this case, is an advantage, allowing users to easily remove air bubbles trapped inside complex microfluidic designs; PDMS is biocompatible, allowing experiments using biological samples and, finally, it is chemically inert for the majority of fluids, although some organic solvents might cause polymer swelling, compromising the channels integrity.[13] PDMS is naturally hydrophobic which can be an obstacle when using hydrophilic samples. This problem can be temporarily overcome by modifying PDMS surface using oxygen plasma. Figure 3.5 presents schematically the main steps performed to produce PDMS channels by soft-lithography.
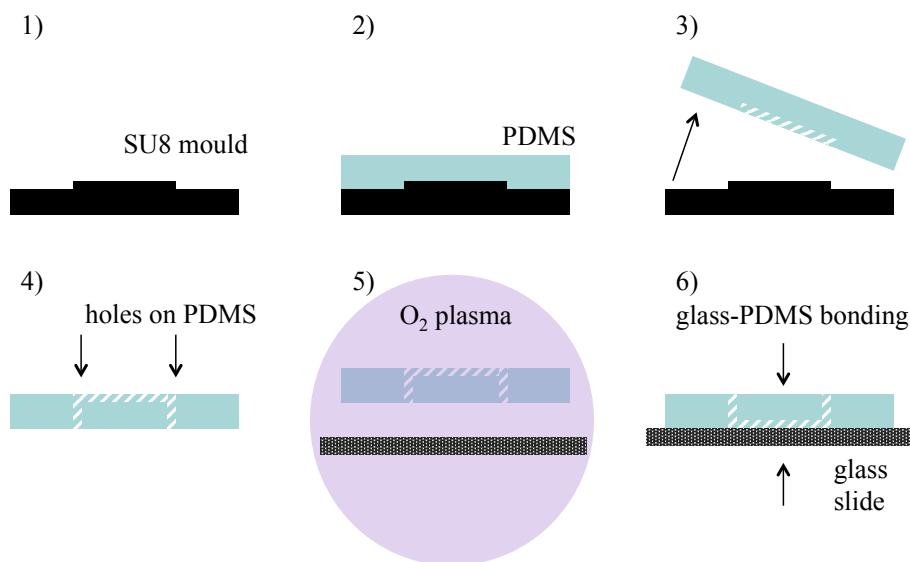
Figure 3.5: Schematic representation of the steps performed for PDMS channel fabrication: (1) mould preparation, (2) PDMS pouring and cure, (3) PDMS release, (4) punching the holes for fluid inlet/outlet, (5) oxygen plasma, (6) irreversible PDMS bonding to the glass slide/ cover slide.

Each of the steps is described in more detail below:

1. *Preparing the mould*

The SU8 mould is washed using isopropanol and dried carefully using compressed air. Aluminium foil around the mould is used to avoid PDMS spillage, and saved in a clean Petri dish until contact with the polymer.

2. *PDMS mixture and curing*

PDMS (Sylgard 184, Dow Corning®) is mixed with the curing agent at a ratio of 9:1 (w/w). This process can be made by hand, vigorously, or using a mixer (THINKY ARE-250 CE) as long as the entire crosslinking agent is uniformly brought into contact with the pre-polymer. After degassing the mixture, the PDMS is poured into the mould and allowed to degas again in a desiccator connected to a vacuum pump, for about 10-15min, so that the polymer wets all the features on the mould surface avoiding the presence of all air bubbles, which might result in defects. The mixture is then cured in the oven using one of the two temperature-time sets: 70°C for 2 hours or 80°C for 25min.

3. *Release of the PDMS replica*

After PDMS hardening, the mould is cooled down. To avoid mechanical stress, smaller layers of PDMS should be carefully removed from below the mould and released using a sharp razor. Only afterwards the PDMS should be carefully separated from the mould.

4. *Trimming the PDMS and defining the inlet ports*

The PDMS block is cut using a sharp blade so the entire channel design fits a standard glass slide or a cover slip; the holes for fluid inlet and outlet were punched perpendicularly to the PDMS surface and as aligned as possible with the design, using appropriate needles (Harris Uni-core Punch, 1mm diameter, Whatman). All inlets/outlets were created this way, except when stated otherwise. The surfaces are then cleaned using scotch tape (Scotch® Magic Tape) to remove larger pieces of PDMS debris. The structures are washed with isopropanol and dried using compressed air. At the end, the PDMS block surface is again cleaned with scotch tape, as well as the glass slide to which the PDMS will bond.

5. *Plasma treatment and microchip assembly*

One limitation of PDMS is its low adhesion to glass. This means that when both surfaces are brought together, the microfluidic device might not stand the pressure of the flowing samples, resulting in fluid leakage. One way to circumvent this problem is to use oxygen plasma. This treatment is quite effective on removing hydrocarbon groups from both materials' surface, leaving exposed silanol groups on the PDMS surface and hydroxyl groups on the surface of glass. The reaction between these two groups generates a strong and irreversible Si-O-Si covalent bond and the microdevice can withstand considerably higher pressure without leaking.[14]

Before bonding the PDMS to the glass, the oxygen plasma is run in empty chamber to remove impurities. Each plasma series comprises three cycles of vacuum alternated with oxygen inflow, followed by plasma generated at a stable low pressure of 0.2 – 0.3mbar (75 seconds at 50W, frequency 40KHz). After exposure to plasma, PDMS and glass surfaces are brought in contact for permanent bonding. In some cases, a small pressure is applied on top of the PDMS and against the glass, to avoid the entrapment of air bubbles. The oxygen plasma treatment also changes temporarily the wettability of the PDMS surface, from hydrophobic to hydrophilic (contact angle with water decreases from $100 \pm 8°$ to $13 \pm 3°$),[15] which simplifies the infusion of aqueous solutions into the channels.

6.   Post sealing treatment

Even though the oxygen plasma treatment is quite efficient, a post heating treatment reinforces the adhesion between the two surfaces and the microchip becomes very resistant to pressure. This is achieved by placing the assembled microchip in the oven at 80 - 90°C for 10-15min. After that, the microchip is allowed to cool down and the inlet ports are covered with scotch tape until further using. Figure 3.4b shows a microfluidic device built in the laboratory.

Even though the photo- and soft-lithography methodologies previously described are now well established, the production of SU8 moulds by photo-lithography entails complicated logistics due to the requirement of a clean room. For this reason, three dimensional (3D) printing[16,17] was also considered to produce the moulds, since this technique has matured significantly in the last decade and is available at a very competitive costs. Currently, both the printer resolution and the quality of the printing material already allowed the fabrication of devices of larger dimensions for microfluidic applications, as well as master moulds.[16] Several tests were performed using the 3D printer available at the University of Strathclyde (Form2, Formlabs), as well as printing machines from two local companies. Appendix A describes the 3D printing methodology used to produce the master mould as well as the main results achieved. Even though the production was fast, the PDMS channels obtained using this technology, either present a slightly rough surface or a smooth cross-section, in contrast with the desired rectangular cross-section, which are not satisfactory for the level of accuracy required for the current experiments. Nonetheless, these new moulds represent an interesting alternative to test microfluidic geometries *in-house*, for applications using channels of larger dimensions, on the orders of millimetres.

3.2 Flow characterisation

3.2.1 Microfluidic and imaging setup

All the microfluidic experiments performed throughout this project were carried out using a similar setup, as shown in Figure 3.6. An inverted microscope (1) was used to observe the sample, allowing enough space for the manipulation of the microfluidic device and tubing connections. The sample was pushed or withdrawn into the channel via Tygon tubing, using a precise syringe pump (2) and the microscope stage was manipulated using a console (4). The images were acquired by a digital camera (3) and processed using appropriate software (5). Because of the different properties of the samples considered in this study, either fluorescence (6) or bright field (7) illumination was used. The light path inside the microscope is described in more detail for the two types of illumination used. Further details on the microfluidic setup are provided in each relevant chapter.
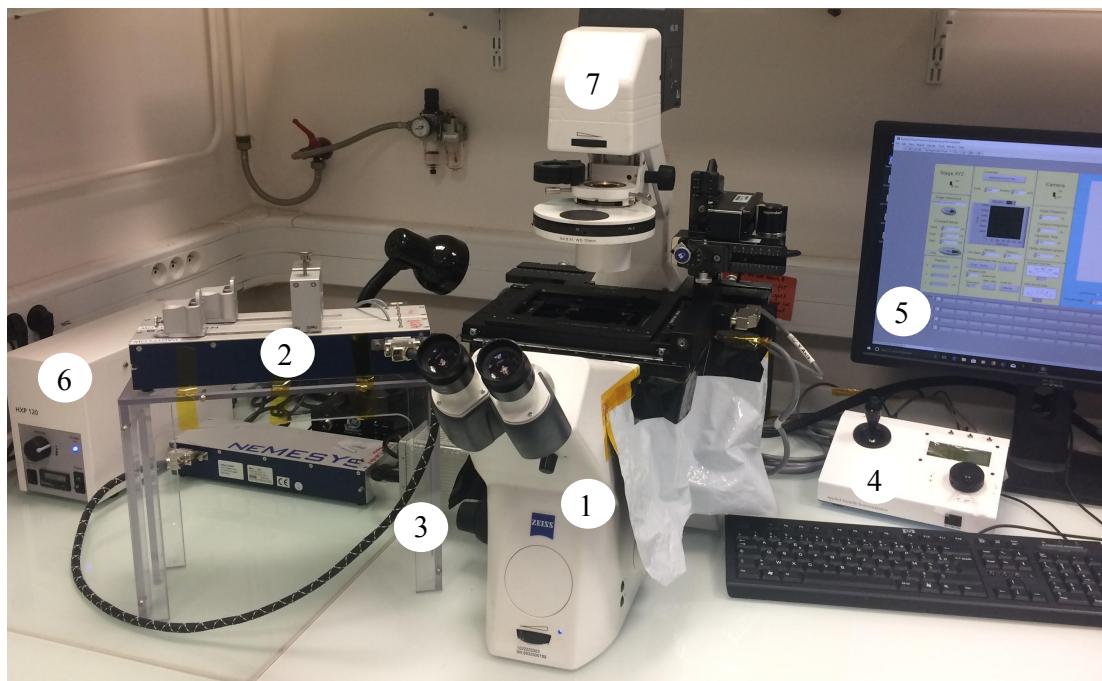
Figure 3.6: Image of one of the microfluidic setups used for the experiments, including an inverted microscope (1), a syringe pump (2), a digital camera (3), a console for controlled microscope platform displacement (4), computer (5), fluorescence illumination (6) and bright field illumination (7).

3.2.2 Illumination and optical path setup

Bright field illumination

Bright field microscopy is the most common and simple method used for observing samples with dark objects in a clear background,[18] as is the case e.g. of opaque red blood cells

flowing in aqueous solutions.[19] The image obtained is a result of the absorbance, scattering and deflection of the light passing through the sample.[20] Figure 3.7 shows the scheme of the light path in bright field microscopy.

In this particular case, the light source and the microscope objective are situated on opposite sides of the sample. In an inverted microscope, such as the one used in this work, the halogen lamp is located above the microscope stage and the light passes through the collector lens, condenser aperture diaphragm and condenser lens before illuminating the sample. The light scattered by the sample is then recovered by the microscope objective and travels inside the microscope until detection by the digital camera or eyepiece.
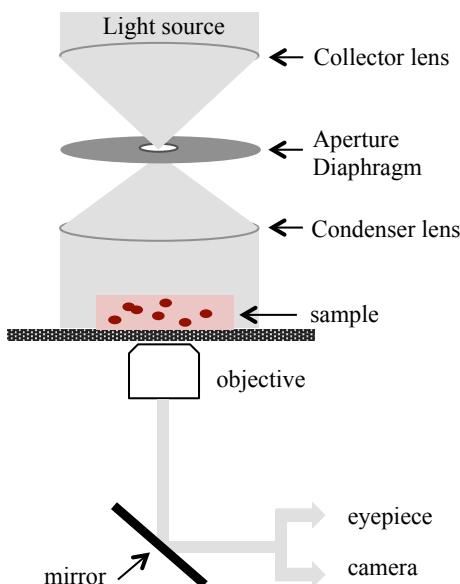
Figure 3.7: Schematic representation of the light path in bright field microscopy.

Fluorescent illumination

Epi-fluorescence microscopy is based on the ability of the sample to emit energy at a larger wavelength, λ_{EM}, upon excitation at a specific lower wavelength, λ_{EX}. Fluorescence microscopy is particularly useful when the signal to noise ratio is low using bright field, allowing us to observe the flow patterns, quantify the kinematics, or even identify changes in configuration at molecular level.

Figure 3.8 presents the light path of the optical system used for epi-fluorescence microscopy. In this case, the source of illumination is typically a laser, a mercury lamp or a metal halide lamp. Lasers emit light at a single wavelength, while the others emit a large spectrum of wavelengths. Since each fluorescent sample has a specific excitation and emission

wavelengths, a filter cube is located inside the microscope to select the suitable bands of wavelengths to produce better quality images.

The excitation filter selects a (typically narrow) band of wavelengths from the emitted spectrum, which is then reflected into the objective using a dichroic mirror. This band includes the samples excitation wavelength, λ_{EX}. After excitation, the sample emits at a wavelength of lower energy, λ_{EM}, and the difference between λ_{EX} and λ_{EM} is called Stokes' shift. The light emitted by the sample λ_{EM}, as well as the light on the microscope surroundings, is captured by the objective and passes through the dichroic mirror. The emission filter in the filter cube allows only a selected range of wavelengths, including the emitted wavelength λ_{EM}, to be detected by the camera or eyepiece, allowing images with increased definition.
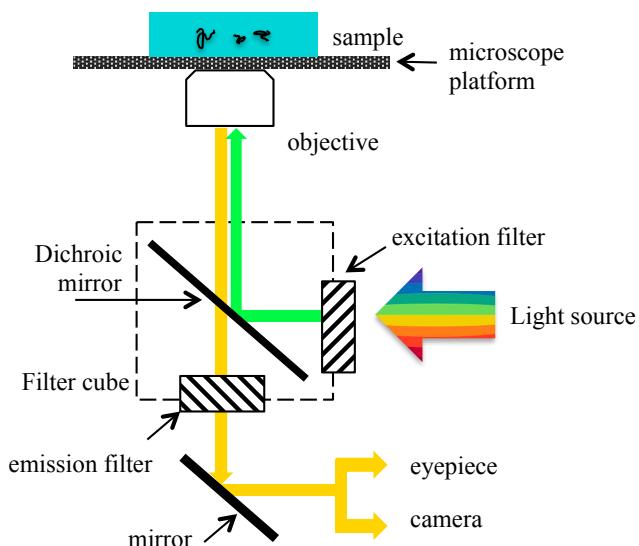
Figure 3.8: Schematic representation of the light path used for epi-fluorescence microscopy.

3.2.3 Particle tracking velocimetry (PTV)

Particle Tracking Velocimetry is one of the most frequently used techniques to determine the velocity field of a moving fluid.[21] Usually tracer particles are added to the fluid and the technique relies on measuring the individual displacement of the dispersed particles, during a certain period of time to obtain their velocity. For a correct measurement, the particles should be:

1. neutrally buoyant, i.e. particle density $\rho_{particle}$ should be similar to the density of the fluid ρ_{fluid};

2. small enough not to disturb the natural fluid flow;

3. chemically inactive, avoiding producing any changes in the fluid properties;

4. easily detected. For this reason, fluorescence particles are commonly used as tracers in the fluid;

In our experiments, 1μm latex particles were used with excitation and emission wavelengths of 535 and 575nm, respectively (Nile Red, Molecular Probes, Invitrogen). In addition, the number of particles per volume of sample should be small enough to allow identification of their position. The time interval between images Δt should be small enough so that the distance travelled by each particle, between consecutive frames, is much smaller than the distance between two particles in the same frame.

In PTV experiments, the time step Δt is determined by the frame rate of the camera, so high-speed cameras are usually employed for these measurements. In this study, a high-speed camera (FASTCAM SA4, Photron) is used to capture the images for PTV. Exposure times should be small enough to obtain perfectly defined particles without blur and high enough to obtain a large signal to noise ratio. The set-up is adjusted to focus on the particles travelling at the centreplane ($z = h/2$, where h refers to the depth of the channel) of the microfluidic channel. The images are then post-processed.

First, the position of each particle in focus is determined and second, the velocity of each individual particle is calculated by dividing the displacement of each particle in consecutive frames, Δx, by the time between frames Δt. This data analysis is performed using the ImageJ and Matlab codes. Further details about PTV are provided in Chapter 4.

For validation and when appropriate, the experimental velocity profiles obtained by PTV were compared with the theoretical velocity profiles calculated using an analytical solution for fully developed flow of a Newtonian fluid in a channel of rectangular cross-section,[22] presented in Chapter 2, equation 2.6.

3.2.4 Streak imaging

In order to provide information on the streamlines inside the microfluidic channels, streak imaging was performed using fluorescent tracer particles (the same type of particles used for PTV). These images are obtained by significantly increasing the exposure time, depending on the fluids' velocity, allowing the camera to register the path described by the particle during flow. This technique can also be used for non-stationary flows.

3.3 Fluid characterisation

3.3.1 Shear rheology

The characterisation of the samples under steady shear measurements was performed using rotational rheometers (Physica MCR 501, Anton Paar and DHR2, TA Instruments). For this purpose, distinct geometries can be used, according to the sample nature,[23] and the experiments consist mainly in applying a rotational motion to the confined sample, in order to subject it to a shear flow. Dispersions and suspensions are particularly challenging to analyse since the presence of particles, its volume fraction or rigidity may interfere with the accuracy of the measurement.

For the characterisation of the samples in this work, both cone-plate (CP, Figure 3.9a) and plate-plate (PP, Figure 3.9b) geometries were used. In these systems, the sample is contained between the lower stationary plate and the upper plate or cone, which is rotated with an angular velocity, Ω, at given torque M. In our measurements, the flow curves were obtained as a function of the shear rate, $\dot{\gamma}$.
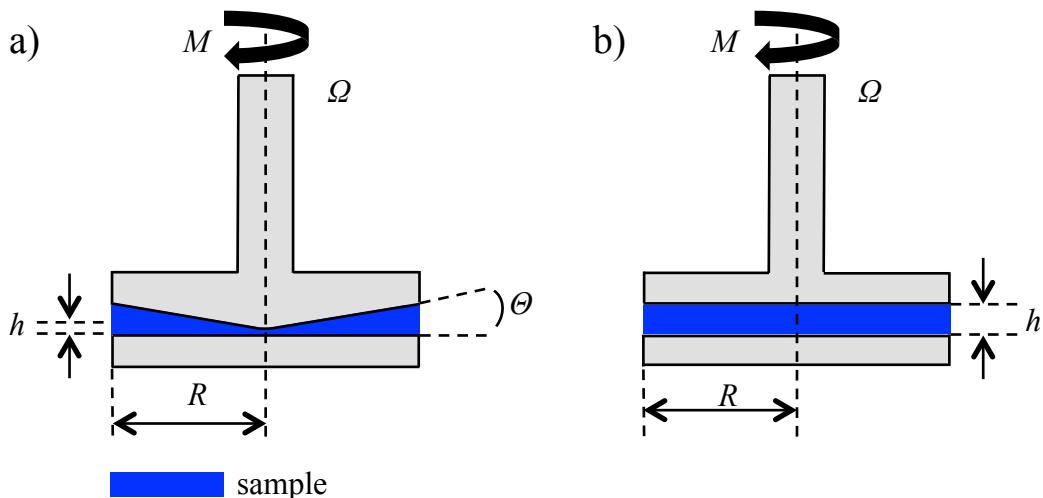
Figure 3.9: Schematic representation of cone-plate (a) and plate-plate (b) geometries used to characterise the samples under shear conditions. Drawings not to scale.

Cone-plate geometry

The cone-plate geometry is arguably the mostly used geometry for rheological measurements due to its accuracy and precision.[24] This configuration presents several advantages like generating a constant shear rate across the entire sample and using a small volume of sample to measure the viscosity in a wide range of shear rates. However, this geometry is not recommended to analyse suspensions unless the particle diameter is smaller than ~10 times

the geometry gap h, defined in this configuration by the truncated cone pit size (cf. Figure 3.9a), which is usually very small (for example, for the CP geometry of radius $R = 30$mm and angle $\theta = 1°$, the gap set at the centre of the cone is 30μm and 52μm for rheometers DHR2, TA Instruments and Physica MCR 501, Anton Paar, respectively). The gap should be maintained at these exact values to ensure the shear rate is constant throughout the sample. If the truncation height is increased, then the shear rate can present important variations throughout the sample, compromising the accuracy of the measurement.

In this work, a cone-plate geometry ($R = 30$mm and $\theta = 1°$) was used to characterise polymeric solutions of xanthan gum, sucrose (Chapter 4) and Dextran40 (Chapter 6), as well as the suspension of λ-DNA molecules (Chapter 4).

As previously mentioned, the shear rate, $\dot{\gamma}$, applied to the sample is considered constant and is determined by the ratio of the angular velocity, Ω, and the angle, θ, of the rotating cone,[23] for small angles θ:

$$\dot{\gamma} = \frac{\Omega}{\theta} \tag{3.1}$$

The shear stress τ_{xy} can be calculated from the torque M applied on the cone to impose a certain angular velocity:

$$\tau_{xy} = \frac{3M}{(2\pi R^3)} \tag{3.2}$$

where R is the radius of the cone. Finally, the viscosity is given by $\tau_{xy} = \eta(\dot{\gamma})\dot{\gamma}$ to be

$$\eta = \frac{3(M\theta)}{2\Omega\pi R^3} \tag{3.3}$$

It is important to determine the lower and upper limits between which the measured values of viscosity are considered reliable. The lower limit of measurable shear viscosity depends on the rheometer minimum resolvable torque (M_{min}) and the geometry characteristics. For the cone-plate geometry considered, a limit of 20xM_{min} was considered and the minimum shear viscosity measured is then given by the equation 3.4:

$$\eta_{min} = \frac{3(20M_{min})}{2\pi R^3 \dot{\gamma}} \tag{3.4}$$

The upper limit of measurable shear viscosity, above which inertial instabilities might arise, can be defined as:[25]

$$\eta_{max} = \frac{\Omega\theta^2\rho R^2}{6} \qquad (3.5)$$

Plate-plate geometry

Plate-plate geometries require only small sample volumes (like in CP geometries) and allow the gap h (Figure 3.9b) to be adjusted as necessary (unlike the CP case) and are therefore useful for testing dispersions with large particles. A plate-plate geometry (R = 20mm with a gap h = 400μm) was used to determine the flow curves of RBC suspensions. The recommended gap sizes to use in these geometries are in the range of   0.3 – 3mm, even though a small gap is preferable to avoid a temperature gradient across the sample height. If a larger gap is needed, then a thermal cover should be used to reduce temperature gradients in the sample and measuring system. When the samples to be characterised contain particles, the gap should be larger than 10 times the particle size, so the particle spatial distribution is not affected by the walls, which could translate in inaccurate measurements.[23] The presence of the wall boundaries changes the sample microstructure and, in the case of suspensions, a lubrication layer depleted of particles may form close to the geometry surfaces. This problem results in underestimated values of shear viscosity and can be overcome by replacing the smooth surface of the upper moving plate by a rough surface.[26] In our experiments, we have used a layer of P800 grit silicon carbide sandpaper, carefully trimmed and attached to the upper plate, in order to match its surface area.

Contrarily to the cone-plate, this geometry presents a heterogeneous shear rate distribution across the sample,[27] being zero at the centre of the plate (r = 0) and maximum at the rim (r = R). The equation 3.6 described the shear rate at the rim:

$$\dot{\gamma}_R = \frac{R\Omega}{h} \qquad (3.6)$$

where h corresponds to the gap between upper and lower plates.

The shear viscosity is given by equation 3.7, where the term between brackets corresponds to the correction for the variable shear rate profile along the distance r:

$$\eta(\dot{\gamma}_R) = \frac{2M}{\dot{\gamma}_R}\pi R^3\left(\frac{3}{4} + \frac{1}{4}\frac{d\ln M}{d\ln\dot{\gamma}_R}\right) \qquad (3.7)$$

In the case of the plate-plate geometry, the minimum and maximum limits of the measured viscosity can be expressed as equations 3.8 and 3.9, respectively:

$$\eta_{min} = \frac{2h(20M_{min})}{\pi R^4 \Omega} \tag{3.8}$$

$$\eta_{max} = \frac{\Omega \rho h^2}{6} \tag{3.9}$$

3.3.2 Pycnometry

The densities, ρ, of the fluids were determined using a glass pycnometer of volume $V = 10mL$. The sample density is simply determined by the difference in mass between the filled and empty pycnometer, divided by the volume of the sample:

$$\rho = \frac{(m_2 - m_1)}{V} \tag{3.10}$$

where m_1 is the mass of the empty pycnometer (container and lid, cf. Figure 3.10a) and m_2 is the mass of the pycnometer totally filled with the sample of interest (m_2), as shown in Figure 3.10b. The outside of the container should be perfectly clean, to ensure that the mass of the sample corresponds to the accurate 10mL. For the same reason, it is important to ensure that no air bubbles are trapped inside the container. These measurements were performed at the temperature of 20±1°C.
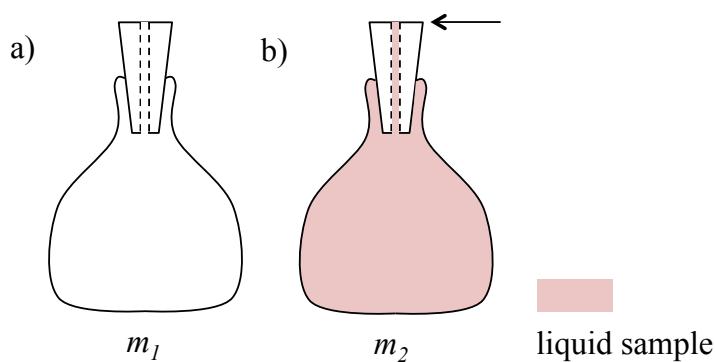
Figure 3.10: Schematic representation of the density measurement, using liquid pycnometry: (a) empty pycnometer with lid, for reference value and (b) pycnometer totally filled with sample up to the reference level indicated by the arrow.

In this chapter we described the typical methods used for the fabrication of microfluidic devices as well as the techniques used for fluid and flow characterisation. Further details on the techniques used will be provided in each respective chapter.

References

1. Silverio, V. & Freitas, S. C. de. in *Complex Fluid-Flows in Microfluidics* (ed. Galindo-Rosales, F. J.) 25–51 (Springer International Publishing AG, 2017). doi:10.1007/978-3-319-59593-1

2. Martinez-Duarte, R. & Madou, M. J. in *Microfluidics and Nanofluidics Handbook: Fabrication, Implementation and Applications* (eds. Chrakaborthy, S. & Mitra, S. K.) 231–268 (CRC Press, 2009).

3. Qin, D. *et al.* Microfabrication, Microstructures and Microsystems. *Microsyst. Technol. Chem. Life Sci.* **194,** 1–20 (1998).

4. Xia, Y. & Whitesides, G. M. Soft lithography. *Annu. Rev. Mater. Sci.* **28,** 153–184 (1998).

5. Sia, S. K. & Whitesides, G. M. Microfluidic devices fabricated in poly(dimethylsiloxane) for biological studies. *Electrophoresis* **24,** 3563–3576 (2003).

6. Qin, D., Xia, Y. & Whitesides, G. M. Soft lithography for micro- and nanoscale patterning. *Nat. Protoc.* **5,** 491–502 (2010).

7. Mcdonald, J. C., Duffy, D. C., Anderson, J. R. & Chiu, D. T. Review General Fabrication of microfluidic systems in poly (dimethylsiloxane). (2000).

8. McDonald, J. C. & Whitesides, G. M. Poly(dimethylsiloxane) as a material for fabricating microfluidic devices. *Acc. Chem. Res.* **35,** 491–499 (2002).

9. Selba S.A. (2017). Available at: http://www.selba.ch/angl/photomask.html.

10. MICROCHEM Company. (2018). Available at: http://www.microchem.com/pdf/SU-82000DataSheet2000_5thru2015Ver4.pdf.

11. www.elveflow.com/microfluidic-tutorials/. (2018). Available at: http://www.elveflow.com/microfluidic-tutorials.

12. Tsao, C. W. Polymer microfluidics: Simple, low-cost fabrication process bridging academic lab research to commercialized production. *Micromachines* **7,** (2016).

13. Lee, J. N., Park, C. & Whitesides, G. M. Solvent Compatibility of Poly(dimethylsiloxane)-Based Microfluidic Devices. *Anal. Chem.* **75,** 6544–6554 (2003).

14. www.plasmatreatment.co.uk. (2018).

15. Bodin-Thomazo, N., Malloggi, F. & Guenoun, P. Marker patterning: A spatially resolved method for tuning the wettability of PDMS. *RSC Adv.* **7,** 46514–46519 (2017).

16. Ho, C. M. B., Ng, S. H., Li, K. H. H. & Yoon, Y.-J. 3D printed microfluidics for biological applications. *Lab Chip* **15,** 3627–3637 (2015).

17. Waheed, S. *et al.* 3D printed microfluidic devices: enablers and barriers. *Lab Chip* **16,** 1993–2013 (2016).

18. www.edmundoptics.com. (2018).

19. Chu-Su, Y. *et al.* Enhancing the Detection of Dysmorphic Red Blood Cells and Renal Tubular Epithelial Cells with a Modified Urinalysis Protocol. *Sci. Rep.* **7,** 40521 (2017).

20. Thorn, K. A quick guide to light microscopy in cell biology. *Mol. Biol. Cell* **27,** 219–222 (2016).

21. T., D. in *Three-Dimensional Velocity and Vorticity Measuring and Image Analysis Techniques* (Springer, Dordrecht, 1996). doi:https://doi.org/10.1007/978-94-015-8727-3_7

22. Bruus, H. Theoretical microfluidics. (2006).

23. Barnes, H. A. *Handbook of Elementary Rheology*. *Science* (2000). doi:10.1126/science.1201543

24. Strivens, T. A. & Schoff, C. K. *Rheometry, Ullmann's Encyclopedia of Industrial Chemistry*. (Wiley-VCH Verlag GmbH & Co. KGaA, 2002).

25. Sdougos, H. P., Bussolari, S. R. & Dewey, C. F. Secondary flow and turbulence in a cone-and-plate device. *J. Fluid Mech.* **138,** 379–404 (1984).

26. Sousa, P. C. *et al.* Shear viscosity and nonlinear behavior of whole blood under large amplitude oscillatory shear. *Biorheology* **50,** 269–282 (2013).

27. TA Instruments New Castle DE. Ten Steps to a Better Rheological Measurement. *Rheol. Train. Semin.* 1–44 (2005). doi:10.15343/0104-7809.20143803251259

CHAPTER 4

Biomimetic bifurcating networks for studying biological fluids and suspensions

This chapter describes the experimental implementation of biomimetic microfluidic networks for studying biological fluids and suspensions under specific shear stress conditions. The microfluidic devices were designed according to a biomimetic design rule, inspired by Murray's law, where the wall shear stress distribution along the consecutive channel generations is predictable. Such geometries are suitable for use with Newtonian and power-law fluids.

The microfluidic geometries were first tested using Xantan gum solutions, as an example of power-law fluid (shear-thinning) and, later on, with a solution of λ-DNA molecules. By analysing the molecule deformation under flow, we were able to infer about the performance of the microfluidic device.

Finally, the limitations of the experimental study are presented and discussed.

4.1 Introduction

Microfluidic devices are currently used for numerous types of applications due to cost efficiency, low volume sample consumption and disposability.[2,3] Some applications are related to cell culture and tissue engineering,[4] bio-sensing and point-of-care diagnosis,[3,5,6] particle synthesis[7,8] or separation.[9,10] Microfluidics are also used in the context of rheology research since the typical flow conditions achieved at these small scales allow studying the response of solutions and individual particles to imposed stresses in conditions such that viscous and elastic forces dominate relative to inertia. The information gathered from these experiments may help to understand the macroscale behaviour of complex fluids and polymer solutions.[11] An interesting application of these rheological micro-platforms is to use them for probing shear sensitive microscopic structures. As an example, in one single experiment one would ideally determine the mechanical resistance of shear sensitive bio-structures such as molecules, vesicles or liposomes, under a range of flow conditions. The latter are considered particularly promising drug carriers for local drug release when triggered by a peak of shear stress in the blood stream.[12] This flow abnormality is commonly seen in cardiac patients, due to atherosclerosis, in which cholesterol plaque deposits at the inner wall of blood vessels, generating an up to 10 fold increase in shear stress as compared to an equivalent healthy vessel.[12] If this constriction is found in the coronary artery, then it can lead to a lack of blood irrigation in the heart muscle possibly resulting in myocardial infarction. An ingenious idea to tackle this problem consists in injecting a drug loaded carrier in the blood stream for which the release is only triggered by the physical stress variation in the constricted region.[12,13] However, it was found that for standard liposomes built for this purpose, the range of shear stresses attained in healthy and stenosed vessels is not enough to disrupt their membranes and release the entrapped drug. There is now evidence that lenticular vesicles are more sensitive to shear stress and, as consequence, more appropriate for targeted drug delivery.[14] Therefore, essential research is still lacking to conceive shear sensitive carriers of optimised size and shape, able to successfully deliver the drugs in the critical areas.

For this purpose, the use of microfluidic devices with several branches, such as bifurcating networks, in which multiple well-controlled shear stresses can be imposed, could be highly beneficial. These devices would allow examining the mechanical resistance of such structures in a single experiment, determining the required shear stress threshold or history necessary to disrupt them for precise drug release.

The bifurcating networks used in this study were designed according to the biomimetic design rule proposed by Zografos et al.[15] inspired by Murray's law.[16] According to this rule, the customised geometries, of constant depth and rectangular cross section, are suitable to be used with both Newtonian and power-law fluids. A main feature of this design is the ability to control the variation of the average wall shear stress along consecutive network generations. Even though the design rule was successfully validated by performing numerical simulations using a computational fluid dynamics (CFD) code, an experimental verification of the proposed design rule was still missing.

The main idea of the present work is to establish the potential of the customised bifurcating networks to perform shear sensitive tests. We performed particle tracking velocimetry (PTV) to characterise the flow kinematics inside the channels for geometries of constant and increasing average wall shear stress, using both Newtonian and shear-thinning fluids. After finding a good agreement between experimental (PTV) and theoretical velocity profiles, these geometries were used to probe the response of individual molecules. For this purpose, a dilute solution of lambda bacteriophage DNA molecules (λ-DNA) was studied in customised networks of constant and increasing average wall shear stress. The λ-DNA molecule was previously studied in several microfluidic devices[17,18] and it is known to be sensitive to the local shear stress applied. By measuring the degree of deformation of individual λ-DNA molecules, when flowing along consecutive channels of the network, we were able to demonstrate the predictable effect of flow conditions imposed in the geometry on the confined flowing sample.

This work represents a crucial first step towards establishing these geometries as micro devices to test the response (and limits) of shear sensitive biological structures, such as vesicles, liposomes, cells or polymer molecules to local or cumulative stresses. The latter are particularly relevant when the shear loading history and exposure time play an important role.

4.2 Materials and Methods

4.2.1 Design rule

The microfluidic geometries used in this study consist of a series of symmetric bifurcations. Figure 4.1a presents the schematics of the network where the main channel corresponds to generation $i = 0$ and subsequent channels are distributed along generations $i = 1, 2$ and 3. All networks considered in this chapter have an approximately constant depth (h) throughout the

entire domain and the length of each generation (L_i) is set to be twenty times its hydraulic diameter (D_{hi}), $L_i = 20\ D_{hi}$.
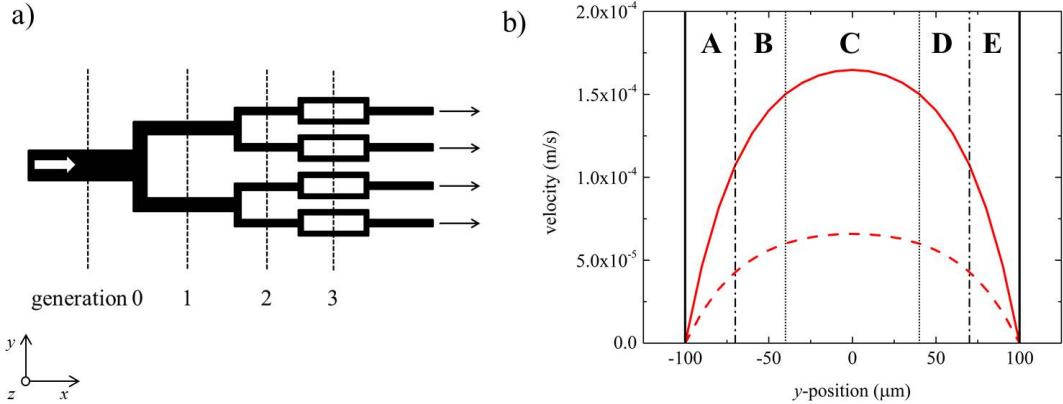
Figure 4.1: (a) Schematic representation of a typical bifurcating network used in this study. The four black arrows correspond to the channel outlets from where the fluid is withdrawn. (b) Theoretical parabolic velocity profiles for a Newtonian solution, at flow rates of 40nL min^{-1} (dashed line) and 100nL min^{-1} (solid line) for the $z = h/2$ centreplane of the main channel (generation $i = 0$ with width $w_0 = 200\mu m$, depth $h = 100\mu m$); sections A to E used for λ-DNA molecule analysis are also shown.

The width (w_i) of the channels in each generation i is determined by the biomimetic design rule proposed by Zografos $et\ al.$[15] according to the specific gradient of the average wall shear stresses desired along the network and the fluid of interest:

$$\alpha_i{}^n(1 + \alpha_i)^n \left(b_i{}^* + \frac{a_i{}^*}{n}\right)^n = \alpha_0{}^n(1 + \alpha_0)^n \left(b_0{}^* + \frac{a_0{}^*}{n}\right)^n (2^i)^n X^i \qquad (4.1)$$

where α_0 and α_i are the aspect ratios (defined as the ratio of depth to width) in the main channel and channels of generation i, respectively; a^* and b^* are geometrical parameters defined as:

$$a^* = \frac{1}{2\left(1+\frac{1}{\alpha_i{}^*}\right)^2} \frac{1}{\left[1+4\sum_{j=0}^{\infty}\frac{(-1)^{j+1}}{(\frac{2j+1}{2}\pi)^3}\frac{1}{\cosh\left(\frac{2j+1}{2}\pi\alpha_i{}^*\right)}\right]} \qquad (4.2)$$

$$a^* + b^* = \frac{1}{2\left(1+\frac{1}{\alpha_i{}^*}\right)^2} \frac{3}{\left[1-\frac{192}{\pi^5}\frac{1}{\alpha_i{}^*}\sum_{j=1,3,5,\ldots}^{\infty}\frac{1}{j^5}\tanh\left(\frac{j\pi\alpha_i{}^*}{2}\right)\right]} \qquad (4.3)$$

and X is the branching parameter, which relates the average wall shear stress in the channels of different generations ($\overline{\tau_i}$) with the average wall shear stress imposed in the main channel ($\overline{\tau_0}$):

$$X^i = \frac{\overline{\tau_i}}{\overline{\tau_0}} \tag{4.4}$$

Please note that in equations 4.2 and 4.3, the aspect ratio $\alpha_i{}^*$ is defined as

$$\alpha_i{}^* = \begin{cases} \frac{h}{w_i} \text{ if } h \leq w_i \\ \frac{w_i}{h} \text{ if } h > w_i \end{cases} \tag{4.5}$$

The design rule is suitable for both Newtonian and power-law fluids, exhibiting a shear-dependent viscosity:

$$\mu = k\dot{\gamma}^{n-1} \tag{4.6}$$

where μ is the viscosity, k the consistency index, $\dot{\gamma}$ the magnitude of shear rate and n the power-law index of the fluid (for $n = 1$, the viscosity is not shear dependent and the Newtonian model is recovered). More details about the biomimetic design rule can be found in Zografos *et al.*[15]

4.2.2 Microfabrication and network characterisation

Geometries are named according to the gradient of average wall shear stress imposed along the network using the branching parameter X. In this work, we consider two geometries: $X = 1$ corresponding to a network with uniform average wall shear stress and $X = 1.9$ corresponding to a network with increasing average wall shear stress along the consecutive generations. The microchannels used in the experiments were produced with PDMS (polydimethylsiloxane, Sylgard 184, Dow Corning) by soft lithography and bonded to a glass slide using oxygen plasma (Zepto, Diener) (cf. Section 3.1.3 for further details on the experimental procedure). The channel geometries were first drawn in autoCAD and printed in a film photomask. The epoxy mould (SU8-100, Microchem) with the same design was fabricated in house by photolithography (cf. Section 3.1.2) and the corresponding channel widths and depths were measured by optical microscopy and surface profilometry (Dektak 6M, Veeco), respectively.

Table 4.1 provides a comparison between the channel's theoretical dimensions (T) and the real dimensions of the microfluidic devices used in the experiments (R). The small differences in depth between channels in the same network is inherent to the fabrication technique used and were taken into consideration to ensure that all visualisation experiments were performed at the channels' centreplane (i.e. for $z = h/2$).

Table 4.1: Comparison between channels experimental (R) and theoretical (T) dimensions for the width w and the height h for the two different branching parameters used.

geometry	dimension (μm)		channel generation			
			0	1	2	3
$X = 1$	w	T	200.0	114.7	73.5	50.0
		R	202.5	120.0	80.0	55.0
	h	T		100.0		
		R	97.8	97.5	97.0	96.5
$X = 1.9$	w	T	200.0	75.7	36.8	18.9
		R	200.0	80.0	40.0	26.0
	h	T		100.0		
		R	100.9	100.5	100.5	100.0

4.2.3 Fluid preparation and rheological characterisation

As an example of a shear sensitive molecule, λ-phage DNA (Sigma-Aldrich, 48kbp, $M_w = 31.5 \times 10^3$ kDa) was used in this study. The corresponding contour and persistence lengths are 16.3μm and 50nm, respectively.[19]

The experiments were performed using a slightly viscous buffer solution composed by 10mM Tris buffer (pH = 8.0), 10mM NaCl, 1mM EDTA, β-mercaptoethanol 4%(v/v), oxygen scavenger solution and sucrose. Both β-mercaptoethanol and the oxygen scavenging solution (the latter composed of glucose, glucose oxidase and catalase) were added to the main solution in order to remove the reactive species of O_2, which are responsible for photo bleaching.

λ-DNA was fluorescently labelled using YOYO-1 dye (YOYO-1 Iodide (491/509) – 1mM solution in DMSO, Life Technologies) using the procedure described in Teclemariam.[20] A volume of 29.2μL of a λ-DNA intermediate solution (2μg/mL) and 3.6μL of YOYO-1 intermediate solution (5μM) were added to the final sample such that the homodimer would bind to the λ-DNA double strand at a 1:5 dye: bp ratio. The labelling process takes place overnight, at room temperature, under gentle stirring and the resultant contour and persistence lengths of the labelled molecule increase to 21–22μm and 70nm,[20] respectively. Further details on the preparation of DNA solution can be found in Appendix B.

The steps of polymer dilution in the buffer solution and subsequent fluorescent labelling with YOYO-1 were performed in the dark to avoid photo bleaching.

The concentration of λ-DNA in the solutions used in the experiments is 0.04ppm. This value is significantly lower than the overlap concentration c^* of 36.4ppm estimated using[21]

$$c^* = 3\, M_w\, /\, (N_A\, 4\pi\, R_g{}^3) \tag{4.7}$$

where M_w is the λ-DNA molecular weight, N_A the Avogadro's number and R_g the radius of gyration. For such dilute solutions, molecules are expected not to interact with each other in the surrounding medium, allowing their individual characterisation in a simple shear flow.

The λ-DNA in viscous buffer solution was characterised using a rotational rheometer (Physica MCR 501, Anton Paar) with a cone-plate geometry (R = 30 mm, Θ = 1°) in the range $0.1 < \dot{\gamma} < 1000 s^{-1}$, at a temperature of 20°C (which corresponds to the temperature set for the microfluidic experiments). As expected, the solution exhibited a constant shear viscosity $(\mu = 38.2 \times 10^{-3} \pm 0.015 \text{Pa s})$ as a result of the low polymer concentration.

For preliminary tests to characterise the kinematics within the various branches of the channels, Newtonian and shear-thinning solutions of Xanthan gum (XG) were used. In Figure 4.2, we show the flow curves for two XG solutions of 100ppm and 50ppm, characterised using the same procedure used in DNA solution characterisation. The linear decay region of the flow curve was fitted by a power-law model and the power-law index (n) determined for the two XG solutions tested in the microfluidic networks is $n = 0.62$ (for XG 100 ppm) and $n = 0.79$ (for XG 50 ppm).
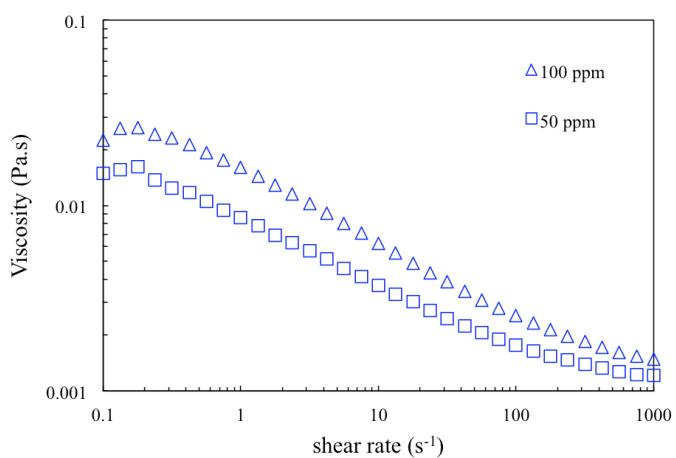
Figure 4.2: Flow curves of the Xanthan gum solutions used in experiments, of concentration 100ppm (triangles) and 50ppm (squares).

4.2.4 Experimental setup and data acquisition

4.2.4.1 Particle Tracking Velocimetry (PTV)

PTV experiments were performed with a Newtonian fluid without λ-DNA to confirm the velocity fields in the regions where visualisation of λ-DNA transport dynamics will be carried out on both $X = 1$ and $X = 1.9$ geometries. For that purpose, fluorescent tracer particles were added to distilled water in small concentrations so that individual particles could be tracked along consecutive frames without being mistaken with other surrounding particles. The particles are 1μm in diameter and have excitation and emission wavelengths of 535nm and 575nm, respectively. The experiments were performed on an inverted microscope (AX10, Zeiss) employing a 63x water immersed magnification objective with numerical aperture NA = 1.2 (C-Apochromat, Zeiss) and a HXP-120 Light Source for fluorescence illumination. The images were acquired using a high-speed camera (FASTCAM SA4, Photron) and both the time between frames and the exposure time were adjusted according to the flow conditions, so that the particles could be successfully tracked. The images were analysed using Image J and Matlab to determine the average velocity of each detected particle.

The fluid was withdrawn from the 4 outlets of the geometry, using a precision syringe pump (Nemesys, Cetoni) and four 100μL glass syringes. This protocol ensured identical flow rates in all channels of each generation.

The experimental velocity profiles obtained by PTV were compared with the analytical profiles for fully-developed flow of a Newtonian fluid in a channel of rectangular cross-section,[22] described by equation 2.6 in section 2.1.2. In this case, the z-position for which the measurements were taken corresponds to half of the channel height ($z = h/2$).

The shear rate profiles are determined using equation 2.7, which has been simplified to equation 4.8 since the experiments were performed at the channel mid height where the corresponding velocity derivative relative to z is zero.

$$\dot{\gamma} = \sqrt{\left[\frac{-\Delta P}{2\mu L}\sum_{j=0}^{\infty} a_j \cos\left(\frac{2\lambda_j z}{h}\right)\frac{2\lambda_j}{h}\sinh\left(\frac{2\lambda_j y}{h}\right)\right]^2} \qquad (4.8)$$

where $\lambda_j = \frac{(2j+1)\pi}{2}$, $a_j = \frac{h^2(-1)^j}{\lambda_j^{3}\cosh\left(\lambda_j\frac{w}{h}\right)}$, h is the channel height and w is the channel width.

We calculated the average shear rate in each branch for the channel sections considered in Figure 4.1b. The results will be shown in section 4.3.

4.2.4.2 λ-DNA visualisation

λ-DNA visualisation experiments were performed using the same flow control, microscope and illumination source, but a CCD camera (Orca Flash 4.0, HAMAMATSU) was used to determine the λ-DNA molecule extension, which allowed a better signal to noise ratio. All the videos were recorded with the focus at the channels centreplane ($z = h/2$). A dichroic filter was selected to adjust the appropriate wavelengths for the excitation and emission of λ-DNA-YOYO-1 complex (491nm and 509nm, respectively).[23]

λ-DNA was fluorescently stained and the exposure time was set to ~60ms in order to observe its structure with satisfactory contrast and definition. As a consequence, molecules traveling at large velocities appeared as blurred elongated bodies, leading to erroneous measurements biased towards larger extensions than reality. To mitigate this problem, the microscope stage was displaced in the opposite direction of the flow at constant speed. Several distinct velocities were used according to the flow rate and channel under consideration in order to follow molecules positioned across the entire channel width during image acquisition. This allowed us to obtain sharp images and to capture precisely the typical deformation behaviour of a single molecule, such as stretching, recoiling and tumbling along the channel length.[24] It is important to note that for the procedure used for the visualisation, each molecule could be tracked for long enough to cover the residence time in each channel before significant photo bleaching occured.

The molecules were considered deformed if their maximum extension was larger than 1.5μm, which is approximately two times the radius of gyration of a similar labelled molecule complex (0.73μm for the labeled molecules using TOTO-1 dye).[25] This parameter corresponds to the radius of the coil formed by the polymer complex in its relaxed state since λ-DNA is a semi-flexible polymer. So, for sizes smaller than 1.5μm, it was assumed that the molecule was in equilibrium, this is, no deformation is considered. The microscopic depth of field (DOF) was estimated to be 2.07μm, according to the DOF formula provided by Zeiss:

$$DOF = \frac{1000}{7 NA\, \text{M}} + \frac{\lambda}{2NA^2} \tag{4.9}$$

where *NA* is the numerical aperture of the objective, M is the total magnification, λ is the excitation wavelength (μm) and DOF is the depth of field expressed in the same units (μm).

In order to simplify the analysis, the channel width was divided into different areas (Figure 4.1b) and an average of molecule extension *<x>* was determined for each of these areas. More specifically, for $i = 0$ and $i = 1$, five sections were considered: A and E correspond to

the areas close to the channel lateral walls (each one corresponding to 15% of the total channel width); B and D correspond to intermediate sections of the channel (15 % of the total channel width) and a large section C, in the centre of the channel, occupying 40 % of the total width. For $i = 2$ and $i = 3$, it is more difficult to accurately define the molecule position in the lateral sections, given the small width of the channels. For these cases, it was decided to consider an identical area in the middle (section C, 40 % of total channel width) and the two lateral areas close to the channel walls grouped together (A + B and D + E, each occupying 30 % of the total channel width).

4.3 Results and Discussion

In this section, we validate the proposed design of the networks and demonstrate their potential to examine the behaviour of shear sensitive molecules. We have chosen λ-DNA as this is a well characterised molecule in terms of behaviour under simple shear.[26] First, we analyse the velocity field in the various generations to ensure bulk fluid flow kinematics are as expected; secondly, we examine the individual dynamics of λ-DNA along a channel, and we then make full use of the customised geometries to study the effect of shear rate on the molecules' maximum extension.

4.3.1 Velocity profiles characterisation

The velocity profiles obtained by PTV, for the various branches of geometries $X = 1$ and $X = 1.9$, are presented in this section. To simplify the PTV analysis, a Newtonian fluid without the presence of λ-DNA is used to quantify the velocity profiles in the regions of interest, where the flow is expected to be fully-developed. The normalised axial velocity profiles along y at the $z = h/2$ centreplane (scaled here using the average inlet velocity $\overline{u_0}$) for each generation of the network (cf. Figure 4.3a for $X = 1$ and Figure 4.3b for $X = 1.9$) are in good agreement with the theoretical profiles evaluated by equation 2.6. Figures 4.3c and 4.3d illustrate the evaluated normalised average shear rates (scaled here with the average shear rate at the inlet channel $\overline{\dot{\gamma}_0}$, being $\overline{\dot{\gamma}_0} = 2\overline{u_0}/ 0.5w_0$) in each of the observation areas considered for each generation.

For both geometries, it can be seen that the shear rate in the central section (Section C) is smaller, and increases for the sections closer to the walls (Sections A, B, D and E). For $X = 1$, the maximum velocity decreases along the network as the flow divides (Figure 4.3a) while for $X = 1.9$, the maximum velocity variation along the generations is non-monotonic according to the channel width (Figure 4.3b). As a result, the average shear rates in the

various sections exhibit similar values for all generations in geometry $X = 1$ and can be considered nearly constant (Figure 4.3c), while a strong increase along consecutive generations is observed for $X = 1.9$ (Figure 4.3d) as expected by setting a design with branching parameter greater than unity ($X > 1$ predicts increasing average wall shear stresses). For these points, the horizontal error bars correspond to the channel width of the corresponding section and the vertical error bars indicate the range of shear rates found in that same section. In each subsequent generation a different range of shear rates is achieved and one can impose a large range of flow conditions in a single experiment by considering all the channels along the consecutive network generations. It is also worth to note that due to Poiseuille flow profile in each channel, we can also obtain several average shear rates for a given generation of the network, corresponding to the different regions considered in each channel (Figure 4.1b).

As observed in Figure 4.3d, the increase in shear rate from generations $i = 2$ to $i = 3$ (geometry $X = 1.9$) is smaller when compared to the increment between the first generations (from $i = 0$ to $i = 1$ and $i = 1$ to $i = 2$). When producing the mould from a film mask using photolithography, there are typically small differences (within $\pm$ 5μm) between the theoretical and real channel widths due to errors inherent to the manufacturing process. In general, these deviations effectively impose a limit in the smallest dimension of channels that can be used to achieve a required accuracy in terms of the average wall shear stress. In our particular case, manufacturing errors result in non-negligible relative deviations for the smallest channels (i.e. the last generation) of geometry $X = 1.9$ thus limiting the number of generations that can be used accurately in experimental model systems. A more detailed analysis of the impact of manufacturing errors, and associated discussion, is provided in Section 4.3.3.
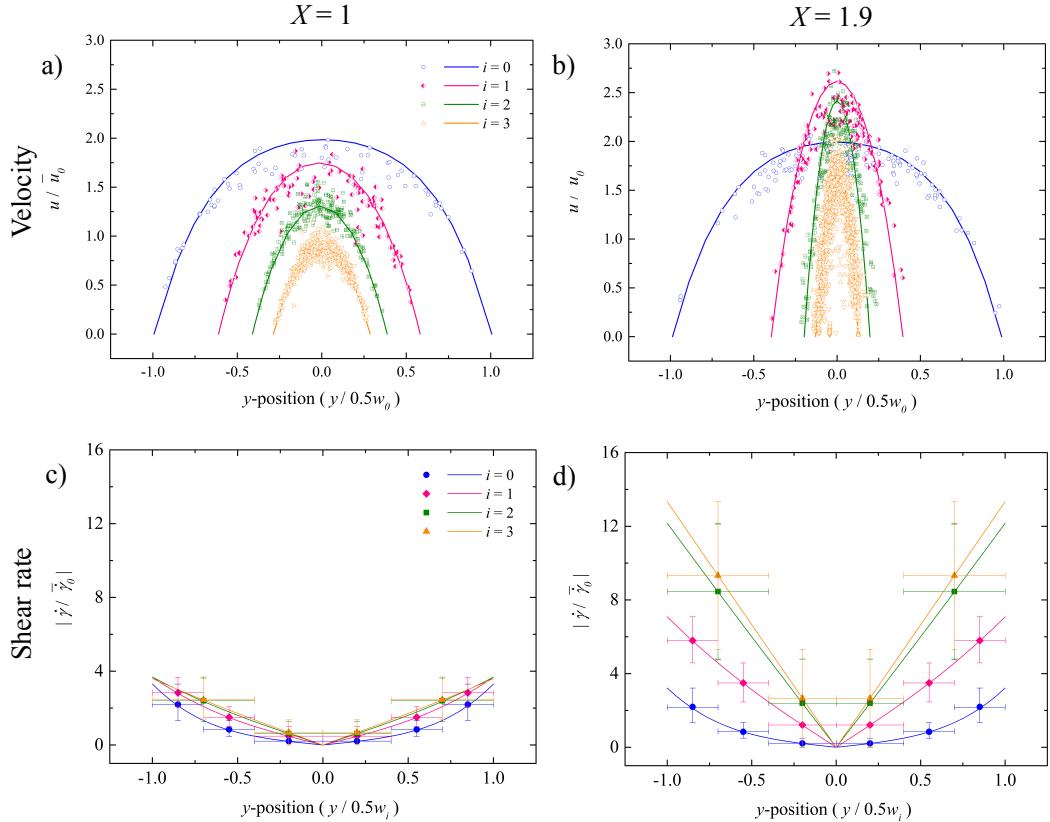
Figure 4.3: Flow kinematics in the various generations of geometries $X = 1$ (a,c) and $X = 1.9$ (b,d). Comparison between the normalised velocity profiles (local velocity u is normalised using the average velocity in the main channel, $\overline{u_0}$) obtained by experimental PTV (symbols) and theoretical prediction (solid lines) for Newtonian fluids in geometry $X = 1$ (a) and $X = 1.9$ (b) at $z = h/2$ centreplane. Corresponding normalised shear rate profiles (using the average shear rate in the main channel, $\dot{\overline{\gamma}}_0 = 2\overline{u_0}/0.5w_0$, as reference) for network $X = 1$ (c) and $X = 1.9$ (d); the symbols represent the average value in each of the sections used for the analysis (cf. Figure 4.1b). Note that the y-coordinate has been shifted so that $y = 0$ corresponds to the centreline of each channel.

Taking advantage of the universality of the $X = 1$ geometry (i.e. the same design is valid for both Newtonian and a range of power-law fluids[15]), the same chip was used to test two different Xanthan gum solutions, which exhibit a shear thinning behaviour ($n = 0.62$ and $n = 0.79$). These results are reported in Figure 4.4. The velocity profiles are flattened compared to the Newtonian case, as expected for shear thinning fluids, and are in good agreement with the numerical simulations obtained using a finite volume method described in detail in Zografos et al.[15,27]
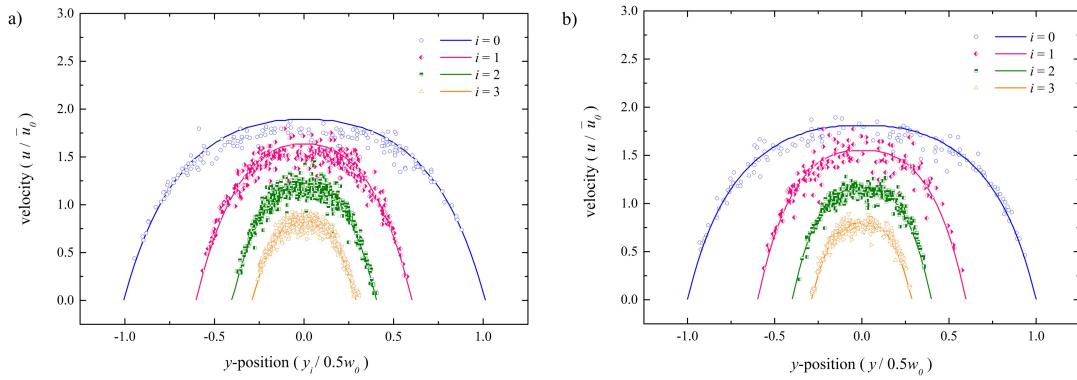
Figure 4.4: Flow kinematics of the XG solutions in geometry $X = 1$: (a) $n = 0.79$; (b) $n = 0.62$. Comparison between the normalised velocity profiles, given by the local velocity u divided by the average velocity in the main channel $\overline{u_0}$, obtained by experimental PTV (symbols) and numerical simulations (solid lines).

Summarising the previous findings, an overall good agreement was found between the experimental velocity profiles determined by PTV and both theoretical and numerical velocity profiles obtained for Newtonian and power-law fluids, respectively. This provides confidence in the experimental biomimetic geometries for further use with specific applications.

4.3.2 Behaviour of shear sensitive biopolymers in customised networks

4.3.2.1 Dynamics of λ-DNA molecules

Individual molecule deformation in a shear flow is known to exhibit a combination of different mechanisms such as tumbling, stretching and recoiling, depending on the polymer relaxation time and the shear rate.[26]

Figure 4.5a presents an example of a typical deformation sequence experienced by a λ-DNA molecule in a Newtonian medium transported along the last generation ($i = 3$) of geometry $X = 1.9$. These images were obtained by displacing the microscope stage at appropriate velocities as explained in the Section 4.2.4.2, which allowed us not only to record the full deformation cycle of each examined molecule, but above all to capture sharp images in which the length observed and measured is due to the molecule extension rather than a technical artefact associated with the large exposure times used.

a)

b)
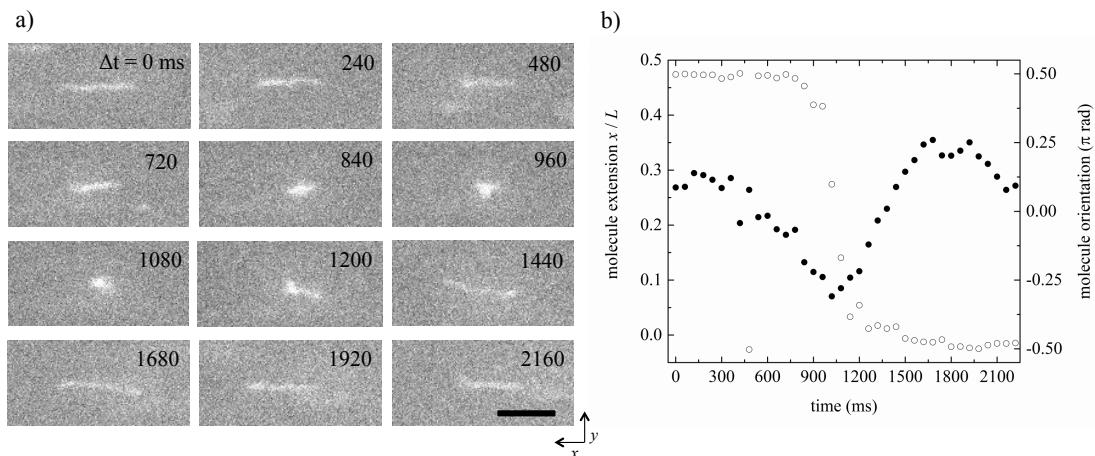
Figure 4.5: (a) Typical images of λ-DNA molecule undergoing deformation in a Newtonian viscous solution; Q_{total} = 100nL min^{-1}; μ = 38.2x10^{-3} ± 0.015Pa s; geometry X = 1.9 (generation i = 3); scale bar corresponds to 5µm. (b) Evolution of molecule extension normalised using the contour length L_c = 21µm (●) and orientation (○) corresponding to the deformation cycle presented in Figure 4.5a.

4.3.2.2 λ-DNA molecule extension along the networks

In this section, we evaluate the maximum extension observed for each analysed λ-DNA molecule during its cycle of deformation to quantify the average value of the maximum extension in the various sections of each generation in the two networks (X = 1 and X = 1.9). We analysed an average of 50 molecules in each channel section to guarantee good statistics. Figure 4.6 presents the mean fractional extension $<x>$ / L (where $<x>$ is now the average value calculated from a set of molecules at their maximum extension within the observation regions defined in Figure 4.1b) for a total flow rate of 40nLmin^{-1}. For the geometry with X = 1, the molecule deformation observed is modest (Figure 4.6a) although higher at the walls than at the centre as expected given the shear rate distribution (Figure 4.3c). The mean fractional extension value of ~0.1 is a result of the molecule fluctuations, commonly observed due to Brownian motion.[26] The values of mean fractional extension for the molecules traveling along the channels of all generations practically superimpose. On the contrary, for the X = 1.9 geometry (Figure 4.6b), the average wall shear stress is expected to increase along the consecutive generations and we observe a significant increase on molecule average extension along the various generations in the network. The higher shear stress at the walls in subsequent generations leads to a stronger hydrodynamic drag force acting on the molecule. If this force overcomes the entropic forces responsible for keeping the λ-DNA in a coiled structure, then the molecule will stretch and the average elongation is expected to increase in the range of shear stresses applied until a plateau of 0.4 - 0.5 is reached in shear flows.[26,24] As a consequence of the distinct shear rate profiles generated in

the geometry $X = 1.9$ (Figure 4.3d), the values for λ-DNA extension could be obtained for a large set of shear rate conditions, using a single imposed flow rate.
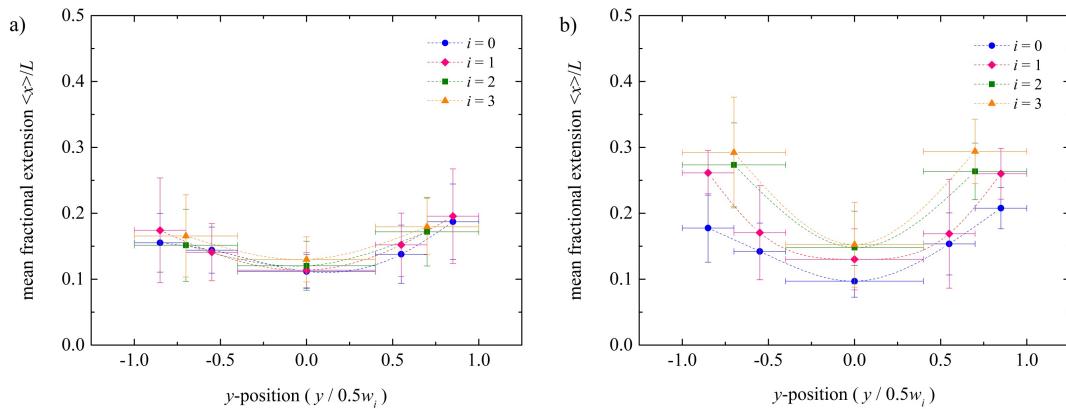
Figure 4.6: Mean fractional extension of λ-DNA molecules determined for each section of the channels (as defined in Figure 4.1b) along the various generations of the geometries $X = 1$ (a) and $X = 1.9$ (b) for $Q_{total} = 40$nL min^{-1}. Dashed lines are guidelines connecting the average molecule extension in the different channel sections.

The error bars in Figure 4.6 represent the standard deviation of the molecule elongation for each specific section of the channel. These relatively large values of the standard deviation may be a combined result of the range of shear stresses the molecules are subjected to in each channel section under analysis, and the so called "molecular individualism" of λ-DNA, describing the unpredictability of individual molecule behaviour under similar flow conditions.[28] Simple shear flow is characterised by the contribution of both fluid elongation and vorticity in the same proportion. As such, the deformation of the λ–DNA semi-flexible molecule is a combination of different behaviours, such as stretching, tumbling and recoiling. Typically, after molecule stretching and aligning along the x-axis, the hydrodynamic forces decrease and the molecule retracts until it reaches an equilibrium shape, i.e. the coiled shape. Because of the molecule size and Brownian motion, the molecule feels the rotational component of the flow, resulting in tumbling phenomena.[29] Since this deformation is stochastic, the maximum length registered can change for the set of molecules analysed in the same channel section.[28]

To corroborate the good performance of the microfluidic designs, we now concentrate on the region close to the wall for which the devices tested are expected to give us the ability to increase ($X = 1.9$) or maintain ($X = 1$) the average shear stresses at the wall along subsequent generations. Figure 4.7 presents the comparison between the maximum fractional lengths in the lateral sections of the channels (i.e. in the sections close to the walls as shown in Figure

4.1b), along the four generations in both geometries at the total flow rate of 40nLmin[-1]. It is clear that for geometry $X = 1$, the maximum extension is similar for all generations, while for $X = 1.9$, the maximum extension becomes stronger when progressing along the geometry in accordance to the wall shear stress variation along the network as prescribed by the branching parameter selected.
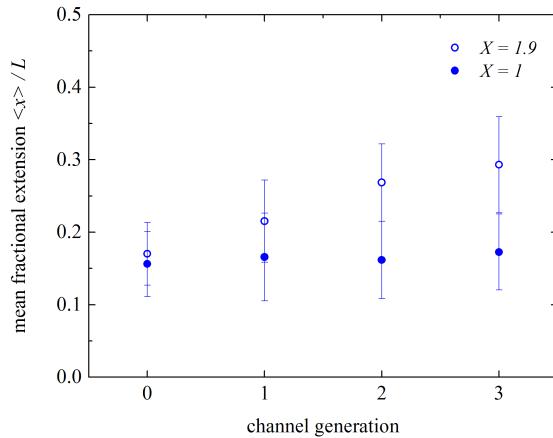
Figure 4.7: Comparison between mean fractional extension of the molecules in the lateral channel sections for both geometries $X = 1$ (●) and $X = 1.9$ (○) at $Q_t = 40$nL min^{-1}.

To summarise, the data set collected in all our experiments is plotted in Figure 4.8 as a function of the Weissenberg number (Wi), defined as the product of the longest relaxation time of the polymer ($t_{relaxation}$) and the shear rate ($\dot{\gamma}$). Here, to evaluate the shear rate, we considered the average value ($\overline{\dot{\gamma}_i}$) for each channel section. The relaxation time was estimated to be 3.6s based on the relaxation time determined for a similar molecular complex in a sucrose buffer solution of 41cP viscosity.[30] The evolution of the mean fractional extension with the Wi number is in good agreement with the trends observed by Smith et al.[26] and Teixeira et al.[24] for the extension of λ-DNA in simple shear flow using two parallel plates. In their work, λ-DNA molecules were also labelled using YOYO-1 dye at a similar proportion as used here (1:4 dye:bp ratio).
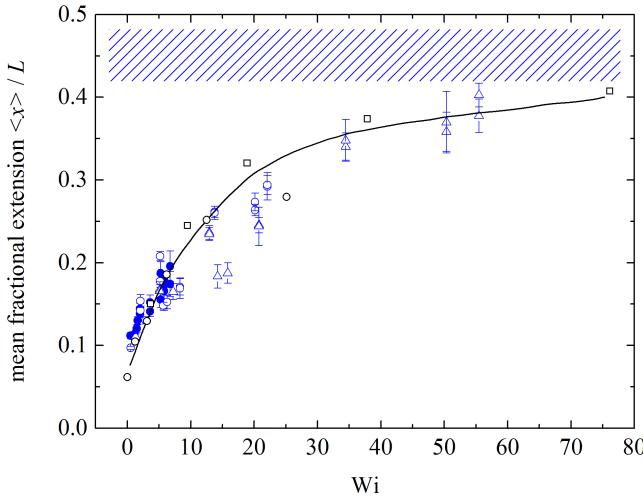
Figure 4.8: Mean fractional extension of λ–DNA as a function of Wi number for geometries $X = 1$ for $Q_{total} = 40$nLmin^{-1} ($\bullet$), $X = 1.9$ for $Q_{total} = 40$nL min^{-1} ($\circ$) and $X = 1.9$ for $Q_{total} = 100$nL min^{-1} (Δ) determined in the present study. Comparison with the data obtained by Smith et $al.$[26] for a similar molecular complex in shear flow using 60cP ($\circ$) and 220cP ($\square$) viscous solutions as medium and respective data fit to guide the eye, represented by the black line. The dashed region represents the asymptotic range for mean fractional extension for this similar molecular complex.

For both cases, the maximum fraction length tends to plateau at high Wi approaching values of ~0.4–0.5, corresponding to the maximum mean fractional extension for this molecule in a simple shear flow.[26,24] Teixeira et $al.$[24] also found an identical plateau for the extension of a λ-DNA molecule of different contour length (of 80μm), in a shear flow for a larger range of Wi numbers, reaching 600.

It is worth highlighting that, by performing a single experiment in an appropriate microfluidic customised network, we are able to characterise the full curve of mean fractional length for the whole range of relevant Weissenberg numbers (see data shown as triangles corresponding to $X = 1.9$, $Q_{total} = 100$nLmin^{-1} in Figure 4.8).

4.3.3 Analysis of experimental limitations

In this section we discuss the experimental limitations associated with the microfluidic geometries used in this study.

As can be seen from Table 4.1 with the description of channels dimension, the absolute error for most channels is about 5μm. This is consistent with current precision levels[1] found for microchannel fabrication using photo- and soft-lithography methods with a plastic photomask, which are the most commonly used to produce microfluidic devices. However, because we are using different sized channels in the same geometry, this error has a distinct

impact on the deviations found between the real and theoretical flow conditions that will be discussed in detail below.

Figure 4.9 compares the shear rate profiles obtained in the real channels (solid lines) and those expected for the theoretical dimensions (symbols). For generations $i = 0$, 1 and 2, this absolute error translates into a small relative error (at the most about 15% for generation 2), and the results agree reasonably well with the theoretical predictions. As such, we can safely consider that our approach is robust for generations $i = 0$, 1 and 2. For the last generation, however, the much smaller channel dimensions lead to a larger relative error in channel width and, in consequence, to a significant deviation in terms of shear rate profiles between experimental results and theoretical predictions. It should however be noted that despite the fact that the shear rate profile in the last channel generation deviates from the desired profile and as a consequence the range of shear rates desired could not be reached for this generation, the shear rate profile remains perfectly well known and the average shear rates in the different areas of this channel generation are well defined.
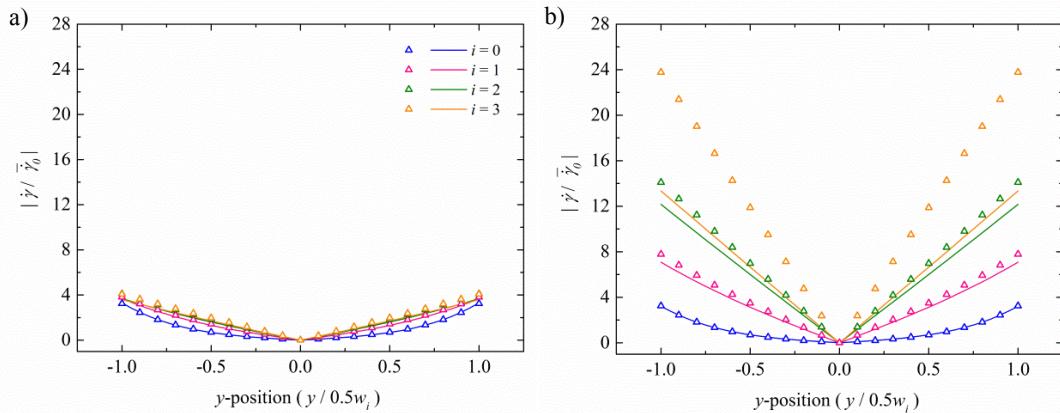
Figure 4.9: Comparison between the normalised shear rate profiles obtained for the channels used in the experiments (solid lines) and for channels with the theoretical dimensions (symbols), for geometries $X = 1$(a) and $X = 1.9$ (b).

A more systematic study of potential deviations of the real shear rate profiles from the desired profiles for the geometries used in our study can be performed by investigating the effect of an absolute error of 5μm on the channel width on the wall shear stress in the different generations $\bar{\tau}_i$, calculated using equation 4.10:

$$\bar{\tau}_i = \frac{8^n \bar{u}_i{}^n K_i}{D h_i{}^n} \tag{4.10}$$

where

$$K_i = k \left(b^* + \frac{a^*}{n} \right)^n \tag{4.11}$$

Figure 4.10 presents the normalised average wall shear stress profiles along the 4 generations of channels for the geometries with theoretical dimensions (T), geometries with channels 5µm wider (T$^+$) and 5µm narrower (T$^-$) relative to the theoretical dimensions and, finally, the real geometries used for this study (R). For the theoretical geometries and respective deviations of ±5µm, a constant depth of 100µm was considered. The wall shear stress has been normalised by the theoretical wall shear stress obtained for the generation 0 using the theoretical dimensions. The corresponding values are given in Table 4.2. Note that this analysis could easily be extended to also include an error on the channel height, which we found however to be less important than the error on the channel width, and which has thus for clarity reasons not been included here.
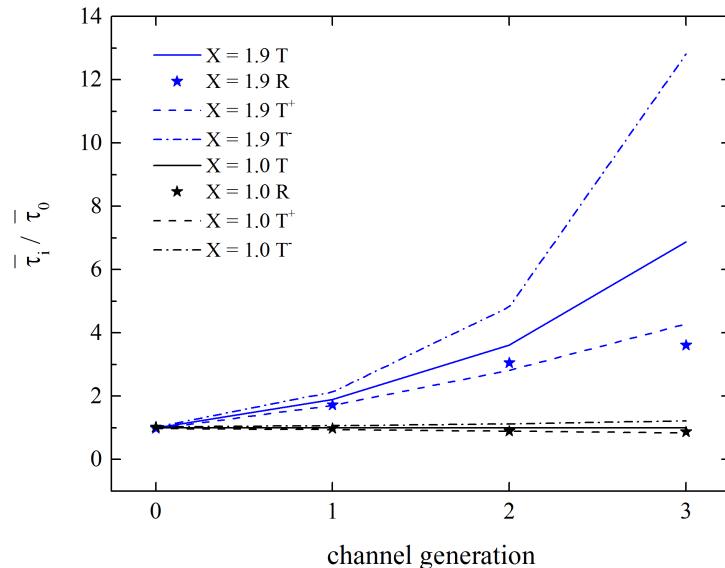
Figure 4.10: Normalised wall shear stress obtained for geometries described in Table 4.1, corresponding to geometries with theoretical (T) and real dimensions (R), as well as geometries with channel widths 5µm larger (T$^+$) and 5 microns narrower (T$^-$) than the theoretical dimensions. For the theoretical case (T) and corresponding deviations (T$^+$ and T$^-$), the depth was considered constant (100µm). The wall shear stress has been normalised by the theoretical wall shear stress obtained for generation 0 using the theoretical dimensions.

For both branching parameters the error increases for subsequent generations as a result of the channel dimensions decrease for subsequent generations. The effect is more pronounced for the geometry $X = 1.9$ as in this case even smaller dimensions are required. This kind of analysis allows determining how many generations can be used when working with soft lithography techniques as a function of the absolute or relative error that can be tolerated for a specific application.

Table 4.2: Normalised wall shear stress values corresponding to the data points displayed in Figure 4.10.

Geometry		channel generation			
		0	1	2	3
$X = 1$	T	1.000	1.000	0.999	1.000
	T^+	0.973	0.942	0.895	0.837
	T^-	1.029	1.065	1.128	1.222
	R	1.029	0.978	0.904	0.872
$X = 1.9$	T	1.000	1.901	3.616	6.876
	T^+	0.973	1.709	2.818	4.280
	T^-	1.029	2.136	4.828	12.813
	R	0.983	1.722	3.054	3.612

Another possibility is of course to work with different types of micro fabrication techniques to increase the precision of the channel dimensions. A similar analysis should then be performed to decide on the number of generations that can be used with a given precision.

To increase the resolution of the mould (and subsequently of the channel geometries) a different type of mask could be used. For example, the use of a precision chrome mask, even if significantly more expensive, instead of a high resolution transparency mask is expected to increase the resolution to 1-2μm, allowing thus to work with a channel width as small as 1μm.[2-4] Other fabrication techniques, for example micro-milling, might also lead to an increased precision on the channel width, but will make the exact control of the geometry of the bifurcations more difficult. In addition these techniques are not as widely used as soft lithography.

Finally, another option would be to consider increasing the size of all channels by a constant factor (hence reducing the relative error), but this would potentially lead to other issues such as increased inertial contributions or lower precision in flow rate control.

In summary, as every microfabrication technique has a limitation on the precision of the channel dimensions, some error on the experimentally obtained shear rate profiles are unavoidable. The branched channel geometries, having very different channel width are particularly sensitive to this kind of fabrication errors and an analysis of the potential errors for subsequent generations should always be performed before designing a specific experiment to assess potential limitations.

4.4 Summary

The experimental results presented in this study confirm the potential of the microfluidic bifurcating networks of customised dimensions[15] to investigate the behaviour of shear sensitive molecules. The ability to customise the design of microfluidic devices *a priori*,

according to the desired average wall shear stress distribution required for a specific application is a major advantage.

λ-DNA is a perfect example of a shear sensitive polymer to be used for testing complex microfluidic geometries since it has been extensively studied in the past. Using the microfluidic networks, we were able to confirm the expected effect of flow strength on the molecule deformation. As predicted, different dynamics were observed for λ-DNA molecules in the two geometries tested: for $X = 1$, with uniform average wall shear stress distribution, a similar moderate extension of the molecules was observed in all the channels of this network; for the geometry designed with $X = 1.9$ at the same total flow rate, the molecular deformation is stronger in the consecutive channels of the network due to the increasing shear stress imposed ($X > 1$). The data obtained on molecule deformation is in good agreement with previous studies done using λ-DNA subject to a simple shear flow between two parallel plates.[24,26] One of the advantages of the microfluidic networks proposed here is that by using one simple geometry and a single flow condition, we were able to cover a large range of Weissenberg numbers and assess the corresponding effect on molecule deformation.

We demonstrate the advantage of using bifurcating networks, in which multiple well-controlled shear stresses can be imposed simultaneously for investigating single molecule dynamics under a range of shear stress or shear history in a single device. We believe these networks have the potential to be employed in the future also for other complex fluids and are particularly valuable for cumulative shear stress studies, where the shear loading history and residence time play an important role.

References

1.   Fidalgo, J., Zografos, K. & Casanellas, L. Customised bifurcating networks for mapping polymer dynamics in shear flows Customised bifurcating networks for mapping polymer dynamics in shear flows. *Biomicrofluidics* **064106,** (2017).

2.   Chin, C. D., Chin, S. Y., Laksanasopin, T. & Sia, S. K. in *Point-of-Care Diagnostics on a Chip* (eds. Issadore, D. & Westervelt, R. M.) 3–21 (Springer Berlin Heidelberg, 2013). doi:10.1007/978-3-642-29268-2_1

3.   Kiilerich-Pedersen, K. & Rozlosnik, N. Cell-Based Biosensors: Electrical Sensing in Microfluidic Devices. *Diagnostics* **2,** 83–96 (2012).

4.   Li, X., Valadez, A. V., Zuo, P. & Nie, Z. Microfluidic 3D cell culture: potential application for tissue- based bioassays. **100,** 130–134 (2012).

5.   Sharma, S., Zapatero-Rodríguez, J., Estrela, P. & O'Kennedy, R. Point-of-Care diagnostics in low resource settings: Present status and future role of microfluidics. *Biosensors* **5,** 577–601 (2015).

6.   Weaver, W., Kittur, H., Dhara, M. & Carlo, D. Di. Research highlights: microfluidic point-of-care diagnostics. *Lab Chip* **14,** 1962–1965 (2014).

7.   Fidalgo, J., Dias, A., Mendes, A. M. & Magalhaes, F. D. Production of monodisperse multivesiculated polyester particles with a T-junction microfluidic device. *Chem. Eng. J.* **233,** 323–330 (2013).

8.   Yang, S. *et al.* Microfluidic synthesis of multifunctional Janus particles for biomedical applications. *Lab Chip* **12,** 2097–2102 (2012).

9.   Lenshof, A. & Laurell, T. Continuous separation of cells and particles in microfluidic systems. *Chem. Soc. Rev.* **39,** 1203–1217 (2010).

10.   Sajeesh, P. & Sen, A. K. Particle separation and sorting in microfluidic devices: A review. *Microfluid. Nanofluidics* **17,** 1–52 (2014).

11.   Lindner, A. & Arratia, P. E. Preface to Special Topic: Invited Articles on Microfluidic Rheology. *Biomicrofluidics* **10,** 043301 (2016).

12.   Saxer, T., Zumbuehl, A. & Müller, B. The use of shear stress for targeted drug delivery. *Cardiovasc. Res.* **99,** 328–333 (2013).

13.   Epshtein, M. & Korin, N. Shear targeted drug delivery to stenotic blood vessels. *J. Biomech.* (2016). doi:10.1016/j.jbiomech.2016.11.015

14.   Holme, M. N. *et al.* Shear-stress sensitive lenticular vesicles for targeted drug delivery. *Nat. Nanotechnol.* **7,** 536–543 (2012).

15.   Zografos, K., Barber, R. W., Emerson, D. R. & Oliveira, M. S. N. A design rule for

constant depth microfluidic networks for power-law fluids. *Microfluid. Nanofluidics* **19,** 737–749 (2015).

16.   Murray, C. D. The Physiological Principle of Minimum Work. I. The Vascular System and The Cost of Blood Volume. *Proc Natl Acad Sci U S A* 207–14 (1926). doi:10.1085/jgp.9.6.835

17.   Mai, D. J., Brockman, C. & Schroeder, C. M. Microfluidic systems for single DNA dynamics. *Soft Matter* **8,** 10560–10572 (2012).

18.   Rems, L., Kawale, D., James Lee, L. & Boukany, P. E. Flow of DNA in micro/nanofluidics: From fundamentals to applications. *Biomicrofluidics* **10,** (2016).

19.   Ladoux, B., Quivy, J.-P., Doyle, P. S., Almouzni, G. & Viovy, J.-L. Direct imaging of single molecules: from dynamics of a single DNA chain to the study of complex DNA-protein interactions. *Sci. Prog.* **84,** 267–290 (2001).

20.   Teclemariam, N. P., Beck, V. A., Shaqfeh, E. S. G. & Muller, S. J. Dynamics of DNA polymers in post arrays: Comparison of single molecule experiments and simulations. *Macromolecules* **40,** 3848–3859 (2007).

21.   Hur, J. S., Shaqfeh, E. S. G., Babcock, H. P., Smith, D. E. & Chu, S. Dynamics of dilute and semidilute DNA solutions in the start-up of shear flow. *J. Rheol.* **45,** 421–450 (2001).

22.   Bruus, H. Theoretical microfluidics. (2006).

23.   Kurita, H. *et al.* Fluorescence Observation and Manipulation of Individual DNA Molecules in a Microfluidic Channel. in 295–299 (IEEE, 2010). doi:10.1109/MHS.2010.5669539

24.   Teixeira, R. E., Babcock, H. P., Shaqfeh, E. S. G. & Chu, S. Shear thinning and tumbling dynamics of single polymers in the flow-gradient plane. *Macromolecules* **38,** 581–592 (2005).

25.   Smith, D. E., Perkins, T. T. & Chu, S. Dynamical Scaling of DNA Diffusion Coefficients. *Macromolecules* **29,** 1372–1373 (1996).

26.   Smith, D. E., Babcock, H. P. & Chu, S. Single-Polymer Dynamics in Steady Shear Flow. *Science (80-.).* **283,** 1724–1727 (1999).

27.   Zografos, K. Intelligent design of microfluidic components for Newtonian and complex fluid systems. (2017).

28.   Teixeira, R. E., Dambal, A. K., Richter, D. H., Shaqfeh, E. S. G. & Chu, S. The individualistic dynamics of entangled DNA in solution. *Macromolecules* **40,** 2461–2476 (2007).

29. Schroeder, C. M., Teixeira, R. E., Shaqfeh, E. S. G. & Chu, S. Characteristic periodic motion of polymers in shear flow. *Phys. Rev. Lett.* **95,** 1–4 (2005).

30. Perkins, T. T., Smith, D. E. & Chu, S. Single Polymer Dynamics in an Elongational Flow. *Science (80-.).* **276,** 2016–2021 (1997).

CHAPTER 5

Tracking biological objects in extensional flows generated by optimised converging-diverging channels

This chapter describes the development of a tracking system allowing the continuous observation of individual objects transported in extensional flows, generated by converging-diverging channels. The latter were numerically optimised to provide a wide region of constant strain rate along the centreline. In a first stage, a Labview interface was created to allow the microscope stage to be displaced with a non-monotonous velocity, as that expected for an object transported along the centreline of the microfluidic geometry. In order to take into account the response time of the stage and other tracking limitations, a Mathematica code was written to include suitable corrections for both stage position and velocity, so the real and theoretical stage displacements become closer.

Finally, the developed system was tested using dilute solutions of λ-DNA molecules. The experimental limitations when observing such small molecules were identified and discussed.

A manuscript regarding the tracking system is currently under preparation.

5.1 Introduction

In the last decade, a few microfluidic geometries have been proposed to study the flow of complex fluids (non-Newtonian solutions or suspensions of individual deformable objects) in strong extensional flow. The geometries most commonly employed for this purpose are the cross-slot,[1,2] flow focusing devices,[3] and converging diverging channels (abrupt contractions[4] and hyperbolic channels[5,6]).

The cross-slot geometry generates a stagnation point, which allows trapping the object of interest by purely hydrodynamic means,[7] in a vorticity-free environment, resulting in a large extensional deformation and orientation of the objects' microstructure.[8] While the stagnation point allows observing the deformation for long periods of time (in some cases, from minutes to hours[7]), the flow control is challenging since the flow rates at the two inlets and two outlets need to be precisely the same.

While writing this thesis, an interesting study was published by Pimenta *et al*.[3] The authors propose the use of optimised flow focusing geometries for studying objects under extensional flow where it is possible to generate a constant strain rate along the device centreline for different extension rates, by adjusting the ratio between the flow rates of the lateral and central channel entrances (assuming all the entrance channels present the same aspect ratio). Numerical simulations were also done, predicting the elongation of λ-DNA molecules as an example of a deformable object transported in such geometries, but no experiments were performed so far testing the same flow conditions. These geometries could represent an interesting alternative to study the object dynamics under constant strain rate conditions. For the case of the optimised flow focusing geometry, if one wants to study both extension and compression in the same geometry, a symmetric channel structure would need to be introduced at the end of the original geometry meaning that, at least, 5 fluid ports would need to be controlled, turning the experiment rather complex.

Converging-diverging geometries are therefore particularly interesting to study viscoelastic solutions, for example blood analogs,[9] prepared with XG or PAA, or concentrated DNA solutions,[4,10,11] since the analysis of the flow patterns by streak imaging allows the detection of emerging instabilities such as vortices. In abrupt contraction-expansion geometries, the objects are subjected to a strong acceleration and deceleration when transported along the channel contraction and expansion, respectively. The residence time of the object under extensional and compressive flow is very small and the strain rate generated is not constant, impeding the good conditions necessary for studying the objects' dynamics. In (non abrupt) converging-diverging geometries, such as hyperbolic channels, the object is transported

along the device and subjected to both extensional and compressive flows, respectively. In this case, the main advantage of the device is the ability to subject the object to a nearly constant strain rate along the channel centreline and for a larger residence time. Oliveira *et al.*[12] studied experimentally and numerically the flow of a Newtonian fluid along an hyperbolic contraction and confirmed that this channel configuration is not able to provide a constant strain rate throughout the entire region of observation, due to a constant change in channel aspect ratio (taking into account that common microfluidic channels obtained by photo- and soft-lithography present a constant depth). Therefore, these geometries are not optimal to study the deformation of biological elements under extension.

In this study, we used optimised converging-diverging channels, previously proposed and studied by Zografos *et al.*[13] using numerical simulations, for which the velocity profile at the channel centreline is well-known. Compared to standard abrupt contraction-expansion, such optimised geometries have the advantage of generating an extensional and compressive flow of constant strain rate for a large section of the channel centreline. Figure 5.1 shows the comparison between the velocity and strain rate profiles obtained along the centreline of abrupt contraction-expansion geometry and optimised converging-diverging geometry with similar channel aspect ratio.
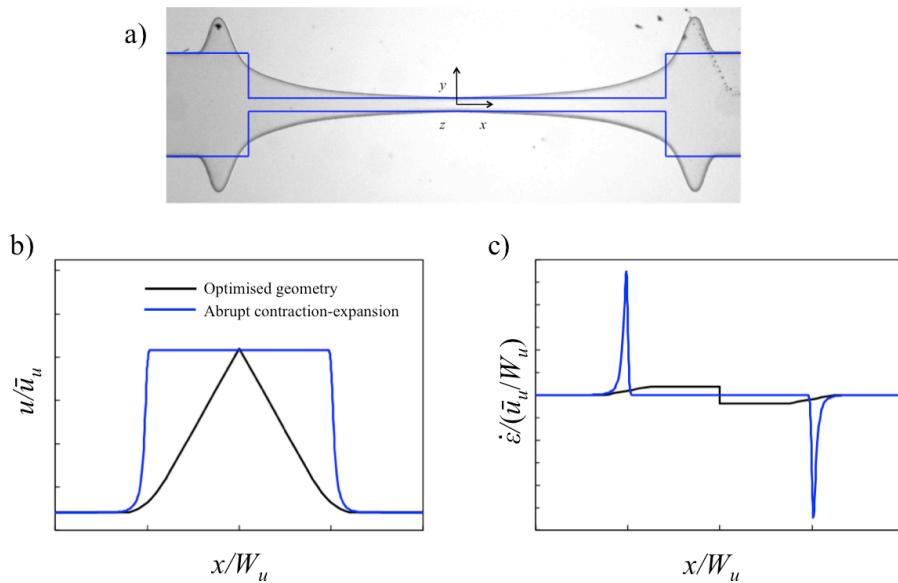
Figure 5.1: Comparison between abrupt contraction-expansion and optimised converging-diverging geometry for studying objects under extensional and compressive flow. (a) channel boundaries of optimised geometry (background image) and abrupt contraction-expansion (solid blue line); (b) velocity profiles along the geometry centreline and (c) strain rate profiles along the centreline; geometry aspect ratio AR = channel width (at the entrance)/ depth = 8. The profiles on the abrupt contraction-expansion geometry were kindly provided by Konstantinos Zografos.

In this work, we propose and implement a new system for object observation along geometries of non-continuous velocity. It consists of tracking the individual object along the entire channel length or any other region of interest, by displacing the microscope stage at the same velocity as the transported object of interest. In this particular study, we aim at capturing the behaviour of individual molecules of λ-DNA, by tracking the molecule throughout its entire course along the centreline of the optimised converging-diverging geometry. By using this method, we aim to understand how the object deforms taking into account the strain rate imposed by the channel topology.

This study was performed in collaboration with PhD student Yanan Liu and engineer Thierry Darnige, (PMMH - ESPCI, Paris).

5.2 Materials and Methods

5.2.1 Preparation of λ-DNA solution

The λ-DNA solutions were prepared following the procedure described in Chapter 4.

5.2.2 Microfluidic devices

The microfluidic devices employed in this study consist of converging-diverging channels previously optimised, by means of numerical simulations, as described in the reference Zografos *et al.*[13] The main advantage of such geometries, in comparison with standard contraction channels, is the ability to generate a larger region of constant strain rate along the centreline of the device, for testing objects of interest.

The microfluidic geometries were produced by photo and soft-lithography (following the procedure described in Chapter 3) and sealed to a thin glass slide using oxygen plasma, allowing the microscopic observation with a large magnification objective 63x/NA1.2.

A scheme of the microfluidic geometry (as well as important geometrical parameters) is provided in Figure 5.2. The image on the right hand side corresponds to the optimised section of the geometry, with a converging-diverging symmetric channel. The coordinate system is also shown in Figures 5.2 and its origin is defined at the centre point of the cross-section at the contraction (where the channel width is the minimum). The sample is either introduced in the device through a straight channel connected to the optimised region (image not shown here) or by using a flow focusing geometry (Figure 5.2, left), where the central channel (with flow rate Q_1) corresponds to the inlet of the fluid containing the objects (molecules) under study, and the lateral channels (with equal flow rates Q_2) correspond to the entrance of the continuous medium (same fluid without the objects of interest). The flow

focusing solution is used to direct the object of study towards the channel centreline, increasing the probability to find the object in the region of interest where the strain rate is constant.

Important geometrical parameters are the width of the upstream straight channel W_u, the width at the channel contraction W_c and the length of contraction l_c (defined by $l_c = n_1 W_u$ where $n_1 = 2$) and the depth of channel h. The geometries considered here present a contraction ratio of $CR = W_u / W_c = 8$.

In addition, the optimised channels present a transition region over a length l_ε at the entrance of the converging region and at the exit of the diverging region, where the velocity changes smoothly and the strain rate varies linearly from zero to the desired value (and vice-versa) (see Zografos *et al.*[13] for further discussion). For the geometries studied here, the smoothed region is considered to be the same length as the upstream width W_u, this is, $l_\varepsilon = n_2 W_u$. For the geometries here studied, $n_2 = 1$. The region of constant strain rate in the converging section and in the diverging section is given by $l_{\dot{\varepsilon}constant} = l_c - l_\varepsilon / 2$.
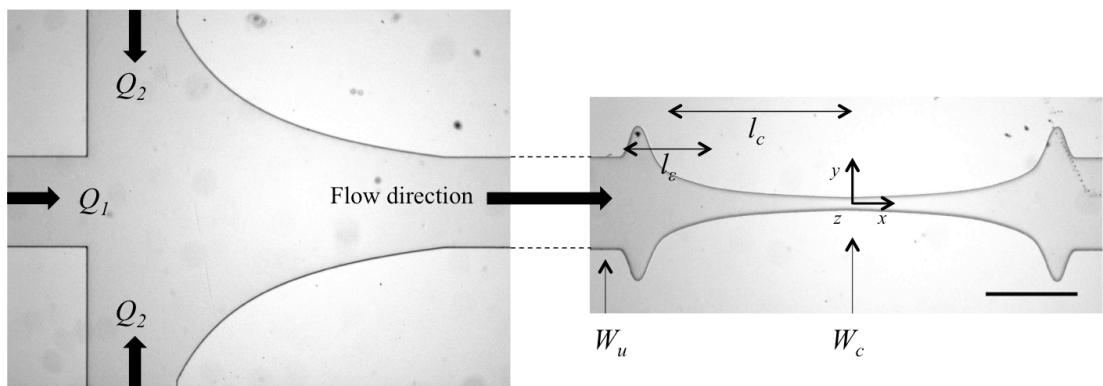
Figure 5.2: Microscopic image of a microfluidic channel with optimised converging-diverging design, produced *in-house*. The origin of the coordinate system corresponds to the point along the centreline, at the channel contraction and half height; Scale bar 400μm. The left side of the image presents a flow focusing feature used to direct the object of study towards the channel centreline.

Figure 5.3 presents the comparison between the ideal velocity profile and strain rate profile at the centreline for converging-diverging channels ($l_\varepsilon = 0$, dashed black line) and with the smoothing region ($l_\varepsilon = n_2 W_u$, blue line).

a)

b)
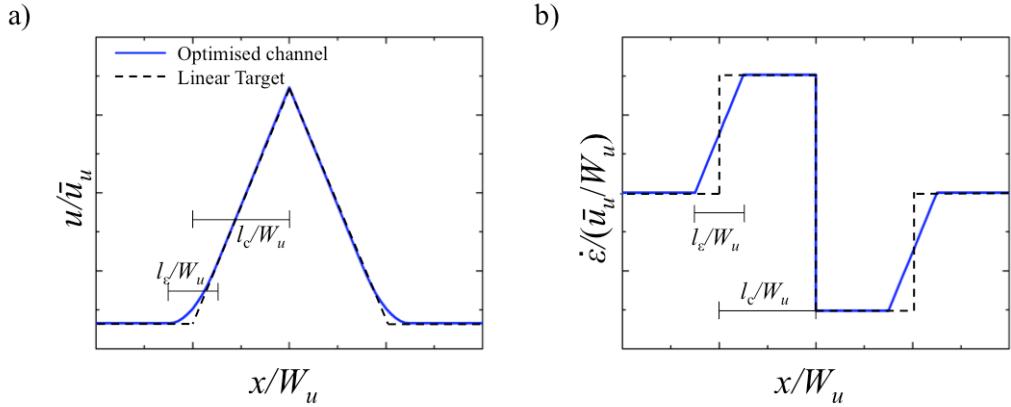
Figure 5.3: Comparison between the performance of the converging-diverging channels (linear target, dashed black line) and optimised converging-diverging channels (optimised channel, blue line). (a) normalised velocity profile and (b) strain rate profile along the channel centreline. Image adapted from Zografos *et al.*[13]

Regarding the optimised geometry, the velocity profile is defined by the set of equations 5.1, where the symbols with tilde represent normalised values. The position is normalised using the upstream width as $\tilde{x} = x/W_u$ and the velocity is normalised with the average velocity as $\tilde{u} = u/\bar{u}_u$. The geometrical parameters f_1 and f_2 are dimensionless, given by equations $f_1 = (\tilde{u}_c - \tilde{u}_u)/n_1$ and $f_2 = (\tilde{u}_c - \tilde{u}_u)/2n_1n_2$.

$$
\tilde{u} = \begin{cases}
\tilde{u}_u & \tilde{x} \leq -n_1 - \frac{n_2}{2} \\
f_2\left[\tilde{x} + n_1 + \frac{n_2}{2}\right]^2 + \tilde{u}_u & -n_1 - \frac{n_2}{2} \leq \tilde{x} \leq -n_1 + \frac{n_2}{2} \\
f_1\tilde{x} + \tilde{u}_c & -n_1 + \frac{n_2}{2} \leq \tilde{x} \leq 0 \\
-f_1\tilde{x} + \tilde{u}_c & if \quad 0 \leq \tilde{x} \leq n_1 - \frac{n_2}{2} \\
f_2\left[\tilde{x} - n_1 - \frac{n_2}{2}\right]^2 + \tilde{u}_u & n_1 - \frac{n_2}{2} \leq \tilde{x} \leq n_1 + \frac{n_2}{2} \\
\tilde{u}_u & \tilde{x} \geq n_1 + \frac{n_2}{2}
\end{cases}
\tag{5.1}
$$

The normalised strain rate profile is given by the set of equations 5.2:

$$
\dot{\varepsilon}/(\bar{u}_u/W_u) = \begin{cases}
0 & \tilde{x} \leq -n_1 - \frac{n_2}{2} \\
\frac{f_1}{n_2}\left[\tilde{x} + n_1 - \frac{n_2}{2}\right] & -n_1 - \frac{n_2}{2} \leq \tilde{x} \leq -n_1 + \frac{n_2}{2} \\
f_1 & -n_1 + \frac{n_2}{2} \leq \tilde{x} \leq 0 \\
-f_1 & if \quad 0 \leq \tilde{x} \leq n_1 - \frac{n_2}{2} \\
\frac{f_1}{n_2}\left[\tilde{x} - n_1 - \frac{n_2}{2}\right] & n_1 - \frac{n_2}{2} \leq \tilde{x} \leq n_1 + \frac{n_2}{2} \\
0 & \tilde{x} \geq n_1 + \frac{n_2}{2}
\end{cases}
\tag{5.2}
$$

The strain rate is therefore a continuous function, except for the point corresponding to the channel contraction $\tilde{x} = 0$. However, it was proven by numerical simulations that despite such discontinuity, the target profile is well approximated[13]. Table 5.1 summarises the channel real dimensions as well as the velocities and strain rate conditions used in the experiments. The channel theoretical dimensions as well as the respective theoretical strain rates are presented in Table C1, in Appendix C, for comparison.

Table 5.1: Real dimensions and flow conditions used for microfluidic geometries considered in this study.

Geometry	1	2	3	
Channel inlet	Straight channel	FFD	FFD	
W_u (µm)	392	401.3	785	
W_c (µm)	50.5	57.14	105.8	
h (µm)	51.7	100.2	99.9	
l_c (µm)	800	800	1600	
l_ε (µm)	400	400	800	
$l_{\dot{\varepsilon}\text{constant}}$ (µm)	600	600	1200	
Q (nL/s)	1.7	5.5	5.5	10.0
u_u (µm/s)	131.6	242.6	114.3	208.0
u_c (µm/s)	1330.6	1946.4	1091.4	1982.6
$\dot{\varepsilon}$ (s^{-1})	1.50	2.13	0.61	1.11
residence time (s)	1.48	1.01	3.67	2.02

5.2.3 Microfluidic setup

The visualisation setup here employed presents some similarities with that used to observe λ-DNA molecules in shear flow (Chapter 4), in the sense that the microscope platform aims to displace at the same velocity as that of the object transported along the region of interest, allowing to observe its dynamics. While for the study under shear flow, the molecule velocity was constant along the length of each straight channel segment of the network and the tracking could be easily done *by hand*, for the tracking under extensional flow in the current geometries, the molecule velocity is a function of the position along the channel length (see Figure 5.3a), which makes the manual tracking impractical for this purpose. In addition, even when working with small flow rates, the molecules can easily reach a high velocity at the contraction, on the order of a few mm/s.

To overcome this problem, a new tracking program was created using Labview to displace the microscope stage with variable velocity, according to the *x*-position in the geometry. It consists of introducing discrete velocity points for the different positions along the length of the microfluidic channel, so the microscope platform can displace at the same velocity as that predicted for the object, assuming this is positioned at the channel centreline, for which

the velocity equations are already known (equations 5.1). This program also allows controlling the frequency of the microscope stage displacement (f_{stage}) as well as the frequency of image acquisition by the digital camera (f_{camera}), making it possible to capture images of the object/molecule at different positions along the channel, during the process of object deformation. In order to generate multiple orders from a single command given to Labview, a NI 9402 digital module (National Instruments) was used.

5.3 Results and Discussion

This section is separated into two parts. The first one concerns the setup of the Labview interface for the tracking procedure where a manual approach was used to determine the stage displacement. The system was tested with a dilute solution of λ-DNA molecules and the first limitations of this implementation were studied. The second part consists in the improvement of the tracking methodology, by predicting the stage displacement and taking into account some of the process limitations. The improved tracking system was implemented using again the solution of λ-DNA molecules and the relevant results and experimental limitations are described here.

5.3.1 Part I: Set up of the Labview program and evaluation of the experimental limitations

Figure 5.4 presents the diagram of pulses and information exchange to control the displacement of the microscope stage and image acquisition by the camera, using a single Labview command (double trigger). When the Labview program sends simultaneous signals to the camera and stage, at frequencies of 10Hz (f_{camera}) and 20Hz (f_{stage}), respectively, the image is acquired and the stage displaces at velocity u_i, which is calculated based on the x-position at the previous time step P_{i-1}. At the same time, the stage sends a feedback of the current position P_i, which will be used to calculate the velocity for the next time step u_{i+1}. This means that for each command, there is a delay of 50ms, corresponding to the duration of one time step, given by the frequency of the stage used ($1/f_{stage}$). Also, this means that the microscope stage displaces at constant velocity in each time step.

A preliminary study was performed to determine the optimal frequencies for both signals. For the camera, we assumed that the frequency of 10Hz would provide enough images to describe the object deformation along the channel length. As for the stage frequency, we set it to be 20Hz, meaning that the stage displacement is fast enough to minimise the difference between the objects' continuous velocity and the constant stage velocity for each time step,

but not too fast avoiding noisy stage velocity profiles. Taking into account that each time step takes 50ms, the exposure time for image observation and acquisition was set to be smaller than this value and as small as possible, minimising image blur. While for the previous study in shear flow, an exposure time of 60ms was used and the λ-DNA molecules were easily detected throughout the experiment, for this case, the exposure time was decreased to 10ms and 20ms. This means that the direct observation of the object during the experiment becomes more challenging, but it ensures a smaller image blur resulting from the tracking system.
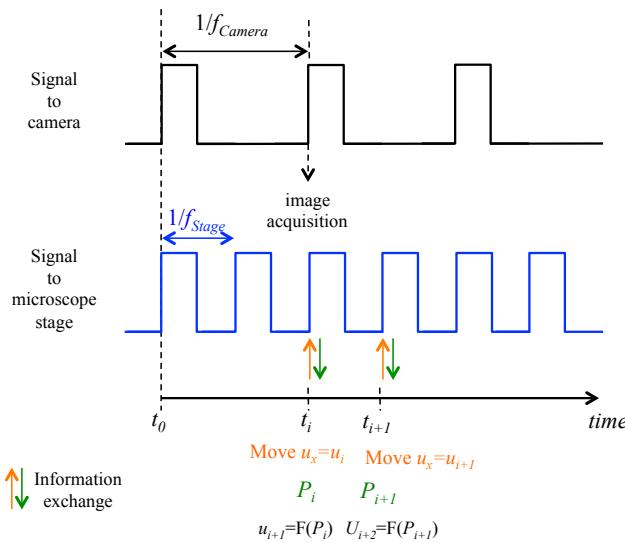
Figure 5.4: Diagram of pulses generated in Labview program to control the microscope stage displacement and the image acquisition by the digital camera.

Preliminary tests were performed to evaluate the tracking system, using geometry 1 presented in Table 5.1, with a straight channel at the entrance (W_u ~400μm, W_c ~50μm, d ~50μm). In this case, the velocity along the centreline u_x was calculated for different positions along the channel length (x-position), taking into account the channel real dimensions. Table 5.2 describes the velocity points as a function of the x-position, imposed to the tracking system for a flow rate of $Q = 1.7$nL/s.

Table 5.2: Velocity discrete points imposed to the tracking system for $Q = 1.7$ nL/s, geometry 1.

x-position (μm)	-3000	-1000	-800	-600	0	600	800	1000	3000
corrected x-position (μm)	-3000	-1000	-800	-660	-110	600	800	1000	3000
u (μm/s)	131.6	131.6	179.6	420.8	1330.6	420.8	179.6	131.6	131.6

Figure 5.5 presents the *theoretical* velocity profile (black line) determined with the real channel dimensions and the *no correction* profile (red squares), which corresponds to the stage velocity obtained from the real stage displacement, when imposing the velocity data points for the *x*-position provided in Table 5.2. As it can be seen, there is a considerable discrepancy between the real and theoretical velocity profiles. Therefore, we determined a correction, by educated guess, to be introduced for the *x*-position of the channel (drift), to minimise such discrepancy. In this case, we imposed the same velocity values but for a *corrected* x-*position*. The velocity data points are also presented in Table 5.2. In the same image (Figure 5.5), we present the corrected velocity profile (blue squares) obtained when imposing the velocity for corrected *x*-positions, which is in a closer agreement with the expected theoretical one.

For larger flow rates, which would allow stronger molecule deformation, the problem of image blur and loss of molecules in the field of view becomes more pronounced. Also, determining the manual correction for larger flow rates becomes a time-consuming task, where the drift is tested for individual segments of the velocity profile, by trial-and-error. This is, a drift (corrected *x*-position) is imposed for each segment and the velocity profile is tested using the Labview tracking system.
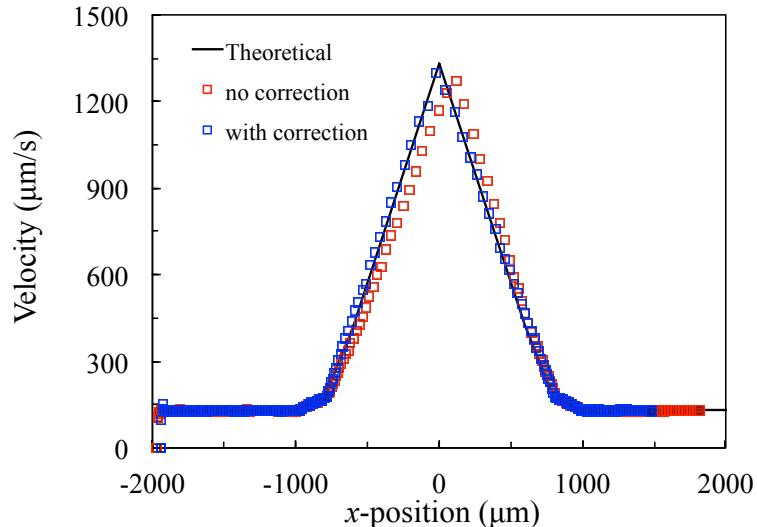
Figure 5.5: Velocity profiles as a function of *x*-position along the channel length, taking into account the real channel dimensions, showing the theoretical velocity profile (black solid line), the stage real velocity without any correction (red square symbols) and the stage real velocity imposing a correction drift (blue square symbols).

For this stage displacement, it was possible to track a few molecules along the region of interest (see an example in Figure 5.6), even though their extension was absent. It is important to note that the tracking is not perfect because, for that, we would need to capture the image of the molecule at the exact reference position while starting the tracking (this is, perfectly aligned with the channel centreline and occupying the centre of the frame, for which the velocity functions are well-known). Since the velocities are imposed for this reference position, any deviation in molecule position will present a different transporting velocity compared to the theoretical one. If the molecule is not at the centreline ($y \neq 0$), then it will travel at a smaller velocity than the stage, meaning it will move towards the left side of the frame where, in some cases, the molecule is completely lost from the field of view. This can also happen if the focus plane is erroneously positioned, capturing molecules away from the expected midplane ($z = h/2$). The molecule observed will then flow at a smaller velocity than the stage.
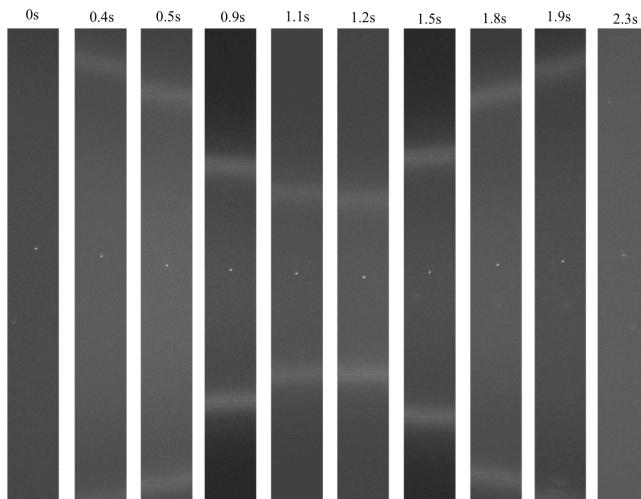
Figure 5.6: Image of a λ-DNA molecule at various *x*-positions along the microfluidic channel. The values in each image correspond to the experiment time, in seconds. The brighter horizontal marks correspond to the channel walls. $Q = 1.7$ nL/s, exposure time of 10ms.

The problem of losing the object results mainly from the use of an objective with large magnification and numerical aperture to observe the DNA, were the DOF was calculated to be only ~2μm (see Chapter 4). The fact that DNA molecules present a diameter of approximately 1.5μm makes it extremely difficult to detect the molecule and start the tracking while the molecule is still in the reference position and it is easy to understand that a small slope in the channel depth will also affect the ability to focus the molecule. Since we

are observing the molecule over a large distance along the channel, any deviation in the z-direction will lead to a molecule out of focus and any deviation in x- or y- directions will send the molecule away from the reference position (centre of the frame), eventually even out of the field of view. One way to overcome the problem and increase the probability to find the molecules at the centreline ($y = 0$) is to use a flow focusing device at the entrance of the channel, such as that presented in Figure 5.2, left. The object can be directed towards the centreline (by adjusting the flow rate ratio between the lateral channels (Q_2) and the main channel for object entrance (Q_1), as exemplified in Figure 5.7 using fluorescent particles in an aqueous medium. The larger the ratio between the flow rates, the stronger is the ability to focus the objects to flow near the centreline.

At the end, the correction found may not be sufficiently good for tracking such a small molecule as DNA. Please note that this problem is not significant when tracking larger objects, where the observation can be done using a smaller magnification objective, or for the investigation of objects that deform at smaller velocities/ strain rates.
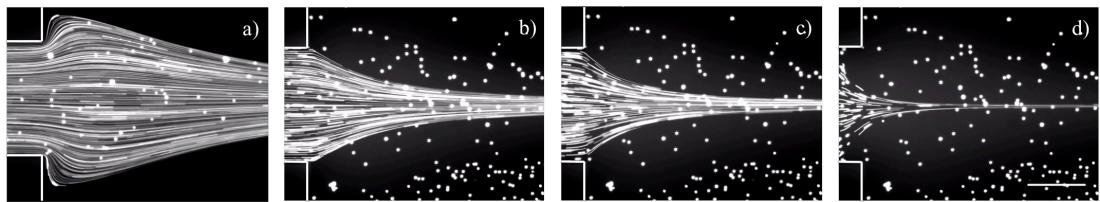
Figure 5.7: Effect of the flow rate ratio Q_2/Q_1 imposed in the feature at the channel entrance to position the objects of interest near the centreline. (a) $Q_2/Q_1 = 1$, (b) 5, (c) 10, (d) 50; exposure time = 200ms; scale bar 200μm.

Further tests using this tracking system allowed to detect a systematic delay in the hardware, ranging from 8 to 14ms per time step, the cause of which could not yet be found. The value of this delay changes each time the program is used and, therefore, the stage displacement should be tested right before starting an experiment.

Finally, we realised that when imposing constant velocity values for moving the microscope stage, the real velocity was always smaller than the imposed one. Figure 5.8 presents a calibration curve comparing the theoretical velocity (imposed) and the real stage velocity for a large range of velocities tested. Even though the velocity factor ($u_{real}/u_{imposed}$) is not exactly the same for all the velocities tested, it can be averaged to a value of 0.982. Therefore, we can impose a corrected velocity to the stage using such fator ($u_{real} = 0.982 u_{imposed}$).
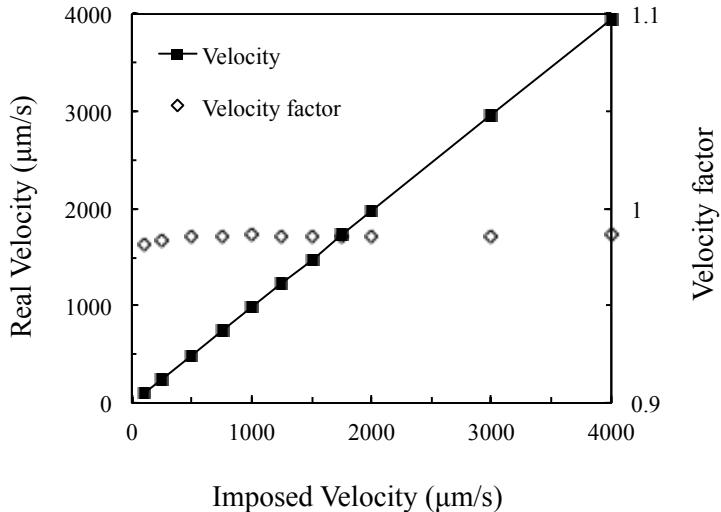
Figure 5.8: Calibration curve relating the imposed velocity to the stage and the real velocity calculated by the stage displacement.

5.3.2 Part II: Prediction of the stage displacement taking into account the experimental limitations

Taking into account the limitations previously presented, a Mathematica code was written to optimise the stage displacement. The code reproduces a predicted stage displacement as a function of the commands sent to the stage, taking the experimental constrains as maximum frequency and delays into account. In this case, the corrections applied for each velocity segment are tested in silico, without the need to run the experiment itself. While the use of such code saves a great amount of time, it also allows predicting the cumulative difference between the object and stage displacement dx, assuming the object is travelling along the channel centreline (see Figure 5.9a). Taking into account that the field of view is $203x203\mu m^2$ (for each frame), this means that the object remains inside the frame throughout the entire tracking procedure. Even though there is a difference between the object and the stage velocities at each time step, since the former is a continuous function and the latter is a step function, a blur will always be present in each image. However, by trying different correction drifts on the Mathematica code, one can minimise the blur in each image Δdx (see Figure 5.9b), to values smaller than 1 μm. The Mathematica code is therefore an essential tool, allowing to test different drifts, minimising the parameters dx and Δdx, before running the experiment.

a)

b)
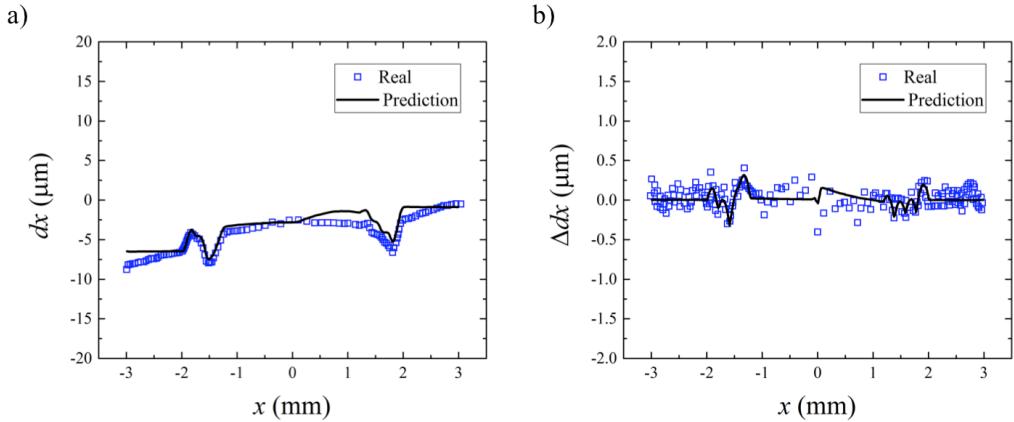
Figure 5.9: Cumulative difference between object and stage displacements during tracking (a) and prediction of the blur in each frame, due to the difference of velocities described by object and stage (b). Solid black line corresponds to the prediction using Mathematica code while open squares correspond to real data obtained for stage displacement.

Using the Mathematica code, the process of finding the velocity correction for each velocity segment is much simpler than the manual process and several velocity points were added to the velocity transition region, allowing the stage and object velocities to be as close as possible. Figure 5.10 presents the comparison between the theoretical stage performance (solid lines) and the real stage performance (symbols), for velocity and displacement, when imposing the conditions provided by the Mathematica code. For the flow conditions using geometries 2 and 3 (described in Table 5.1), a good agreement between theoretical and real stage performances proves that the methodology here proposed works successfully.

a)

b)
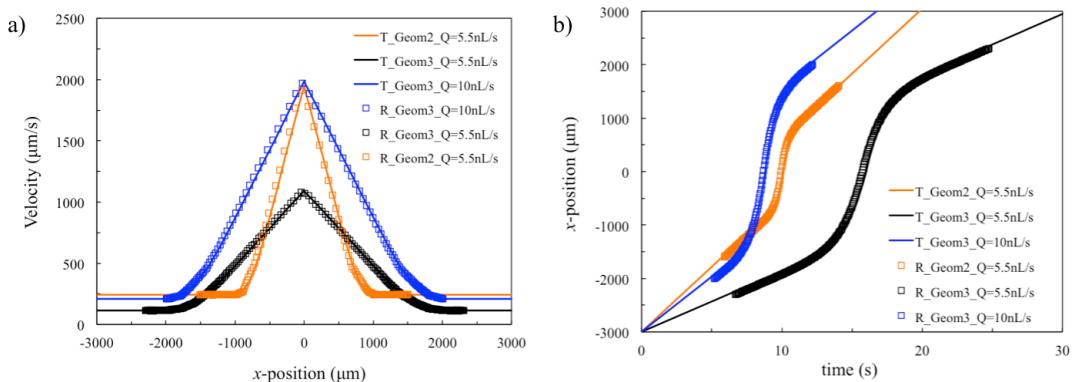
Figure 5.10: Comparison between the theoretical stage performance ('T', solid lines) and real stage performance ('R', symbols) after selecting the correct drifts using the Mathematica code. (a) Velocity profile as function of the channel length and (b) displacement as a function of time.

We tested the improved methodology using a dilute solution of λ-DNA, inserted in the microfluidic device using a flow focusing device (see Figure 5.2, left). The results on

molecule measured length along the channel length (*x*-position) and molecule position deviation from the reference position (distance between molecule position in the frame and the centre of frame) are presented Figure C1, in Appendix C. For the flow conditions here considered, the strain rate is estimated to be $\dot{\varepsilon} \approx 2.1\text{s}^{-1}$, so we expect the molecule to deform towards a length of approximately 7-8μm. In fact, from the set of molecules observed (see Figure C1), only one molecule reached such a large extension (named molecule 28_1). Image blur can occur due to a difference of stage and flow velocities and is increased if the particle is not in the middle of the frame (corresponding to the reference position) as this leads to a larger difference. Taking into account that molecule position relative to the centre of the frame (for which the velocity profile is predicted) the tracking of such molecule starts when it is already ~25μm away from the reference point and achieves a maximum distance of 100μm away from the reference point, meaning the extension is possibly an effect of blur. It is important to mention that all the molecules observed in these flow conditions are apparently in a good position when starting the tracking system (along the centreline and close to the centre of the frame). However, none of them is actually at the reference position, for which the velocity equations are defined. This means that all the molecules will present a different velocity than expected and some blur may contribute to the extension measured.

Figure 5.11a presents an example of the evaluation of the molecule extension. The molecule presents a coiled structure until reaching a channel position close to the contraction, for which a significant extension is observed. Figure 5.11b presents the comparison between the molecule velocity and the step function described by the stage velocity. Figure 5.11c presents the measured length of the molecule (red line) and the contribution of the blur (black line) based on the difference in displacement of the molecule and the stage during the exposure time used to capture each image (20ms). This data confirms that the blur, although small (≤1.5μm), contributes to the total length measured in the images with the maximum found in the region slightly after the channel contraction, where the velocities are high and a larger difference is found between molecule and stage velocity in each time step. The real molecule length could then be determined by subtracting the estimated blur to the measured length. However, when considering such small molecule extension (as in the Figure 5.11) the errors become significant.
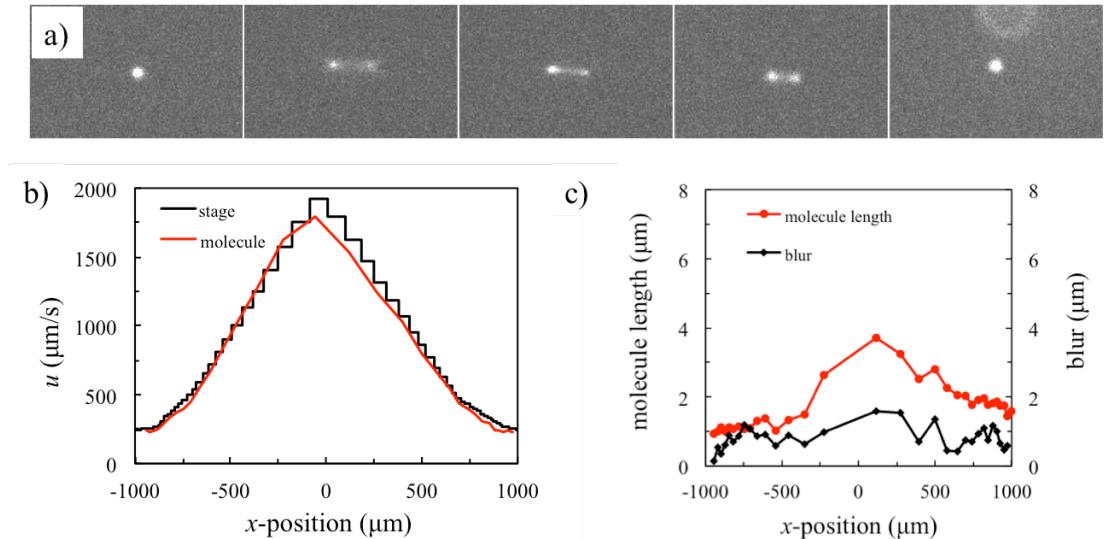
Figure 5.11: Evaluation of the molecule extension along the channel length. (a) Example of molecule observation during transport along the optimised geometry; (b) comparison between the molecule velocity (red line) and the velocity steps described by the microscope stage (black line); (c) comparison between the molecule measured extension (red line) and the expected blur contribution due to the difference between molecule and stage velocities for each time step (black line).

There are a few parameters contributing to these non-optimal results such as the suspension integrity, poor statistics, observation away from the focusing plane or the flow conditions tested which may be not as strong as necessary to deform the molecule. We assume the suspension to be in good shape since it was previously tested in a straight channel, where strong deformation was observed in positions close to the walls (similarly to what was observed in Chapter 4, with molecules transported in shear flow). As previously mentioned, no molecule was found perfectly aligned with the reference position (centre of the frame), even when directing the object towards the channel centreline, using the flow focus entrance. Since we intend to observe individual object dynamics, the suspension needs to be dilute and, therefore, the number of molecules analysed was small. Also, after performing the tracking system for a few times, we noticed that the reference position $x,y,z = (0,0,0)$ at the channel contraction is slightly deviated from the midplane, perhaps due to the tension generated by the large velocities used to displace the microscope stage and the existence of a viscous medium between the glass slide and the microscope objective (oil immersed objective). We minimised this tension by using water instead of immersion oil. In addition, the zero position (channel contraction) was calibrated prior to each tracking to minimise such error.

Finally, it would be preferable to use larger strain rates to observe stronger molecule deformation. However, that would be achieved by using larger velocities, which easily translate in a stronger discrepancy between molecule and stage velocity in each time step and consequent image blur.

In general, these limitations are not significant if the tracked objects present a minimum size larger than a few micrometers (>10μm), as is the case of actin filaments, or if the strain rate necessary to deform such objects is small, minimising the blur effects. Figure 5.12 presents the deformation of actin filaments of different size travelling along an optimised converging-diverging geometry using the Mathematica code previously described. In this case, the errors associated with experimental limitations are not significant and we can follow clearly the behaviour of the filaments as they flow along the converging-diverging region, and the molecule extension can be quantified. A clear difference is found for the three filaments presenting some fluctuations while traveling along the straight part of the channel ($\dot{\varepsilon} = 0$), a significant alignment with the flow while subjected to extensional flow ($\dot{\varepsilon} \geq 0$) and contraction of the filament while traveling along the compressive region of the channel ($\dot{\varepsilon} \leq 0$).
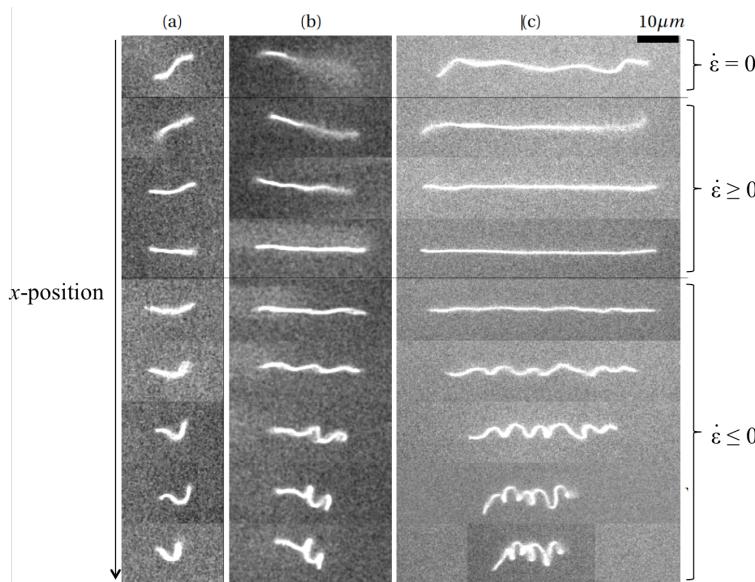
Figure 5.12: Example of actin filament deformation achieved along the optimised geometry using the methodology presented in this chapter. The filament lengths are $L_a = 12.2$μm, $L_b = 27.4$ μm and $L_c = 57.8$μm. The strain rates applied to deform the filaments are $\dot{\varepsilon}_a = 0.65$s^{-1}, $\dot{\varepsilon}_b = 0.65$s^{-1} and $\dot{\varepsilon}_c = 0.34$s^{-1}, respectively. Adapted from Liu.[14]

5.3.3 Other practical limitations

PDMS is known to expand and shrink during the curing process and subsequent cooling to room temperature, respectively. When the PDMS block containing the channels is bonded to a glass slide, this expansion can cause bending of the glass cover slip used to seal the device (thickness ~0.14-0.18 mm) (Figure 5.13a). After cooling to room temperature, an apparent flat surface is recovered (Figure 5.13b), but the channels may present slight deviations in the depth along the channel, in particular for geometries of larger length. Please note that if the experiments are performed using a device with PDMS bonded to a typical glass slide (thickness ~1.5 mm) such bending does not occur. If having a constant depth along the channel is an important requirement, like in this study, alternative bonding substrates should be considered, for example, quartz slides, in particular when the channel length is large.
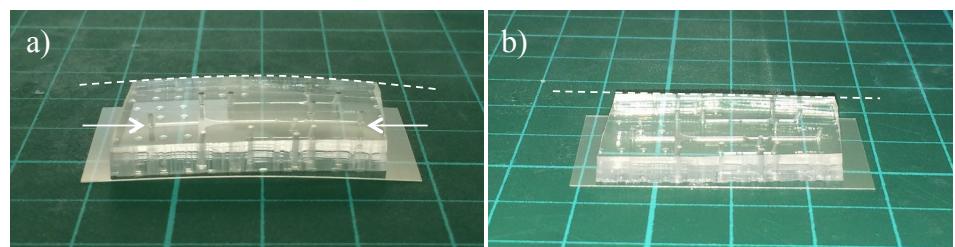
Figure 5.13: Effect of PDMS swelling on the structure of the microchip. (a) After curing in contact with glass slide at $T = 90°C$, where the bending of the PDMS block and cover slip used to seal the channels is clearly visible; (b) The same PDMS device after 10 minutes at room temperature where the bending is clearly reduced.

For the application here consider, the DNA tracking is done along large portions of the channel, for a minimum length of 1 mm in two of the geometries and 2mm in another. For the former, the molecules were tracked successfully along the whole ROI. For a larger length of ~2 mm, however, the existence of a slope together with the small dimension of the λ-DNA molecule, is translated into its loss during tracking, as exemplified in Figure 5.14.
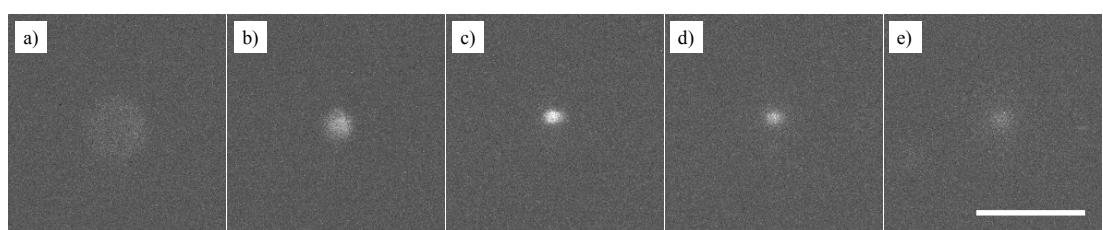
Figure 5.14: Example of λ-DNA molecules transported along the channel, going in and out of focus due to the slope in the channel.

5.4 Summary

In this chapter, we presented a new methodology for tracking objects in extensional flow, generated by optimised converging-diverging channels. The microfluidic geometries are complex, and the velocity profile at the centreline is non-constant but well-known. The first approach, using a Labview interface, provided a simple way to track objects of larger sizes, for which the microscopic observation can be done using smaller magnification or for which the velocity (strain rate) necessary to deform the object is small. If these conditions are not met, the object will move away from the field of view or the blur generated by the relative velocity between object and stage will be significant and compromise the measurement.

A further approach consisted in using a Mathematica code which takes into account some of the tracking limitations and allows predicting the commands to be sent to the stage, by introducing velocity and position corrections, such that the blur in each frame is minimised, assuming the tracked object is transported along the channel centreline. This new method allows optimising drifts within the code, instead of the manual approach, a characteristic that made the previous method time-consuming.

Finally, this method proved successful for slightly larger objects in the range of a few micrometers and for which the change in configuration is observed using smaller strain rates, minimising the difference between object and stage velocities. It was proven that, for small molecules, such as the λ-DNA used here as a model, the error inherent to the measurement is still significant, due to the non-optimal molecule position in the channel, deviated from the focusing plane ($z \neq h/2$) or deviated from the centreline ($y \neq 0$). It is still possible to track such small molecules but further calculations need to be done to subtract the contribution of image blur to the real molecule measured length.

Also, it was found that for longer geometries, the bending of the glass slide caused by the expansion and shrinking of PDMS during the curing process, generates a small slope in the channel, causing the transported molecules to go out of focus during tracking. Even though a significant blur is found for the experiments using λ-DNA molecule, these were of great importance to test the limitations of the tracking system. In the future, this concept should be tested using a larger molecule such as the T4 DNA (169Kbp) whose contour length ranges between 70-80μm and for which the conformational changes are easier to detect at lower strain rates.

References

1. Dylla-Spears, R., Townsend, J. E., Jen-Jacobson, L., Sohn, L. L. & Muller, S. J. Single-molecule sequence detection via microfluidic planar extensional flow at a stagnation point. *Lab Chip* **10,** 1543 (2010).

2. Haward, S. J. Microfluidic extensional rheometry using stagnation point flow. *Biomicrofluidics* **10,** 1–26 (2016).

3. Pimenta, F., Sousa, R. G. & Alves, M. A. Optimization of flow-focusing devices for homogeneous extensional flow. *Biomicrofluidics* **12,** (2018).

4. Gulati, S., Muller, S. J. & Liepmann, D. Direct measurements of viscoelastic flows of DNA in a 2 : 1 abrupt planar micro-contraction. *J. Non Newton. Fluid Mech.* **155,** 51–66 (2008).

5. Ober, T. J., Haward, S. J., Pipe, C. J., Soulages, J. & Mckinley, G. H. Microfluidic extensional rheometry using a hyperbolic contraction geometry. *Rheol. Acta* **52,** 529–546 (2013).

6. Yaginuma, T., Oliveira, M. S. N., Lima, R., Ishikawa, T. & Yamaguchi, T. Human Red Blood Cell Behavior under Homogeneous Extensional Flow in a Hyperbolic-Shaped Microchannel. *Biomicrofluidics* **7,** 054110 (2013).

7. Tanyeri, M., Johnson-Chavarria, E. M. & Schroeder, C. M. Hydrodynamic trap for single particles and cells. *Appl. Phys. Lett.* **96,** 22–24 (2010).

8. Pipe, C. J. & McKinley, G. H. Microfluidic rheometry. *Mech. Res. Commun.* **36,** 110–120 (2009).

9. Sousa, P. C., Pinho, F. T., Oliveira, M. S. N. & Alves, M. A. Extensional flow of blood analog solutions in microfluidic devices. *Biomicrofluidics* **5,** (2011).

10. Gulati, S., Muller, S. J. & Liepmann, D. Flow of DNA solutions in a microfluidic gradual contraction. *Biomicrofluidics* **9,** 054102 (2015).

11. Hemminger, O. L., Boukany, P. E., Wang, S. Q. & Lee, L. J. Flow pattern and molecular visualization of DNA solutions through a 4:1 planar micro-contraction. *J. Non Newton. Fluid Mech.* **165,** 1613–1624 (2010).

12. Oliveira, M. S. N., Alves, M. A., Pinho, F. T. & McKinley, G. H. Viscous flow through microfabricated hyperbolic contractions. *Exp Fluids* **43,** 437–451 (2007).

13. Zografos, K., Pimenta, F., Alves, M. A. & Oliveira, M. S. N. Microfluidic converging/diverging channels optimised for homogeneous extensional deformation. *Biomicrofluidics* **10,** 1–21 (2016).

14.	Liu, Y. Dynamics of flexible and Brownian filaments in viscous flow. (PhD thesis, ESPCI, 2018).

CHAPTER 6

Red blood cell distribution in microfluidic flows using dilute suspensions

In the present chapter, we describe the investigation of RBC dilute suspensions flowing in microfluidic devices. The study focuses on the counterintuitive RBC distribution inside microfluidic channels of rectangular section, where the cells tend to accumulate at certain equilibrium positions inside the channel. This distribution resembles that obtained for experiments using inertia (Segré-Silberberg effect), even though the present study is performed in Stokes regime, where the inertial effects are negligible (Re << 1). By means of experiments and numerical simulations, we intend to unravel the cell transport dynamics underpinning such distribution profile.

We found that, independently of the sample inflow conditions considered (for example an aligned and non-aligned sample entrance in the straight channel, as well as different flow rates) the cells tend to accumulate at equilibrium positions, resulting in a two-peak density distribution. Also, the homogeneous cell distribution is not recovered for, at least, a channel length of $46D_h$, for experiments, and $28D_h$, for numerical simulations.

This fact might be of crucial importance when designing microfluidic geometries and planning experiments using dilute suspensions.

6.1 Introduction

Microfluidics has been widely used to investigate the behaviour of complex suspensions, including blood flow. The typical small channel dimensions allow representing the vessels structure at the microcirculation level and, therefore, mimicking the interesting phenomena occurring *in vivo*, at this scale. The effects of channel topology, cell volume concentration or flow characteristics have been proven to interfere with the cell transport and respective partitioning along microfluidic customised networks (see conference paper in Appendix E and preliminary results in Chapter 7). For *in vivo* conditions, the phenomenon of heterogeneous hematocrit distribution has critical impact on the oxygen and nutrient supply to the body tissues since some of the vessels are almost, if not completely, depleted of cells.[1] Since the late 1960s, several studies have been performed using individual RBCs or RBCs suspensions.[2,3] RBCs are the most abundant constituent of the blood sample (~45% in volume) and are responsible for some interesting blood flow effects,[4] as discussed in Section 2.5.4. Even though there are important literature reviews and papers on the individual RBC behaviour[5–7] and blood flow[8–10], and despite the progress made using microfluidics, allowing a broader knowledge on RBC behaviour under flow, a quantitative correspondence between RBC dynamics at microscopic level and the overall RBC suspension behaviour, which dictates the blood flow in microcirculation, is still missing.[11]

Experiments using blood present a series of practical difficulties, including channel clogging, blood sample availability or the short sample shelf life. In this sense, the use of data from numerical simulations is an essential tool, allowing the prediction and the analysis of certain flow conditions, which would otherwise be difficult to gather, experimentally. Numerical simulations also allow optimising the time and resources spent in the laboratory. In summary, there is an emergent need to approach experimental and numerical initial conditions, so that a realistic agreement between results and simulations can be achieved. At the same time, there is a need for numerical methods allowing the simulation of blood as a suspension of deformable objects in complex geometries, as the ones employed in experiments mimicking *in vivo* conditions.

In this chapter, we investigate the RBC distribution inside microfluidic devices of simple geometry, as a straight channel of constant depth and rectangular cross-section, typically used for microfluidic applications. One important detail, while designing the microfluidic geometry, is the flow inlet used to insert the sample. In scientific papers describing the flow of RBC suspensions along microfluidic devices, only the region of interest is shown and compared with numerical simulations, for example, a specific section of a channel. However,

if the goal is to compare the flow conditions in experiments and numerical simulations, the entire device configuration should be taken into account, including the geometrical feature used for sample inlet(s) and outlet(s). Microfluidic devices typically present a geometrical expansion for the sample inlet and outlet. Such sections can present different geometrical details and the most common shapes used are presented in Figure 6.1. The sample is injected into a rectangular, square or disk shaped extension, with a smooth or abrupt transition to the main microfluidic channel.[12–14] The disk shape inlet adopted in this work is, arguably, the most frequently used (Figure 6.1c), since it directly results from the process of inlet opening, by punching a hole into the PDMS bulk, using a circular needle.
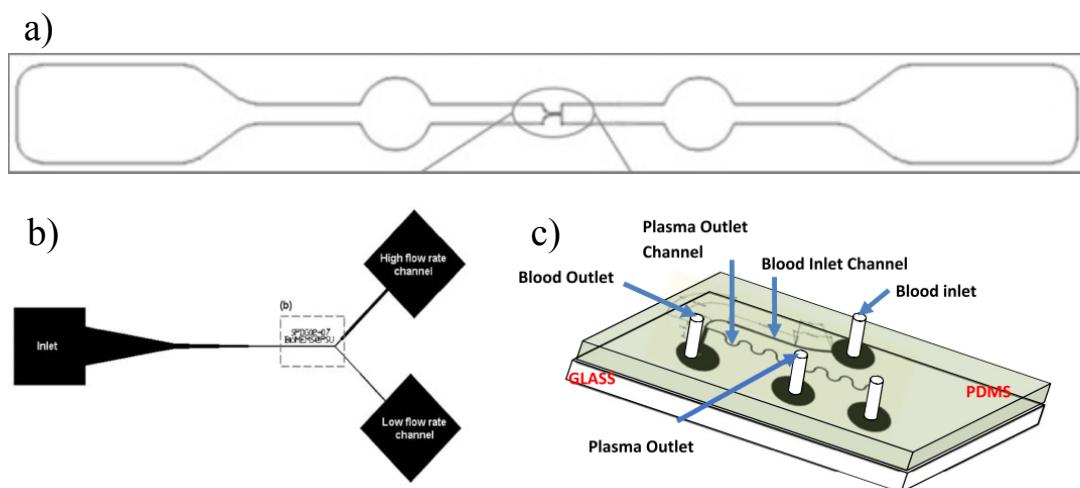
Figure 6.1: Examples of flow inlets typically used to inject the sample into the microfluidic device. (a) Rectangular shaped with smooth transition,[12] (b) square shaped with smooth or abrupt transition[13] and (c) disk shaped with abrupt contraction.[14]

When manipulating suspensions of small objects, such as tracer particles, the particles follow the fluid flow. However, when dealing with suspensions of larger objects, other parameters such as the size and deformability might interfere with the natural fluid flow, possibly resulting in migration across streamlines. There is a vast research on particle separation using inertial focusing in microfluidic devices. These experiments allow separating suspensions according to the particle size but they require channel Reynolds numbers typically larger than 1. For deformable objects, such as vesicles or red blood cells, even in the absence of inertia (Re < 1), migration may occur, as discussed in Section 2.5.5.[9]

In this chapter, we investigate the flow of a dilute RBC suspension (Hct ≤ 1%) along a straight channel, where the cells can be individually detected. We believe that the collective

behaviour of cells might provide important information relating the microscopic dynamics of the cells and the macroscopic complex behaviour of the blood itself. The experiments here performed are intended to provide the cell distribution across the channel width, at different positions along the channel length and, with that information, conclude about the cell dynamics inside the channels. The effects of sample inflow, channel length and flow rate, on the RBC distribution, were experimentally inspected.

To complement the experimental work, numerical simulations of RBC suspensions in such microchannels were performed by Qi Zhou, Timm Kruger (from the Institute for Multiscale Thermofluids at University of Edinburgh) and Miguel O. Bernabeu (Usher Institute at University of Edinburgh), in order to better understand the physics underlying the peculiar RBC distribution found.

6.2 Materials and Methods

In this study, suspensions of horse RBC were used instead of human RBCs, due to laboratory limitations. Horse RBCs present an average diameter of 5.7μm,[15] a mean cell volume of 45fL[16] and are slightly more flexible than human RBCs, with a faster shape recovery.[17] One of the particularities of horse RBCs is the stronger tendency to form rouleaux, i.e., structures of RBCs packed together due to the presence of fibrinogen in plasma. These experiments were performed with suspensions of RBC in dextran solution (avoiding cell agglomeration), using small and intermediate nominal hematocrits ($\leq 20\%$), so rouleaux structures were not observed.

Figure 6.2 presents the images of a horse RBC suspension using two different magnifications. For the larger magnification (40x), it is possible to detect the typical RBC biconcave shape, even though this feature is not as prominent as in human RBCs. When the same suspension is observed at smaller magnification (10x) as used in our experiments, this detail is no longer detected (Figure 6.2).
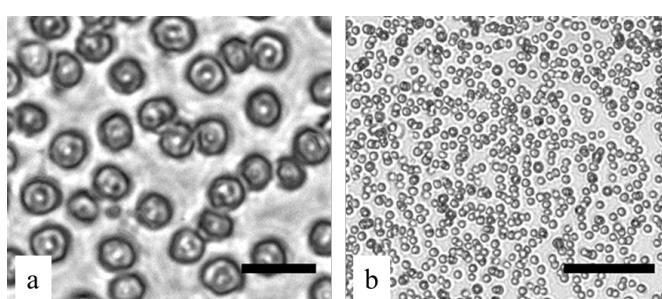
Figure 6.2: Photomicrography of a RBC suspension in physiological saline solution, at different magnifications: (a) 40x, scale bar 10μm and (b) 10x, scale bar 50μm.

All methods and techniques used in these experiments are in accordance to the health and safety requirements at University of Strathclyde. Prior to starting the new experiments, important discussions were taken with the university safety advisor and both new risk assessment and COSHH documents were implemented. Even though the sample was provided from healthy animals, the experiments were always performed in a contained environment and a proper residue disposal plan was executed to ensure the safety of laboratory workers as well as a good lab practice.

6.2.1 Sample preparation

The horse blood sample was provided by TCS Biosciences (UK), in anticoagulant ethylenediaminetetraacetic acid (EDTA) 1.5mg/mL, and stored at 4°C until further use. Figure 6.3 presents the sample at different stages of preparation. An Eppendorf with 1.5 mL of whole blood (WB) was centrifuged at 6000 rpm for 1 min (miniFUGE) and the supernatant containing the plasma and buffy coat (white blood cells and platelets) was discarded. The RBCs were washed twice with physiological saline PS (NaCl 0.9% w/v). The transparent supernatant was discarded leaving what is called a cell pellet containing the RBCs. The final sample was prepared by suspending the desired volume of cell pellet in Dextran 40 solution (Dx40 $M_w = 40000$g/mol, 0.1g/mL in isotonic medium). This suspending medium avoids quick cell sedimentation during the experiments, which is a common problem when the suspension is prepared in PS or in the original blood plasma.
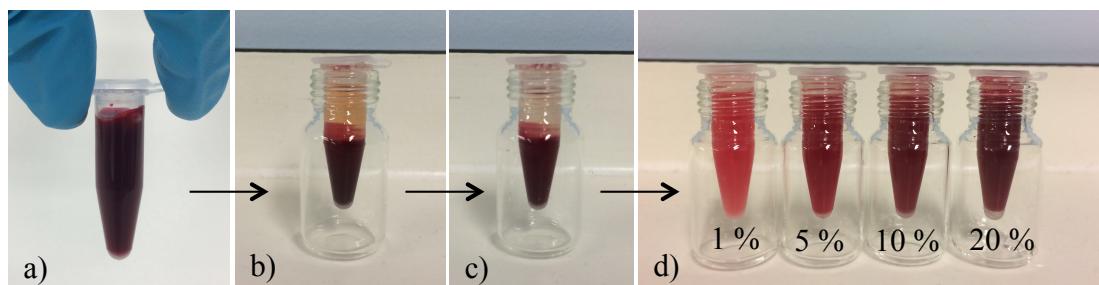
Figure 6.3: Preparation of RBC suspension. (a) Whole blood in eppendorf; (b) separation of plasma and buffy coat by centrifugation; (c) RBC and physiological saline after cell washing and centrifugation; (d) RBC suspended in Dx40, at different nominal hematocrits.

For simplicity, the samples prepared in this work will be identified using their nominal hematocrit, defined as the cell volume fraction in the sample, considering the cell pellet as 100% RBCs.

It is important to mention that the real hematocrit is smaller than the nominal one, since there is a residual amount of solution between the cells in the sediment (cf. Figure 6.3c). For example, Flormann *et al*[18] described a pellet with approximately 80% cells and 20% suspending medium for a sample of human blood at specific centrifuging conditions (704*g*, 3min). Here, we calculated the real hematocrit indirectly, by using the cell concentration in each suspension using an improved Neubauer counting chamber (see Appendix D). We calculated the corresponding cell volume concentration, assuming that the mean cell volume of a horse cell corresponds to 45fL.[16] A calibration curve was then determined relating the nominal and real hematocrits. We found that the sample preparation procedure previously described provides a blood sample with real hematocrit corresponding to approximately 60% of the nominal one. In the chapters we will refer to the nominal Hct for simplicity.

6.2.2 Properties of RBC suspensions

The RBC suspensions were characterised by liquid pycnometry and shear rheology to determine their density and shear viscosity, respectively. The main procedure was previously described in Chapter 3 and specific details will be provided below.

The shear rheology experiments were performed in a rotational rheometer (DHR2, TA Instruments, minimum resolvable torque 0.1nN m), using a plate-plate geometry with 40 mm diameter (PP40) and a 400μm gap. A sandpaper layer was used on the upper plate to minimise slip effects. Dx40 solution was characterised using the same geometry, for direct comparison with the viscosity obtained for RBC suspensions, and also using a cone-plate geometry of 60 mm diameter, angle $\theta = 1°$ (CP60/1) and a 30μm truncation gap. The latter geometry allows a more accurate measurement for a homogeneous sample since the shear rate is homogeneous at any point throughout the sample contained between cone-and-plate.

Figure 6.4 presents the flow curves for different RBC suspensions in Dx40, as a function of the shear rate, obtained using a rotational rheometer with PP40 geometry. As expected, the sample with lower hematocrit (Hct = 1%) presents a viscosity very close to the Dx40 solution alone with small differences observed only for the smaller shear rates. The low shear rate viscosity increased substantially with hematocrit and the shear thinning behaviour becomes stronger for increasing hematocrit as expected.[19,20]
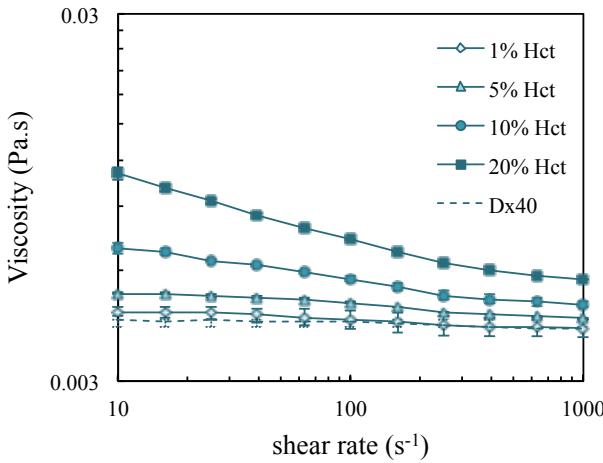
Figure 6.4: Rheological characterisation of RBC suspensions, using rotational rheometer with PP40 geometry and sandpaper on the upper plate ($T = 20$˚C), for distinct nominal hematocrits.

Sample density was determined using a pycnometer of 10mL volume and again no significant difference was found between the density of Dx40 solution alone and that of the RBC suspension of lower hematocrit (Hct = 1%). The summary of density and characteristic viscosity values for Dx40 and RBC suspensions, at 20°C, is described in Table 6.1.

Table 6.1: Summary of density and viscosity values for Dx40 solution and RBC suspensions in Dx40 at 20°C, for distinct nominal hematocrits.

sample	Density (g/mL)	Viscosity (mPa s)		
		$\dot{y} = 10s^{-1}$	$\dot{y} = 100s^{-1}$	$\dot{y} = 1000s^{-1}$
Dx40	$1.0748 \pm 1.15 \times 10^{-5}$	$5.04 \pm 9.37 \times 10^{-5}$*	$5.03 \pm 1.11 \times 10^{-3}$*	$4.98 \pm 9.98 \times 10^{-5}$*
		$4.39 \pm 9.20 \times 10^{-5}$	$4.33 \pm 1.30 \times 10^{-4}$	$4.17 \pm 1.00 \times 10^{-4}$
1% Hct	$1.0749 \pm 1.15 \times 10^{-5}$	$4.64 \pm 1.18 \times 10^{-4}$	$4.41 \pm 2.58 \times 10^{-3}$	$4.18 \pm 2.32 \times 10^{-4}$
5% Hct	$1.0759 \pm 1.06 \times 10^{-4}$	$5.20 \pm 1.23 \times 10^{-5}$	$4.91 \pm 3.00 \times 10^{-5}$	$4.44 \pm 1.86 \times 10^{-5}$
10% Hct	$1.0786 \pm 1.15 \times 10^{-5}$	$6.88 \pm 2.38 \times 10^{-4}$	$5.69 \pm 1.05 \times 10^{-4}$	$4.84 \pm 8.48 \times 10^{-5}$
20% Hct	$1.0824 \pm 2.52 \times 10^{-5}$	$11.00 \pm 4.01 \times 10^{-4}$	$7.28 \pm 2.21 \times 10^{-5}$	$5.67 \pm 9.76 \times 10^{-6}$

(*) Viscosity values obtained using CP60/1 geometry. The remaining viscosity values were determined using PP40 geometry.

6.2.3 Experimental setup and microfluidic devices

6.2.3.1 Experimental setup

The experiments were performed using an inverted microscope (Olympus IX71), an halogen lamp for sample illumination and a precise syringe pump (Nemesys, Cetoni) for fluid control. The sample was infused into the microdevice by using the withdraw function of the

syringe pump, as shown in Figure 6.5. This procedure was employed to circumvent the problem of cell sedimentation along time, which typically limits the time of experiment. In this proposed system, the Eppendorf containing the sample is gently stirred at regular time intervals to keep cells uniformly distributed in the sample.
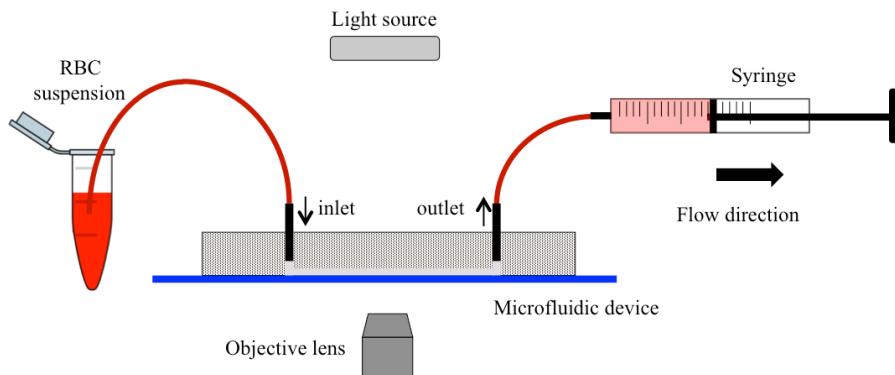
Figure 6.5: Schematic representation of microfluidic setup used.

6.2.3.2 Microfluidic device and flow conditions

The microfluidic devices were built *in-house* in PDMS, following the soft-lithography method described in Chapter 3. In this case the SU8 mould, used in the soft-lithography procedure, was designed in AutoCAD and produced, by photo-lithography, in a specialised microfluidics company (MicroLIQUID, Spain). Figure 6.6a shows a scheme of the microfluidic device consisting of a single straight channel, with cylindrical shaped regions located at the ends of the channel, for sample inflow and outlet. Figures 6.6b1 and 6.6b2 present real images of the two devices used, showing the location of the inlet hole punched on the PDMS for sample infusion. Figure 6.6b1 presents a channel with sample entrance aligned with the channel centreline while Figure 6.6b2 presents a channel with a deliberately misaligned entrance. The origin of the coordinate system used is also shown in Figure 6.6b1 and is located immediately downstream the inlet region, at the channel entrance, mid-way between bottom and top walls (depthwise centreline) and mid-way between lateral walls (widthwise centreline). Figure 6.6c presents a scheme of the regions of interest (ROIs) considered for this study.

Three important parameters are used to define the geometry: the inflow contraction ratio α, relating the diameter of the entrance region to the microfluidic channel characteristic dimension width w or depth h. For experiments, $\alpha = d_{inlet}/w$, while for simulations α was calculated using both width w or depth h; the channel aspect ratio, defined as the ratio of

channel width to depth (AR = w/h), and the geometrical confinement β, relating the cell diameter to the microfluidic channel width ($\beta = d_{RBC}/w$).
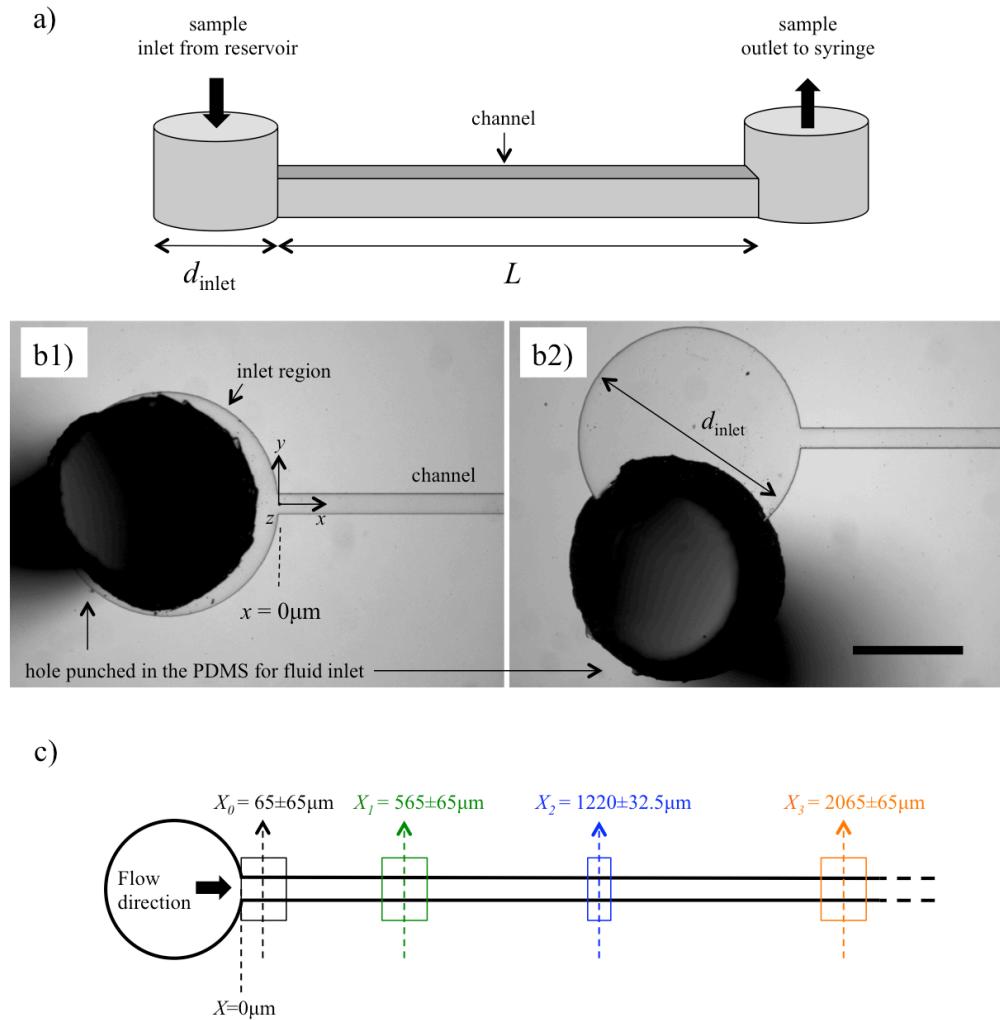
Figure 6.6: Microfluidic device configuration used in this study. (a) Scheme of the microfluidic straight channel with cylindrical regions for sample inflow and outlet. Photomicrography of the inlet region, seen from below, when the entrance hole on PDMS is (b1) aligned and (b2) misaligned with the channel centreline. (c) Scheme of the regions of interest (ROIs) considered in this study. Scale bar 500μm.

In addition to the geometrical parameters defined previously, the important dimensionless numbers that define the problem are the channel Reynolds number (Re_c), the particle Reynolds number (Re_p) and Capillary number (Ca) defined by equations 6.1, 6.2 and 6.3, respectively. The latter refers to the ratio of viscous stress to the characteristic membrane stress, which is related to the elasticity of the RBC and is an important parameter for

comparison with numerical simulations. A larger Ca number (Ca ~1) corresponds to stronger RBC deformations under shear and the limit of a negligible Ca (Ca ~0) corresponds to a rigid cell under flow.

$$\text{Re}_c = \frac{\rho_{Dx40} \, U_{avg} \, Dh}{\mu_{Dx40}} \tag{6.1}$$

$$\text{Re}_p = \text{Re}_c \left(\frac{d_{RBC}}{Dh}\right)^2 \tag{6.2}$$

$$\text{Ca} = \frac{\mu_{Dx40} \, \dot{\gamma}_{wall} \, 0.5 d_{RBC}}{k_s} \tag{6.3}$$

where $\dot{\gamma}_{wall}$ is the wall shear rate, approximated here as $\dot{\gamma}_{wall} = 8U_{avg}/D_h$ and K_s is the cell membrane shear elasticity.

Table 6.2 summarises the important parameters used in this experimental study, where the properties of Dextran 40 solutions were previously determined by liquid pycnometry and shear rheology measurements.

Table 6.2: Symbols and parameters used in this study.

Parameter	Symbol	Value
Flow rate	Q	0.2, 0.8, 4.0 µL/min
Channel width	w	86±1 µm
Channel depth	h	30.5±0.5µm
Channel aspect ratio	w/h	2.8
Flow inlet diameter	d_{inlet}	1000 µm
Hydraulic diameter	D_h	45.71 µm
Average velocity	$U_{avg} = Q/wh$	1.24×10^{-3}-2.47×10^{-2} m/s
Inflow contraction ratio	$\alpha = d_{inlet}/w$	11.50
Geometrical confinement	$\beta = d_{RBC}/w$	0.07
Geometrical parameter	$K = U_{max}/U_{avg}$	1.89
Maximum velocity	U_{max}	2.33×10^{-3}-4.66×10^{-2} m/s
Wall shear rate	$\dot{\gamma}_{wall} = 8U_{avg}/D_h$	216.3-4326.0 s^{-1}
Dextran40 Viscosity	μ_{Dx40}	5.0 mPa s
Dextran40 Density	ρ_{Dx40}	1.0748 g/mL
RBC diameter	d_{RBC}	5.7 µm
Viscosity ratio	$\Lambda = \mu_{RBC}/\mu_{Dx40}$	1
RBC membrane shear elasticity*	K_s	5.3 µN/m
Reynolds in the channel	$Re_c = \rho_{Dx40} U_{avg} D_h/\mu_{Dx40}$	1.21×10^{-2}-2.43×10^{-1}
Reynolds for the particle	$Re_p = Re_c (d_{RBC}/D_h)^2$	1.89×10^{-4}-3.78×10^{-3}
Capillary number	$Ca = \mu_{Dx40} \dot{\gamma}_{wall} 0.5 d_{RBC}/K_s$	0.6-11.6

(*) Note that the value of RBC shear elasticity (K_s), here used to calculate the dimensionless Capillary number, refers to the human RBC.[21]

After changing the flow parameters, the system was allowed to stabilise for a few minutes before image acquisition.

6.2.4 Data acquisition and image analysis

For each flow condition tested, videos of the regions of interest (ROI) were acquired by a sensitive monochrome CCD camera (Olympus, XM10), at the frame rate of 15Hz. For each video, a stack with a minimum of 300 frames (capturing in excess of 8000 cells) was analysed to determine the RBC distribution across the channel width. The exposure time was set to 100μs allowing well-defined images of the cell boundaries. The ROIs have lengths of 65μm or 130μm and are located along different channel length positions (x-position) as shown in Figure 6.6c. A microscope objective of 10x and 0.25NA (Olympus, Plan N) was used in order to capture a large field of view and to be able to observe all the cells travelling along the depth of the channel. The depth of field is ~61μm calculated using the equation 4.9 and all the images were obtained at the channel centreplane ($z = h/2$).

Image analysis was carried out using ImageJ open software and consisted in improving the image quality to subsequently determine the cell free layer developed close to the channel walls, as well as the RBC distribution along the channel width.

Since bright field images often present an unbalanced intensity distribution (cf. the example in Figure 6.7), in particular close to the channel inlets and outlets, where the fittings are connected to the device, the videos were first corrected by subtracting the background. For this purpose, the function *Rolling ball radius* was used, applying a pixel size of 10, corresponding to the mean diameter of a horse RBC (i.e. ~6μm). This procedure allowed obtaining a clear and balanced image without the lost of information, allowing to retain even those cells located further away from the focal plan, as observed in Figure 6.7a. Figure 6.7b presents the corresponding intensity profiles, where a much more homogeneous intensity baseline is found for the corrected image.
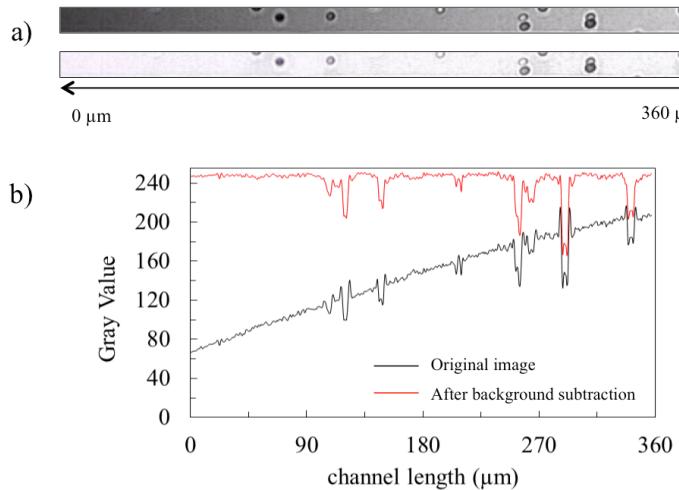
Figure 6.7: Background subtraction. (a) Image section before (top) and after background subtraction (bottom) and (b) corresponding average intensity profiles.

6.2.4.1 CFL measurement

In this thesis we report the CFL as the difference between the average channel width ($w_{channel}$) and the average RBC core thickness ($w_{RBC\ core}$), for a certain region of interest (ROI) along the channel length. Figure 6.8 presents the procedure used for CFL measurement.

After correcting the image intensity (Figures 6.8a1 and a2), the next step of analysis consists in generating an image compiling the information on the entire stack of images. Such image is produced using the Z-projection function, on Image J, using the minimum intensity parameter. Briefly, in this methodology, the intensity of each pixel in the image is compared to that in the corresponding pixel on the remaining frames of the stack, and the overall minimum intensity is recorded. This operation is successful for treating images with light background,[12] corresponding to the suspending medium, and objects of darker core or darker limit, such as the red blood cells in our images. The resulting image (Figure 6.8a3) allows identifying the areas occupied by the RBCs and the areas depleted of cells (cell-free layer CFL). A binary image is then produced from the projection image, allowing a more clear definition of the threshold separating the RBC core and the CFL formed close to the channel walls (Figure 6.8b). Please note that the individual CFL developed in each side of the channel is very similar, as evidenced in Figure 6.8c, and in the results presented in the following sections, we will refer to the CFL as the sum of the two individual CFLs (on the left and right channel walls). The RBC core thickness ($w_{RBC\ core}$) is defined by the average thickness along the total length of the ROI considered (Figure 6.8b). Figure 6.8c presents the

individual CFL measured close to the channel walls (left and right walls), showing their similarity.
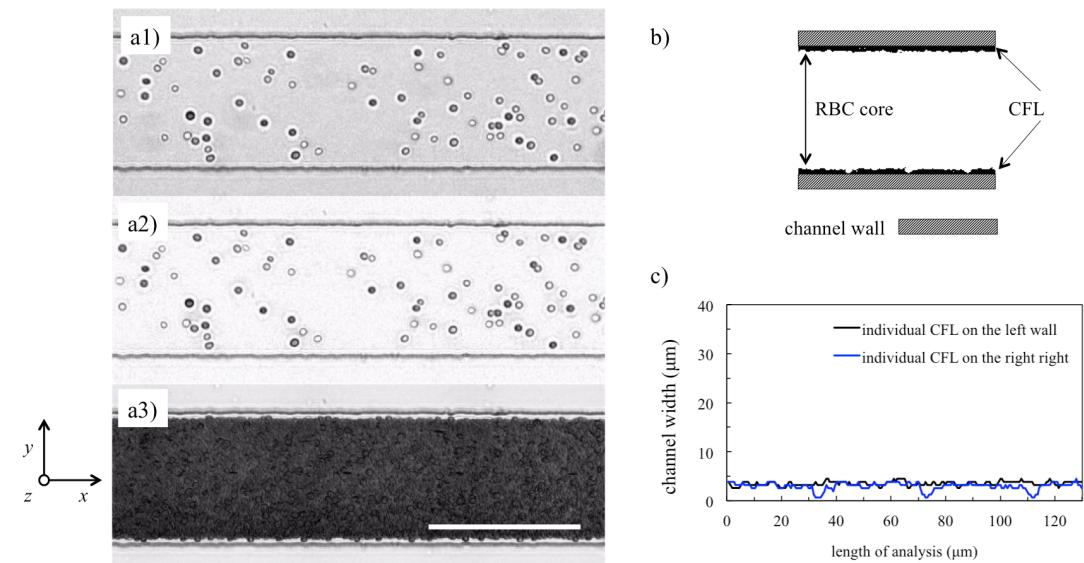
Figure 6.8: Procedure used for CFL measurement: (a1) original image showing a typical ROI; (a2) corresponding image after background subtraction; (a3) Composed image combining multiple frames of the same ROI at different times obtained using the z-projection method based on minimum intensity, highlighting the development of the cell free layer along the channel length (scale bar 100μm); (b) binary image, evidencing the CFL close to the channel walls; (c) comparison of the individual CFL developed in each side of the channel walls.

6.2.4.2 RBC distribution along the channel width

RBC distributions were determined using an automatic routine implemented into ImageJ open software. Figure 6.9 describes some of the most important intermediate steps involved on the improvement of image quality and cell detection, based on the image with subtracted background described previously.

A binary image is generated from the image with balanced pixel intensity (Figure 6.9b), followed by functions dilate (Figure 6.9c), which allows to extend and close the cell borders; and fill holes (Figure 6.9d), which fills up the total area corresponding to the cell. This procedure allows recovering the cell contour for brighter cells, located away from the focusing plan. The function watershed (Figure 6.9e) provides the separation of slightly overlapped cells and a filter was applied to detect objects with circularity (4π[cell area]/[perimeter]^2) in the range of 0.5-1.0 (Figure 6.9g). A circularity value of 1 corresponds to a perfectly rounded cell. Cells are then identified and the (x,y) position of the centre of mass of each identified cell is recorded. Another filter is subsequently applied to

the perimeter of the automatic detected object, in order to delete the objects/cells presenting a smaller size than a small cell ($d_{RBC} \approx 4\mu m$).
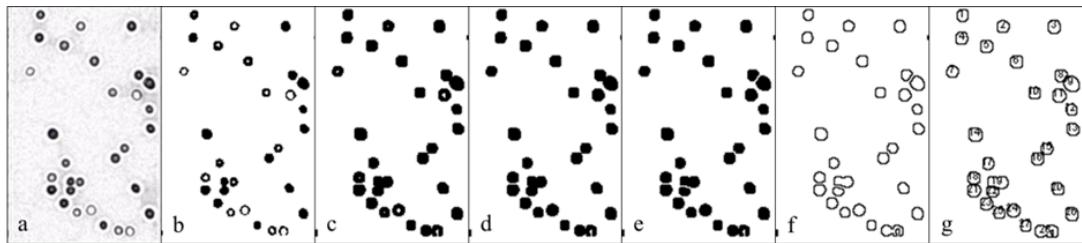
Figure 6.9: Procedure used for cell detection and RBC distribution building. Image obtained after background subtraction (a); corresponding binary image (b) after applying function *dilate* (c); function *Fill Holes* (d); and function *Watershed* (e); image highlighting the outline of the cells (f); image highlighting detected cells after applying circularity filter (g).

Using the (x,y) position of the centre of mass of all cells identified in a certain video, we determined the cell distribution along the width of the channel (*y*-direction). For this purpose, the microfluidic channel width is divided into a certain number of bins ($i \geq 26$) and the number fraction of cells on each bin i is given as a percentage determined as:

$$\text{RBC number fraction } i = \frac{\text{number of detected cells in } y-\text{position corresponding to bin } i}{\text{total number of detected cells in the video}} \qquad (6.4)$$

Since white light is used for these experiments, the channel walls and fittings might generate shadow effects. This only occurred for some conditions and can be overcome, in the future, by illuminating the sample through the microscope objective, instead of using the halogen lamp above the microscope stage. For this case, in which the image quality is poor to apply the automatic counting, the cells were counted manually.

Accuracy of distribution profile

To confirm the accuracy of the obtained RBC distribution based on the aforementioned automatic counting method, a preliminary test was performed in two steps. First, we verify how many frames are necessary to ensure good statistics. To this end, for a given ROI, the RBC distribution was determined using four different image stacks, involving 50, 100, 200 and 300 image frames, respectively. The results are presented in Figure 6.10a. The distributions obtained from a smaller stack of frames, namely 50 and 100 frames, present significant noise in contrast with the distributions obtained from 200 and 300 frames which

are much smoother and very similar. As such, for all subsequent experiments a stack of 300 frames is used to generate the RBC distribution for each ROI.

We have also compared the difference between the RBC distributions based on our automatic counting method and based on manual counting (both using a stack of 300 frames). The results (Figure 6.10b) present a high-level similarity between the two distributions, validating the accuracy of our proposed method for RBC distribution analysis for experiments using low hematocrit (Hct ≤ 1%), where the boundaries of individual cells are well defined.
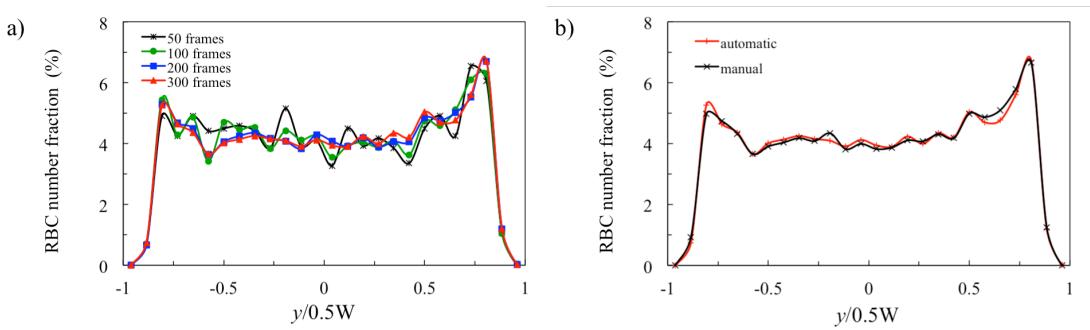
Figure 6.10: (a) Effect of the total number of frames analysed on the RBC distribution. Stack with 50 frames (black line), 100 frames (green line), 200 frames (blue line) and 300 frames (red line); (b) Automatic (red line) versus manual cell counting (black line) for a stack of 300 images.

Effect of cell overlapping

The effect of cell overlapping was also investigated. In Figure 6.9(g), it is possible to observe the presence of false "agglomerates" (eg. cell 19) caused by the overlapping of individual cells in the channel depth direction. It is important to mention that given the concentration of RBC and nature of the fluid used in our experiments, we would not expect any physical cell agglomeration.[22] To study the impact of these "agglomerates" on the RBC distribution, they were identified and excluded from a test case. The resulting RBC distribution was then compared to the original RBC distribution, where the two distributions obtained are found to be identical (see Figure 6.11). This suggests that cell overlapping found during our analysis has a negligible statistical effect on the final cell distribution obtained from our automatic counting method.
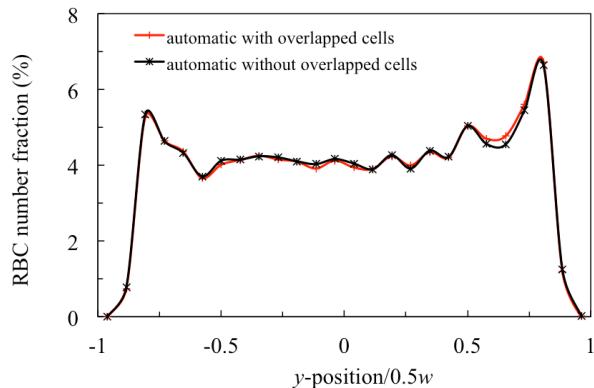
Figure 6.11: Impact of overlapped cells on the final RBC distribution (using a stack of 300 frames). RBC distribution obtained from automatic counting including overlapped cells (red line) versus that excluding overlapped cells (black line).

6.3 Experimental results

6.3.1 Counterintuitive RBC distribution for dilute suspensions of deformable objects

Figure 6.12a presents the RBC distribution profile in the y-direction for various x-positions along a straight channel with an aligned sample entrance, for Q = 0.2μL/min (Re = $1.21\text{x}10^{-2}$). At the first position analysed, $X_0 \sim 65 \pm 65$μm (black line), the RBC distribution is approximately symmetric and presents a pluglike profile forming a plateau in the central region. Even though cells enter the channel occupying its entire width (see Figure 6.12b), the concentration is lower close to the walls due to size exclusion effect.[10] At a certain distance away from the channel entrance, $X_1 \sim 565 \pm 65$μm (green line), a peculiar distribution is found such that of an off-centre two-peak density profile, showing an increased cell concentration at a short distance from the lateral walls. The location of the two peaks is approximately symmetric about the centreline. For locations further down the channel, the region close to the walls becomes progressively depleted of cells, the magnitude of such density peaks increases, and their location moves inwards until a certain distance to the walls is reached (about 0.2 to 0.25 of the half channel width w/2) (see $X_3 \sim 2065 \pm 65$μm, orange line). At the same time, a nearly unchanged distribution profile remains in the central region of the channel. Even though at the locations of the density peaks, the cell concentration is larger than the feeding hematocrit, we believe such concentration is still low and there is negligible cell-cell interaction. Therefore, the density-peaks persist along the channel.
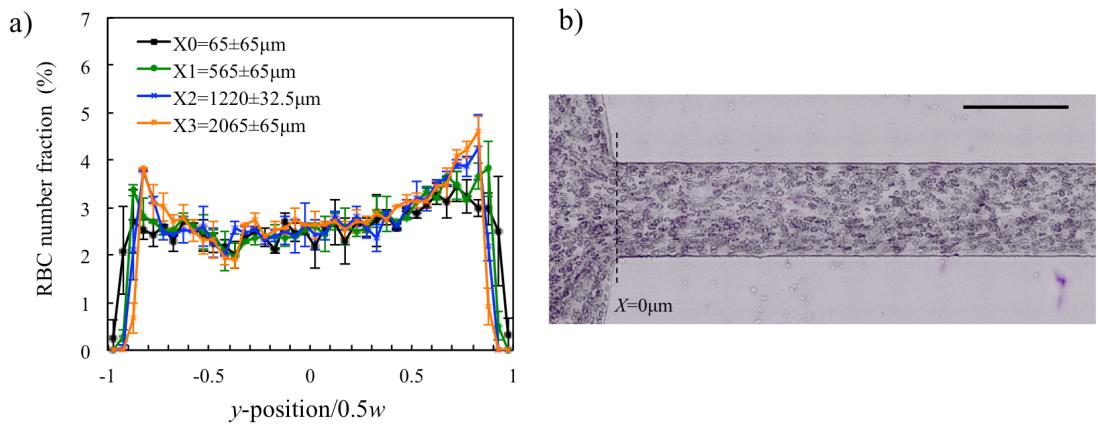
Figure 6.12: Results obtained for a straight channel with aligned sample inlet. (a) RBC distribution along the channel length. (b) Composed image combining 25 frames of the same region at different times, obtained using the Z-projection method based on the minimum intensity, for the corresponding experiment. Scale bar 100μm; Hct ≤ 1%; $Q = 0.2$ μL/min.

Our findings in terms of distribution of cells do not agree with reported cell density profile in microfluidic flows, which shows a core of cells in the central region of channels while a cell free layer would be developed close to the walls.[23] The phenomena of cell migration away from the walls, at low Reynolds numbers, is well-known to be caused by the hydrodynamic lift (a combination of wall repulsion and shear rate variation) and the interaction between cells.[10] It is important to mention, however, that the cell-cell interaction is expected to be negligible in the present study as a dilute suspension of Hct ≤ 1% was used.

6.3.2 Cell-free layer development

Figure 6.13a presents composed images combining multiple frames of the same region, at different times, obtained using the Z-projection method using 300 frames and minimum intensity for the various ROIs considered in Figure 6.6c. The wall effect is almost immediate and a small CFL is developed even at the first ROI. At position $X_1 \sim 565 \pm 65$μm, the CFL is well defined and the largest CFL thickness is found for the last position considered, which is in accordance with the density profiles presented on Figure 6.12a. Figure 6.13b presents the thickness of the RBC core for the corresponding ROIs and the slope of the line used to fit the points for RBC core in each ROI, describes the rate of the CFL development. The thickness of the RBC core decreases almost immediately as the suspension enters the channel (~20μm) and continues to decrease as highlighted by the negative slopes found for the fitting lines in ROIs $X_0 \sim 65 \pm 65$μm and $X_1 \sim 565 \pm 65$μm. For the third position investigated, $X_2 \sim 1220 \pm 32.5$μm, the fitting line presents a nearly zero slope which would apparently

indicate a stable CFL thickness, but this however is not the fact since we continue to observe a further decrease on RBC core for the last ROI considered, $X_3 \sim 2065 \pm 65\mu m$. Also, by observing the orange line on Figure 6.12a, corresponding to the length position $X_3 \sim 2065 \pm 65\mu m$, one can realise that there are still cells in the region between the density peak and the channel wall. This fact means that the cell migration away from the wall is not complete after such a long distance of $\sim 25w$ or $\sim 46D_h$.

In Figure 6.13c, we quantify the average value of total cell free layer thickness for each ROI. For the first point considered, corresponding to the entrance of the channel $X_0 \sim 65\mu m$, the CFL is very small. In fact, for the position $X = 0\mu m$, there is no visible CFL as result of the cells being squeezed by the entrance region walls into the channel width. For the remaining positions considered, the CFL increases along the length of the channel, as seen previously, but the increase becomes less significant as the contribution of cell migration away from the walls becomes smaller. We found that a power law of ~ 0.5 fits the values for experimental CFL. The fitting curve does not seem to have plateaued even at the last point analysed, $X_3 \sim 2065 \pm 65\mu m$, which is in accordance with the cell distribution presented in Figure 6.12a for the same ROI. This fact is in disagreement with the predictions made by Katanov et al.[24] According to these authors, by using numerical simulations of RBCs where the ratio between inner and outer fluid viscosity is also the unity, the length of the vessel necessary to achieve a fully developed cell free layer is $\lesssim 25D$, for vessel diameters D in the range between $10\mu m$ and $100\mu m$. By observing the CFL developed in Figure 6.13c, it is clear that after 25 channel diameters (length considered in the experiment), the curve has not reached a plateau yet and that further development of the CFL would probably be achieved if the channel was longer.
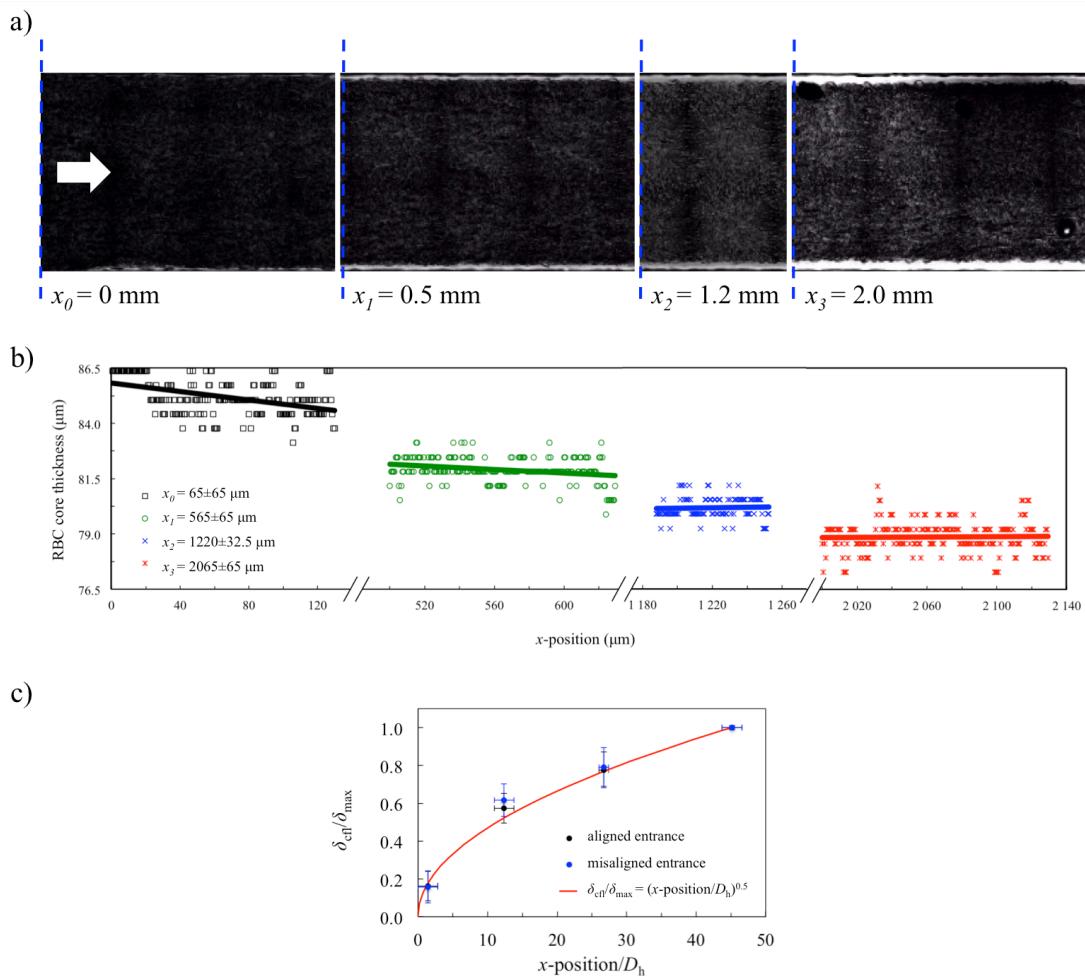
Figure 6.13: (a) Composed image combining multiple frames of each ROI at different times obtained using the Z-projection method based on minimum intensity, highlighting the development of the cell free layer along the channel length; experiment with aligned sample inflow; $Q = 0.2$ µL/min; white arrow indicates the flow direction. (b) RBC core thickness along the corresponding ROIs along the channel length. (c) Normalised CFL (obtained by dividing the CFL by the maximum CFL found for distance x-position = 0-2130µm, $\delta_{cfl}/\delta_{max}$) as a function of the normalised channel length (x-position/D_h) when sample inflow is aligned (black symbols) and misaligned (blue symbols); comparison with power law fitting $\delta_{cfl}/\delta_{max} = (x\text{-position}/D_h)^{0.5}$.

6.3.3 Effect of the flow rate on the RBC distribution

In order to verify if the peculiar cell distribution was exclusive of the flow conditions tested before ($Q = 0.2$µL/min), other flow rates were also tested ($Q = 0.8$µL/min and $Q = 4.0$µL/min), for which the channel and particle Reynolds number are still below unity (see values in Table 6.1). Figure 6.14 presents the cell distribution obtained at the ROIs closer to the channel entrance ($X_0 \sim 65 \pm 65$µm, Figure 6.14a) and further away from the channel entrance ($X_3 \sim 2065 \pm 65$µm, Figure 6.14b). It is possible to conclude that, regardless

of the cell distribution obtained at the entrance of the channel (where, for larger flow rates, a two-peak density is already found at the channel entrance compared to the flat profiles found for the two other flow rates $Q = 0.2\mu L/min$ and $Q = 0.8\mu L/min$), the two-peak density is always achieved for positions further down the channel ($X_3 \sim 2065 \pm 65\mu m$).
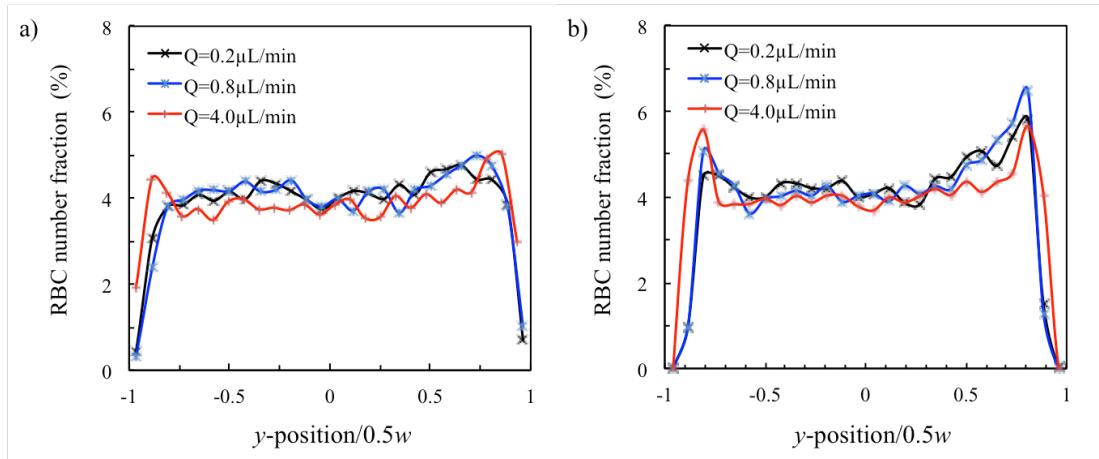
Figure 6.14: RBC density profiles for $Q = 0.2\mu L/min$, $Q = 0.8\mu L/min$ and $Q = 4.0\mu L/min$ at (a) channel entrance $X_0 \sim 65 \pm 65\mu m$ and (b) further away from the entrance $X_3 \sim 2065 \pm 65\mu m$.

6.3.4 Impact of an asymmetric sample inflow on RBC distribution and cell-free layer

For the previous experiment where the dilute RBC suspension was introduced through the aligned entrance hole, a small asymmetry on the RBC distribution is observed, in this case, towards the right hand-side of the channel (Figure 6.12a). Since the microfluidic geometry is quite simple and the syringe pump withdraws the sample at a stable flow rate, we believe this deviation is related to the experimental setup, for example, by a possible inclination of the connections used for sample inflow or by the tension on the fittings. Even when micro device fabrication and assembly is performed with extra care, none of these effects are easily avoidable and we assume that a slight asymmetry in the cell distribution at the entrance is inherent to the experiment.

To verify the impact of an asymmetric flow inlet on the RBC distribution and cell free layer we used a straight channel with the same dimensions as before, but this time the PDMS hole was punched intentionally with a strong misalignment relative to the channel centreline (Figure 6.6b2). The RBC distribution was determined for the same ROIs previously investigated, for comparison (Figure 6.15b).
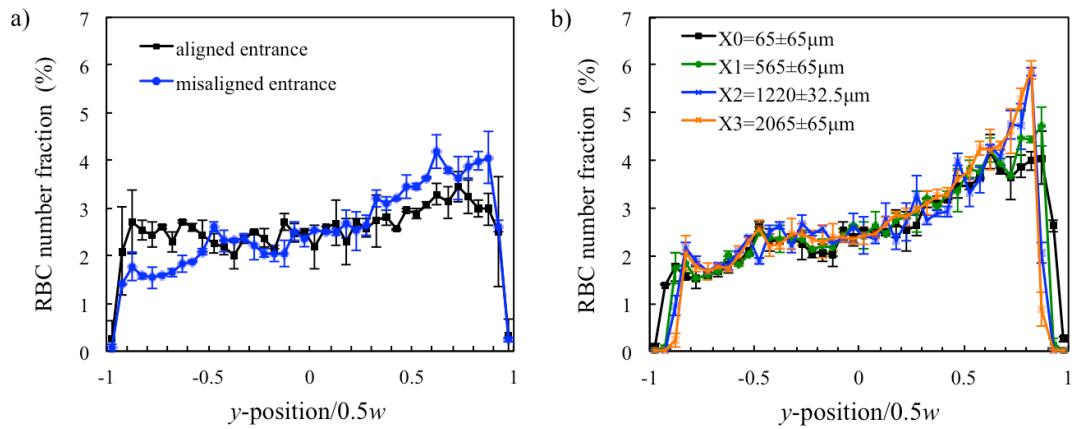
Figure 6.15: (a) Comparison between the RBC distribution obtained with aligned (black line) and misaligned (blue line) inlet at the channel entrance at ROI $X_0 = 65 \pm 65\mu m$; (b) RBC distribution profile for various positions along the length of the straight channel when sample inflow is misaligned with the channel centreline at different ROIs; $Q = 0.2\ \mu L/min$.

The RBC distribution obtained at the channel entrance, for the misaligned case (Figure 6.15a, blue curve), is significantly biased towards the right hand-side of the channel (positive y-values), which is in accordance with the position of the hole punched on the PDMS for sample inflow (Figure 6.6b2). Even though it is difficult to naturally produce such a strong misalignment during fabrication, here we show that the geometrical configuration for sample inflow strongly affects the RBC distribution at the entrance of the channel.

Similarly to what was observed for the case of a symmetric sample inflow, the strongest variation on RBC distribution is found for the two first ROIs analysed (at $X_0 \sim 65\mu m$ and $X_1 \sim 565\mu m$). In this case, since there is a cell accumulation on the right side of the distribution curve, already at the channel entrance, the corresponding density peak becomes more prominent along the channel length, while a minor peak is developed on the left side of the channel. The blue line ($X_2 \sim 1220\mu m$) and orange line ($X_3 \sim 2065\mu m$) are almost the superposition of each other so we expect these profiles to be close to the equilibrium distribution, although a longer channel would be required to confirm this.

It is interesting to notice that the total CFL measured presents similar values for both aligned and misaligned sample entrance (see Figure 6.13c) meaning that the initial cell distribution has negligible impact on the development of the CFL along the channel length.

These results reinforce the idea that for dilute suspensions under conditions of negligible inertia even for very large channel lengths, the RBC distribution is strongly dependent on the initial distribution. If there is any bias at the channel entrance, this will have an impact along the channel length and possibly interfere with the hematocrit distribution when there is a

geometrical feature downstream the channel, such as a bifurcation. For this case, the final cell concentration in a certain region of the channel is not only the combination of the channel topology and the Fåhræus effect, but also the inlet configuration and consequently the initial cell distribution.

6.4 Discussion

6.4.1 Influence of kinematics in microfluidic channel

Knowing that the hydrodynamic lift is a combined effect of wall repulsion and velocity gradient (shear rate),[25] the theoretical fully developed velocity and shear rate profiles that would be achieved for Newtonian fluid flow were calculated at different (y,z) positions inside the channels, to help understand the cell migration phenomena. Figure 6.16 presents the normalised velocity and shear rate profiles on the widthwise and depthwise directions of the channel to help understand the flow field (please note that the channel exhibits rectangular cross-section of aspect ratio AR = 2.8 and therefore the 3D profiles need to be considered). The velocity and shear rate profiles were calculated using equations 2.6, and equation 2.7, respectively, taking into account the real dimensions of the channel. The velocity is normalised using the average velocity $\bar{u}_0$ in the channel, and the shear rate is normalised using the maximum shear rate $\dot{\gamma}_{max}$.

As a consequence of the rectangular cross-section, the velocity profiles are quite distinct in both directions of the channel: while a blunt profile is found widthwise ($z = 0\mu m$), a parabola describes the velocity profile depthwise ($y = 0\mu m$) as shown in parts a1 and b1 of Figure 6.16. Also, when moving away from these reference planes, towards the wall, the shear rate profiles are significantly different in both directions (Figure 6.16a2 and b2). On the depthwise, it increases almost linearly from the channel centre towards the walls while, on the widthwise direction, the shear rate remains constant in the central region of the channel, presenting a small decrease for regions closer to the walls and, finally, an increase at the wall. On the widthwise direction, the shear rate value found at the centre of the channel changes significantly when moving away from the $y = 0\mu m$ plane.

Taking into account that the shear rate profile is responsible for the cell migration across the streamlines, it is expected that the asymmetric flow kinematics on the widthwise and depthwise directions will cause a distinct lift on the individual cells and will, therefore, have an impact on the overall flow of the cell suspension.

6.4.2 Hydrodynamic lift for vesicles/ cells in shear flows

Knowing that for the viscosity ratio $\Lambda{\sim}1$ no tumbling motion occurs, independently of the cell deflation,[26] the presence of the wall as well as the curvature of the flow will interfere with the cell shape and orientation. For example, when the cell is inserted in the channel, it is highly deformed and the wall lift force causes the cell to move away from the wall, as observed by the increased slope of the fitting curve in Figure 6.13c, between positions $X_0 \sim 65 \pm 65\mu m$ and $X_1 \sim 565 \pm 65\mu m$. While moving away from the wall, the curvature of the velocity will affect the shape of the cell, where the latter becomes more symmetric and also less prone to the effect of lift velocity.

To understand the importance of the wall lift effect, we first considered Olla's theoretical derivation, presented in reference Olla 1997.[27] According to this reference, the lift velocity u_{lift} refers to a tank-treading ellipsoid travelling in bounded Stokes flow, ideally at a certain distance from the wall l, such as $u_{\text{lift}} \sim \dot{\gamma}/l^2$, where l is the distance between the cell and the wall. However, other recent studies suggest that the gradient of the shear rate verified, for example, in our experimental channel may lead to a complex particle motion and that the flow curvature could modify the lift scaling law proposed before. In fact, Coupier *et al.*[26] tested the non-inertial lift in vesicles transported in bounded 2D Poiseuille flow and revealed that the scaling law proposed by Olla could not fit the experimental data. Instead, a new scaling law was proposed, which provided a much better fit:

$$u_{lift} \sim \frac{\dot{\gamma}}{l} \tag{6.5}$$

Note that this scaling law is valid for individualised vesicles or cells, which is the case in our experiments since the hematocrit is rather low Hct = 1%. Finally, since this scaling law is valid for a certain distance away from the wall l, the values obtained are normalised using a reference position. In this case, the reference position was set to be one diameter away from the lateral walls ($y = \pm 0.87$) and one radius away from the bottom and top walls ($z = \pm 0.82$).

Figures 6.16a3 and b3 present the normalised lift velocity $u_{lift}{}^{*}$ in both directions. It is interesting to notice that, despite the considerably different shear rate profiles presented on the widthwise and depthwise, the $u_{lift}{}^{*}$ profile is similar in both directions. In both cases, the maximum velocity is achieved at positions close to the channel walls and once the cells move away from these reference positions, a sharp decrease in $u_{lift}{}^{*}$ is observed. This means that the cells migrate faster at the entrance of the channel, due to a higher proximity to the wall and once they assume a minimum distance away from it, the migration towards the

centreline is slowed down. It is important to mention that in experiments, only the CFLs on the left and right channel walls can be followed. The type of setup used does not allow to infer about the migration away from the upper and bottom walls, which is expected to be more significant since the shear rate gradient close to the centreplane (depthwise) is steeper than the one verified in the surroundings of the centreline (widthwise).
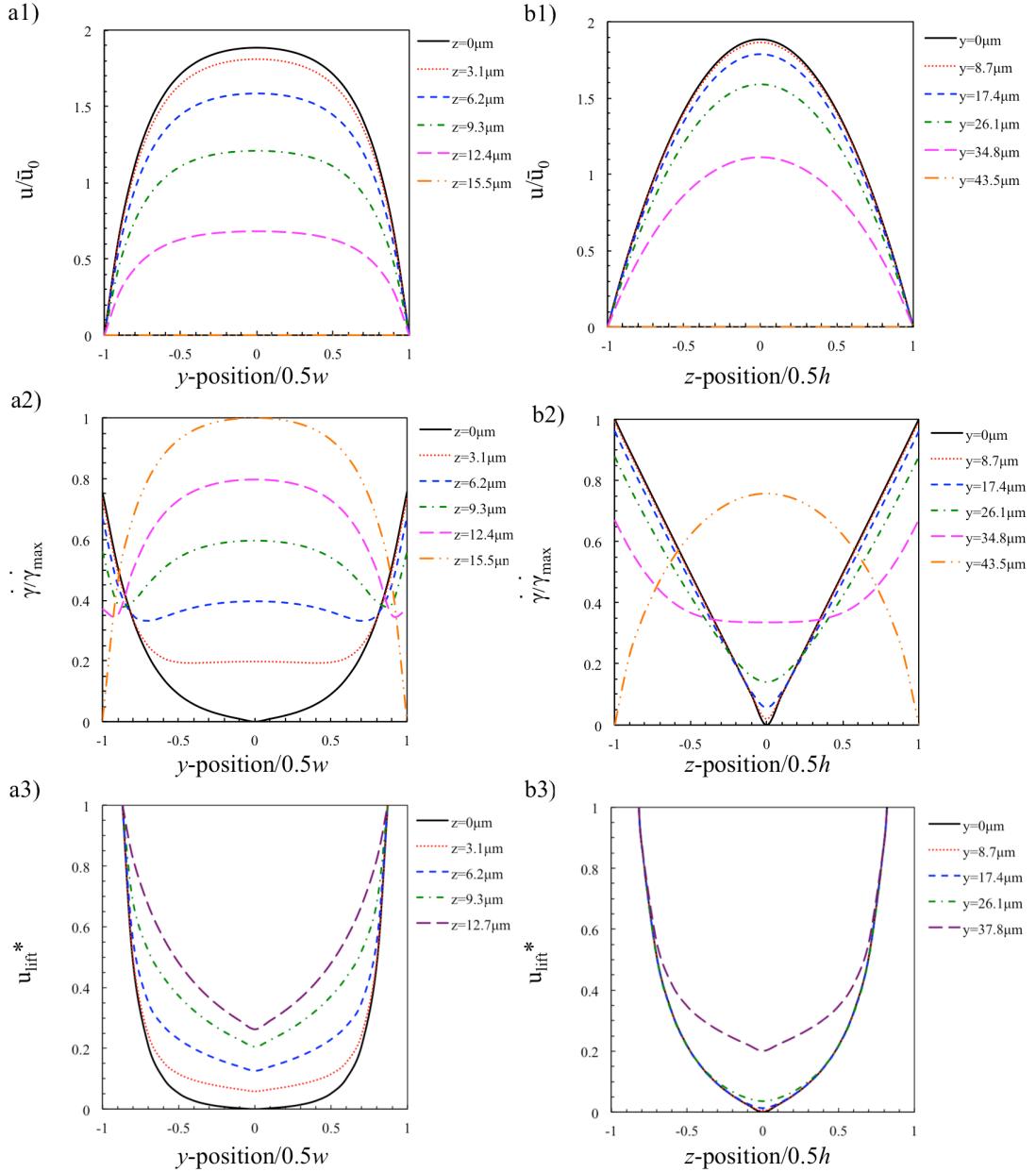
Figure 6.16: Fully developed flow kinematics inside the straight channel. Comparison between the normalised velocity profiles, along the channel width (a1) and depth (b1), for different channel positions. (The local velocity u is normalised using the average velocity in the channel $\bar{u}_0$). Corresponding normalised shear rate profiles along the channel width (a2) and depth (b2), at different channel positions. (The local shear rate $\dot{\gamma}$ was normalised using the maximum shear rate $\dot{\gamma}_{max}$ found for widthwise and depthwise). Normalised lift velocity $u_{lift}{}^*$ along the channel width (a3) and depth (b3) (assuming the viscosity ratio and cell shape are constant).

In summary, even though the RBC distribution curves resemble the ones presented by Park *et al.*[28] for experiments where inertia is significant, or the RBC equilibrium positions proposed by Segré-Silberberg[29] (see Figure 6.17), for our case study, no evidence of the outward migration was found and the inertia can be neglected since the Reynolds number in the channel and particle are very low, $Re_c = 1.2 \times 10^{-2}$ and $Re_p = 2.0 \times 10^{-4}$, respectively. In this case, the two peaks presented on the cell distribution are a combined effect of the hydrodynamic lift and the lack of cell-cell interaction in dilute suspensions. The experiments show that, even for a simple geometry as a straight channel, and making sure that the sample entrance is perfectly aligned with the channel centreline, the RBC distribution will evolve into a curve with two prominent density peaks.
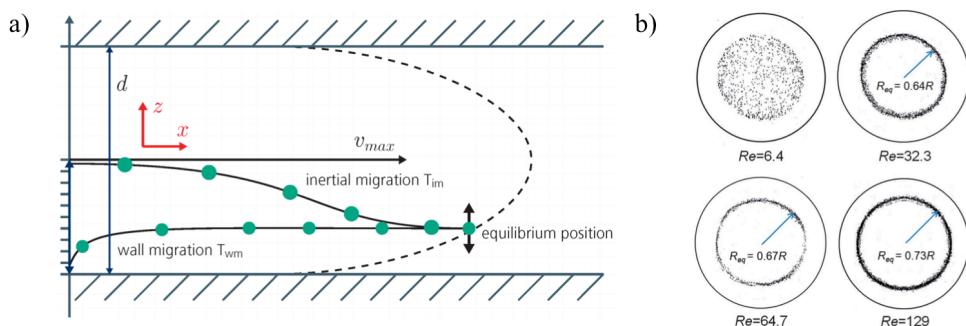
Figure 6.17: Segré-Silberberg effect. (a) scheme of a particle focusing inside a microfluidic channel due to the combined effects of wall repulsion and inertial migration (adapted from Schott *et al.*[30]); (b) development of the Segré-Silberberg effect in a straight tube, as a function of the Reynolds number. The image presents the tube cross-section (350mm diameter) where suspended particles (15mm diameter) are transported in a Newtonian fluid and focused at specific channel radial distances (adapted from Seo *et al.*[31]).

6.5 Numerical simulations

Numerical simulations were performed by collaborators at University of Edinburgh in order to elucidate the physics causing the peculiar RBC distribution profiles previously described, as well as to understand the cell dynamics along the channel depth, which is currently impossible to achieve by experiments due to setup limitations.

The 3D model employed consists of an immersed boundary-lattice Boltzmann method,[32] considering the blood flow as a suspension of deformable objects. Very briefly, the fluid flow is governed by Navier-Stokes equations while the RBCs are modeled as Lagrangian membranes using a finite element approach. The fluid flow and the RBC dynamics are coupled using the immersed boundary method.[33] The numerical model used, HemeRBC, is

based on the highly parallel open-source blood flow simulator, HemeLB,[34] and is suitable for the simulation of computationally expensive cellular flows in simple or complex geometries. Figure 6.18 presents a scheme of the microfluidic geometry considered for the numerical simulations. It consists of a straight channel with dimensions 96 x 30 x 1300µm for the width, depth and length, respectively. Two geometries were considered, differing on the size of the flow inlet (d_{hole} = 96µm or d_{hole} = 180µm) located at the entrance and outlet of the channel, for cell inflow and outlet, respectively. With the numerical simulations, we were able to test the effect of inflow contraction parameter $\alpha = d_{hole} / w$, on the RBC distribution at the channel entrance and also at different positions along the channel length.
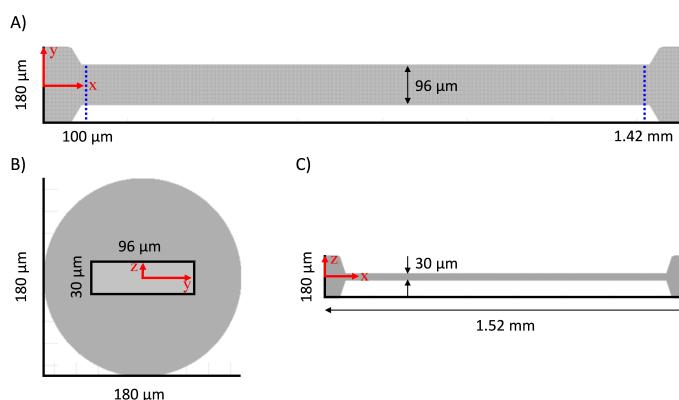
Figure 6.18: Schematic representation of the straight channel used for numerical simulations, including the flow extension for sample inlet and outlet.

Similarly to the experimental analysis, several ROI were defined along the channel, each one with 80µm length. Since there are no optical restrictions when performing numerical simulations, the RBCs distributions were determined for the widthwise and depthwise directions of the two geometries, corresponding to 4 inflow contractions α = 1, 1.875, 3.2 and 6.0.

Figure 6.19 presents the RBC distribution along the channel length for all the inflow contractions considered. The four density histograms are quite distinct at the entrance of the channel. On the widthwise, a normal distribution is found only for the case when the flow extension and channel diameters are the same size (d_{hole} = 96µm, α = 1.0). In this case, the CFL is already formed at the entrance of the channel. For an entrance region with diameter larger than the channel diameter (d_{hole} = 180µm, α = 1.875), a blunt profile, similar to the one found in experiments, is observed at the entrance of the channel (x-position = 50µm). At this length position, the cells occupy the entire channel width and migrate towards the channel

centre while flowing away from the entrance. For the last ROI analysed (x-position = 950μm), there is still a small concentration of cells close to the walls, meaning that the migration due to wall repulsion is not complete.

It is important to mention that, independently of the flow extension impact on the initial distribution, the two-peak density is developed along the channel length, for both cases α = 1.0 and α = 1.875. While for α = 1.0, the peaks are located at the normalised width position 0.25 - 0.5, for inflow contraction α = 1.875, these are shifted towards positions 0.75 - 0.8, similar to the equilibrium positions found in experiments.

The density histograms corresponding to the depthwise direction (Figures 6.19c and 6.19d for inflow contractions of α = 3.2 and α = 6.0, respectively) present different profiles when compared to those in Figures 6.19 a and b. In the depthwise direction, the CFL is present at the entrance of the channel (x-position = 50μm) for both cases (α = 3.2 and α = 6.0) and the peaks are more prominent in the last ROI analysed (x-position = 950μm), at equilibrium positions much closer to the channel centreline ($y/0.5w$~0.25-0.5).
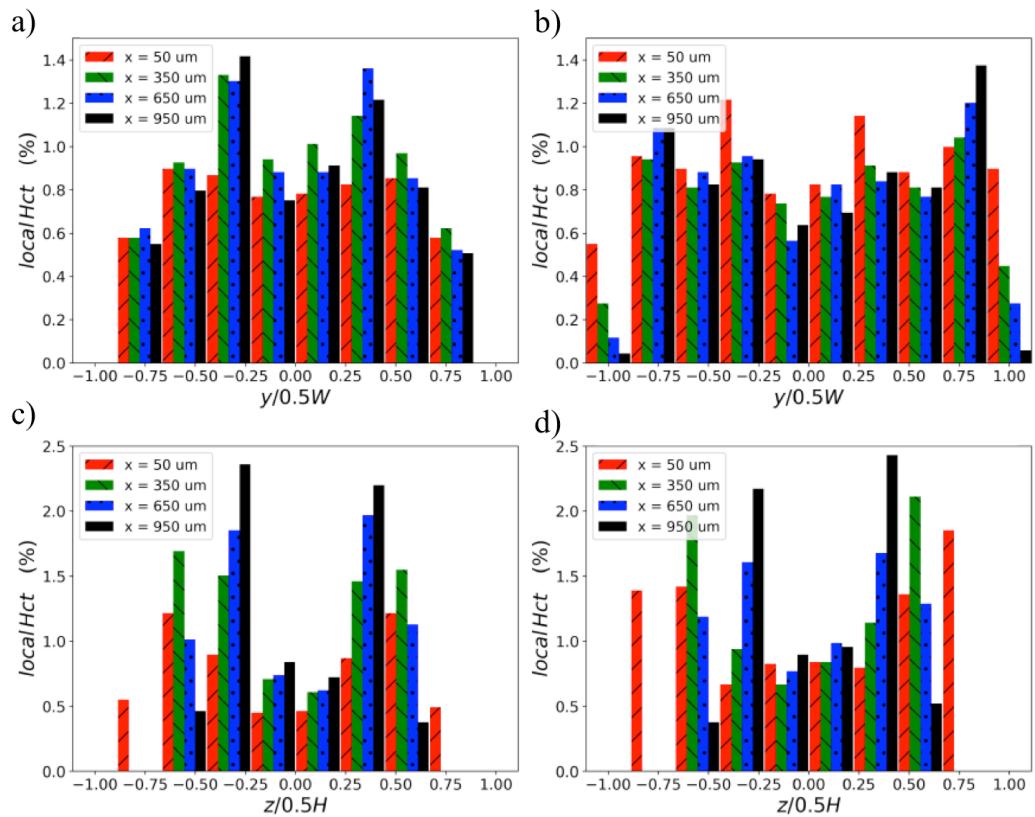
Figure 6.19: Evolution of the density histogram alongside the channel subject to an upstream inflow contraction of (a) α = 1.0; (b) α = 1.875 (along widthwise direction); (c) α = 3.2; (d) α = 6.0 (along depthwise direction). The four colours red, green, blue and black indicate different ROI (x-position 50μm, 350μm, 650μm and 950 μm away from the entrance, respectively).

Figure 6.20a presents the CFL developed close to the 4 walls of geometry with the d_{hole} = 180μm entrance region. It is important to notice that only the CFL close to the bottom and top walls seems to reach a stable plateau for the channel length analysed, while the CFL near the lateral walls seems to be still under development for the same position (*x*-position = 1300μm). This information is in qualitative agreement with the CFL profile measured experimentally (Figure 6.13c) and the lift velocity theoretically predicted (Figure 6.16a3 and b3). Figure 6.20b presents the log-log plot of the normalised cell-free layer $\delta_{CFL}/\delta_{max}$ as a function of the normalised distance *x*-position/D_h. A power-law dependence with exponent 1/3 is found, in agreement with data presented by Katanov et al.[24] for numerical simulations, where the viscosities of inner and outer fluids are the same. While their results lie slightly below the exponent 1/3, our numerical results actually fit this power-law, fact that could be explained by the smaller hematocrit used here Hct = 1% in comparison with the larger hematocrits used in their study (Hct = 15-45%), where cell-cell interaction was important. Even though these authors state that the CFL should be steady for a channel length of ~25*D*, in our experiments and numerical simulations, the CFL was not fully developed after a distance of 46D_h and 28D_h, respectively.

The CFL development is also in agreement with the cell migration velocity measured from individual cell trajectories (from numerical simulations) presented in Figures 6.20c and d. The migration towards the channel centre occurs faster on the depthwise direction, meaning that a constant CFL is quickly reached. On the other hand, even after a channel length of 1300μm, the CFL is not fully developed on the widthwise direction.

The data obtained from numerical simulations confirms that the entrance region configuration has a significant impact on the RBC distribution at the entrance of the channel. However, despite the initial conditions used, a final two-peak density is developed along the channel length, also verified in experiments, and the equilibrium positions are dependent on the channel cross-section.

Taking into account that this density profile might interfere with experimental results, using dilute suspensions of deformable objects, a few suggestions can be proposed to mitigate this problem: the first consists in applying a micro pillar array described by Kaminaga et al.,[35] right before the main channel entrance, in order to homogenize the cell distribution. This method is only valid for specific conditions, for example, suspensions of deformable objects with uniform sizes. The micro pillar works as a sieve, where the deformable objects are trapped between the pillars and then homogeneously released into the channel due to an increase in pressure. If the objects are rigid, they will clog the array, turning the experiment

ineffective. It means this method could never be used for experiments where the microfluidic device intends to detect, study or separate rigid RBCs from deformable healthy red blood cells. Also, even though it would avoid the immediate entrance effect on the distribution, we expect the final two-peak density would still develop at longer distances from the channel entrance, since this is a result of hydrodynamic effects inside the channel. Another idea would be to approximate the dimensions of the flow inlet and the ones of the microfluidic channel. For the typical setup used in microfluidics, this would translate in using tubing with internal diameter closer to the hydraulic diameter of the channel. Since the channel dimensions are on the order of micrometers, it is obvious that tubing with such dimensions would generate the Fåhræus effect prior to the cells entering the channel. In any case, the cell distribution downstream the microfluidic geometry would still develop into a two-peak curve. Another reason not to adopt this method is the fact that for each channel dimension, different tubing would be used. This option is not practically viable. Finally, since the entrance effect is difficult to avoid experimentally, this should be taken into account when performing numerical simulations. Only then we could consider the RBC distribution obtained through numerical simulations, as a realistic one.
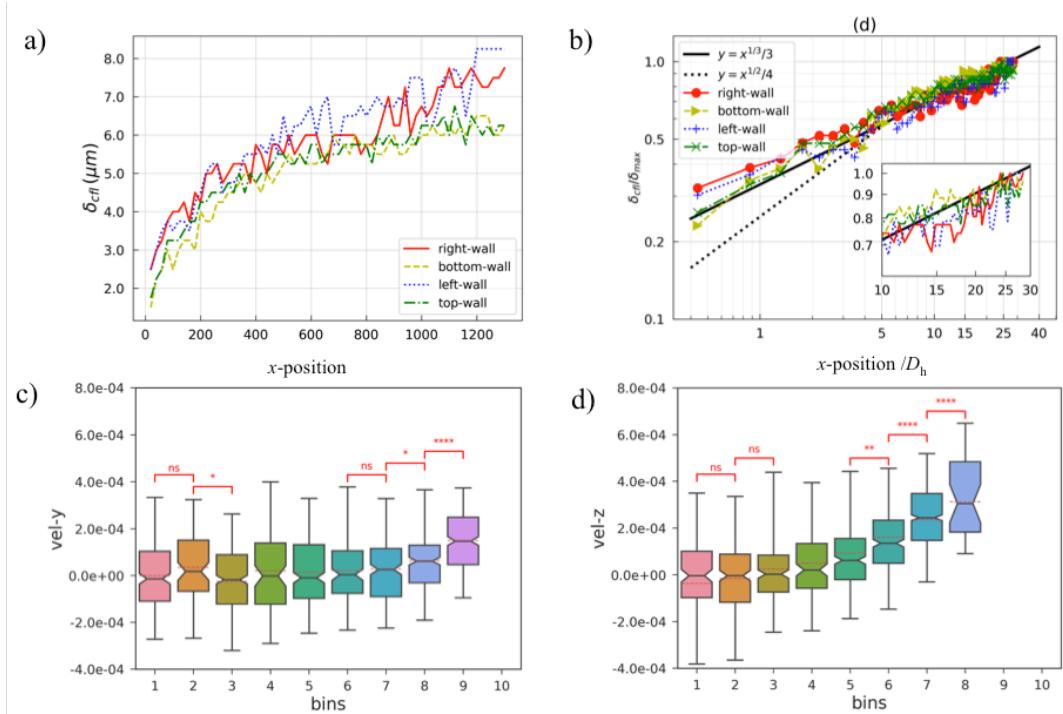
Figure 6.20: Cell free layer and hydrodynamic lift achieved by numerical simulations. (a) CFL developed close to the 4 walls of geometry with flow extension $d_{hole} = 180\mu m$; (b) log-log plot of the normalised CFL as a function of normalised distance x-position $/D_h$; (c) cell migration velocity on the widthwise and (d) cell migration velocity on the depthwise. The first bin corresponds to the centre of the channel while the 10th bin corresponds to the region close to the wall. A positive velocity corresponds to cell inwards migration and negative velocity corresponds to cell outwards migration.

6.6 Summary

The experimental and numerical data presented in this chapter, for dilute blood suspensions, demonstrate the emergence of an off-centre two-peak distribution of RBCs in the channel reminiscent of the "tubular pinch effect" described by Segré-Silberberg,[29] for flows where inertia plays an important role. However, for the flow conditions considered here, inertial effects are negligible (Stokes flow) and, therefore, the cell distribution is explained by the non-inertial hydrodynamic lift of deformable objects, causing the migration inwards.[36] The absence of cell-cell interaction in such dilute regime prevents the shear induced cell diffusion towards the channel walls, which explains why the two peaks found in the distribution profiles are not smoothed along the channel length. Since the entrance effects considered in experiments and numerical simulations are not exactly the same (for example, the geometry extension for sample inflow), a direct quantitative comparison is still not possible. However, the numerical simulations here performed demonstrate good ability to describe qualitatively the real cell dynamics observed in experiments.

Both experiments and simulations confirm the importance of the sample inflow configuration on the initial RBC distribution. For suspensions of large and deformable objects, as the RBCs traveling in bounded Stokes flow, the variability of initial distribution profile brings extra complexity to the reestablishment of a converged distribution profile and the development of an equilibrium cell free layer. The presence of the two-peak density profiles are shown to be independent of the flow rate (under conditions of low Reynolds number) and related to the cell equilibrium distribution, this is, a position in the channel where the lift velocity becomes negligible.

The results presented in this chapter reveal the importance of local and transient characteristics in the cell distribution when planning experiments with dilute suspensions in microfluidics. It is thus crucial to take into account the initial flow conditions and the impact of the shortage of hydrodynamic interactions between cells when making assumptions on cell dynamics using dilute suspensions.

References

1.   Shen, Z. *et al.* Inversion of hematocrit partition at microfluidic bifurcations. *Microvasc. Res.* **105,** 40–46 (2016).

2.   Chien, S. *et al.* Blood viscosity: influence of erythrocyte aggregation. *Science (80-.).* **157,** 829–31 (1967).

3.   Chien S, King, R., Skalak, R., Usami, S. & Copley, A. Viscoelastic properties of human blood and red cell suspensions. *Biorheology* **12,** 341–6 (1975).

4.   Vlahovska, P. M., Barthes-Biesel, D. & Misbah, C. Flow dynamics of red blood cells and their biomimetic counterparts. *Comptes Rendus Phys.* **14,** 451–458 (2013).

5.   Lanotte, L. *et al.* Red cells' dynamic morphologies govern blood shear thinning under microcirculatory flow conditions. *Proc. Natl. Acad. Sci.* **113,** E8207–E8207 (2016).

6.   Abkarian, M. & Viallat, A. Vesicles and red blood cells in shear flow. *Soft Matter* 653–657 (2008).

7.   Tomaiuolo, G. Biomechanical properties of red blood cells in health and disease towards microfluidics. *Biomicrofluidics* **8,** 1–19 (2014).

8.   Sebastian, B. & Dittrich, P. S. Microfluidics to Mimic Blood Flow in Health and Disease. *Annu. Rev. Fluid Mech.* 483–504 (2018).

9.   Geislinger, T. M. & Franke, T. Hydrodynamic lift of vesicles and red blood cells in flow — from Fåhræus & Lindqvist to microfluidic cell sorting. *Adv. Colloid Interface Sci.* **208,** 161–176 (2014).

10.   Secomb, T. W. Blood Flow in the Microcirculation. *Annu. Rev. Fluid Mech.* **49,** 443–461 (2017).

11.   Gompper, G. & Fedosov, D. A. Modeling microcirculatory blood flow: Current state and future perspectives. *Wiley Interdiscip. Rev. Syst. Biol. Med.* **8,** 157–168 (2016).

12.   Calejo, J., Pinho, D., Galindo-Rosales, F. J., Lima, R. & Campo-Deaño, L. Particulate blood analogues reproducing the erythrocytes cell-free layer in a microfluidic device containing a hyperbolic contraction. *Micromachines* **7,** 1–12 (2016).

13.   Yang, S., Ündar, A. & Zahn, J. D. A microfluidic device for continuous, real time blood plasma separation. *Lab Chip* **6,** 871–880 (2006).

14.   Prabhakar, A., Kumar, Y. V. B. V., Tripathi, S. & Agrawal, A. A novel, compact and efficient microchannel arrangement with multiple hydrodynamic effects for blood plasma separation. *Microfluid. Nanofluidics* **18,** 995–1006 (2015).

15.   Adili, N., Melizi, M. & Belabbas, H. Species determination using the red blood cells

morphometry in domestic animals. *Vet. World* **9,** 960–963 (2016).

16. Windberger, U., Bartholovitsch, A., Plasenzetti, R., Korak, K. J. & Heinze, G. Whole blood viscosity, plasma viscosity and erythrocyte aggregation in nine mammalian species: Reference values and comparison of data. *Exp. Physiol.* **88,** 431–440 (2003).

17. Baskurt, O. O. K., Farley, R. A. & Meiselman, H. J. Erythrocyte aggregation tendency and cellular properties in horse, human, and rat: a comparative study. *Am. J. ...* **273,** H2604–H2612 (1997).

18. Flormann, D., Schirra, K., Podgorski, T. & Wagner, C. On the rheology of red blood cell suspensions with different amounts of dextran: separating the effect of aggregation and increase in viscosity of the suspending phase. *Rheol. Acta* **55,** 477–483 (2016).

19. Sousa, P. C., Pinho, F. T., Alves, M. A. & Oliveira, M. S. N. A review of hemorheology: Measuring techniques and recent advances. *Korea Aust. Rheol. J.* **28,** 1–22 (2016).

20. Fedosov, D. A., Noguchi, H. & Gompper, G. Multiscale modeling of blood flow: from single cells to blood rheology. *Biomech. Model. Mechanobiol.* **13,** 239–258 (2014).

21. Krüger, T. Effect of tube diameter and capillary number on platelet margination and near-wall dynamics. *Rheol. Acta* **55,** 511–526 (2016).

22. Namgung, B., Ong, P. K. & Kim, S. Effect of low molecular weight dextrans on erythrocyte aggregation. *Macromol. Res.* **21,** 1042–1044 (2013).

23. Fedosov, D. A., Caswell, B., Popel, A. S. & Karniadakis, G. E. M. Blood Flow and Cell-Free Layer in Microvessels. *Microcirculation* **17,** 615–628 (2010).

24. D., K., G., G. & D.A., F. Microvascular blood flow resistance: Role of red blood cell migration and dispersion. *Microvasc. Res.* **99,** 57–66 (2015).

25. Hariprasad, D. S. & Secomb, T. W. Prediction of non-inertial focusing of red blood cells in Poiseuille flow. *Phys. Rev. E - Stat. Nonlinear, Soft Matter Phys.* **92,** (2015).

26. Coupier, G., Kaoui, B., Podgorski, T. & Misbah, C. Noninertial lateral migration of vesicles in bounded Poiseuille flow. *Phys. Fluids* **20,** (2008).

27. Olla, P. The lift on a tank-treading ellipsoidal cell in a bounded shear flow. 1–10 (1996). doi:10.1051/jp2:1997201

28. Park, J., Song, S. & Jung, H. Continuous focusing of microparticles using inertial lift force and vorticity via multi-orifice microfluidic channels. 939–948 (2009). doi:10.1039/b813952k

29. Segré, G. & Silberberg, A. Radial Particle Displacements in Poiseuille Flow of Suspensions. *Nature* **189,** 209–210 (1961).

30. Schott, L. *et al.* Cell size discrimination based on the measurement of the equilibrium velocity in rectangular microchannels. *Micromachines* **6,** 634–647 (2015).

31. Seo, K. W., Byeon, H. J., Huh, H. K. & Lee, S. J. Particle migration and single-line particle focusing in microscale pipe flow of viscoelastic fluids. *RSC Adv.* **4,** 3512–3520 (2014).

32. Krüger, T., Gross, M., Raabe, D. & Fathollah, V. Crossover from tumbling to tank-treading-like motion in dense simulated suspensions of red blood cells. *Soft Matter* **9,** 9008–9015 (2013).

33. Peskin, C. S. The immersed boundary method. *Acta Numer.* **11,** 479–517 (2002).

34. Bernabeu, M. O. *et al.* Computer simulations reveal complex distribution of haemodynamic forces in a mouse retina model of angiogenesis. *J. R. Soc. Interface* **11,** (2014).

35. Kaminaga, M., Ishida, T., Kadonosono, T., Kizaka-Kondoh, S. & Omata, T. Uniform cell distribution achieved by using cell deformation in a micropillar array. *Micromachines* **6,** 409–422 (2015).

36. Goldsmith, H. L. & Mason, S. G. Axial Migration of Particles in Poiseuille Flow. *Nature* **190,** 1095 (1961).

CHAPTER 7

Behaviour of RBC suspensions flowing in microfluidic devices of different configurations

The present chapter describes the preliminary results on the flow of RBC suspensions in microfluidic networks with different configurations. It was inspired by the experimental results obtained using RBC suspensions flowing in a microfluidic network, which are presented in the conference paper Fidalgo *et al.*[1] (available on Appendix E).

We investigate the influence of several parameters on the suspension flow, such as the sample hematocrit, the flow rate, the bifurcation angle in network devices similar to those used in Chapter 4, as well as other geometrical features such as sudden expansions and bends, for devices composed of networks with straight channels of different sizes, arranged in series. In some of the experiments, we address the ability to perform the separation of the suspending medium from the cells, since this is an important challenge in the context of applications of lab-on-chip devices for purposes of diagnostics. It is important to mention that this chapter compiles preliminary results and that further experiments and improved analysis would be required in order to achieve logical conclusions.

147

7.1 Introduction

Blood or red blood cell suspensions have been an iterant subject of study for the last decades, due to the interesting flow effects described in section 2.5. In particular, the red blood cell suspensions have received great attention due to the cell inherent deformability and also due to the fact that these are the main component in the blood sample (about 45-50% in volume). Microfluidics has been used not only to study the fundamental properties of such cell suspensions under flow using microvessels, mimicking the microcirculation structure, but also to assess the microdevice ability to separate the cells from the suspending medium for subsequent point-of-care analysis. A simple example on the use of microfluidics for diagnostics consists in separating a dilute suspension of red blood cells from a blood sample or concentrated RBC suspension, and submit those cells to extensional flow conditions, which are able to cause their deformation. The analysis of cell deformability allows, in a simple way, to distinguish between a healthy blood sample (with highly deformable RBCs) from a blood sample obtained from a diseased patient (since some diseases as malaria, diabetes mellitus or sickle cell anemia strongly affect the cell deformability, turning them stiffer and less prone to deformation).

In this chapter, we describe preliminary results when using microfluidic devices of different shapes. We mainly observe the cell free layer developed close to the channel walls and, in some cases, explore the geometries potential for cell dilution or separation of the suspending medium.

7.2 Materials and Methods

The experiments and methods reported in this chapter are obtained using procedures similar to those described in Chapter 6. In this section, we describe the procedure used to prepare suspensions of rigid RBCs, as well as the full description of the geometries used.

7.2.1 Sample Preparation

The RBC suspensions were prepared following the procedure described in Chapter 6. In this chapter we also present results using a suspension of rigid cells with low nominal hematocrit (Hct = 1%). The procedure used to prepare such suspension is provided below.

Usually, diamide or gluteraldehyde are used to rigidify the RBCs, even though their mechanism of action is different.[2] While diamide acts on the membrane proteins alone, the gluteraldehyde is a non-specific fixative acting on all the cell components, making the stiffening process more efficient.[2] For this reason, gluteraldehyde was used in this study and

the protocol used was adapted from the reference Rodrigues *et al.*[3] As such, a few additional steps had to be included in the standard procedure described in Figure 6.3 for preparing samples with more rigid RBCs. After sample centrifugation and RBC washing using PS solution, the cell pellet was brought into contact with a dilute solution of glutaraldehyde (25% in water, Sigma Aldrich). A small amount of 0.5μL was added to a cell volume of 400μL in the Eppendorf, achieving a glutaraldehyde concentration of ~0.125% (v/v). The suspension was gently stirred to allow the solution to be in contact with all the cells without compromising their viability. After 15 minutes of contact, the cells were washed with PS, following the procedure previously described in Chapter 6, and suspended in Dx40 solution to produce a low hematocrit suspension of rigid RBCs (Hct ≤ 1%).

7.2.2 Experimental setup and microfluidic devices

In similarity with the setup described in Chapter 6, the experiments were performed using an inverted microscope (Olympus IX71), an halogen lamp for sample illumination and a precise syringe pump (Nemesys, Cetoni) for fluid control. In this chapter we report experiments using microfluidic devices of different shapes where, in some cases, there are multiple sample outlets. For experiments using 4 outlets, the syringes were coupled two by two in each syringe pump module, as described in Chapter 4.

The microfluidic devices were produced using the photo- and soft-lithography methods described in Chapter 3. For this set of experiments, the candidate designed the geometries and produced the PDMS channels. The film photomask and SU8 mould were produced by an external company (microLiquid, Spain). Two sets of geometries were used for this study:

- *Geometries A* corresponding to bifurcating networks with different features (see detailed description in Figure 7.1) and

- *Geometries B* corresponding to channels in series with different features (where, in some cases, a perpendicular channel is opened for experiments on plasma/RBC removal, see detailed scheme in Figure 7.2).

Geometries A: The set of geometries A corresponds to bifurcating networks, designed using the biomimetic design rule presented in Chapter 4. The main difference between the current geometries and those used for studying DNA molecules in shear flow is the angle of the bifurcation, which in this case is 90° or 60°, instead of 180°. Also, the child branches on generations $i = 1$ and $i = 2$ have shorter lengths than before ($L = 10D_h$). Figure 7.1 presents the image of Geometry A1, which will be considered as the reference geometry. It consists

of a customised network with 3 generations of channels ($i = 0$, 1 and 2) and 4 outlets, with a bifurcation angle of 90°. A similar geometry was used (Geometry A2) in which the bifurcating angle is set to be 60° instead of 90°, keeping constant all the other geometrical parameters described for Geometry A1.
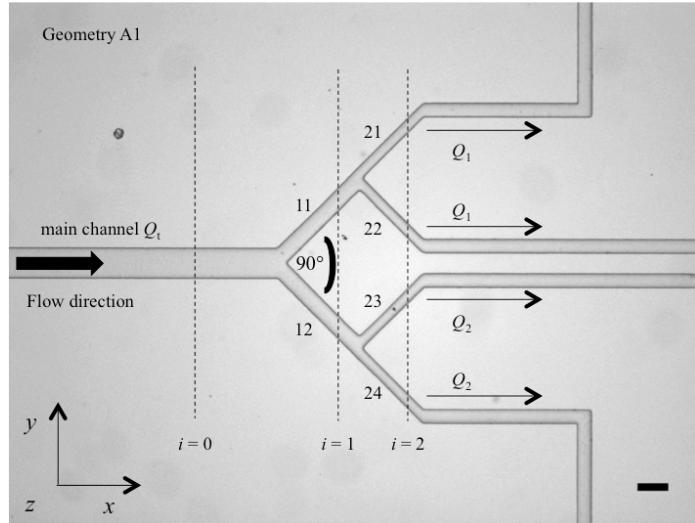
Figure 7.1: Microscope photography of the microfluidic geometry A1 with 4 outlets controlled by flow rates Q_1 and Q_2; bifurcation angle 90°; Scale bar 100μm.

Since several geometries were used for different experiments, Table 7.1 summarises the nominal dimensions of the bifurcating networks considered here. However, all the calculations for experimental data analysis considered the real channel dimensions.

Table 7.1: Nominal dimensions of the bifurcating network used for blood experiments (set of geometries A).

Dimension	Network generation (i)		
(μm)	0	1	2
Width, w	96.0	50.5	30.0
Depth, h		30.0	

Geometries B: This set of geometries was designed to study the effect of sudden increase in channel diameter and the existance of curvature between the channel segments on the CFL. For this purpose, we used three channel geometries, where a straight channel is considered as the reference. Figure 7.2 shows a scheme of Channels B1, B2 and B3, were the arrow defines the flow direction. Channel B1 is a straight channel with approximate length of

14 mm and will be considered as the reference geometry. Channel B2 is a sequence of aligned straight segments of increasing diameter connected by sudden expansions. Channel B3 is similar to Channel B2, with segments of increased diameter, but differing from the previous geometry due to the introduction of bends between channel segments.
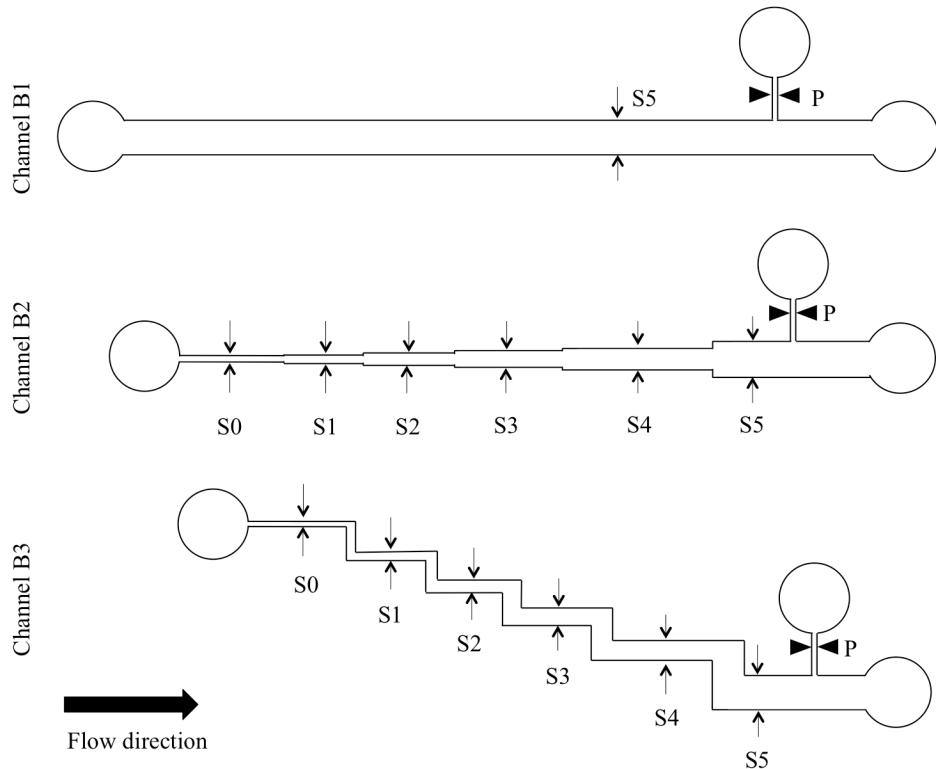
Figure 7.2: Schematic representation of the set of geometries B used for this study, where the suspension flows from the left to the right (not made to scale).

Table 7.2 summarises the real dimensions of Channels B1, B2 and B3 used in this study.

Table 7.2: Real dimensions of Channels B1, B2 and B3 used in this study.

Channel	Dimensions (μm)	Channel generation (i)						P
		S0	S1	S2	S3	S4	S5	
B1	Width, w	-	-	-	-	-	436	34
	Depth, h				30.6			
B2	w	34.7	50	75.3	119.5	217	439	33
	h				30.7			
B3	w	33	48	73	118	213	433	33
	h				29.9			

151

7.2.3 Data acquisition and image analysis

In similarity to the experiments described in Chapter 6, the videos were acquired by a CCD camera (Olympus, XM10) at 15Hz, using a minimum of 300 frames for each flow conditions tested. The preliminary analysis carried out consisted in monitoring the CFL developed close to the channel walls and quantifying its thickness for various ROI along the channel (see procedure in section 6.2.4.1), as well as the average intensity profile which is obtained by a direct function on ImageJ open software.

7.3 Results and Discussion

7.3.1 Part I: Network geometries

In this section, we present the preliminary results on the CFL development, using microfluidic geometries composed of networks with channels in parallel (set of Geometries A in Figure 7.1, Table 7.1).

7.3.1.1 Effect of suspension hematocrit

In the first experiment performed, using geometry A1 (network with four outlets and two controllable flow rates Q_1 and Q_2, where $Q_2/Q_1 = 1$), we verified the development of a cell free layer along the main channel walls (Figure 7.3a). The same CFL persists along the outer wall of the channels in the subsequent network generations, while in the inner walls, no cell free layer was detected, meaning that a longer channel length would be necessary to allow the full development of the CFL. When repeating the same experiment with a higher hematocrit (Hct = 10%), the CFL is barely noticeable (see Figure 7.3b). While for Hct = 1%, the cell migration is mainly a result of the channel wall repulsion and the shear-induced migration, driving the cells towards specific locations in the channel, as described in Chapter 6, for Hct = 10%, besides the contribution of these two effects, the cell-cell interactions also play an important role. The collisions and repulsive forces occurring between cells tend to make the suspension disperse across the entire channel width, reducing the CFL thickness.
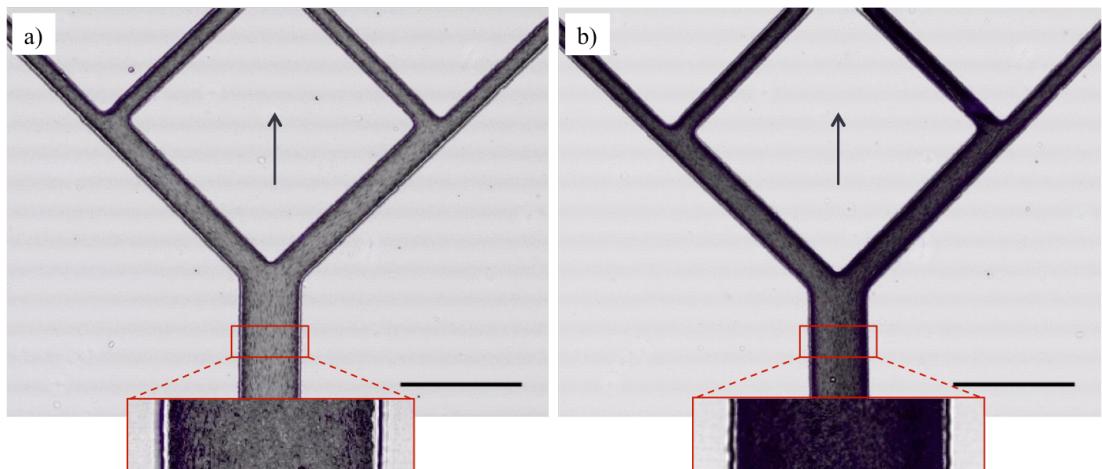
Figure 7.3: Effect of suspension hematocrit on the CFL developed close to the channel walls in the main channel (composed images combining 300 frames obtained using the Z-projection image); (a) Hct = 1% and (b) Hct = 10%; Geometry A1, Q = 4x0.2 µL/min; scale bar 200 µm.

7.3.1.2 Effect of flow rate

A set of experiments was performed to assess the effect of the flow rates applied at the end of the network. By keeping the flow rate Q_1 constant and increasing Q_2 (for different ranges of total flow rate), the cell free layer emerging on the channel 21 becomes more and more noticeable to the point where only a few cells are detected in this channel (see Figure 7.4a). Also, while keeping the total flow rate constant (by decreasing Q_1 and increasing Q_2), the overall CFL developed as a function of flow rate ratio presents a similar trend (Figure 7.4b). Figures 7.4c and d correspond to the intensity profiles inside the blue and red areas identified in in Figure 7.4a. While for the main channel, the CFL seems to be constant as a function of the increasing total flow rate, the intensity inside the channel 21 corroborates with the increase of the CFL as a function of the flow rate ratio.
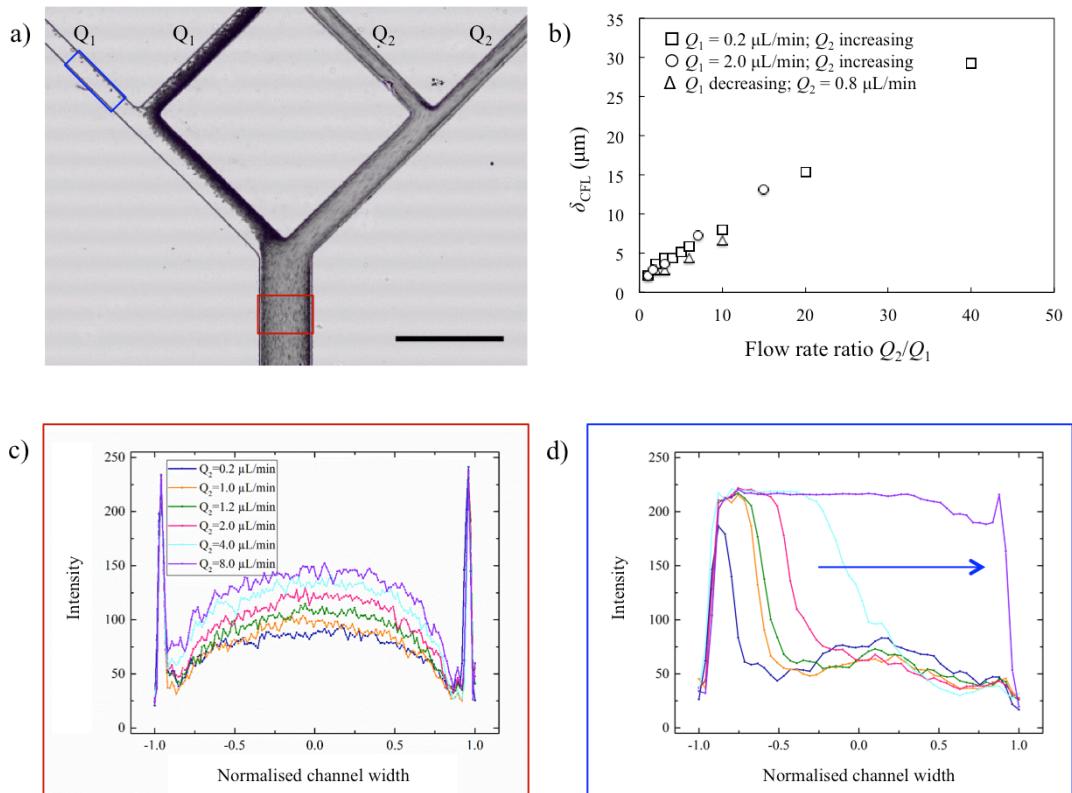
Figure 7.4: Effect of the flow rate variation at the end of the network, on the CFL developed along the channel 21. (a) Composed images combining 300 frames for each of the ROI obtained using the Z-projection image of geometry A1, for flow conditions Q_1 = 0.2µL/min and Q_2 = 8.0 µL/min (Q_2/ Q_1 = 40) scale bar 200 µm; (b) thickness of cell free layer δ_{CFL} measured in channel 21 as a function of the flow rate ratio Q_2/Q_1: (O) Q_1 = 2µL/min and Q_2 increasing; (□) Q_1 = 0.2µL/min and Q_2 increasing; (Δ) Q_1 decreasing and Q_{total} constant = 0.8µL/min; (c) intensity profile obtained for the main channel width (red square in Figure 7.4a) as a function of the flow rate Q_2, for constant Q_1 = 0.2µL/min; (d) intensity profile obtained for channel 21 width (blue square in Figure 7.4a) as a function of the flow rate Q_2, for constant Q_1 = 0.2 µL/min. Hct = 1%.

Another test concerned the effect of the bifurcation angle for the range of flow rates Q_1 = 0.2 µL/min and Q_2 = 0.2-8.0 µL/min in Geometry A2 (Figure 7.5). The results obtained for the two angles tested (60° and 90°) are very similar, yielding a practically cell depleted channel (21) for a flow rate ratio of 40.
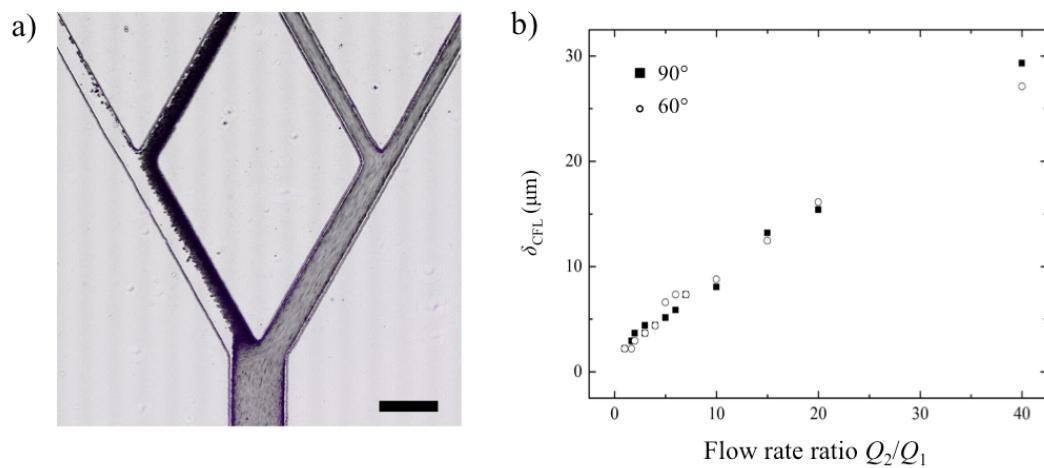
Figure 7.5: Effect of bifurcation angle on the CFL developed along the channel 21. (a) Composed images combining 300 frames using the Z-projection image of geometry A2, for flow conditions $Q_1 = 0.2\mu L/min$ and $Q_2 = 8.0$ $\mu L/min$ ($Q_2/Q_1 = 40$), scale bar 100 μm; (b) thickness of cell free layer measured in channel 21 as a function of the flow rate ratio Q_2/Q_1, for experiments using 90° (closed symbols) and 60° (open symbols) bifurcation angle; Hct = 1%.

7.3.2 Part II: Single channels of different topology

In this section, we investigate the effect of geometrical features such as the presence of sudden expansions (Geometry B2) and bends (Geometry B3) along the channel and compare it to the reference case of a straight channel (Geometry B1). In a first approach we determine the CFL developed in each of the geometries, using a small hematocrit. For the channel presenting the most significant CFL, additional experiments were conducted on the ability to separate the suspending medium from the cells, by opening a plasma channel perpendicular to the last channel segment.

7.3.2.1 Comparison of the CFL developed in different geometries

Figure 7.6 presents the total CFL measured in the reference straight channel (see characteristics of channel B1 in Table 7.2), in the regions close to the channel entrance and close to the channel outlet for flow rates ranging from 0.1μL/min to 30μL/min. Even though we do not expect a significant CFL to be found in this channel, since its diameter (~430-440 μm) is larger than the threshold diameter for which Fahraeus effect is expected to become noticeable (<300μm),[4] a CFL still develops along the channel length, as observed in Figure 7.6a and quantified in Figure 7.6b.
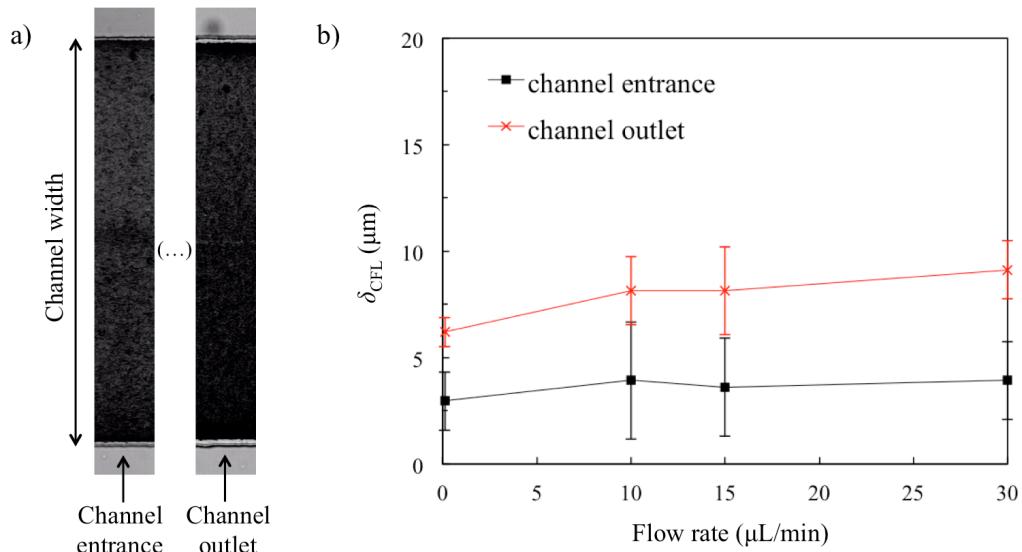
Figure 7.6: Comparison of the CFL developed at the channel entrance and outlet, on Channel B1 (straight channel). (a) Composed images combining 300 frames for each of the ROI obtained using the Z-projection image for $Q = 15\mu L/min$ and (b) thickness of CFL developed at the channel entrance and outlet at different flow rates. Hct = 1%.

The effect of the presence of successive sudden expansions along the channel was studied using geometry B2 (see Table 7.2 and Figure 7.2). The development of the CFL in the various regions of the channel are shown in Figure 7.7a1 and a2 for $Q = 0.1\mu L/min$ and Hct = 1% and 5%, respectively. It is clear that when imposing the same flow conditions, a distinct CFL is found for hematocrits Hct = 1% and Hct = 5%, as previously observed in Figure 7.3. Even though the thickness of the CFL increases continuously from the thinner (segment S0 near the inlet) to the larger channel segments (segment S5 near the outlet) for all the conditions tested, the relative CFL, measured here as the ratio between the local thickness of the CFL and the width of the corresponding section of the channel, exhibits a maximum for an intermediate segment (S3) where the CFL can occupy as much as 25% of the channel width for the cases tested. This phenomenon occurs for both values of hematocrit tested and at different flow rates (see Figure 7.7b2). We expect this to be related to the abrupt velocity decrease occurring due to the channel expansion.

The thickness of the CFL found in the case of the channel with expansion is much larger than the one obtained in the straight channel.[5,6]
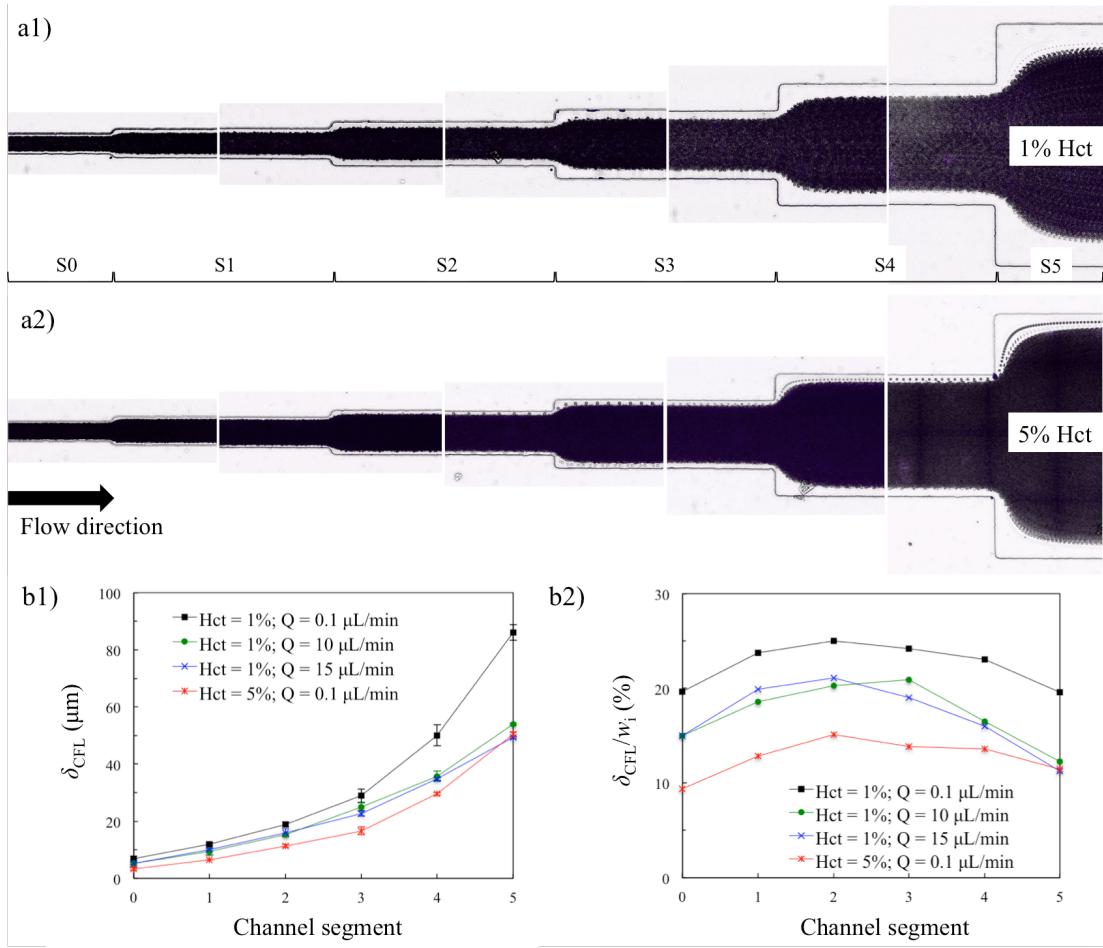
Figure 7.7: CFL development along Channel B2. (a) Composed images combining 300 frames for each of the ROI obtained using the Z-projection image using minimum intensity for 1% (a1) and 5% Hct (a2); $Q = 0.1\mu L/min$. (b1) Thickness of CFL and (b2) relative CFL δ_{CFL}/w_i along the segments of Channel B2.

We have also analysed the development of CFL in three sections (S0, S3 and S5) of Channel B3 (see Figure 7.8), which includes the presence of bends between channel segments in addition to increasing channel diameters. We found that the CFL formed at the entrance (S0) and middle (S3) positions in the channel, is nearly independent of the flow rates imposed, while for the position analysed close to the channel outlet (S5), the CFL tends to decrease with the flow rate. This was also observed for experiments in Channel B2.
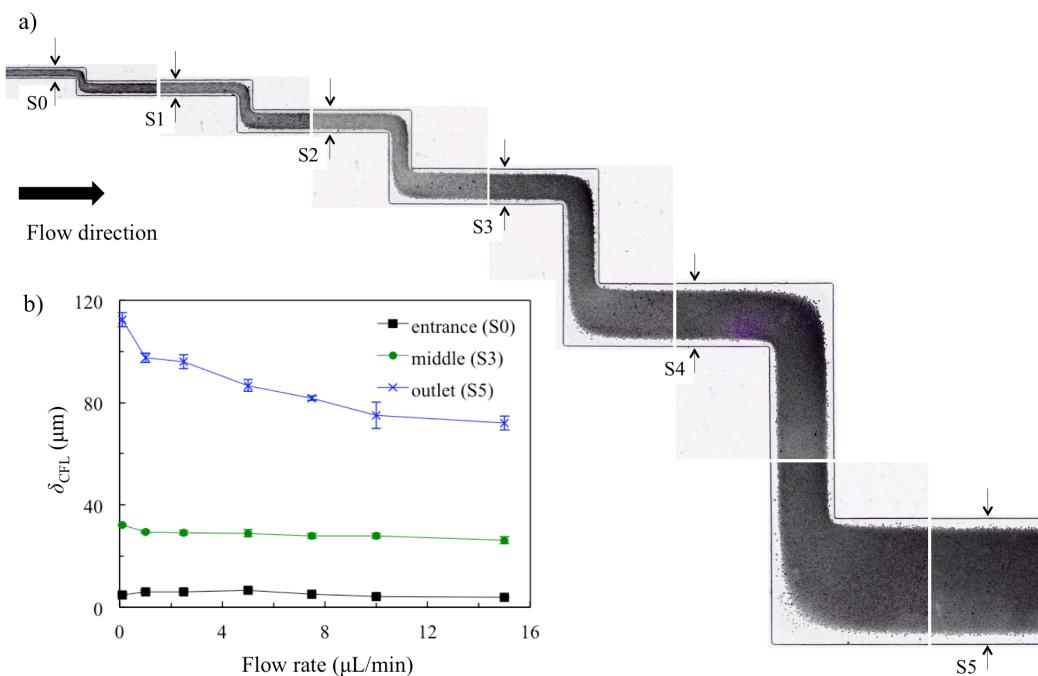
Figure 7.8: Cell-free layer development along the Channel 3. (a) Composed images combining 300 frames for each of the ROI obtained using the Z-projection image using minimum intensity for Hct = 1%; Q = 15µL/min; (b) CFL as a function of the flow rate in segments S0, S3 and S5 along the channel.

In Figure 7.9 we compare the thickness of the cell free layer close to the outlet for the three geometries tested. In this region, corresponding to segment S5 in Figure 7.7 and 7.8, all channels have similar widths and depths. There is a clear enhancement of the CFL developed in the case of geometries B2 and B3 as expected. For larger flow rates, Channel B3 corresponding to the channel of consecutive increased diameter and channel curvature, presented the largest cell free layer close to the walls. For this reason, we decided to use this geometry for testing the separation of RBCs from the suspending medium.
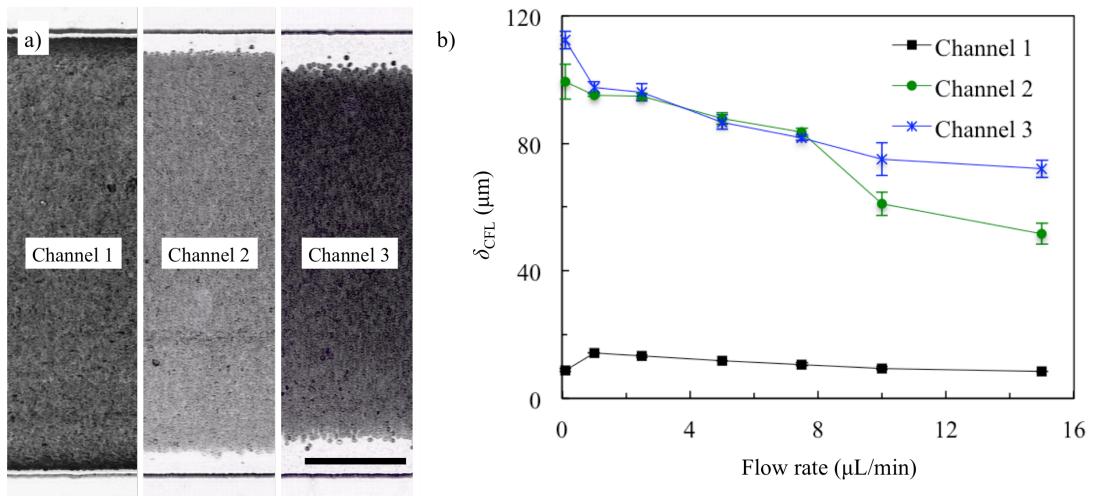
Figure 7.9: Comparison between the CFL developed in the last segment (S_5) of Channels B1, B2 and B3; (a) Composed images combining 300 frames for each of the ROI obtained using the Z-projection image of channel section (S5), $Q = 15\mu L/min$, scale bar 100μm; (b) thickness of the CFL measured as a function of flow rate Q; Hct = 1%.

7.3.2.2 Separation of the suspending medium from the RBCs

For the study on the separation of suspending medium (mimicking plasma) from the RBC suspension, a *plasma* channel (channel identified with a P in Figure 7.2) was opened perpendicularly to the original segment S5, where the CFL thickness was found to be more significant. In this case, instead of one outlet, two outlets were independently controlled using two syringe pump modules.

The plasma flow rate (Q_{plasma}) was kept constant while increasing the main flow rate (Q). The separation efficiency is qualitatively demonstrated in Figure 7.10 by comparing the amount of cells in the plasma channel (in individual images of the experiment as well as in combined images using Z-projection) for different conditions and quantitatively by the separation efficiency, which is defined here as the ratio of the number of cells entering the plasma channel and the total number of cells in the main channel:

$$\text{Separation efficiency} = 1 - \left(\frac{\text{number of cells in the plasma channel per volume}}{\text{number of cells in the main channel per volume}} \right) \qquad (7.1)$$

	Hct = 1%							Hct = 20%						
$Q + Q_{plasma}$	0.4	0.7	1.2	2.2	3.2	3.7	4.2	0.4	0.7	1.2	2.2	3.2	3.7	4.2
Q/Q_{plasma}	1	2.5	5	10	15	17.5	20	1	2.5	5	10	15	17.5	20
individual frame														
Z-projection														

Figure 7.10: RBCs transported in the plasma channel. Comparison between experiments using hematocrits 1% and 20%, for different flow rate ratios Q/Q_{plasma} (Q_{plasma} = 0.2µL/min). Arrow indicates the flow direction along the plasma channel.

For a small hematocrit (Hct = 1%), the concentration of cells in the plasma channel is small for the conditions tested and a complete separation is achieved for a flow rate ratio of 15 and above, as seen in Figure 7.10. Using a larger hematocrit (Hct = 20%), the amount of cells transported in the plasma channel is still significant (even for a larger flow rate ratio of 20).

Arguably, in order to separate the suspending medium efficiently, a larger total flow rate could be used. However, this alternative would require a larger volume of sample for each experiment, which might not be ideal for practical applications.

The same geometry B3 was also used for the purpose of separating the suspending medium from a suspension of rigid RBCs. Using the same range of flow rates previously tested, a larger amount of rigid cells was found in the plasma channel (Figure 7.11a) but no significant differences were found in the separation efficiency for healthy deformable RBCs and rigid RBCs.
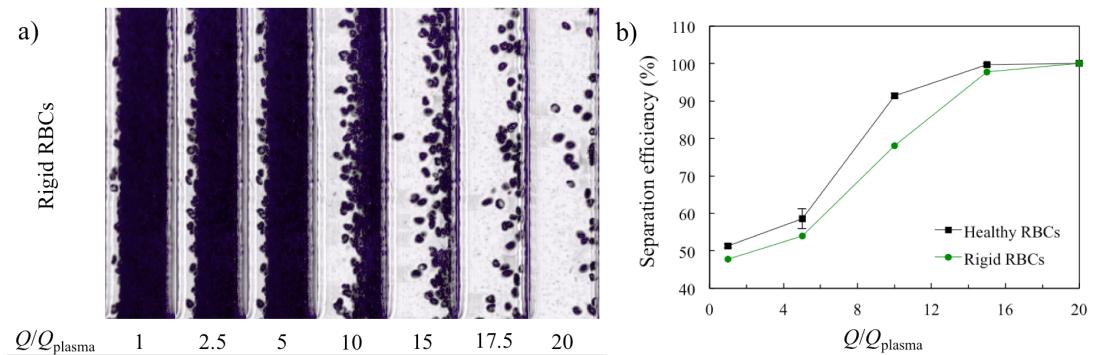
Figure 7.11: Separation of suspending medium using rigid RBCs. (a) Composed images combining 300 frames for each of the ROI obtained using the Z-projection image showing RBCs transported in the plasma channel as a function of the flow rate ratio Q/Q_{plasma}; (b) separation efficiency using healthy (black line) and rigid (green line) RBC suspension, as a function of the flow rate ratio Q/Q_{plasma}; Hct = 1%.

7.4 Summary

The preliminary results presented in this chapter were important as a first approach on how to manipulate the RBC suspensions, as well as to detect some limitations of the setup. We were able to separate the suspending medium from the main sample when using suspensions of small hematocrit (Hct = 1%). For larger hematocrits (Hct = 20%), the microfluidic devices presented here showed poor separation efficiency and, therefore, could not be used for subsequent analysis. Moreover, the experiment using a suspension of rigid RBCs provided a slightly worst, but not competitive separation efficiency when compared to the one achieved using healthy RBCs.

It is important to mention that these preliminary experiments were carried out before the detailed analysis of cell distribution inside microfluidic channels for low hematocris and low inertia carried out in Chapter 6. In fact they were the drive for such study. It is therefore likely that the peculiar RBC distribution inside the channel will have important implications on the suspension behaviour in the microfluidic features appearing downstream the main channel (for example on the cell separation when facing a bifurcation).

References

1. Fidalgo, J., Pinho, D., Lima, R. & Oliveira, M. S. N. VipIMAGE 2017. **27,** (2018).

2. Forsyth, A. M., Wan, J., Ristenpart, W. D. & Stone, H. A. The dynamic behavior of chemically 'stiffened' red blood cells in microchannel flows. *Microvasc. Res.* **80,** 37–43 (2010).

3. Rodrigues, R. O., Faustino, V., Pinto, E., Pinho, D. & Lima, R. Red Blood Cells deformability index assessment in a hyperbolic microchannel : the diamide and glutaraldehyde effect. *Webmedcentral* 1–11 (2010).

4. Fahraeus, R. & Lindqvist, T. The viscosity of the blood in narrow capillary tubes. *Am. J. Physiol.* 562–568 (1931).

5. Calejo, J., Pinho, D., Galindo-Rosales, F. J., Lima, R. & Campo-Deaño, L. Particulate blood analogues reproducing the erythrocytes cell-free layer in a microfluidic device containing a hyperbolic contraction. *Micromachines* **7,** 1–12 (2016).

6. Tripathi, S., Varun Kumar, Y. V. B., Prabhakar, A., Joshi, S. S. & Agrawal, A. Passive blood plasma separation at the microscale: a review of design principles and microdevices. *J. Micromechanics Microengineering* **25,** 083001 (2015).

CHAPTER 8

Conclusions and Future Work

In this thesis, we make use of a range of microfluidic geometries intelligently designed to generate specific flow dynamics for the study of deformable biological objects under flow. Biological polymers, such DNA, and biological particles, such as red blood cells, were used to probe the efficiency of these devices, identify practical challenges to their use and propose and/or develop enhanced approaches. The work performed also provides some new insight on the behaviour of biological deformable objects transported along microfluidic geometries.

The first experiments reported in this thesis were performed in bifurcating microfluidic networks, the dimensions of which are defined according to a biomimetic design rule.[1] These networks were designed to generate specific shear stress distribution along the consecutive channel generations as a function of the varying channel dimensions. Such geometries have already been studied by means of numerical simulations but, in this thesis, we performed the first experimental investigation. We have shown the ability of the networks to provide a customised flow field, and in particular a customised wall shear-stress along the network as predicted numerically/theoretically and have, in addition, identified the experimental limitations of such an approach, difficult to predict from a theoretical or numerical point of view. Using typical microfluidic fabrication techniques, the devices were produced in PDMS and the flow characteristics inside the devices were studied using particle tracking velocimetry and by visualising a dilute solution of fluorescently labeled λ-DNA molecules. Our results showed the expected kinematics and that the molecules' deformation along the consecutive branches is a function of the channel dimensions, and therefore, a function of the shear stress there applied. The results obtained from two distinct geometries, of constant and increasing shear stress, were plotted in a master curve of fractional extension versus Wi, showing a good agreement with the results previously obtained for DNA molecules under shear flow generated by two parallel plates. The results validated the use of the network geometry for the investigation of the response of suspended particles or polymers to well controlled shear stresses. The major difficulty found when using such geometries is the error between expected and real geometry dimensions, which eventually leads to smaller shear

stresses than expected. We understand this discrepancy is a limitation of the fabrication process and suggest using a more accurate procedure when producing such geometries, for example, using chrome masks to achieve more accurate dimensions and, therefore, an overall performance closer to the theoretical prediction.

The same model polymer was subsequently used to assess the performance of microdevices designed to provide a region of homogeneous extensional flow. In this case, we intended to observe the dynamics of DNA molecules travelling along optimised converging-diverging channels, which are able to generate extensional flow of constant strain rate, over long distances along the channel centreline and at channel mid-height. As in the previous study, the channels were initially investigated using numerical simulations,[2] but no experimental implementation had been done. To observe molecules with good image quality over long times, molecules need to be tracked during their transport in the flow geometry. While in the customised networks experiments, the molecules travel at a slow and constant velocity along each of the straight channels, and the tracking can be performed manually by moving the microscope stage at constant velocity, here, the molecules displace at a non-constant velocity as they flow through the contraction-expansion region, reaching high velocity values at the channel contraction. In order to overcome this problem, a new experimental tracking mechanism was developed with the aim of displacing the microscope stage with a velocity as close as possible to the velocity of the transported object. In this way the molecule can be kept in the image frame and image blur can be minimised. The tracking is triggered manually when a molecule is found close to the region of interest (on the channel centreline and in the centre of the image frame). Small deviations from this desired position lead to increased discrepancy between the microscope stage movement and the velocity of the object, which would generate a relative velocity, causing blur and consequent inaccuracy in the data analysis. The tracking mechanism was found successful for objects of larger sizes, as actin filaments with a length around 12-60μm. It however turned out to be more difficult when tracking λ-DNA molecules. The reason is mainly due to the small molecule size in equilibrium (coiled shape), where it becomes difficult to detect the molecule and trigger the tracking at a precise moment and thus position of the molecule. Also, a larger extension rate, compared to actin filaments, is necessary to deform the molecule implying a larger velocity at the contraction, making the process more likely to generate a relative velocity and blur. Possible improvements as an automatic trigger will hopefully make it possible in the future to also work with small molecules as DNA in our optimised geometries. We believe the combination of an optimised flow geometry with the particle tracking that has been

developed in this thesis, in collaboration with colleagues at ESPCI, will prove very useful for the study of deformation and transport of biological particles as red blood cells, protein aggregates or even bacteria.

The second part of this thesis focused on the study of dilute suspensions of animal RBC flowing in microfluidic geometries of different topology. During the analysis of the cell distribution inside the microfluidic networks, we observed a peculiar two-peak density profile of cells along the width of the channel, and have decided to investigate it in more detail. For this purpose we used simple straight channels of rectangular cross-section, typical of microfluidics and analysed the distribution of the cells as well as the thickness of the cell-free layer along the channel. To complement the experimental results, numerical simulations were performed by colleagues at the University of Edinburgh, representing a dilute RBC suspension flowing in a straight channel of similar dimensions.

Overall, a qualitative agreement was found between experiments and numerical simulations, with both confirming the presence of regions with higher cell concentration close to the cell free layer developed at the channel walls. This type of distribution has previously been observed for flow conditions where inertia plays a role and is known as the Segré-Silberberg effect. In our experiments, however, inertia is negligible since we work in the Stokes flow regime (in our experiments Re << 1) and the two-peak distribution has therefore a different origin. Our understanding is that the distribution found in our case is related to the deficiency of hydrodynamic interactions among cells in the dilute limit, where cell diffusion is weak and unable to smoothen the density heterogeneities induced by the lateral migration of cells. As a consequence, the density profiles are predominantly determined by the distribution of lift velocities within the suspension, which exhibits distinct patterns for the horizontal and vertical directions of the rectangular cross-section microchannels (where the depth is different from the width and therefore the aspect ratio is different from 1). We found in our experiments that we require at least ~46D_h for the development length of the distribution profile and cell free layer, which is clearly in excess of previous values referred to in the literature[3] and the typical lengths used in experimental microfluidics. Additionally, depending on the inlet configuration, the initial distribution of cells upon their entry into the channel varies substantially, which brings extra complexity to the restoration of a converged density profile and the development of an equilibrium cell free layer. These factors highlight how important it is to consider the design of the channels and inlet conditions in experiments and to have a proper simulation initialisation strategy for the simulations.

Therefore, our findings highlight the importance of local and transient characteristics in the

distribution of cells that should be considered when designing experiments and simulations in dilute suspensions of cells under conditions of low-inertia. In addition, numerical simulations have been proven to be in good agreement with experimental results and can in the future be used to help designing the microfluidic devices.

Finally, we tested other microfluidic geometries on the flow of RBC suspensions, analysing the impact of parameters such as the hematocrit, the flow rate or the bifurcating angle on the development of the CFL along the channels of customised networks. Also, a new set of microfluidic geometries were used to study the dynamics of dilute and semi-dilute RBC suspensions, where the parameters of study were the effect of sudden expansions and bends along the channel. We verified that the introduction of these geometrical features in the microfluidic geometry improves the thickness of the CFL developed close to the channel walls. Therefore, making use of the geometry for which the CFL formed was the more significant, we tested the separation of the suspending medium from the RBCs, for a semi-dilute suspension, by opening a plasma channel perpendicular to the region of the channel where the CFL was thicker (segment closer to the channel outlet). Using suspensions of healthy and rigid RBCs, we found that the separation efficiency between the two experiments was very similar and thus further changes would need to be implemented in the microfluidic geometry to improve its performance.

In summary, we believe the experiments performed in this thesis are of significant importance when planning studies using dilute suspensions/solutions of deformable objects. We provided new insight on customised network geometries, presenting the experimental details and respective limitations. We also developed a new tracking mechanism, able to follow microfluidic objects transported along microfluidic devices of non-continuous velocity. Finally, we provide interesting information on RBC dilute suspensions flowing inside microfluidic channels typically used for microfluidic purposes, which may be of great importance for the design of future experiments.

References

1. Fidalgo, J., Zografos, K. & Casanellas, L. Customised bifurcating networks for mapping polymer dynamics in shear flows Customised bifurcating networks for mapping polymer dynamics in shear flows. *Biomicrofluidics* **064106,** (2017).

2. Zografos, K., Pimenta, F., Alves, M. A. & Oliveira, M. S. N. Microfluidic converging/diverging channels optimised for homogeneous extensional deformation. *Biomicrofluidics* **10,** 1–21 (2016).

3. D., K., G., G. & D.A., F. Microvascular blood flow resistance: Role of red blood cell migration and dispersion. *Microvasc. Res.* **99,** 57–66 (2015).

Appendix A

Mould production using 3D printing

The mould design used to test the 3D printing techniques is very simple. It consists of a flat base with a T-junction printed in positive relief (as for the SU8 moulds) with dimensions presented in Figure A1. The edges of the mould are taller (~4mm) to avoid the spillage of liquid PDMS. Since all the experiments presented in this thesis were performed in microchannels of depth ≤ 100µm, a constant depth of 100µm was also considered here.
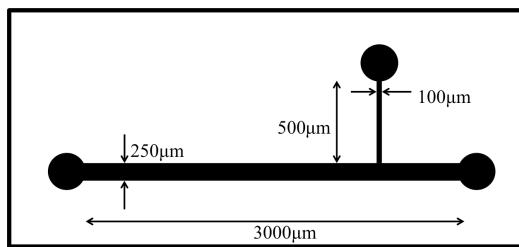

Figure A1: Schematic representation of the mould: T-junction with a main channel (width = 250µm) and side channel (width = 100µm); constant depth = 100 µm.

The moulds were produced using two distinct technologies: stereolithography (SLA) and Polyjet. SLA consists in using a laser to cure the solid parts of a liquid photopolymer resin placed inside a container. The laser cures a constant layer at the bottom of the container while the solid part is continuously moved vertically. This technique requires posterior washing and post-curing of the solid part. In Polyjet 3D printing, tiny droplets of photopolymer are deposited in the substrate followed by curing using a UV light, before another polymer layer is deposited again.

In a first approach, we used the SLA printer (Formlabs Form2) available in the laboratory (University of Strathclyde). This experiment was performed at an early stage and the protocol for printing in such device was not yet optimised. The mould obtained presented a very rough surface. After achieving these first results, we contacted the platform 3D Hubs UK, were foreign companies produce moulds by 3D printing using different technologies.

In the following section, we describe the features of the moulds obtained and the major limitations. It is important to mention that for the moulds here studied, a longer curing time than 2 hours at 70°C (standard procedure) was necessary to cure the PDMS bulk.

1. **Stereolithography (SLA)**

Institution/ Company: University of Strathclyde and Lightning Lab
Material: Formlabs clear resin (FLPCL02) and Formlabs standard black (FLGPBL02),
respectively.
Printer: Formlabs Form 2
Layer resolution: 25 μm
PDMS curing parameters: 70°C (17 hours)
Printing cost/mould: ~15£

The mould printed by SLA presents a slightly ribbed surface, due to the position of the solid while printing (Figure A2a and Ab). Despite that, the PDMS was successfully cured and posteriorly bonded to a glass slide using the standard procedure described in Chapter 3 (Figure A2c). The microdevice is functional and does not present leakage for flow rates smaller than 10mL/h.
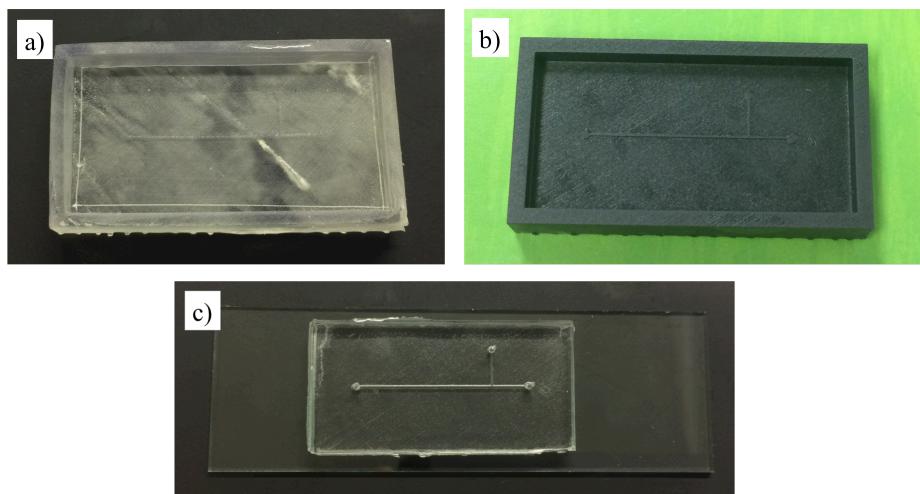

Figure A2: SLA methodology: (a) mould printed at the University of Strathclyde using clear resin; (b) mould printed by external company using black resin; final microdevice using mould produced with black resin, which provides better resolution.

The microscopic analysis of the PDMS surface and channel cross-section is presented in Figure A3. The PDMS in contact with the mould presents a slightly rough texture and the cross-section is very different than the one achieved by photo and soft lithography techniques. The channel base is much wider than the theoretical dimensions and the channel depth at the centre is always smaller than 100μm.

The moulds produced by SLA methodology presented here can still be improved, for example, by increasing the number of printing hours. However, we believe that the final

microdevices would always present limitations to perform the type of experiments described in this thesis, where the channel dimensions should be as accurate as possible.
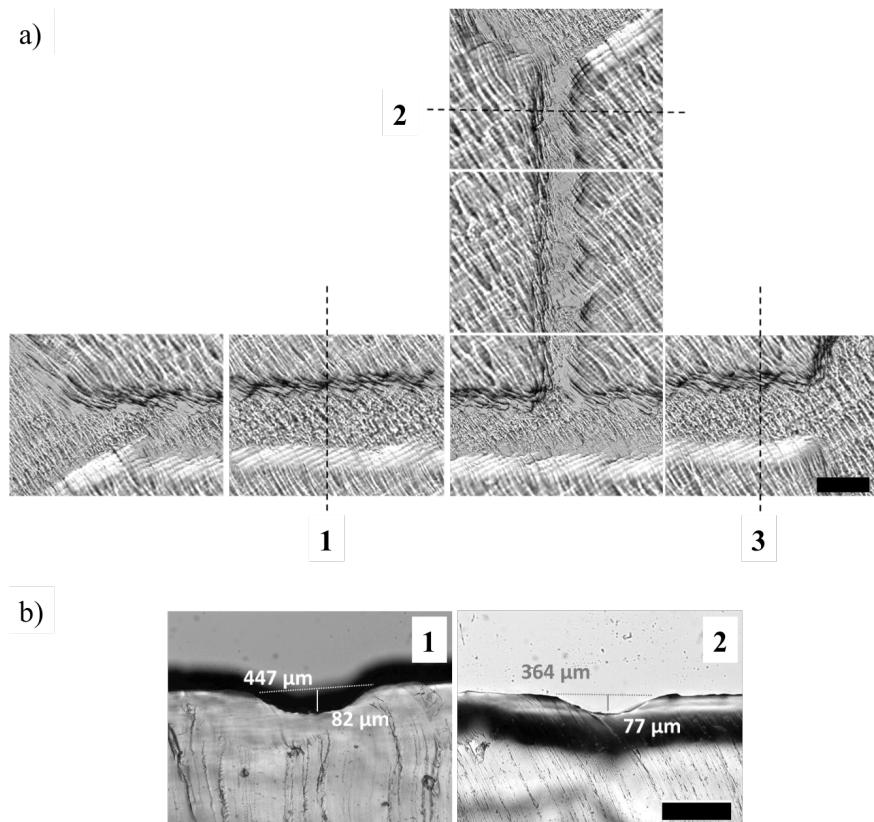

Figure A3: Microphotograph of the (a) PDMS surface and (b) channel cross-section (SLA methodology). Scale bar 200 μm.

2. **POLYJET**

Company: STEP 3D
Material: VeroGrey RGD850 (RIGID OPAQUE MATERIALS)
Printer: Objet Eden 250
Layer resolution: 30μm
PDMS curing parameters: 70°C (24hours)
Printing cost/mould: ~64£

Since the mould obtained by polyjet technology is far more expensive than SLA, we analysed a sample provided by the company with part of the original channel design (T-junction). The mould surface is much smoother than the one obtained by SLA and the PDMS bonding to the glass substrate is stronger, allowing to manipulate flow rates smaller than 100mL/h without leakage. Figure A4 presents the image of the mould sample and the microdevice.
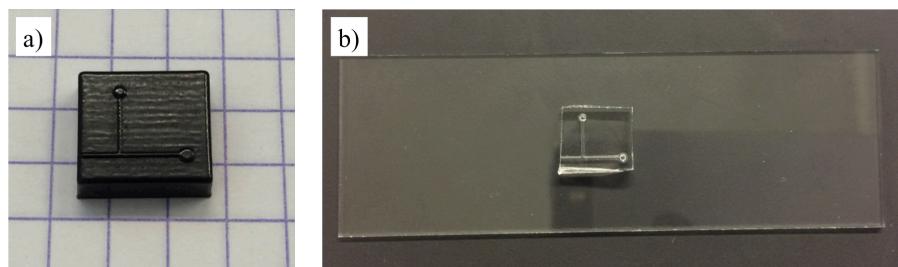
Figure A4: POLYJET methodology: (a) mould printed by external company; (b) PDMS microdevice.

Finally, the analysis of the PDMS surface and channel cross-section at the microscope revealed a much smoother channel, with better-defined limits (FigureA5a). Unfortunately, the channel dimensions are still much different than expected (larger and shallower channels), which can present a problem for experiments using particles since these might get trapped in the channel edges in contact with the glass slide.

Despite the results here presented, we believe both moulds tested can be used for simple experiments developed in the microfluidics laboratory.
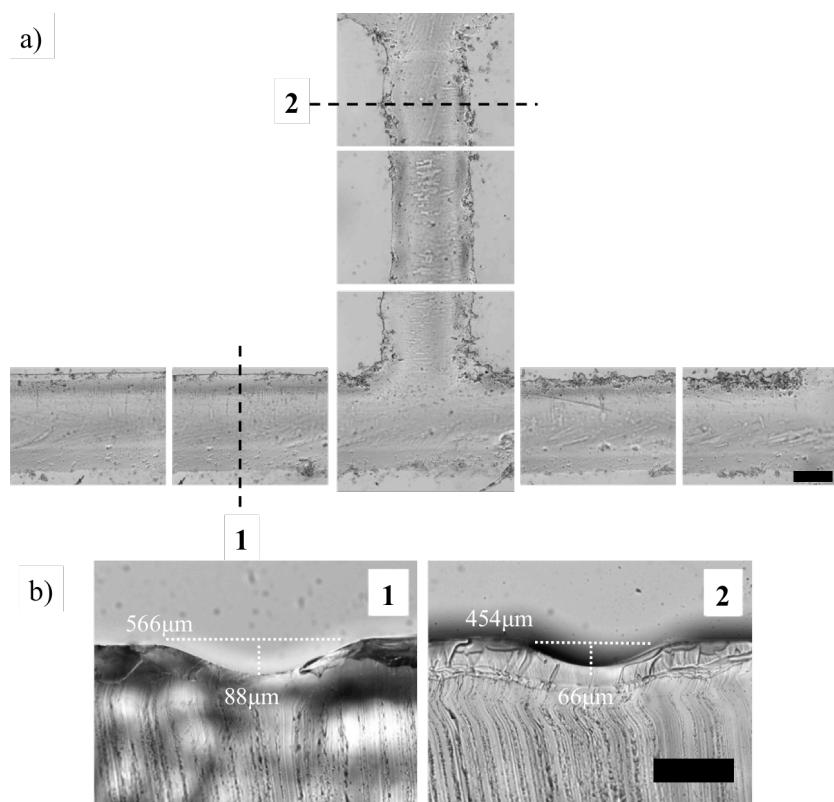

Figure A5: Microphotograph of the (a) PDMS surface and (b) channel cross-section (POLYJET methodology). Scale bar 200 μm.

Appendix B

Preparation of λ-DNA solution

The following section details the preparation of *λ-DNA in viscous buffer solution* used in the microfluidic experiments. This solution is composed of sucrose buffer solution Tris-HCl 10mM, β-mercaptoethanol 4%, oxygen scavenger solution, λ-phage DNA primary solution and YOYO-1 solution in the proportions presented below:

λ-DNA in viscous buffer solution (v/v):
1354 µL of sucrose buffer solution Tris-HCl 10 mM
58.4 µL of β-mercaptoethanol
14.6 µL of oxygen scavenger solution
29.2 µL of λ-phage DNA primary solution
3.6 µL of YOYO-1 solution

Each of the components mentioned previously are prepared using the following primary solutions:

Buffer solution Tris-HCl 10 mM (v/v):
145 µL of Tris 1 M
145 µL of NaCl 1 M
145 µL of EDTA 0.1 M
Adjust to pH = 8 if necessary and fill up with ultrapure water until the volume 14000 µL.

Sucrose buffer solution Tris-HCl 10 mM:
Similar solution to *Buffer solution Tris-HCl 10 mM* (described above) but using viscous sucrose aqueous solution instead of ultrapure water. The viscosity of this intermediate sucrose solution is 60 mPa s.

β-mercaptoethanol (v/v):

20 µL of β-mercaptoethanol (99% in water)

475 µL of ultrapure water

Oxygen scavenger solution (m/v):

3 mg of α-D-glucose

7.1 mg of glucose oxidase

2.5 mg of catalase

Water is added until completing the volume of 15 mL.

λ-phage DNA primary solution (v/v):

135 µL of buffer solution Tris-HCl 10 mM

0.5 µL of λ-phage DNA (in a solution of Tris-HCl 10 mM with 1mM EDTA;

$M_w = 31.5 \times 10^3$ KDa; concentration = 556 µgmL^{-1})

YOYO-1 solution (v/v):

497 µL of buffer solution Tris-HCl 10 mM

2.5 µL of YOYO-1 (in a solution of 1 mM in DMSO)

The λ-DNA in viscous buffer solution (0.04 ppm) was prepared the day before the experiments and kept overnight at room temperature protected from light to avoid photo bleaching. It is left under smooth stirring (5-10rpm) to allow the full labeling of DNA with the fluorescent dye.

Appendix C

Tracking biological objects in extensional flows

Table C1 presents the theoretical dimensions of the converging-diverging geometries used in the experiments on extensional flow. As expected, the real channels present larger dimensions, possibly due to the micro fabrication techniques used (photo- and soft-lithography) and consequently the real strain rate generated by the geometries in the optimised converging-diverging region is found smaller than the theoretical one.

Table C1: Nominal dimensions of the microfluidic geometries considered for the study on extensional flow and corresponding theoretical strain rate.

Geometry	1	2	3	
Wu (μm)	400	400	800	
Wc (μm)	50	50	100	
d (μm)	50	100	100	
Q (nL/s)	1.7	5.5	5.5	10
$\dot{\varepsilon}(s^{-1})$	1.61	2.43	0.65	1.18

Figure C1 presents the results from one of the experiments using optimised converging-diverging channels, where each number corresponds to one individual molecule. In Figure C1a we present the measured extension of each molecule at different x-positions along the channel length, denoting a stronger extension close to the channel contraction. Figure C1b presents the difference between the molecule x-position (centre of mass) in the frame relative to the reference position in the channel (centre of the frame for which the velocity conditions are predicted).
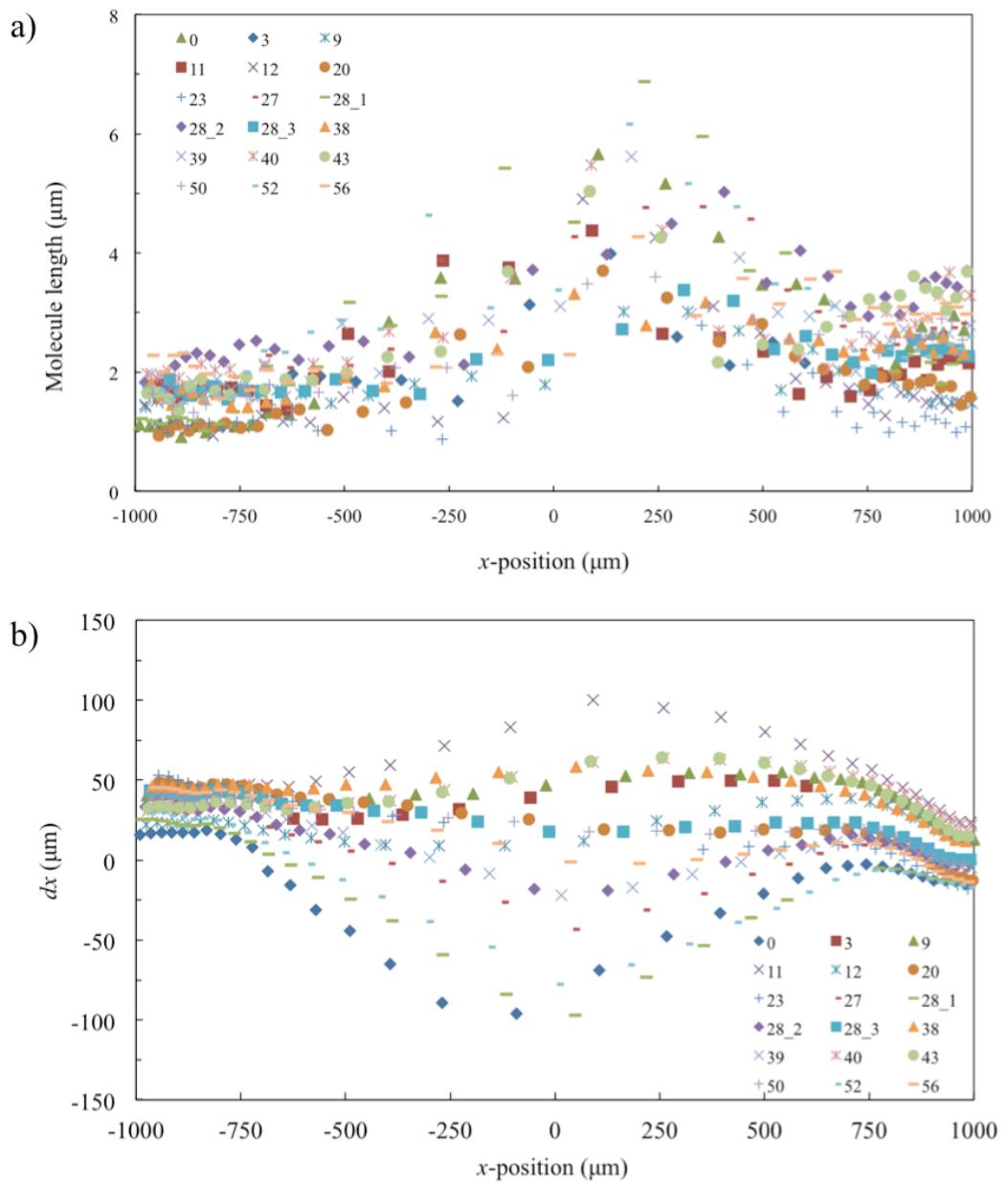
Figure C1: Tracking λ-DNA molecules along optimised converging-diverging geometry. (a) Measured molecule length as a function of the channel length (x-position); (b) Distance between the molecule position in the frame (centre of mass) and the reference position (centre of the frame) as a function of the channel length position (x-position). Geometry 2, Q_{total} = 5.5nL/s, Q_2/Q_1 = 10.5.

Appendix D

Calculation of the real hematocrit (%)

The hematocrit test is the most commonly used method to determine the real hematocrit in a blood sample. It consists in introduced the sample into a glass capillary and subject it to a strong rotation in a centrifuge. The hematocrit is then determined by the ratio of the length occupied by the packed red blood cells over the total length of the sample, in percentage (Figure D1).
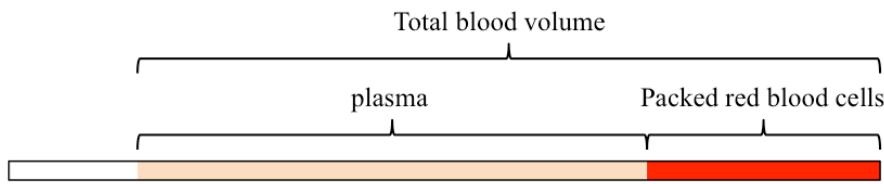

Figure D1: Measurement of the blood sample real hematocrit using a glass capillary tube.

The centrifuge available in our laboratory does not allow providing the required protocol. Therefore, we calculated the real hematocrit using an indirect measuring technique, based on the cell concentration determined by using a counting chamber. In our experiments we used an improved Neubauer chamber, with typical structure presented in Figure D2. This specific chamber is divided into 3x3 large squares of $1mm^2$ and for the counting of RBC it is recommended to use the central square (red limit). This one is divided into 5x5 smaller squares of 0.2mm length and 5 of those squares were used for the cell counting (the 4 square corners and the central square). The chamber depth is 0.1mm. The samples were diluted in physiological solution to keep cell integrity and the cells were allowed to sediment at the chamber bottom before counting. The cell concentration is then determined by the following equation:

$$\text{Cell concentration } (\frac{cell}{\mu L}) = \frac{\text{counted cells}}{\text{Volume of the squares counted x dilution factor}}$$
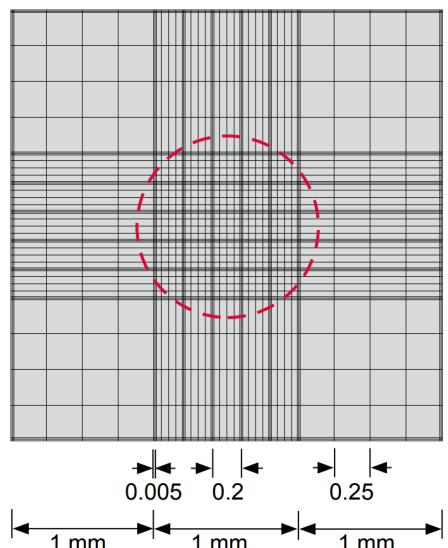
Figure D2: Scheme of the improved Neubauer chamber with respective dimensions.[1]

Assuming that the mean cell volume (MCV) of horse blood cells is 45fL[2], we estimated the real hematocrit corresponding to the nominal hematocrits prepared (1, 5, 10, 20 and 45%). Figure D3 presents the calibration curve relating real and nominal hematocrits (%).
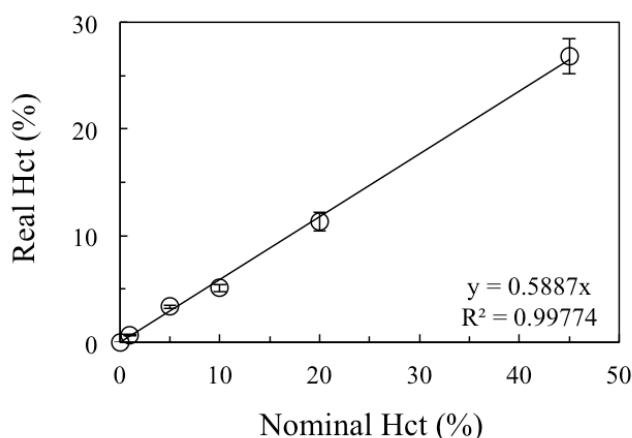

Figure D3: Calibration curve used to determine the real hematocrit.

References

1. Science Services. Counting Chambers. Available at: http://www.brand.de/fileadmin/user/pdf/GK900/Zaehlkammern/GK900_05_Clinical_ Lab_Zaehlkammern_e.pdf.
2. Windberger, U., Bartholovitsch, A., Plasenzetti, R., Korak, K. J. & Heinze, G. Whole blood viscosity, plasma viscosity and erythrocyte aggregation in nine mammalian species: Reference values and comparison of data. *Exp. Physiol.* **88,** 431–440 (2003).

Appendix E

Conference paper

Red blood cells (RBCs) visualisation in bifurcations and bends

Joana Fidalgo[1a], Diana Pinho[2,3], Rui Lima[2,4], Mónica S. N. Oliveira[1]

[1] James Weir Fluids Laboratory, Department of Mechanical and Aerospace Engineering, University of Strathclyde, Glasgow G1 1XJ, UK;
[2] Transport Phenomena Research Center, Department of Chemical Engineering, Engineering Faculty, R. Dr. Roberto Frias, 4200-465 Porto, Portugal
[3] Polytechnic Institute of Bragança, ESTiG/IPB, C. Sta. Apolonia, 5301-857 Bragança, Portugal.
[4] MEtRiCS, DME, School of Engineering, University of Minho, Campus de Azurém, 4800-058 Guimarães, Portugal;

Abstract

Bifurcating networks are commonly found in nature. One example is the microvascular system, composed of blood vessels consecutively branching into daughter vessels, driving the blood into the capillaries, where the red blood cells (RBCs) are responsible for delivering O2 and up taking cell waste and CO2.

In this preliminary study, we explore a microfluidic bifurcating geometry inspired by such biological models, for investigating RBC partitioning as well as RBC-plasma separation favored by the consecutive bifurcating channels.

A biomimetic design rule [1] based on Murray's law [2] was used to set the channels' dimensions along the network, which consists of consecutive bifurcating channels of reducing diameter. The ability to apply differential flow resistances by controlling the flow rates at the end of the network allowed us to monitor the formation of a cell-free layer (CFL) for different flow conditions at haematocrits of 1% and 5%. We have also compared the values of CFL thickness determined directly by the measurement on the projection image created from a stack of images or indirectly by analyzing the intensity profile in the same projection.

 The results obtained from this study confirm the potential to study RBC partitioning along bifurcating networks, which could be of particular interest for the separation of RBCs from plasma in point-of-care devices.

Keywords: RBC; bifurcating networks; cell-free layer; microcirculation

Introduction

Microfluidic devices have been widely studied for applications in medical diagnostics [3]. In particular, they present a good alternative for the process of plasma separation from whole blood since it requires a small volume of sample taking advantage of the geometry design and complex blood rheology at the microscale [4]. Ideally, the efficiency of this process should be high enough to allow the pure plasma to be analysed *in-line*, on the same platform device, usually for protein or other analyte detection. Even though several distinct approaches have been explored so far, the passive separation methods are always preferred since they require simpler setup, are cost effective and easier to integrate with biosensors. In addition, these methods usually subject the cells to smaller stresses ensuring the integrity of the original sample [5].

In this preliminary study, we investigate the use of bifurcating networks for purposes of plasma separation by testing suspensions of RBC in dextran 40 solution. Taking advantage of the typical blood flow effects such as the plasma skimming and Zweifach-Fung effect (bifurcation law), the cell-depleted layer (CFL) formed close to the channel walls continues to flow into the channels of the forward generations. Taking into consideration that the CFL thickness is regularly used to quantify the separation efficiency and that there is no unique way to define it since the boundary outer cell-plasma is diffuse [6], we propose a systematic method for measuring the CFL along the channels based on the intensity profiles obtained after image processing.

Materials and Methods

The preliminary results presented in this paper were obtained from microfluidic experiments using animal blood. The procedures for RBC sample preparation and PDMS device production are described below.

Microfluidic geometry:

The microfluidic geometry consists of a series of 180° bifurcations, with each channel dividing into two equal daughter branches, followed by a 90° bend. Figure E1 illustrates the schematics of the network, which is symmetric along *x*-axis and composed by 4 generations of channels (i = 0, 1, 2 and 3). This geometry was originally designed to impose uniform average wall shear stress distribution along the network to mimic the blood flow conditions found in healthy vessels. The channels' widths determined by a biomimetic design rule [1] are given in Table E1 for a constant depth of ~100 μm.
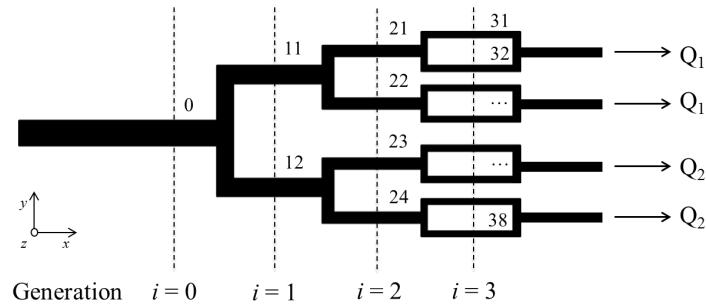
Figure E1: Schematics of the symetric microfluidic geometry used. The bifurcating network is composed of 4 generations (i = 0, 1, 2 and 3) and the fluid is pulled from the 4 outlets; black arrows indicate the flow direction. To study the effect of the flow rate ratio, Q_2 was varied in two of the streams, while Q_1 in the two remaining streams is kept constant.

The SU-8 mould and PDMS microchannels were produced using standard microfluidic technics (photo and soft-lithography, respectively) and the channels were sealed to a glass slide using oxygen plasma treatment (ZEPTO, Diener) for a faster and stronger surface bonding.

Table E1: Channels dimensions.

Dimension (μm)	Channel generation (i)			
	0	1	2	3
Width, w	202.5	120.0	80.0	55.0
Depth, h		97.2		

Blood sample preparation:

The blood sample was collected from healthy sheep and stored at 4oC with anticoagulant ethylenediaminetetraacetic acid (EDTA) until further use. All procedures for the collection of blood were carried out in compliance with the Ethics Committee for Animal Experimentation of IPB (Bragança, Portugal). The sample was centrifuged at 2000 rpm for 15 minutes and the supernatant (including plasma, white blood cells, platelets, proteins and other molecules) was discarded. Red blood cells (RBCs) were washed twice using physiological saline solution (NaCl 0.9% w/v) using the same centrifuging conditions. The cells were then suspended in Dextran 40 (Dx40) according to the desired haematocrit (Hct) as defined by:

$$Hct = \frac{V_{RBC}}{V_{(RBC+Dx40)}} \tag{1}$$

In this work we used Hct of 1% and 5%.

Experimental setup and image analysis:

The microfluidic device was connected to 4 glass syringes of 100μL (SGE) using flexible tubbing and the flow rates Q_1 and Q_2 were independently manipulated using a precise syringe pump (neMESYS, Cetoni) with 2 modules, one for each flow rate.

The images and videos were obtained using an inverted microscope OLYMPUS CKX41 and a high-speed camera (i-speed LT, Olympus). Image analysis was performed using ImageJ open software, based on the Z–projection of the stack of frames, using different intensity criteria (median or standard deviation) depending of the parameters to be analysed. The projections using the median intensity were used for CFL measurement as well as to investigate the RBC distribution inside the channels by examining the correspondent intensity profiles, as will be discussed further in the results. Figure E2 presents typical images obtained during experiments and after image processing. Initially, a stack of bright field images from the region of interest is obtained (see Figure E2a for bifurcation $i = 0 \rightarrow 1$, including branches 11 and 12). Using ImageJ, a median intensity projection using Z-project is created from a stack of at least 80 images and the two regions of interest are defined (Figure E2b) and analysed in detail using intensity profiles.
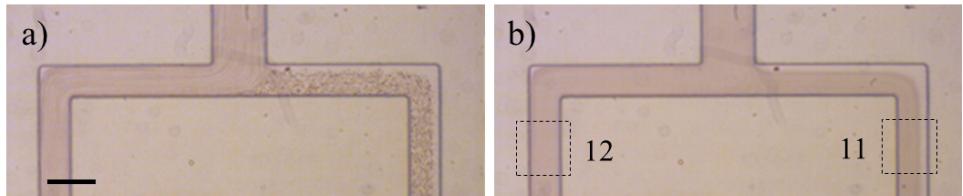

Figure E2: Typical bright field microscopy image obtained in these experiments (a); image obtained from the stack (80 frames) using the median intensity projection method; scale bar corresponds to 200 μm.

Results and discussion

Figure E3 presents the effect of flow rate ratio Q_2/Q_1, in the development and evolution of a CFL downstream of the first bifurcation of the network (for $i = 0 \rightarrow 1$). As it can be observed, the CFL formed in the smaller flow rate channel (named channel 11) increases as a function of the flow rate ratio. This RBC distribution at the bifurcation is a result of the combination of the flow conditions imposed and the blood complex rheology. This behaviour has been well documented in previous blood flow studies in different bifurcation geometries [4], [7].
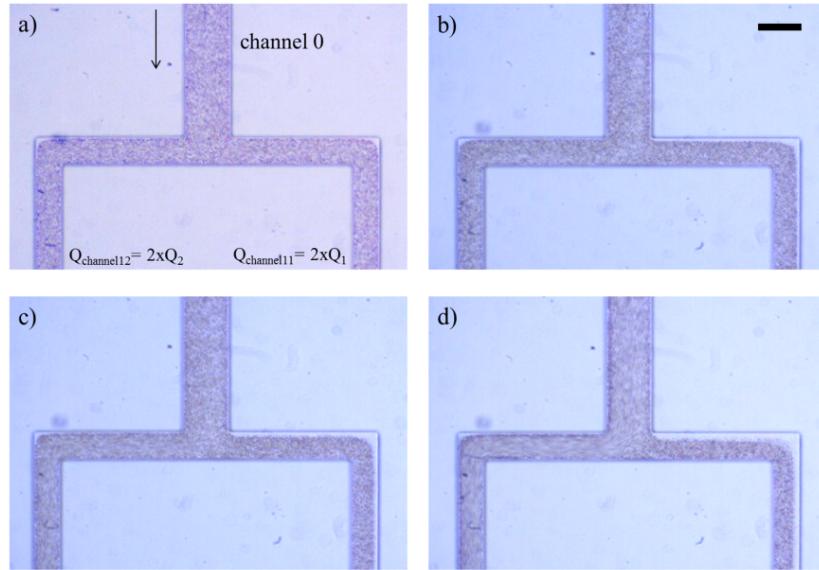
Figure E3: Effect of increasing flow rate ratio (Q_2/Q_1) on the CFL formed downstream of the first bifurcation ($i = 0 \rightarrow 1$) for Hct = 5%, and Q_2/Q_1 of a) 1, b) 10, c) 20, d) 40. The black arrow represents the flow direction and the scale bar corresponds to 200 μm.

Due to the cell deformability, the velocity gradient across the channel width (as a result of parabolic profile in both x- and z-directions) and the effect of the wall, the cells tend to be displaced towards the centre of the channel [8], [9]. This particular effect is enhanced when confinement becomes stronger; this is, with dimensions compared to a few RBC diameters. The cell migration has a strong effect on the suspension viscosity since the higher haematocrit at the centre generates a larger bulk viscosity, while the region depleted of RBC close to the walls (cell-free layer) has a smaller viscosity, acting as a lubricant for the remaining fluid [10], [11]. Even though this CFL is not easily detectable in Figure E3a, it is present even along the main channel due to the small geometry dimensions (this can be seen clearly for 1% Hct using higher magnifications, not shown here due to space considerations). This effect of plasma skimming will influence the way RBC divide when encountering a bifurcation. When the suspension of particles (RBCs) faces an asymmetric bifurcation, which in this case is determined by the unequal flow rates imposed in channels 11 ($2 \times Q_1$) and 12 ($2 \times Q_2$), the volume fraction of RBC is larger in the daughter branch with the larger flow rate (channel 12) than in the branch with the lower flow rate (channel 11). This is the so called Zweifach-Fung effect which is directly influenced by the cell distribution at the inlet [12]. We intend to explore this phenomenon in our customised geometries for plasma separation, since each bifurcation allows the reduction of haematocrit and the formation of a large CFL in specific branches along consecutive generations, as is demonstrated on Figure E4.
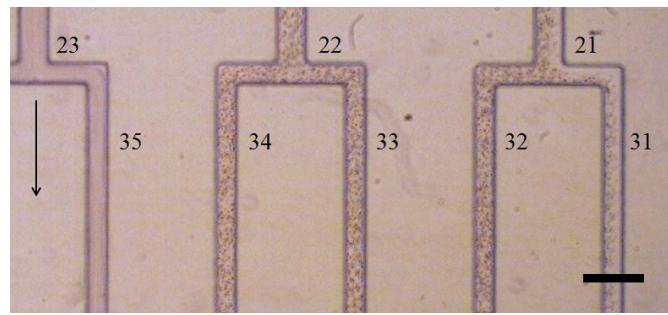
Figure E4: Real image of the channels on the latter generations ($i = 2$ and $i = 3$) corresponding to the flow conditions presented in Figure E2; 1% Hct; $Q_2/Q_1 = 40$; 200 μm scale bar.

Providing accurate measurements of the thickness of the cell-free layer is always a challenge. First, there is no exclusive way to define the CFL as discussed by Kruger [6], since the threshold between the RBC region and the CFL is diffuse, which is further complicated by the fact that in experiments this diffuse layer is uneven. Here, we try to assess the CFL thickness using different methodologies and discuss its impact on the values measured. Figure E5 presents the CFL thickness measured on channel 11 as a function of the flow rate ratio, for Hct = 1% and 5%. This measurement was made by user inspection directly in the image obtained via the median intensity projection method using the Z-project plugin from ImageJ. Qualitatively, it is clear that the CFL thickness is higher for lower Hct and that the size of the cell-free layer in channel 11 increases as Q_2/Q_1 increases for the range of flow rate ratios considered. The right edge of both curves seem to plateau for $Q_2/Q_1 = 100$ since after a certain flow rate ratio, the number of cells entering the smaller flow rate channel (11) continues to decrease, but they tend to occupy a large section of the channel width. Because the cells are more dispersed, the CFL limit becomes highly diffuse and the measurement of its thickness, following this method, is not reliable anymore.
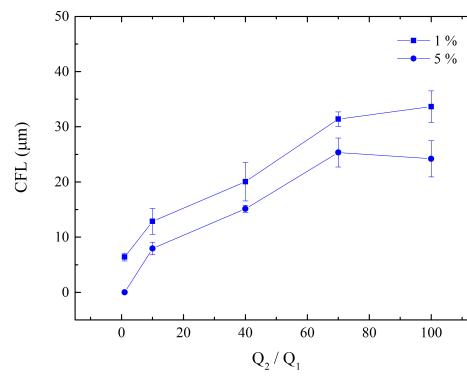

Figure E5: Effect of the flow rate ratio (Q_2/Q_1) on the CFL thickness directly measured along the channel 11 (generation $i = 1$) for Hct of 1% (squares) and 5% (circles) using a median intensity projection method.

Figure E6 presents the RBC diverging point for different flow rate ratios. For $Q_2 = Q_1$, the cells divide in the position corresponding to the main channel centreline and, as the flow rate ratio increases, the RBC diverging point displaces towards the channel 11 (e.g. $Q_2/Q_1 = 40$). For low flow rates ratios the edge between the outermost RBCs and the CFL is relatively sharp (Figure E6a), but for large flow rate ratios, the edge becomes blurred (Figure E6c) and the methodology is particularly user subjective.
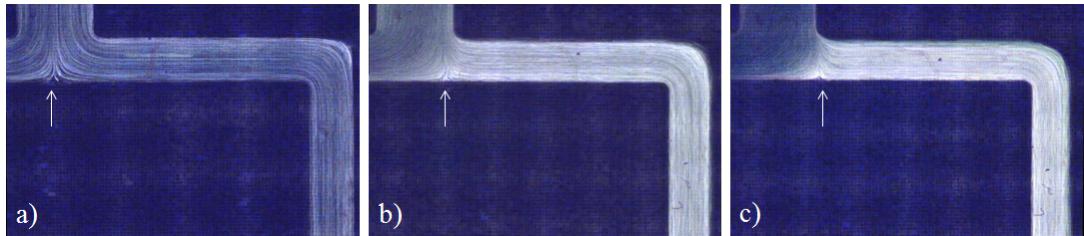

Figure E6: Evolution of RBC diverging point as a function of flow rate ratio $Q_2/Q1$ of 1 (a), 10 (b) and 40 (c) for sample 1% Hct. The images are a Z-Projection of the stack using the standard deviation intensity; 200 μm scale bar.

In the second methodology adopted, we used the intensity profiles obtained from the Z-project to assess the CFL thickness. Figures E7a and E7b show the superposition of the projection image and the intensity profile obtained for channels 12 and 11, respectively. As it is easily observed, the projection for the channel with larger flow rate (12) is very homogeneous suggesting a similar distribution of cells along the channel width. For channel 11, however, there is a lateral peak close to the outer wall corresponding to the CFL. Several thresholds of intensity were considered to determine the limit of the CFL. The final CFL thickness would then correspond to the distance from the channel inner wall to the y-position where the intensity reaches the defined threshold (expressed as % of variation of intensity between the maximum value and the average value within the centre of the bulk cell region). Table E2 shows the comparison between the CFL measured directly in the image using the visual inspection procedure (Figure E7b, dashed line) and the CFL determined using the intensity profile considering different values for the threshold (100, 90, 80, 70, 60 and 50%), where 100% corresponds to the Dx40 solution flowing without cells.
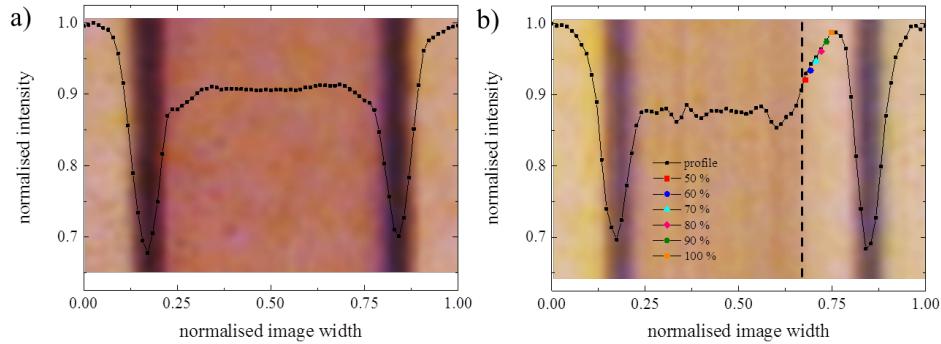
Figure E7: Indirect measurement of CFL thickness using intensity profiles. Superposition of the projection image and the corresponding intensity profile for channels 12 and 11 (a and b, respectively) for 1% Hct and $Q_2/Q_1 = 40$. The colour symbols in part b) identify the different thresholds considered and the vertical dashed line corresponds to the CFL limit determined by visual inspection.

Table E2: Comparison between CFL thickness (μm) measured directly from visual inspection of the median intensity projection and using the intensity profile for 1% Hct and $Q_2/Q_1 = 40$.

Direct measurement from *Z-Projection* image using median intensity	Indirect measurement using the intensity profile (*Z-Projection* median intensity) considering different percentages of the maximum intensity as threshold					
	% of maximum intensity	50	60	70	80	90	100
20.04 μm	CFL (μm)	20.94	18.52	16.10	13.68	11.25	8.83

The value obtained by visual inspection (20.04 μm) is close to the value considering the threshold of 50% using the intensity profile. It is clear that there are still a number of cells flowing inside the CFL and deciding which value of threshold is more meaningful is still a subject of debate. The advantage in the case of this methodology is that the CFL thickness would be systematically measured for all the cases, this is, for flow conditions for which the layer is well defined and for the cases when the boundary CFL-cell bulk is not perfectly clear. This would also avoid the personal subjectivity when defining the CFL limits.

Conclusion

The execution of preliminary experiments in bifurcating networks confirmed the potential of using this type of geometries for blood-plasma separation. Due to the bifurcation law, a CFL is easily formed in the first bifurcation and observed along the consecutive channels with smaller flow rates. In the present geometry with 4 generations of narrowing channels, the relative thickness of the cell depleted layer increases in relation to the total channel width, as the suspension moves along the network. We believe that by controlling the 4 outlets independently, for different ranges of total flow rate, overall separation efficiency could be enhanced. We have also demonstrated that the method for CFL measurement here proposed, based on the intensity profiles, establishes a reliable alternative to monitor the separation

process and, at the same time, allows consistency between measurements under different flow conditions, avoiding personal subjectivity when defining the limit between cell bulk and CFL.

References

[1]   K. Zografos, R. W. Barber, D. R. Emerson, and M. S. N. Oliveira, "A design rule for constant depth microfluidic networks for power-law fluids," Microfluid. Nanofluidics, vol. 19, pp. 737–749, 2015.

[2]   C. D. Murray, "The Physiological Principle of Minimum Work. I. The Vascular System and The Cost of Blood Volume," Proc Natl Acad Sci USA, pp. 207–14, 1926.

[3]   S. Sharma, J. Zapatero-Rodríguez, P. Estrela, and R. O'Kennedy, "Point-of-Care diagnostics in low resource settings: Present status and future role of microfluidics," Biosensors, vol. 5, no. 3, pp. 577–601, 2015.

[4]   V. Leble et al., "Asymmetry of red blood cell motions in a microchannel with a diverging and converging bifurcation," Biomicrofluidics, vol. 5, pp. 44120–15, 2011.

[5]   S. Tripathi, Y. V. B. Varun Kumar, A. Prabhakar, S. S. Joshi, and A. Agrawal, "Passive blood plasma separation at the microscale: a review of design principles and microdevices," J. Micromechanics Microengineering, vol. 25, no. 8, p. 83001, 2015.

[6]   T. Krüger, "Effect of tube diameter and capillary number on platelet margination and near-wall dynamics," Rheol. Acta, vol. 55, no. 6, pp. 511–526, 2016.

[7]   R. T. Yen, Y. Fung, and C., "Effect of velocity distribution on red cell distribution in capillary blood vessels," Am. Physiol. Soc., pp. 251–257, 1978.

[8]   D. Di Carlo, "Inertial microfluidics," Lab Chip, vol. 9, no. 21, p. 3038, 2009.

[9]   J. Zhang et al., "Fundamentals and applications of inertial microfluidics: a review," Lab Chip, vol. 16, no. 1, pp. 10–34, 2016.

[10]   A. S. Popel and P. C. Johnson, "Microcirculation and Hemorheology.," Annu. Rev. Fluid Mech., vol. 37, pp. 43–69, 2005.

[11]   D. A. Fedosov, B. Caswell, A. S. Popel, and G. E. M. Karniadakis, "Blood Flow and Cell-Free Layer in Microvessels," Microcirculation, vol. 17, no. 8, pp. 615–628, 2010.

[12]   A. Kumar and M. D. Graham, "Cell Distribution and Segregation Phenomena During Blood Flow," in Complex Fluids in Biological Systems, Springer, pp. 399–434, 2015.